

NORTHWESTERN UNIVERSITY

Investigation of Liquid-Phase Adsorption Processes in Metal–Organic Frameworks

A DISSERTATION

SUBMITTED TO THE GRADUATE SCHOOL

IN PARTIAL FULFILLMENT OF THE REQUIREMENTS

for the degree

DOCTOR OF PHILOSOPHY

Field of Chemistry

By

Riki J. Drout

EVANSTON, ILLINOIS

June 2021

© Copyright by Riki J. Drout 2021

All Rights Reserved

## Abstract

Commercial agriculture and industrial manufacturing have contaminated freshwater sources with persistent organic pollutants, heavy metals, and radioactive species. Effective mitigation of this pollution is paramount to safeguarding human health, animal and aquatic life, and the environment. Conventional adsorbents such as activated carbon, metal oxides, resins, and polymers attain moderate to high adsorption capacities and are commercially viable; however, these materials are often amorphous and difficult to characterize which impedes the rational design of next-generation sorbents. Metal–organic frameworks (MOFs) are porous, crystalline materials comprised of metal oxide nodes and organic linkers assembled into multidimensional lattices. Given their modular nature, MOFs are an ideal scaffold for systematically investigating the material properties that contribute to rapid and efficient toxin capture. Their inherent porosity facilitates diffusion and the periodic distribution of potential binding sites at nodes and linkers promotes high uptake capacities. After exploring the role that the nodes and linkers play in adsorption in my first publications, I aimed to determine the thermodynamic forces driving adsorption in MOFs. In the most recent studies I published, we demonstrated the suitability of isothermal titration calorimetry for tackling this challenge. I thoroughly examined how analyte and MOF structural features influence adsorption and I directly quantified the thermodynamic profile of the adsorption processes in several well-known Zr-based MOFs. This work advances the field by improving our ability to directly observe adsorption in MOFs, and future applications of this technique can enhance the study of catalysis and diffusion in these porous materials.

## Acknowledgments

I must first acknowledge the immense privilege that contributed to me reaching this position. Naming my privileges does not discount the work I did to get here; rather, I recognize that not all parents can invest large volumes of time and money in their children's education, not all students get to learn from teachers who look like them or have had experiences like their own, and many folks simply cannot attend graduate school because they would be unable to sustain their non-academic responsibilities. Yes, I worked incredibly hard for this degree, but when I started climbing the ladder, I was already a number of rungs from the floor.

My graduate research has earned me the opportunity to stand before you today, but my activities beyond the lab are what made me see this goal through to the end. As a volunteer with the Northwestern Prison Education Program, I have had the honor of working with students at Stateville Correctional Center and I've learned of the severe injustices perpetrated by the US criminal justice system. Benard and William, tutoring you in Study Hall and via correspondence over the past year, has been the single greatest privilege of my Northwestern career. You often wrote how much you appreciated my support, but it's you who have been teaching me, encouraging me, and supporting me, I will be forever grateful to have had this opportunity. To all NPEP students, your devotion to learning inspires me to continue fighting to establish a more equitable nation. To my colleagues on the Graduate Student Advisory Committee, especially Ollie, Jonas, Charlotte, Anne, Andrea, Steven, and Jennifer, I am so thankful I had the opportunity to learn from you and with you. Your conviction to make this world a better place is humbling and inspiring. Thank you, Jonas, for agreeing to speak at the 2019 New TA Conference and for putting

a good word in for me with the folks who managed Study Hall; I'd like to believe I still would have found NPEP, but thanks for being in the right place at the right time.

Omar, thank you for letting me carve my own path in terms of the scientific questions I pursued and in my development as an educator and activist. Joe and Chad, thank you for your insightful feedback, support, and encouragement to never settle. I also appreciate Pat and Shirley Ryan, whose generosity funds the Ryan Fellowship which has supported my graduate work the last three years.

Jonathan, we've been through some graduate school highs and lows together and I'm proud of us. Thank you for always having an open door or Zoom – you are a saint among us, and I am so grateful to have had your support these last five years. I have overwhelming gratitude for my therapist, who has helped me learn to acknowledge my own growth, find pride in the little victories, and believe that I am more than just my science.

I appreciate the God who always fans my spark into a flame at just the right time. My graduate school journey has not passed without rocking my faith, but the communities of St. Nick's and more recently, Old St. Pat's rekindled my belief that the domestic, lowercase c church is enough.

To all of the Northwestern teaching line faculty, working and learning with you has helped me develop my own identity as an instructor and mentor. Steph, I admire your boldness and commitment to always doing what is right; I hope to one day exude your goodness and confidence when standing before my colleagues and students. Thank you to the entire team at Northwestern's Searle Center for Advancing Learning and Teaching, particularly Lauren and Nancy. I appreciate your commitment to improving STEM education and your ability to embrace and work with my stubbornness. Prof. De Guire, thank you so much for letting me TA your class even though I

wasn't an engineer. To this day, I appreciate your willingness to let me experiment with different instructional practices and your deep respect for my commitment to teaching. Ellen and Rebecca, I will be forever grateful for your kindness, friendship, and mentorship, meeting you was the greatest gift of EXCEL. George, Laura, and Kristen, thank you for giving me the opportunity to teach with you at Beloit. To all of my EXCEL, Beloit, and Northwestern Gen Chem students, teaching you and learning from you brought me joy. Thank you for always being the spark that kept my flame burning.

My dearest Farhomies, thank you for your commiseration, sympathy, encouragement, and advice. Working with you made me a better scientist and leader. Timur, you were my first mentor in the group, and I will never forget you sliding a note across the Ryan 1004 table to answer the question I'd scribbled on my first set of subgroup slides. Ashlee, thank you for passing me the water research and for convincing Omar to spend \$600 on brand new pipettes for just me. Satoshi, though you often chuckled at my "lousy data," I am very grateful to have had the opportunity to work with you on the ITC. Chen (Chen), I will always admire your work ethic and unparalleled productivity, but more than that, I will strive to answer questions like you do because you never make people feel small, you are a rare gem in this academic world. Yongwei, you always told me I worked so hard even though you were in lab way more than me—thank you for your constant encouragement, kindness, and friendship. Xinyao(yao), Wei(wei), Kaikai, and Xingjie, without your company and support, there would have been way more ITC-induced meltdowns. Madeleine and Flo, working with you over the last few months handing over the ITC work has reminded me of the joy we can find in science and has certainly made me a better mentor. To all the folks I've worked with on writing, for proposals, for papers, for fellowships, etc. it's been a joy watching

you grow, and editing for and with you helped me grow too, as both a storyteller and a scientist. Thank you to all of the Farhomies who have also become some of my dearest friends, especially Megan, Rod, Kenton, Kent, Zoha, Karam, Louis, Isil, Tim, Sylvia, the list goes on. I am grateful every day to have had the opportunity to work with such an incredible team. I pray you all continue to care for, lift up, and support each other—together, you are stronger than the system.

Jen, Becky, Shaunna, Louis and Kaitlyn, and Zack and Ari, thank you for welcoming me into your circle. I definitely didn't envy you while you were going through the job hunt and defense cycles but having your guidance and support as I've gone through the same process a few months later has steadied my nerves. I am so thankful I had the opportunity to get to know each of you and watching you slay in this world brings me so much joy.

Elamar, Naomi, and Sarah, we did it! All four of us are leaving this place as doctors. How lucky am I to have met such an incredible group of women in my first year?! I can't think of a better group to have had by my side through this journey. Your boundless kindness and empathy gave me the strength to put one foot in front of the other during some of the toughest times in grad school.

To my undergraduate roommates, Christen, Jenny, and Mandy, thanks for your love and support from afar. Knowing you were there whenever I needed you was my security blanket. Dr. Christen Saccucci, your relentless pursuit of your goals despite whatever challenges that came your way has been a constant inspiration to me. Thanks for trekking all the way to Rosemont and Elmhurst to see me as often as you did.

To all of the teachers who nurtured my love of learning, even back when I was a ridiculously stubborn three-year-old trying to solve a puzzle way beyond me, I would have never earned this

Ph.D. if not for you. I am deeply grateful for all my Fairview teachers, specifically Ms. Hudson (now Mrs. Riesenber), Annette Freeman, and Mr. Druffel, who recognized my reading weakness, and ensured I caught up to my peers. I can't imagine having been able to do all the work I did at Walnut, Case, and Northwestern without the skills you first helped me develop. Frau Forbes, Herr Jacoby, and Frau Hofmann, you didn't squash my ferocity, rather, you encouraged me to refine it and use it for good; our world needs more teachers like you (who are hard-asses, but the good kind). Mr. Lazar, I am a chemist because of you and one day, when I return to the classroom, I pray I'll be a teacher like you too. Mr. C., thank you for existing. You kept me grounded at Walnut and your and Maurice's friendship since then has been a blessing. I will pester you to visit NYC (and us, obviously) until you do. Steve and Ray, thanks for being some of my earliest teachers of balance; you knew school was my priority, but you kept me in diving and that kept me sane. This slacker made it alright, didn't she?

I am thankful for my family who has encouraged me every step of the way. Grandma and grandpa, thanks for raising such a strong and independent woman to be my mom and thank you for your love and encouragement over the years. I will cherish our many memories especially Cincinnati State's Science Olympiad, pool day, baking cookies, and visiting papa at night school after a trip to Putz's for malts. Grandpa Bill and Grandma Joyce, thank you for my dad and his goodness and for always watching over us, I wish we could share a toast tonight. Drout Sprouts and company, thank you for your unwavering love, especially these last few years, and thank you for opening your hearts and homes to Lee. We are deeply grateful to know you're in our corner.

Lauren and Tanner, damn, I never knew I could get such an incredible sister- and brother-in-law. When Tanner visited Northwestern's BME department (and showed up for brunch early), I

could have never guessed we'd be family just a few years later, but I really hit a grand slam getting you two. I love you both, and your friendship, love, Snapchats, and Zoom calls revitalize my soul. Jill and Jeff and Dixon and Toni, and the extended Robison Fam Glam, thank you for welcoming me into your family, I'm honored and so very thankful.

Noah, thank you for your love and for fiercely defending my name. Thanks for caring more about being true to yourself than what other people think; you gave me the confidence to go out (or come out) and just be me. I love you and appreciate you.

Mom and dad, I owe it all to you. Thank you for the Discovery Toys and the schools you chose, MIW and Fairview, and the ones you let me choose, Walnut and Case. You never demanded academic excellence, but you gave me the best opportunities to achieve it if I wanted it. Thank you for your never-ending love and support, both emotionally and financially. I will forever appreciate the sacrifices you made to get me here. I one day hope to show my own children the unconditional love you've shown me my whole life, but particularly over these last three years. Dad, you've driven between home and Cleveland or Chicago many times, more often than not in the dark; thank you for always being ready to come see me. Mom, thank you for keeping my freezer stocked, ensuring there was always a taste of home when this was all just too much. And mom, thanks for being my first and longest best friend—I appreciate that you always answered the phone (even when you had a calc exam the next day). I love you two forever and thank you for everything. I am so excited to spend some pharma money with you.

Finally, my dear Lee, you are my greatest graduate school discovery. Getting to this point, emotionally and physically intact, would not have been possible without you by my side. I appreciate the roasting you gave me ahead of my qual and thank you for your rigorous, though

sometimes frustrating, editing. I have become the writer and presenter I am today because I tried so damn hard to win your praises. I know that I am not easy to support, particularly when I am under extreme levels of pressure owing to my unnecessarily-independent approach to challenges, but I thank you with my whole heart for the patience and compassion you've shown me over the last three years, and thousand-fold, during the last two months. I appreciate your unwavering commitment to my success, your tendency to force me to self-care (despite the monstrous fight I undoubtedly put up), and your ability to support all of my pursuits, no matter how consuming I can let them become. Above all, thank you for being my best friend. I'm so excited to see where this one beautiful life takes us. Love you forever.

# Table of Contents

Abstract .....	3
Acknowledgments.....	4
Table of Contents .....	11
List of Figures.....	16
List of Tables .....	24
Chapter 1. Introduction .....	26
1.1 Chapter Summary .....	27
1.2 Anthropogenic Sources of Water Contamination.....	27
1.3 Existing Water Purification Strategies.....	28
1.4 Metal–Organic Frameworks.....	28
1.5 Bulk Adsorption Measurements .....	31
1.6 Isothermal Titration Calorimetry.....	32
1.7 Isothermal Titration Calorimetry Theory.....	33
Chapter 2. Efficient Capture of Perrhenate and Pertechnetate by a Mesoporous Zr Metal–Organic Framework and Examination of Anion Binding Motifs .....	36
2.1 Chapter Summary .....	37
2.2 Pertechnetate Containment at Legacy Nuclear Waste Sites .....	37
2.3 Maximum Uptake Per Node.....	40
2.4 Adsorption Per Gram .....	40
2.5 Competition.....	42
2.6 Regeneration.....	43
2.7 Pertechnetate Screening .....	44
2.8 Single Crystal X-Ray Diffraction.....	45
2.9 Post-Adsorption Characterization.....	47

	12
2.10 Chapter Conclusions .....	48
2.11 Additional Information .....	49
2.11.1 Materials .....	49
2.11.2 Physical Methods and Instrumentation.....	49
2.11.3 Single-Crystal X-Ray Diffraction Data for NU-1000-ReO <sub>4</sub> .....	53
2.11.4 Perrhenate Adsorption Measurements.....	54
2.11.5 Residual Electron Density Plots.....	58
2.11.6 Post-Adsorption Characterization .....	59
Chapter 3. Efficient Extraction of Inorganic Selenium from Water by a Zr Metal–Organic Framework: Investigation of Volumetric Uptake Capacity and Binding Motifs .....	62
3.1 Chapter Summary .....	63
3.2 Selenium Oxyanion Pollution .....	63
3.3 Preliminary Investigation of SeO <sub>3</sub> <sup>2-</sup> and SeO <sub>4</sub> <sup>2-</sup> Uptake .....	66
3.4 Examination of Uptake Kinetics .....	66
3.5 Determination of Gravimetric and Volumetric Uptake Capacity.....	68
3.6 Crystallographic Investigation of Binding Motifs.....	69
3.7 Post-Adsorption Characterization.....	71
3.8 Chapter Conclusions .....	72
3.9 Additional Information .....	72
3.9.1 Materials .....	72
3.9.2 Physical Methods and Instrumentation .....	73
3.9.3 Single-Crystal X-Ray Diffraction Data .....	75
3.9.4 Bulk Adsorption Measurements.....	78
3.9.5 Post-Adsorption Characterization .....	82

Chapter 4. Capitalizing on $\pi$ - $\pi$ Interactions to Design an Efficient Sorbent for Atrazine Removal from Water.....	85
4.1 Chapter Summary .....	86
4.2 Pollution of Fresh Water Sources with Atrazine .....	86
4.3 Screening of Atrazine Affinity .....	90
4.4 Kinetic Studies.....	92
4.5 Adsorption Capacity of NU-1000.....	94
4.6 Effect of Ionic Strength on Adsorption.....	95
4.7 Regeneration and Stability of NU-1000 .....	96
4.8 Chapter Conclusions .....	97
4.9 Additional Information .....	98
4.9.1 Materials .....	98
4.9.2 Physical Methods & Instrumentation .....	98
4.9.3 MOF Characterization .....	105
4.9.4 Atrazine Adsorption Measurements .....	108
4.9.5 Regeneration and Stability of NU-1000 .....	109
Chapter 5. Isothermal Titration Calorimetry to Explore the Parameter Space of Organophosphorus Agrochemical Adsorption in MOFs.....	111
5.1 Chapter Summary .....	112
5.2 Adsorption of Agrochemical Pollutants.....	112
5.3 Monitoring Adsorption Events Using Isothermal Titration Calorimetry .....	114
5.4 Glyphosate Binding in NU-1000.....	115
5.5 Effect of Analyte Structure on Binding Thermodynamics .....	118
5.6 Effect of MOF Structure on Analyte Uptake .....	125
5.7 Influence of Buffer Composition on Binding Thermodynamics.....	128

	14
5.8 Chapter Conclusions .....	130
5.9 Additional Information .....	130
5.9.1 Materials .....	130
5.9.2 MOF Syntheses .....	131
5.9.3 Physical Methods and Instrumentation .....	134
MOF Characterization.....	139
5.9.4 Bulk Adsorption Experimental Data .....	144
5.9.5 Isothermal Titration Calorimetry Experiments .....	148
5.9.6 DFT Energy-Minimized Structures.....	152
Chapter 6. Thermochemical Investigation of Oxyanion Coordination in a Zirconium-based Metal– Organic Framework .....	154
6.1 Chapter Summary .....	155
6.2 Evolution of Studying Adsorption in Porous Materials.....	155
6.3 NU-1000 Characterization .....	160
6.4 Adsorption of Sulfur Oxyanions .....	161
6.5 Adsorption of Selenium Oxyanions.....	163
6.6 Adsorption of Group 15 Oxyanions .....	165
6.7 Displacement of Adsorbed Oxyanions .....	166
6.8 Chapter Conclusions .....	169
6.9 Additional Information .....	170
6.9.1 Materials .....	170
6.9.2 Physical Methods and Instrumentation .....	170
6.9.3 Isothermal Titration Calorimetry .....	172
6.9.4 NU-1000 Characterization.....	174

	15
6.9.5 Isothermal Titration Calorimetry Data .....	177
Chapter 7. Conclusions and Outlook .....	188
References .....	190

## List of Figures

- Figure 1.1** Structures of selected zirconium metal–organic frameworks (MOFs). Zr-MOFs consist of inorganic nodes and multitopic organic linkers assembled into multidimensional, crystalline lattices. ....29
- Figure 2.1** (a) Structure of  $Zr_6$ -node in NU-1000. (b) Structure of the tetratopic pyrene-based linker H4TBAPy. (c) Structure of NU-1000 containing  $\sim 30$  Å hexagonal mesopores and  $\sim 12$  Å triangular micropores. ....40
- Figure 2.2** Amount  $ReO_4^-$  adsorbed (q) vs time at various exposure concentrations of perrhenate per node of NU-1000. ....42
- Figure 2.3** Capture of  $ReO_4^-$  as a percentage vs time from equimolar solutions of perrhenate and various ions. ....43
- Figure 2.4** NU-1000 maintains a  $ReO_4^-$  uptake of  $\sim 150$  ppm (1.8/node) through 5 cycles of exposure and washing with dilute HCl. ....44
- Figure 2.5** Capture of  $TcO_4^-$  or  $ReO_4^-$  as a percentage from solution with initial concentration of  $1.455 \times 10^{-4}$  M (14 ppm Tc, 27 ppm Re) vs time. ....45
- Figure 2.6** The crystal structure of NU-1000 after  $ReO_4^-$  ion capture. (a) Chelating perrhenate binding motifs pointing into the small pore (Re1A). (b) Chelating perrhenate binding motifs pointing into the mesopore (Re2A). (c) Disorder of non-chelating perrhenate ions bound to the node of NU-1000 at the terminal –OH group positions. At each position, there are two crystallographically unique positions (B and C) with one mode disordered between two positions (C and C\*) (d) Non-chelating perrhenate binding sites where Re1B and Re1C point into the small pore and Re2B and Re2C point into the mesopore. ....46
- Figure 2.7** The Type I, linear Langmuir plot (**Table 2.3**) for perrhenate capture by NU-1000. ...55
- Figure 2.8** Capture of  $ReO_4^-$  as a percentage vs time by NU-1000 (2 mg) from an aqueous solution with Re concentration of 1 ppm. ....57
- Figure 2.9**  $F_o-F_c$  contoured Fourier maps around the  $Zr_6$ -node calculated when Re atoms are omitted from the crystallographic information file. PLATON software (b–d) and Shelxl software (e–f) were used for the calculations. (a) The crystal structure of NU-1000 and the (110) plane (red color). Gray, red, and cyan spheres represent carbon, oxygen, and zirconium atoms, respectively. The O5 and O6 oxygen atoms belong to the hydroxyl groups that point toward the small pore and the mesopore, respectively. (b) The contoured map in the (110) plane (contours are from  $-2.40$  to  $4.80$  e Å<sup>-3</sup> in steps of  $0.40$  e Å<sup>-3</sup>). The residual electron densities correspond to the non-chelating Re1B and Re2B. (c) The contoured map in the green-colored plane parallel to the (110) plane and shifted  $0.06$  Å (contours are from  $-2.40$  to  $4.80$  e Å<sup>-3</sup> in steps of  $0.40$  e Å<sup>-3</sup>). The residual electron densities correspond to the chelating Re1A and Re2A. (d) The contoured map in the blue-colored plane parallel to the (110) plane and shifted

0.10 Å (contours are from  $-2.40$  to  $5.80 \text{ e } \text{Å}^{-3}$  in steps of  $0.20 \text{ e } \text{Å}^{-3}$ ). The electron densities correspond to the non-chelating Re1C and Re2C. (e) The 3D contoured map contours from  $-0.90$  to  $0.90 \text{ e } \text{Å}^{-3}$ . (f) The 3D contoured map with contours from  $-2.40$  to  $2.40 \text{ e } \text{Å}^{-3}$  .....58

- Figure 2.10** Powder X-ray diffraction patterns for neat NU-1000 and NU-1000-Re loaded with  $\sim 1.8 \text{ ReO}_4^-$  ions per  $\text{Zr}_6$ -node indicate the MOF retains its crystallinity throughout adsorption.....59
- Figure 2.11**  $\text{N}_2$  isotherms of NU-1000 and NU-1000-Re containing  $\sim 1.8 \text{ ReO}_4^-$  per  $\text{Zr}_6$ -node show a surface area decrease consistent with the installation of anions at the node.....59
- Figure 2.12** Pore size distributions of NU-1000 and NU-1000-Re containing  $\sim 1.8 \text{ ReO}_4^-$  per node confirm the binding of perrhenate in the framework.....60
- Figure 2.13** (a) Full DRIFTS spectra for NU-1000 and NU-1000-Re containing  $\sim 1.8 \text{ ReO}_4^-$  per node. (b) DRIFTS spectra for NU-1000 and NU-1000-Re containing  $1.8 \text{ ReO}_4^-$  per node highlighting the reduced intensity and splitting of the non-hydrogen bonding – OH stretching peak at  $3674 \text{ cm}^{-1}$ . .....61
- Figure 3.1** MOF-808 is comprised of a)  $\text{Zr}_6$ -nodes and b) tritopic trimesic acid linkers. The framework consists of c) large adamantane cages and exhibits the d) **spn** topology. ....66
- Figure 3.2** Uptake isotherms of aqueous a) selenite and b) selenate at various exposure concentrations corresponding to 0.5, 1.0, 1.5, 2.0, and 2.5 ions per node.....67
- Figure 3.3** Selenite (Se(IV)) and selenate (Se(VI)) a) gravimetric uptake capacities and b) volumetric uptake capacities in MOF-808 and NU-1000.....69
- Figure 3.4** Visualizations of selenite and selenate binding at the Hf-MOF-808 node. a) Selenite  $\eta_2\mu_2$  binding motif in which two of selenite oxygen atoms coordinate to two different Hf atoms of a single node. Due to disorder, the terminal oxygen atom could not be resolved. b) Selenite  $\eta_2\mu_2$  with two transparent Hf polyhedrons to demonstrate binding to two different Hf atoms. c) Selenite  $\mu_2$  binding motif in which two oxygen atoms coordinate the same Hf atom in the node. d) Selenite  $\mu_2$  binding motif with transparent Hf polyhedron to demonstrate binding at a single Hf atom. e) Selenate  $\eta_2\mu_2$  binding motif. f) Selenate  $\mu_2$  binding motif. The green, red, black, and purple spheres represent Hf, O, C, and Se atoms, respectively. ....70
- Figure 3.5** The Type I, linear Langmuir plot of  $C_e/q_e$  versus  $C_e$  for selenite capture in MOF-808 at various equilibrium concentrations according to **Eqn. 1.2** reproduced below, in **Table 3.5**, for convenience. ....79
- Figure 3.6** The Type I, linear Langmuir plot of  $C_e/q_e$  versus  $C_e$  for selenate capture in MOF-808 at various equilibrium concentrations according to **Eqn. 1.2** reproduced below, in **Table 3.5**, for convenience. ....79
- Figure 3.7** Powder X-ray diffraction (PXRD) patterns of neat MOF-808 and MOF-808 loaded with  $1.8 \text{ SeO}_3^{2-}$  ions per node or  $1.6 \text{ SeO}_4^{2-}$  ions per node confirm the retention of bulk crystallinity and purity. ....82

- Figure 3.8** a) Volumetric N<sub>2</sub> adsorption/desorption isotherms of neat MOF-808 and MOF-808 loaded with 1.8 SeO<sub>3</sub><sup>2-</sup> ions per node or 1.6 SeO<sub>4</sub><sup>2-</sup> ions per node confirm the retention of porosity throughout the adsorption process. b) The associated gravimetric N<sub>2</sub> adsorption/desorption isotherms show a surface area reduction consistent with the installation of functionality at the MOF node. ....83
- Figure 3.9** DFT pore size distributions for neat MOF-808 and MOF-808 loaded with 1.8 SeO<sub>3</sub><sup>2-</sup> ions per node or 1.6 SeO<sub>4</sub><sup>2-</sup> ions per node reveal a decrease in the pore volume which supports the capture of selenite and selenate within the framework. ....83
- Figure 3.10** SEM images of a) the bulk sample and b) an individual crystal of MOF-808 loaded with 1.8 SeO<sub>3</sub><sup>2-</sup> ions per node, and c) the EDS linescan of the crystal in b. SEM images of d) the bulk sample and e) an individual crystal of MOF-808 loaded with 1.6 SeO<sub>4</sub><sup>2-</sup> ions per node, and f) the EDS linescan of the crystal in e. Both EDS linescans confirm the uniform distribution of selenium throughout the MOF-808 crystals. ....84
- Figure 4.1** The structures of a) the Zr<sub>6</sub>-node, b) atrazine, c) linkers for UiO-66, UiO-66-OH, UiO-66-NH<sub>2</sub>, DUT-67, and UiO-67, d) UiO series topology, e) linker for NU-1000 and NU-901 and f) NU-901 topology, g) linker for NU-1008, and h) NU-1000 and NU-1008 topology. ....89
- Figure 4.2** Atrazine adsorption uptake as a percentage of the total amount of atrazine exposed to MOF samples (3.5 mg of MOF exposed to 10 mL of 10 ppm atrazine solution under ambient conditions for 24h). ....91
- Figure 4.3** a) Atrazine adsorption isotherms as percent (%) uptake of atrazine exposed versus time for various MOFs. b) Atrazine adsorption isotherms as normalized percent (%) of respective saturation uptake versus time for various MOFs. Insets show the uptake between 0 and 5 min. ....94
- Figure 4.4** NU-1000 maintains its atrazine affinity in the presence of competing salt ions. ....96
- Figure 4.5** Through three cycles of atrazine adsorption and regeneration with acetone, a) NU-1000 shows only a slight decrease in atrazine uptake and b) retains its bulk structural integrity as demonstrated by PXRD. ....97
- Figure 4.6** a) Nitrogen adsorption-desorption isotherms at 77 K of all MOFs used in this study and b) nitrogen adsorption-desorption isotherms of MOFs at 77 K over the P/P<sub>o</sub> range from 0 to 0.3. .... 105
- Figure 4.7** DFT calculated pore size distributions for all MOFs used in this study. .... 105
- Figure 4.8** Powder X-ray diffraction (PXRD) patterns of simulated and as-synthesized a) UiO-66, UiO-66-OH, UiO-66-NH<sub>2</sub>, DUT-52 and UiO-67 and b) NU-901, NU-1000 and NU-1008. .... 106
- Figure 4.9** Scanning Electron Microscopy (SEM) images of all Zr<sub>6</sub>-based MOFs used in this study: a) UiO-66, b) UiO-66-OH, c) UiO-67, d) DUT-52, e) NU-901, f) NU-1000 and g) NU-1008. .... 107

- Figure 4.10** Type I Linear Langmuir Fit to determine the maximum uptake capacity of atrazine in mg per g of NU-1000..... 108
- Figure 4.11**  $^1\text{H}$  NMR spectrum of digested NU-1000 after atrazine adsorption and regeneration with acetone (1 mL) shows only  $\text{H}_4\text{TBAPy}$  (NU-1000 linker) and residual solvent peaks. No atrazine peaks are observed demonstrating that NU-1000 can be regenerated with acetone (1 mL) after atrazine adsorption. [MOF digestion protocol:  $\sim 1.5$  mg of NU-1000 is digested in 6 drops of concentrated  $\text{D}_2\text{SO}_4$  and diluted in 700 microliters of DMSO for NMR analysis]. ..... 109
- Figure 4.12** Control  $^1\text{H}$  NMR spectrum of atrazine in the DMSO/ $\text{D}_2\text{SO}_4$  solution used for MOF digestion. .... 110
- Figure 4.13** a)  $\text{N}_2$  adsorption isotherms of pristine NU-1000 and NU-1000 after atrazine adsorption and regeneration with acetone (1 mL) show a slight decrease in surface area. b) The associated DFT calculated pore size distributions. .... 110
- Figure 5.1** Structures of a) glyphosate, b) ethylphosphonic acid, and c) glufosinate and structures of d) NU-1000, e) NU-901, and f) NU-1200. The structural properties of these MOFs are summarized in **Table 5.3**. .... 116
- Figure 5.2** a) ITC thermogram resulting from titration of a NU-1000 suspension (1 mM, 1.4 mL, 50 mM acetate buffer, pH 4) with a glyphosate solution (10 mM, 50 mM acetate, 4  $\mu\text{L}$  injections) exhibits exothermic peaks and b) fitting with a single site model demonstrates a highly favorable binding affinity ( $\Delta G$ , black bar). The inset depicts the magnitude of the calculated thermodynamic parameters. Error bars represent the standard deviations of triplicate measurements. .... 117
- Figure 5.3** Linear relationship of Langmuir constants ( $K_L$ ) and binding association constants ( $K_a$ ) for a) glyphosate, ethylphosphonic acid, and glufosinate chemisorption in NU-1000 and b) glyphosate chemisorption in NU-1000, NU-901, and NU-1200 verify that ITC and bulk adsorption experiments yield comparable and complementary data. .... 120
- Figure 5.4** Lowest energy conformation of glyphosate binding in a) the mesopore of NU-1000 shows minimal non-covalent interactions with the surrounding framework environment. Conversely, when coordinating in the c-pore of NU-1000 (b and c), glyphosate coordinates at one node through the phosphonic acid and H-bonds to the terminal ligands on the adjacent node through the carboxylic acid. .... 123
- Figure 5.5** Thermodynamic parameters of glyphosate binding in NU-1000 (solid) and NU-1000-NDC (hatched) demonstrate that glyphosate chemisorption in NU-1000-NDC is less favorable and less exothermic than glyphosate chemisorption in native NU-1000. .... 124
- Figure 5.6** Lowest energy conformations of glyphosate binding in a) the NU-901 c-pore and b) NU-1200. .... 128
- Figure 5.7** Thermodynamic parameters of glyphosate (10 mM) binding to NU-1000 (1 mM) in various buffer concentrations. Error bars represent the standard deviation of triplicate measurements. .... 129

<b>Figure 5.8</b> PXRD patterns of a) NU-1000 and NU-1000-NDC, b) NU-901 and NU-901-NDC, and c) NU-1200. ....	139
<b>Figure 5.9</b> a) Nitrogen adsorption-desorption isotherms at 77 K and b) DFT-calculated pore size distribution of NU-1000 and NU-1000-NDC. ....	139
<b>Figure 5.10</b> a) Nitrogen adsorption-desorption isotherms at 77 K and b) DFT-calculated pore size distribution of NU-901 and NU-901-NDC. ....	140
<b>Figure 5.11</b> a) Nitrogen adsorption-desorption isotherms at 77 K and b) DFT-calculated pore size distribution of NU-1200. ....	140
<b>Figure 5.12</b> SEM images of a) NU-1000, b) NU-901, and c) NU-1200. ....	141
<b>Figure 5.13</b> Nitrogen adsorption-desorption isotherms at 77 K for NU-1000 soaked in 25 mM (black, BET area: $1740 \text{ m}^2 \text{ g}^{-1}$ ), 50 mM (red, BET surface area: $1740 \text{ m}^2 \text{ g}^{-1}$ ), and 100 mM (green, BET area: $1850 \text{ m}^2 \text{ g}^{-1}$ ) acetate buffer (pH 4) for 3 days. ....	142
<b>Figure 5.14</b> $^1\text{H}$ NMR spectra depicting the incorporation of 2,6-naphthalene dicarboxylic acid into the c-pores of NU-1000 (black trace) and NU-901 (red trace). ....	142
<b>Figure 5.15</b> $^1\text{H}$ NMR spectra of NU-1000-NDC before (black trace) and after (red trace) exposure to glyphosate verifying that glyphosate does not substantially displace the 2,6-naphthalene dicarboxylic acid installed in the c-pores. ....	143
<b>Figure 5.16</b> Preliminary crystallographic data suggested 35% of the coordinated glyphosate binds at sites directed into the a) hexagonal mesopore, while the remaining 65% binds at sites directed into the b) c-pore. Green, black, red, white, and blue spheres represent Zr, C, O, H, and P atoms, respectively. ....	143
<b>Figure 5.17</b> Plots of phosphorus uptake (mg/g) vs. time for each analyte-MOF pair. ....	144
<b>Figure 5.18</b> Relationship between initial phosphorus concentrations and partition coefficients for a) adsorption of analytes on NU-1000 and b) adsorption of glyphosate on NU-1000, NU-901, and NU-1200. ....	146
<b>Figure 5.19</b> Langmuir fits for the capture of various analytes by NU-1000. ....	147
<b>Figure 5.20</b> Langmuir fits for the capture of glyphosate by NU-1000, NU-901, and NU-1200. ....	147
<b>Figure 5.21</b> ITC thermograms for injections of a) glyphosate (10 mM, 50 mM acetate buffer, pH 4) into acetate buffer (50 mM, pH 4) and b) acetate buffer (50 mM, pH 4) into a NU-1000 suspension (1 mM, 50 mM acetate buffer, pH 4). ....	148
<b>Figure 5.22</b> ITC thermograms resulting from injections of a) glyphosate, b) ethylphosphonic acid, and c) glufosinate into a NU-1000 suspension (1 mM, 1.4 mL, 50 mM acetate buffer, pH 4). ....	149
<b>Figure 5.23</b> Graphical representation of thermodynamic parameters of adsorption for various analytes in NU-1000. ....	149
<b>Figure 5.24</b> Thermodynamic parameters of ethylphosphonic acid binding in NU-1000 and NU-1000-NDC. ....	150

- Figure 5.25** Thermodynamic parameters of a) glyphosate and b) ethylphosphonic acid binding in NU-901 and NU-901-NDC..... 151
- Figure 5.26** Scatter plot demonstrating the linear relationship between the thermodynamic parameters ( $\Delta H$ ,  $T\Delta S$ , and  $\Delta G$ ) of glyphosate binding in NU-1000 and buffer concentration..... 151
- Figure 5.27** Lowest energy structural conformations of ethylphosphonic acid binding in a) the NU-1000 mesopore and b and c) the NU-1000 c-pore..... 152
- Figure 5.28** Lowest energy structural conformations of glufosinate binding in the NU-1000 mesopore a) looking down the c-axis and b) rotated 90° around the axis shown and c) in the NU-1000 c-pore..... 152
- Figure 5.29** Lowest energy structural conformation of a) glyphosate binding in the diamond pore of NU-901 and b) trimmed figure of same conformation to show hydrogen bonding..... 153
- Figure 6.1** Structures of a) the  $Zr_6$ -node showing the proton topology, b) the tetratropic pyrene-based linker  $H_4TBAPy$ , c) the **csq** topology characteristic of NU-1000, and d) the sulfur, selenium, phosphorus, and arsenic oxyanions present in aqueous media (pH 5) examined in this thermochemical investigation..... 159
- Figure 6.2** Single-site model fitting of integrated heats of adsorption for each injection of hydrogen sulfite ( $HSO_3^-$ , black) and sulfate ( $SO_4^{2-}$ , red) demonstrate that adsorption of both analytes on NU-1000 produces similar thermodynamic profiles..... 162
- Figure 6.3** ITC thermograms and integrated heat data for adsorption on NU-1000 of a) hydrogen selenite ( $HSeO_3^-$ ) and b) selenate ( $SeO_4^{2-}$ ) indicate that NU-1000 achieves a higher uptake of hydrogen selenite compared to selenate. The extracted thermodynamic parameters for adsorption of hydrogen selenite (c, solid) and selenate (c, slashed) suggest that hydrogen selenite adsorption is more thermodynamically favorable ( $\Delta G$ ) and exothermic ( $\Delta H$ ) compared to selenate adsorption..... 165
- Figure 6.4** Single-site model fitting of integrated heats of adsorption on NU-1000 (black, circle) and NU-1000-0.6  $SeO_4$  (red, triangle) for each injection of phosphate demonstrate that NU-1000 loaded with ~0.6 selenate ions per node records a stoichiometric parameter of only 0.31 ( $\pm 0.01$ ) while parent NU-1000 records a value of 0.60 ( $\pm 0.09$ ). In addition, the extracted thermodynamic parameters indicate that adsorption on NU-1000-0.6  $SeO_4$  is slightly more thermodynamically ( $\Delta G$ ) favorable..... 168
- Figure 6.5** Structure of the c-pore of NU-1000 which is parallel to the hexagonal 1D mesoporous channels and the triangular 1D microporous channels..... 174
- Figure 6.6** NMR spectrum of NU-1000 digested by 0.1 M NaOD in  $D_2O$  indicates each node is capped by ~2.4 formate ions after 2 consecutive acid washes..... 174
- Figure 6.7** NMR spectrum of NU-1000 digested by  $d_2SO_4$  in  $d_6$ -DMSO indicates the complete removal of the benzoic acid modulator..... 175

- Figure 6.8** Powder X-ray diffraction patterns of as-synthesized NU-1000 (red trace) compared to a simulated pattern (black trace). ..... 175
- Figure 6.9** a) Nitrogen adsorption and desorption isotherm of NU-1000 and b) DFT-calculated pore size distribution. .... 176
- Figure 6.10** a) Nitrogen adsorption and desorption isotherms of NU-1000, NU-1000-0.6 SO<sub>4</sub> (denoted NU-1000-S), and NU-1000-0.7 SeO<sub>4</sub> (denoted NU-1000-Se) and b) the associated DFT-calculated pore size distributions. .... 176
- Figure 6.11** a) Thermogram and integrated heat data for the titration of 10 mM acetate buffer (pH 5) with a 10.6 mM sodium sulfite solution. b) Thermogram and integrated heat data for the titration of a 1 mM NU-1000 suspension with a 10.6 mM sodium sulfite solution in a 10 mM acetate buffer matrix (pH 5). .... 178
- Figure 6.12** a) Thermogram and integrated heat data for the titration of 10 mM acetate buffer (pH 5) with a 10.9 mM sodium sulfate solution. b) Thermogram and integrated heat data for the titration of a 1 mM NU-1000 suspension with a 10.9 mM sodium sulfate solution in a 10 mM acetate buffer matrix (pH 5). .... 179
- Figure 6.13** a) Thermogram and integrated heat data for the titration of 10 mM acetate buffer (pH 5) with a 9.8 mM sodium selenite solution. b) Thermogram and integrated heat data for the titration of a 1 mM NU-1000 suspension with a 9.8 mM sodium selenite solution in a 10 mM acetate buffer matrix (pH 5). .... 180
- Figure 6.14** a) Thermogram and integrated heat data for the titration of 10 mM acetate buffer (pH 5) with a 11.2 mM sodium selenate solution. b) Thermogram and integrated heat data for the titration of a 1 mM NU-1000 suspension with a 11.2 mM sodium selenate solution in a 10 mM acetate buffer matrix (pH 5). .... 181
- Figure 6.15** a) Thermogram and integrated heat data for the titration of 10 mM acetate buffer (pH 5) with an 18.0 mM disodium phosphate solution. b) Thermogram and integrated heat data for the titration of a 1 mM NU-1000 suspension with an 18.0 mM disodium phosphate solution in a 10 mM acetate buffer matrix (pH 5). .... 182
- Figure 6.16** a) Thermogram and integrated heat data for the titration of 10 mM acetate buffer (pH 5) with a 20.0 mM sodium arsenate dibasic solution. b) Thermogram and integrated heat data for the titration of a 1 mM NU-1000 suspension with a 20.0 mM sodium arsenate dibasic solution in a 10 mM acetate buffer matrix (pH 5). .... 183
- Figure 6.17** a) Thermogram and integrated heat data for the titration of 10 mM acetate buffer (pH 5) with an 18.0 mM disodium phosphate solution. b) Thermogram and integrated heat data for the titration of a 1 mM NU-1000-0.7 SeO<sub>4</sub> (denoted NU-1000-Se) suspension with an 18.0 mM disodium phosphate solution in a 10 mM acetate buffer matrix (pH 5). .... 184
- Figure 6.18** a) Thermogram and integrated heat data for the titration of 10 mM acetate buffer (pH 5) with an 18.0 mM disodium phosphate solution. b) Thermogram and integrated heat data for the titration of a 1 mM NU-1000-0.6 SO<sub>4</sub> (denoted NU-1000-S) suspension

with an 18.0 mM disodium phosphate solution in a 10 mM acetate buffer matrix (pH 5)..... 185

**Figure 6.19** Single site model fitting of integrated heats of adsorption for each injection of 18.0 mM phosphate into 1 mM suspensions of NU-1000 (black) and NU-1000-0.6 SO<sub>4</sub> (denoted NU-1000-S, red) demonstrate similar adsorption thermodynamic profiles; however, the sulfate loaded sample records a lower stoichiometric parameter as determined from the inflection point of the titration curve. .... 186

**Figure 6.20** a) Thermogram and integrated heat data for the titration of 10 mM acetate buffer (pH 5) with a 22.4 mM sodium selenate solution. b) Thermogram and integrated heat data for the titration of a 1 mM NU-1000-0.6 SO<sub>4</sub> (denoted NU-1000-S) suspension with a 22.4 mM sodium selenate solution in a 10 mM acetate buffer matrix (pH 5). .... 187

## List of Tables

<b>Table 2.1</b> Crystallographic data for NU-1000-ReO <sub>4</sub> .....	53
<b>Table 2.2</b> Perrhenate adsorption per Zr <sub>6</sub> -node of NU-1000 when exposed to aqueous sodium perrhenate solutions with concentrations of 2 to 7 ReO <sub>4</sub> <sup>-</sup> ions per node.....	54
<b>Table 2.3</b> Langmuir Equation and Parameters.....	56
<b>Table 2.4</b> Perrhenate uptake Capacities of several previously examined sorbents.....	56
<b>Table 3.1</b> Crystallographic data for Hf-MOF-808- SeO <sub>3</sub> .....	75
<b>Table 3.2</b> Crystallographic data for Hf-MOF-808-SeO <sub>4</sub> .....	77
<b>Table 3.3</b> Selenite adsorption per Zr <sub>6</sub> -node of MOF-808 when exposed to aqueous sodium selenite solutions with concentrations of 2 to 7 SeO <sub>3</sub> <sup>2-</sup> ions per node.....	78
<b>Table 3.4</b> Selenate adsorption per Zr <sub>6</sub> -node of MOF-808 when exposed to aqueous sodium selenate solutions with concentrations of 2 to 7 SeO <sub>4</sub> <sup>2-</sup> ions per node.....	78
<b>Table 3.5</b> The selenite and selenate uptake isotherms ( <b>Figure 3.2</b> ) and the Langmuir equation ( <b>Eqn. 1.2</b> as reproduced below):.....	80
<b>Table 3.6</b> Comparison of the gravimetric and volumetric selenite uptake capacity of MOF-808 and NU-1000. The shaded box indicates the greater capacity.....	80
<b>Table 3.7</b> Comparison of the gravimetric and volumetric selenate uptake capacity of MOF-808 and NU-1000. The shaded box indicates the greater capacity.....	80
<b>Table 3.8</b> Comparison of gravimetric uptake capacities for selenite and selenate in various materials.....	81
<b>Table 4.1</b> The surface areas, pore sizes, and approximate pore apertures of Zr <sub>6</sub> -based MOFs screened for atrazine adsorption. <sup>a</sup> Reported pore aperture sizes of UiO series MOFs are measured for the node-to-node distance of the tetrahedral pore. <sup>174</sup> .....	92
<b>Table 4.2</b> Comparison of Langmuir constant values reported for atrazine adsorption on various materials reveals that NU-1000 outperforms most reported materials with respect to uptake capacity and sorption kinetics.....	95
<b>Table 4.3</b> Langmuir Fitting Parameters for atrazine adsorption in NU-1000.....	108
<b>Table 4.4</b> Atrazine adsorption capacities of various sorbents.....	109
<b>Table 5.1</b> Uptake capacity (Q <sub>m</sub> ) of NU-1000 and thermodynamic parameters of adsorption for various analytes. Errors are calculated as the standard deviations of triplicate measurements.....	120
<b>Table 5.2</b> Glyphosate uptake capacities (Q <sub>m</sub> ), Langmuir constants (K <sub>L</sub> ), and thermodynamic parameters of glyphosate chemisorption in NU-1000, NU-901, and NU-1200. ....	126
<b>Table 5.3</b> Nitrogen isotherm data, topologies, and node connectivity for Zr <sub>6</sub> -MOFs.....	140

<b>Table 5.4</b> Initial and final concentrations of glyphosate, uptake capacity of NU-1000, and respective partition coefficients. ....	145
<b>Table 5.5</b> Initial and final concentrations of ethylphosphonic acid, uptake capacity of NU-1000, and respective partition coefficients. ....	145
<b>Table 5.6</b> Initial and final concentrations of glufosinate, uptake capacity of NU-1000, and respective partition coefficients. ....	145
<b>Table 5.7</b> Initial and final concentrations of glyphosate, uptake capacity of NU-901, and respective partition coefficients. ....	145
<b>Table 5.8</b> Initial and final concentrations of glyphosate, uptake capacity of NU-1200, and respective partition coefficients. ....	146
<b>Table 5.9</b> Isothermal titration calorimetry measurement conditions. ....	148
<b>Table 5.10</b> The thermodynamic parameters of ethylphosphonic acid binding in NU-1000, NU-901, and NU-1200. ....	150
<b>Table 6.1</b> Thermodynamic parameters of adsorption for various analytes in NU-1000. ....	162
<b>Table 6.2</b> ITC experimental conditions for all analytes. All MOF suspensions were 1.0 mM in 10 mM acetate buffer. ....	173
<b>Table 6.3</b> Analyte uptake as determined by ICP-OES in bulk experiments replicating ITC conditions compared to the stoichiometric parameters extracted for each analyte from the respective ITC thermograms. ....	177

# Chapter 1. Introduction

Portions of this chapter appear in the following manuscripts:

**Drout, R.J.**; Robison, L.; Chen, Z.; Islamoglu, T.; Farha, O.K., Zirconium Metal–Organic Frameworks for Organic Pollutant Adsorption. *Trends in Chemistry*. **2019**, *1*, 304-317.

Kato, S.; **Drout, R.J.**; Farha, O.K., Isothermal Titration Calorimetry to Investigate Uremic Toxins Adsorbing onto Metal–Organic Frameworks. *Cell Rep. Phys. Sci.* **2020**, *1*, 100006.

## 1.1 Chapter Summary

The rapid expansion of manufacturing and the industrialization of agriculture during the 20<sup>th</sup> Century pervaded surface and groundwater sources with organic contaminants including heavy metals, radioactive species, agrochemicals, dyes, and pharmaceuticals. Efficient purification of these water sources is critical to safeguard human health and Earth's ecosystems. Of the numerous strategies investigated for water purification, adsorption has received the most attention; however, the ability to design a sorbent with high uptake capacity and selectivity for a single pollutant continues to elude researchers. The precise synthetic control over chemical functionality offered by metal–organic frameworks (MOFs) make them ideal scaffolds for systematically investigating selectivity enhancing binding interactions. Herein, I introduce a few primary water pollution sources, current purification strategies, and metal–organic frameworks (MOFs). I also overview two primary methods I employed throughout my thesis research to study binding events in MOFs, namely bulk adsorption studies and isothermal titration calorimetry.

## 1.2 Anthropogenic Sources of Water Contamination

Since the Industrial Revolution began over two centuries ago, significant improvements in human health have been observed globally; however, Earth's environment, specifically the freshwater supply, has languished. According to the United Nations Educational, Scientific, and Cultural Organization (UNESCO), water pollution stemming from anthropogenic activities continues to climb worldwide.<sup>1</sup> The agricultural, mining, textile, pharmaceutical, and personal care product industries contribute most substantially to the high levels of agrochemicals, heavy metals, dyes, and persistent organic pollutants (POPs) currently contaminating freshwater supplies.<sup>2</sup> The World Health Organization (WHO) predicts nearly 50% of the world's population will live in water-stressed regions by 2025; therefore, the design and widespread implementation of efficient

water purification strategies is paramount to safeguard the ecosystem and secure a sustainable future.<sup>3</sup>

### 1.3 Existing Water Purification Strategies

Motivated to protect public health and the environment, numerous academic and industrial research teams have investigated techniques to efficiently decontaminate water. Most water treatment processes feature a series of purification strategies such as distillation, reverse osmosis, filtration by activated carbon, and ion exchange. Desalination is regarded as one of the most economically and energetically demanding water purification processes (~\$1 to \$3 per 1000 gallons of water) and can be regarded as the upper cost threshold of water purification methods.<sup>4</sup> An assortment of technically intensive strategies including membrane separation, precipitation, advanced oxidation processes (AOPs), biological processes, and adsorption have also shown promise for capturing and sometimes even destroying water pollutants.<sup>5</sup> However, steep optimization costs and high energy inputs often delay the development of new water-treatment technologies, and infrastructure limitations hinder implementation of even the most basic purification methods in developing countries. Recently, metal–organic frameworks (MOFs), a class of porous materials, have received attention for liquid-phase separations by adsorption, and these materials have shown efficacious removal of many aqueous-phase contaminants.<sup>6</sup>

### 1.4 Metal–Organic Frameworks

Metal–organic frameworks (MOFs) are porous, crystalline materials comprised of inorganic nodes and organic linkers which assemble into multidimensional lattices through coordination bonds.<sup>7</sup> Through the precise choice of MOF building units, namely, the node and linker, we can realize an assortment of material properties (e.g., chemical functionality, surface area, pore volume, and framework topology) (**Figure 1.1**).<sup>8</sup> The post-synthetic modification of parent

frameworks to install ligands or catalysts, exchange linkers, and dope MOF pores allows for further tuning of MOF functionality.<sup>9</sup> Owing to their facile tunability, MOFs have shown promise for a range of applications including, but not limited to, gas storage and separation, catalysis, and sensing.<sup>10-14</sup>

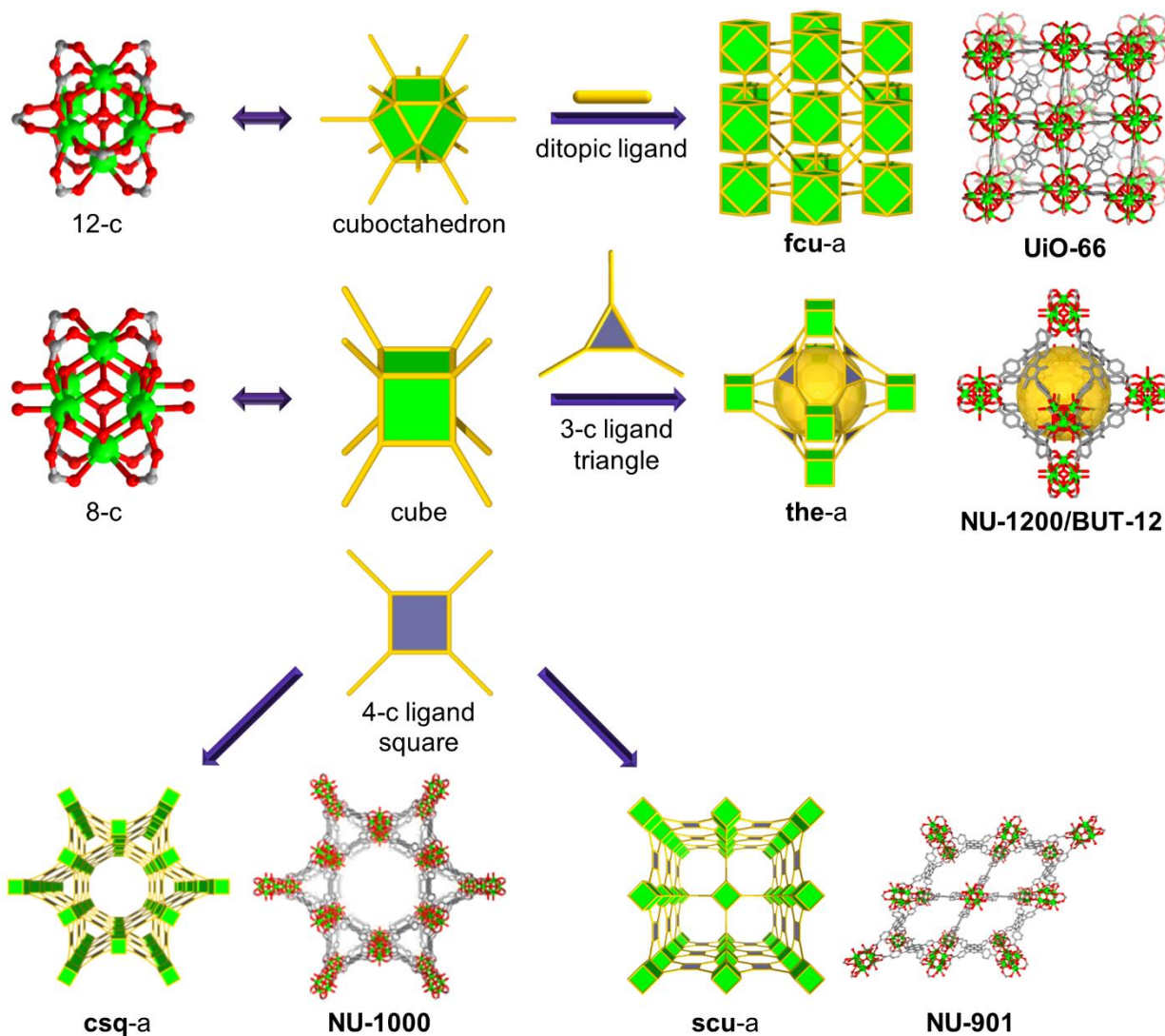


**Figure 1.1** Structures of selected zirconium metal–organic frameworks (MOFs). Zr-MOFs consist of inorganic nodes and multitopic organic linkers assembled into multidimensional, crystalline lattices.

MOFs of various metals (e.g., aluminum, chromium, and zirconium) have been examined as adsorbents for heavy metal cations, oxyanions, and organic contaminants.<sup>15-18</sup> The porosity of MOFs facilitates diffusion of contaminants to binding sites, which promotes rapid uptake saturation, and their chemical functionality can be easily tuned to favor adsorption. Often, inorganic anionic contaminants are captured at MOF nodes through pseudo-ion-exchange processes in which weakly coordinated ligands are displaced by the incoming pollutant.<sup>19</sup> Conversely, capture of organic-based toxins relies primarily on non-covalent interactions (e.g., H-bonding,  $\pi$ - $\pi$  interactions, van der Waals interactions, hydrophobic interactions). Through careful selection of node and linker, MOF chemical and physical structure can be precisely tailored to capitalize on multiple non-covalent interaction sites.<sup>20</sup> Moreover, single-crystal X-ray diffraction can often be employed to characterize binding sites, providing an atomically-precise understanding of the sorbate-sorbent interaction. Furthermore, zirconium-based MOFs, herein denoted as Zr-MOFs, display remarkable chemical and thermal stability due to the strong Zr(IV)-O bonds within Zr-based nodes and between the nodes and carboxylate groups of the linkers (**Figure 1.1**).<sup>21</sup> As confirmed by their retention of crystallinity and porosity, numerous Zr-MOFs are exceptionally stable in aqueous media over a wide pH range, notably within pH 5 to 9 which is typical for freshwater sources.<sup>22, 23</sup> By capitalizing on the modular nature of MOFs to incorporate highly hydrophobic linkers, materials which retain their structural integrity even in boiling water and concentrated acidic and basic media can be realized.<sup>24, 25</sup>

Given that MOF porosity facilitates rapid extraction of contaminants and structural linkers offer a high density of sorption sites, MOFs are promising candidate materials for purification applications. Beyond these properties, the synthetic tunability of MOFs positions this class of

materials as an unparalleled platform by which favorable adsorptive interactions can be systematically investigated.

### 1.5 Bulk Adsorption Measurements

Investigations seeking to assess a material's capacity to function as a sorbent for extracting contaminants from aqueous media largely rely on bulk adsorption studies. In a typical experiment, a sample of material, in my case a MOF (5 mg), is exposed to a fixed volume (15 mL) of solution containing a known concentration of a target contaminant. After a designated amount of time, we separate the MOF sample from the supernatant by centrifugation and/or filtration. To determine the amount of analyte captured, we compare the residual concentration of the analyte in solution to the concentration of the analyte in an identically prepared solution that has not been exposed to MOF. Often, we dilute a small aliquot (e.g., 0.5 mL) of both solutions in an appropriate matrix for analysis by inductively coupled plasma optical emission spectroscopy (ICP-OES) or high performance liquid chromatography (HPLC) depending on the analyte's identity. After taking the dilution factors into consideration, we can determine the amount of analyte adsorbed ( $q$ ) in mg of analyte per g of adsorbent using **Eqn. 1.1**

$$q = \frac{(C_i - C_f) \times V}{m} \quad (1.1)$$

where  $C_i$  = initial concentration (mg/L),  $C_f$  = final concentration (mg/L),  $V$  = volume of solution exposed to NU-1000 (L), and  $m$  = mass of adsorbent (g).

Upon allowing the system to equilibrate, one can determine the maximum adsorption capacity using a Type I Langmuir fit. To employ such a fit, we assume 1) that the binding sites are independent and 2) that upon adsorption bound analytes do not interact. A linear fit of a plot of the ratio of the equilibrium analyte concentration ( $C_e$ ) to the equilibrium uptake ( $q_e$ ) versus the residual

equilibrium analyte concentration according to **Eqn. 1.2** allows for the determination of the theoretical maximum uptake capacity (Q).

$$\frac{C_e}{q_e} = \left(\frac{1}{Q}\right) C_e + \frac{1}{K_L Q} \quad (1.2)$$

where Q is the theoretical maximum uptake capacity in mg of adsorbate per g of sorbent and  $K_L$  is the Langmuir constant in liters of solution per mg of analyte and represents the extent of interaction between the adsorbate and the sorbent.

### 1.6 Isothermal Titration Calorimetry

While bulk adsorption studies allow us to determine the theoretical uptake capacity and adsorption kinetics, quantifying the thermodynamics of adsorption is tedious using such measurements. Isothermal titration calorimetry (ITC), first described in the 1960s, allows for the simultaneous measurement of the association binding constant ( $K_a$ ) and heat of reaction or adsorption ( $\Delta H$ ).<sup>26</sup> This technique quantifies the amount of heat absorbed or released during a given chemical process allowing the direct determination of association binding constants ( $K_a$ ), reaction stoichiometry (n), enthalpy change ( $\Delta H$ ), Gibbs free energy change ( $\Delta G$ ), and entropy change ( $\Delta S$ ).<sup>27</sup> Moreover, varying the temperature at which thermograms are collected allows for the determination of the reaction's heat capacity, thereby providing a complete thermodynamic profile of the molecular interaction.<sup>28</sup> Briefly, an isothermal titration calorimeter consists of two cells, a reference cell and a sample cell, and following each injection of titrant, the instrument records the heat change required to bring the sample cell back into thermal equilibrium with the reference cell. In a typical experiment, a MOF suspension occupies the sample cell, and the syringe titrates the desired analyte while stirring at a fixed speed. Upon integrating the enthalpy data over time, one can extract the thermodynamic profile as described in this chapter's final section.

Early reports using ITC examined acid-base equilibria and the formation of metal complexes.<sup>29</sup> The characterization of the thermodynamic parameters of biochemically relevant ligand-receptor binding interactions (e.g. protein-DNA or drug-enzyme) routinely employs ITC.<sup>30-32</sup> Recent investigations have utilized ITC to characterize the energetics of interactions between chemical toxins and porous materials;<sup>33, 34</sup> however, relatively few systematic investigations of adsorbate-MOF interactions have made use of this technique.<sup>35-37</sup> Several challenges impede implementing ITC in the MOF field including (1) MOF stability in aqueous media; (2) heat changes associated with secondary processes that may obscure the real heat of an interaction;<sup>38</sup> and (3) possible interactions between chemical substrates and pore surfaces (i.e. nodes and linkers in MOFs) which may differ from interactions on the external crystallite surfaces due to varying microenvironments.<sup>39</sup>

### 1.7 Isothermal Titration Calorimetry Theory

This section overviews the theory of ITC and briefly explains the mathematical computation.<sup>3-</sup>  
<sup>5</sup> Following the framework described in Lawrence Indyk *et al.*, the binding of a single ligand L (agrochemical anion or oxyanion in our studies) with a MOF receptor, M (MOF crystals in our study) can be considered:



where ML is the ligand-bound MOF complex (**Eqn 1.3**). The binding stoichiometry is given by  $n$ . In this work, we primarily consider single-site independent binding and one-to-one binding (**Eqn. 1.4**). MOF crystals, especially NU-1000, should have several binding sites, but we initially assume each site is thermodynamically identical. The equilibrium association constant,  $K_a$ , is defined according to **Eqn. 1.5**:

$$K_a = \frac{[ML]}{[M][L]} \quad (1.5)$$

where the terms in brackets represent the equilibrium concentrations of the respective species. The expression for the equilibrium constant (**Eqn. 1.5**) can be combined with mass balances on each component as written in **Eqn. 1.6** and **Eqn. 1.7**:

$$[M_T] = [M] + [ML] \quad (1.6)$$

and

$$[L_T] = [L] + [ML] \quad (1.7)$$

**Eqn. 1.4** and **Eqn. 1.5** can be extended to any binding system of ligands, noting that  $[M_T]$  and  $[L_T]$  are the total concentrations of MOF and ligand in the calorimeter cell, respectively. These variables are used because they are the known quantities in an experiment, and it would be useful to solve for some of the unknown quantities, such as  $[M]$  and  $[L]$  in terms of these two. The dependent variable in ITC experiments is the total amount of heat released per injection of ligand,  $dQ$ , as depicted in **Eqn. 1.6**:

$$\frac{dQ}{d[L_T]} = \Delta H V \frac{d[ML]}{d[L_T]} \quad (1.8)$$

where  $V$  is the volume of the calorimetric cell,  $\Delta H$  is the enthalpy of binding for formation of  $[ML]$ . Substituting **Eqn. 1.5**, **Eqn. 1.6**, and **Eqn. 1.7** into **Eqn. 1.8** allows us to explicitly write  $\Delta Q$  in terms of  $K_a$ ,  $\Delta H$ ,  $[M_T]$  and  $[L_T]$ . The integrated heats from each injection can be fit to a model as a function of molar ratio to determine heat from the standard parameters ( $K_a$ ,  $\Delta H$ , and  $n$ ) in a single experiment. The value of  $\Delta G$  is determined from the standard thermodynamic definition,  $\Delta G = -RT \ln(K_a)$ , and the entropy of adsorption,  $\Delta S$  is calculated from  $\Delta G = \Delta H - T\Delta S$ . The full form of **Eqn. 1.9** for independent binding used to fit the integrated heat data from ITC is given as:

$$\frac{dQ}{d[L_T]} = \frac{1}{2}V\Delta H \left[ 1 - \frac{\frac{[L_T]}{[M_T]} - n + \frac{1}{K_a[M_T]}}{\sqrt{\left(\frac{[L_T]}{[M_T]}\right)^2 + \left(n + \frac{1}{K_a[M_T]}\right)^2 - 2\frac{[L_T]}{[M_T]}\left(n - \frac{1}{K_a[M_T]}\right)}} \right] \quad (1.9)$$

## Chapter 2. Efficient Capture of Perrhenate and Pertechnetate by a Mesoporous Zr Metal–Organic Framework and Examination of Anion Binding Motifs

Portions of this chapter appear in the following manuscript:

**Drout, R.J.**; Otake, K.-i.; Howarth, A.J.; Islamoglu, T.; Zhu, L.; Xiao, C.; Wang, S.; Farha, O.K., Efficient Capture of Perrhenate and Pertechnetate by a Mesoporous Zr Metal–Organic Framework and Examination of Anion Binding Motifs. *Chem. Mater.* **2018**, *30* (4), 1277-1284.

## 2.1 Chapter Summary

At the Hanford Site in southeastern Washington state, the U.S. Department of Energy intends to treat 56 million gallons of legacy nuclear waste by encasing it in borosilicate glass via vitrification. This process ineffectively captures radioactive pertechnetate ( $\text{TcO}_4^-$ ) due to the ion's volatility, thereby requiring a different remediation method for this long-lived ( $t_{1/2} = 2.1 \times 10^5$  years), environmentally mobile species. Currently available sorbents lack the desired combination of high uptake capacity, fast kinetics, and selectivity. Here, we evaluate the ability of the chemically and thermally robust  $\text{Zr}_6$ -based metal–organic framework (MOF), NU-1000, to capture perrhenate ( $\text{ReO}_4^-$ ), a pertechnetate simulant, and pertechnetate. Our material exhibits an excellent perrhenate uptake capacity of 210 mg/g, reaches saturation within 5 minutes, and maintains perrhenate uptake in the presence of competing anions. Additionally, experiments with pertechnetate confirm perrhenate is a suitable surrogate. Single-crystal X-ray diffraction indicates both chelating and non-chelating perrhenate binding motifs are present in both the small pore and the mesopore of NU-1000. Post-adsorption diffuse reflectance infrared Fourier transform spectroscopy (DRIFTS) further elucidates the uptake mechanism and powder X-ray diffraction (PXRD) and Brunauer-Emmett-Teller (BET) surface area analysis confirm the retention of crystallinity and porosity of NU-1000 throughout adsorption.

## 2.2 Pertechnetate Containment at Legacy Nuclear Waste Sites

The nuclear weapons industry in the United States saw the production of 100 tons of plutonium and the generation of over 100 million gallons of hazardous liquid waste during World War II and the Cold War.<sup>40</sup> At its climax, the Hanford Site in southeastern Washington state operated nine nuclear reactors and was responsible for the production of two thirds of the nation's plutonium supply.<sup>41</sup> With 30 years since Hanford's last reactor was shut down, the U.S.

Department of Energy is preparing to treat 56 million gallons of legacy waste currently stored in 177 underground tanks.<sup>42</sup>

Technetium-99 is a high yield (6.1%), long-lived ( $t_{1/2} = 2.1 \times 10^5$  years) fission product.<sup>43, 44</sup> In oxidizing environments, like those of the waste storage tanks at the Hanford Site, Tc-99 is present as the highly soluble, environmentally mobile, and volatile pertechnetate ion ( $\text{TcO}_4^-$ ).<sup>43, 44</sup> The Hanford Tank Waste Treatment and Immobilization Plant will separate waste into high level and low activity waste streams followed by immobilization in borosilicate glass via vitrification. At the high operating temperatures (1150 °C) of the melters, the volatility of pertechnetate hinders its retention in the glass waste form.<sup>45-47</sup> Further, pertechnetate's high solubility (11.3 mol L<sup>-1</sup> at 20 °C) makes it dangerously environmentally mobile.<sup>48</sup> Due to this immense technical challenge and environmental threat, there is a crucial need for an effective strategy for pertechnetate removal from nuclear waste prior to vitrification.

Various routes of pertechnetate capture including ion exchange,<sup>49-51</sup> reductive immobilization,<sup>52-56</sup> and supramolecular recognition<sup>57</sup> have been reported.<sup>48</sup> Ion exchange materials such as organic polymers,<sup>58</sup> coordination polymers,<sup>9, 59-63</sup> inorganic materials (layered double hydroxides, LDHs),<sup>64, 65</sup> and commercial resins<sup>66, 67</sup> have received the most attention; however, a sorbent with high uptake capacity, fast kinetics, and selectivity is yet to be discovered. MOFs are composed of inorganic nodes linked by multitopic organic ligands.<sup>7, 68</sup> These hybrid materials have recorded the highest surface areas to date,<sup>69</sup> and can be designed to be chemically and thermally robust.<sup>21</sup> MOFs have been tailored towards numerous potential applications<sup>9</sup> including but not limited to gas storage and delivery,<sup>12, 70, 71</sup> gas separation,<sup>13</sup> catalysis,<sup>14</sup> drug delivery,<sup>72</sup> chemical sensing,<sup>10</sup> and water remediation.<sup>15, 16, 73</sup> Specifically, Zr<sub>6</sub>-based MOFs are

exceptionally stable in aqueous media over a wide range of pH due to the strong Zr(IV)–O bonds and high connectivity of the Zr node.<sup>11, 21, 23</sup> An extensive collection of connectivities can arise within a Zr<sub>6</sub>-node many of which contain Zr sites terminated by nonstructural labile ligands i.e. –OH/–OH<sub>2</sub> pairs. These spatially oriented Zr–OH sites can be utilized to capture oxyanions in a charge balancing fashion.<sup>74, 75</sup> Here, we capitalize on the lability of the hydroxyl ligands on the Zr<sub>6</sub>-node of the MOF, NU-1000, to efficiently capture perrhenate, a pertechnetate simulant, and exploit the MOF's permanent crystallinity and porosity to crystallographically identify the anion's binding motif.

NU-1000 is comprised of 8-connected Zr<sub>6</sub>-nodes (**Figure 2.1a**) and 1,3,6,8-tetrakis(*p*-benzoic acid)pyrene (H<sub>4</sub>TBAPy) linkers (**Figure 2.1b**). The framework consists of 1D triangular (~12 Å) and hexagonal (~30 Å) channels (**Figure 2.1c**). Additionally, adjacent 1D channels are connected by small pores (~8 Å). NU-1000 is exceptionally stable in aqueous media over a large range of pH (1-11)<sup>23, 76</sup> and can be prepared by a facile large scale synthesis.<sup>77</sup> Further, our group has recently shown that the terminal hydroxyl groups on the Zr<sub>6</sub>-node of NU-1000 can be substituted by selenate/selenite<sup>74</sup> and sulfate<sup>75</sup> thereby facilitating the removal of hazardous oxyanions from aqueous media. We hypothesized that NU-1000 would similarly capture perrhenate (ReO<sub>4</sub><sup>-</sup>), a non-radioactive surrogate for pertechnetate. Here, we evaluate NU-1000 as a sorbent for perrhenate (ReO<sub>4</sub><sup>-</sup>) removal from water to determine its maximum uptake capacity, selectivity for perrhenate in the presence of competing anions, recyclability, and stability to the adsorption process. Further, we briefly analyze pertechnetate capture and the suitability of perrhenate as a surrogate. Finally, we define the various binding motifs of perrhenate at the NU-1000 node via single-crystal X-ray diffraction.

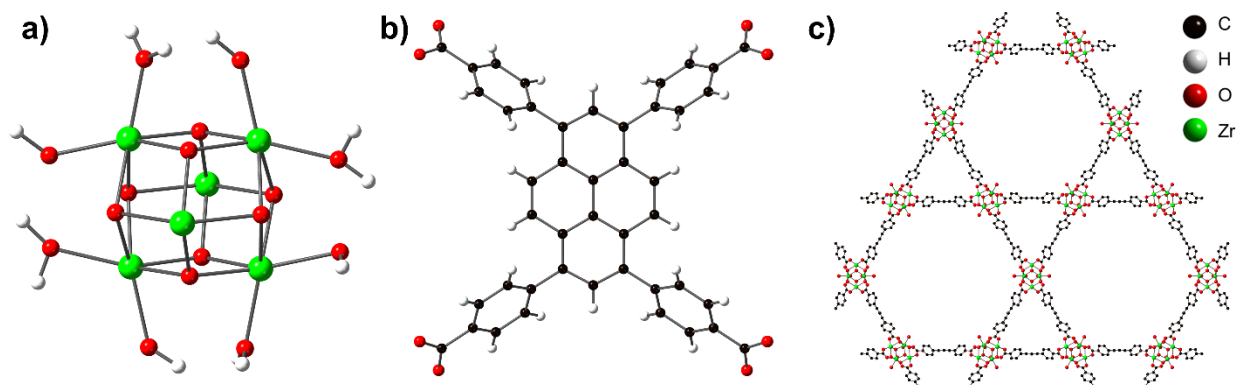


**Figure 2.1** (a) Structure of  $Zr_6$ -node in NU-1000. (b) Structure of the tetratopic pyrene-based linker H4TBAPy. (c) Structure of NU-1000 containing  $\sim 30$  Å hexagonal mesopores and  $\sim 12$  Å triangular micropores.

### 2.3 Maximum Uptake Per Node

Initial experiments involved screening the affinity of NU-1000 for perrhenate ( $ReO_4^-$ ). NU-1000 samples (5 mg) were exposed to 15 mL of an aqueous sodium perrhenate solution with Re concentrations corresponding to 2 – 7  $ReO_4^-$  per  $Zr_6$ -node (57 ppm to 199 ppm). After an exposure time of 26 h, NU-1000 was shown to capture between 1.2 and 2.0  $ReO_4^-$  per node when exposed to 2 and 7  $ReO_4^-$  per node, respectively (**Table 2.2**). These results suggested that NU-1000 might be an effective sorbent for  $ReO_4^-$ .

### 2.4 Adsorption Per Gram

Effective sorbents exhibit high uptake capacity and rapid uptake kinetics. To determine the maximum  $ReO_4^-$  capacity of NU-1000 and examine the associated kinetics, MOF samples (5 mg) were exposed to aqueous sodium perrhenate solutions (15 mL) with Re concentrations corresponding to 1.0, 1.5, 2.0, 2.5, and 3 ions per MOF node (28, 43, 57, 71, and 85 ppm). The amount adsorbed  $q$  in mg of perrhenate per gram of NU-1000 was determined using **Eqn. 1.1** as reproduced below:

$$q = \frac{(C_i - C_f) \times V}{m} \quad (1.1)$$

where  $C_i$  = initial concentration (mg/L),  $C_f$  = final concentration (mg/L),  $V$  = volume of solution exposed to NU-1000 (L), and  $m$  = mass of NU-1000 (g). Adsorption isotherms were constructed by monitoring  $q$  as a function of time (**Figure 2.2**) and indicate that NU-1000 reaches maximum uptake within 5 min of exposure which can be attributed to the rapid diffusion of solvent through the large pores (30 Å) of NU-1000. The maximum adsorption capacity of NU-1000 for perrhenate was determined to be 210 mg/g using the Langmuir equation (

**Table 2.3)** making NU-1000 among the best sorbents reported to date (**Table 2.4**).<sup>58, 59, 78-88</sup>

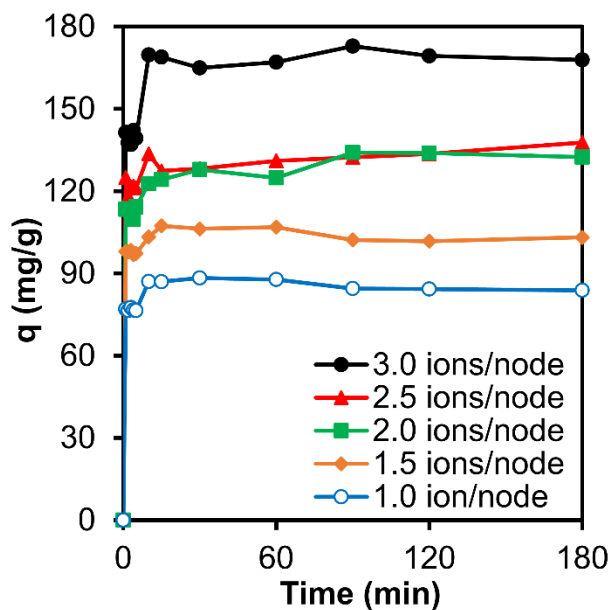


**Figure 2.2** Amount  $\text{ReO}_4^-$  adsorbed ( $q$ ) vs time at various exposure concentrations of perrhenate per node of NU-1000.

## 2.5 Competition

In evaluating a sorbent, high selectivity in the presence of competing anions is equally as important as high uptake capacity and fast kinetics. The waste streams from which perrhenate must be removed include halides, nitrate, and sulfate. Therefore, to evaluate if NU-1000 can sufficiently maintain its perrhenate uptake ability in the presence of competing anions, MOF samples (5 mg) were exposed to equimolar aqueous solutions (15 mL) of perrhenate ( $3.82 \times 10^{-5}$  M) and one of the following: chloride, bromide, iodide, nitrate, or sulfate. The uptake isotherms (**Figure 2.3**) indicate that NU-1000 sustains its original capacity and fast kinetics even in the presence of equimolar amounts of halides and nitrate. We see that the perrhenate uptake is slightly reduced in an equimolar solution of sulfate likely due to stronger electrostatic interactions between the NU-1000 node and the doubly-charged sulfate anion (as compared to singly-charged,

perrhenate). It is worth noting that despite the higher negative charge on the sulfate and similar molecular geometry to perrhenate, more than 86% of the original perrhenate uptake is maintained by NU-1000.

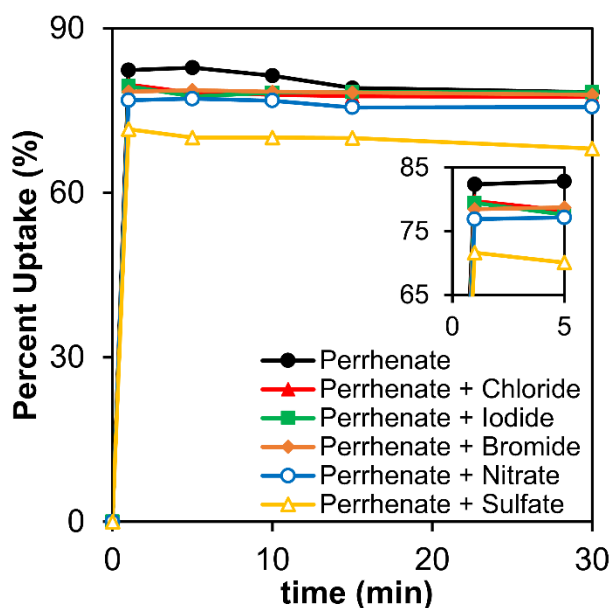


**Figure 2.3** Capture of  $\text{ReO}_4^-$  as a percentage vs time from equimolar solutions of perrhenate and various ions.

## 2.6 Regeneration

The viability of a waste remediation method significantly increases when a sorbent is recyclable. A reusable sorbent reduces both the financial and energy burdens of legacy waste remediation. The reusability of NU-1000 was probed using a glass microanalysis vacuum filtration apparatus equipped with an Anodisc™ filter membrane. MOF (10 mg) was placed on the filter and exposed to 10 mL of an aqueous perrhenate solution with a Re concentration of  $\sim 255$  ppm (equivalent to an exposure of 3.0  $\text{ReO}_4^-$  ions per  $\text{Zr}_6$ -node). Under weak vacuum, the solution was passed through the MOF within one minute. NU-1000 captured 161 ppm of Re ( $\sim 1.9$   $\text{ReO}_4^-$  ions/node) during the first exposure. The MOF was regenerated by washing with 10 mL of a 5% HCl solution which was found to completely remove the captured perrhenate. After washing with

10 mL of water, the same MOF sample was exposed to another 10 mL aliquot of the same perrhenate solution via the same method. The uptake of this second trial was found to be 153 ppm ( $\sim 1.8$  ions/node). Again, the 5% HCl wash entirely removed the captured perrhenate. The MOF was similarly washed with water to prepare for the next cycle. Over three additional cycles of exposure, acid washing, and water washing, NU-1000 sustained a steady uptake of  $\sim 150$  ppm or 1.8  $\text{ReO}_4^-$  ions per node (**Figure 2.4**). Therefore, captured perrhenate is efficiently removed from NU-1000 by washing with dilute hydrochloric acid, and NU-1000 consistently captures at least 1.8  $\text{ReO}_4^-$  ions per node through 5 cycles of exposure and regeneration.

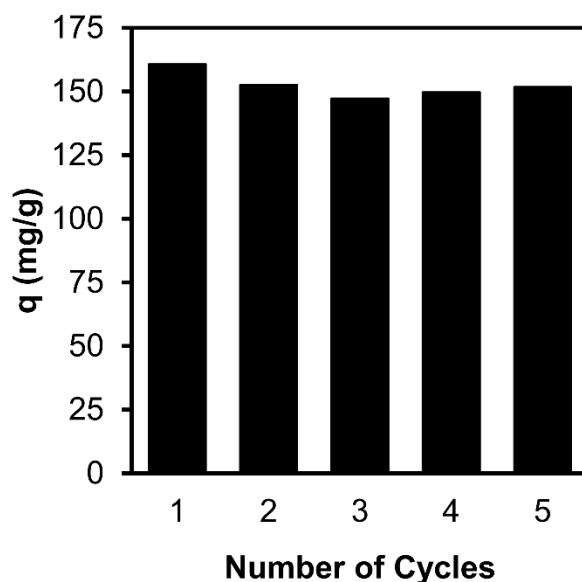


**Figure 2.4** NU-1000 maintains a  $\text{ReO}_4^-$  uptake of  $\sim 150$  ppm (1.8/node) through 5 cycles of exposure and washing with dilute HCl.

## 2.7 Pertchnetate Screening

Perrhenate is the most widely used pertchnetate simulant examined; however, screening of a material for sorption of both perrhenate and pertchnetate is rare. To examine if NU-1000 interacts

similarly with pertechnetate as with perrhenate, NU-1000 (10 mg) was exposed to an aqueous perrhenate or pertechnetate solution ( $1.455 \times 10^{-4}$  M; 14 ppm Tc or 27 ppm Re). NU-1000 was found to capture 89% of the perrhenate or 93% of the pertechnetate exposed to the MOF within 5 minutes of exposure (**Figure 2.5**). Further, the selectivity of NU-1000 for the targeted analyte compared to nitrate was examined by exposing NU-1000 (10 mg) to an aqueous equimolar solution of perrhenate or pertechnetate and nitrate ( $1.94 \times 10^{-4}$  M). NU-1000 was found to still capture 88% of the exposed pertechnetate, and similarly, 83% of exposed perrhenate. This work further confirms that perrhenate is a suitable surrogate for pertechnetate and that NU-1000 is a promising sorbent for pertechnetate.

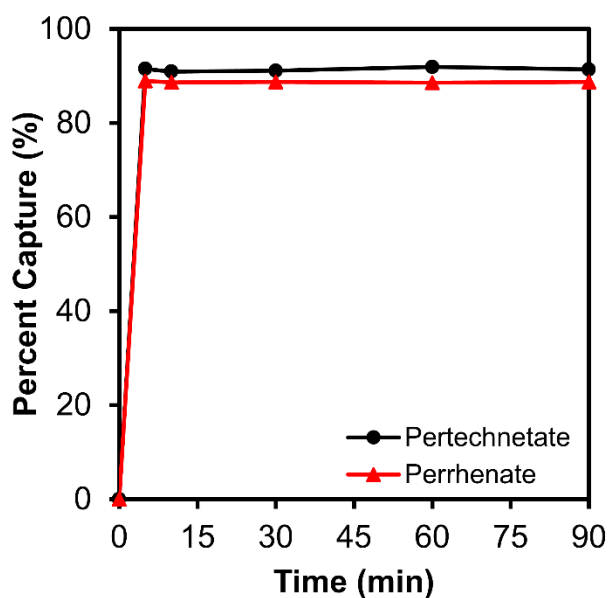


**Figure 2.5** Capture of  $\text{TcO}_4^-$  or  $\text{ReO}_4^-$  as a percentage from solution with initial concentration of  $1.455 \times 10^{-4}$  M (14 ppm Tc, 27 ppm Re) vs time.

## 2.8 Single Crystal X-Ray Diffraction

Many sorbents have been investigated for oxyanion remediation; however, very few have the advantage of containing well-defined binding sites and associated analyte binding motifs that can be characterized crystallographically. To determine the binding motif of perrhenate in NU-1000,

single crystals of the MOF were exposed to an aqueous sodium perrhenate solution and examined via single-crystal X-ray diffraction analysis (Table 2.1). Structure refinement reveals that there are both chelating and non-chelating, or terminal, perrhenate binding modes in both the small pore and the mesopore of NU-1000 (Figure 2.6). Residual electron density plots ( $F_o - F_c$  contoured maps) of the structure without rhenium atoms indicate that hydroxyl ( $-OH$ ) and water ( $-OH_2$ ) groups at the node are displaced by perrhenate via a pseudo-ion exchange mechanism (Figure 2.9). Therefore, both an  $-OH$  and an  $-OH_2$  group are displaced by perrhenate when the analyte is bound via a chelating motif. Similarly, a single  $-OH$  group is exchanged when perrhenate is bound in a non-chelating manner.

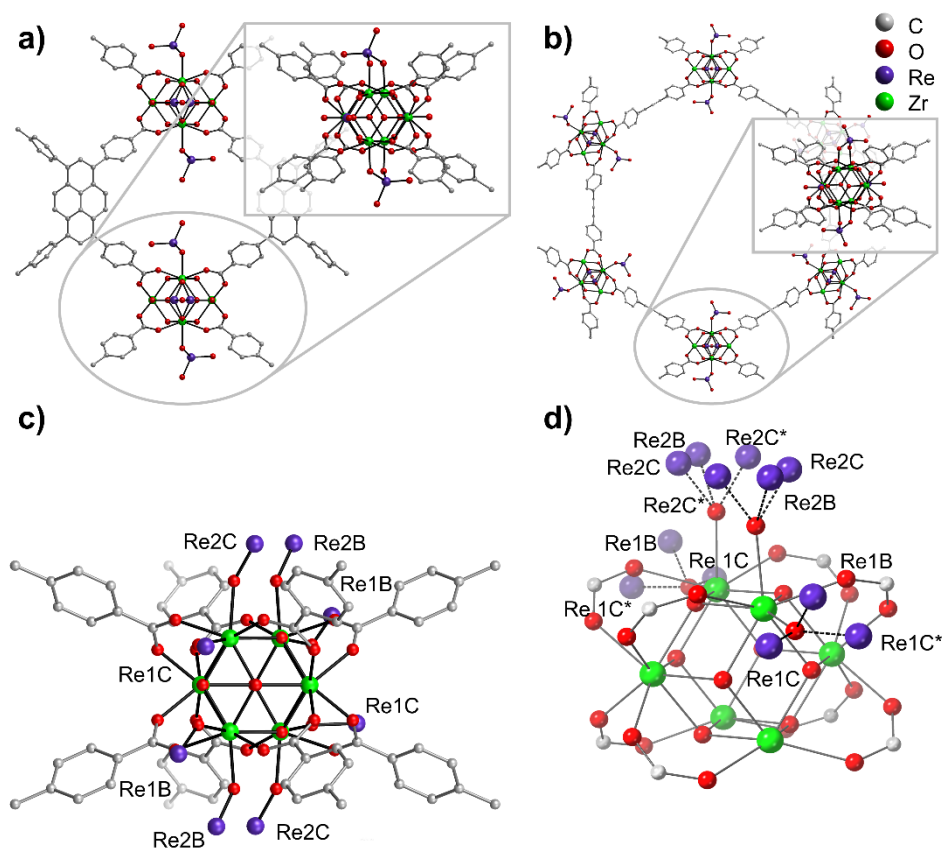


**Figure 2.6** The crystal structure of NU-1000 after  $ReO_4^-$  ion capture. (a) Chelating perrhenate binding motifs pointing into the small pore (Re1A). (b) Chelating perrhenate binding motifs pointing into the mesopore (Re2A). (c) Disorder of non-chelating perrhenate ions bound to the node

of NU-1000 at the terminal –OH group positions. At each position, there are two crystallographically unique positions (B and C) with one mode disordered between two positions (C and C\*) (d) Non-chelating perrhenate binding sites where Re1B and Re1C point into the small pore and Re2B and Re2C point into the mesopore.

The chelating sites in the small pore (Re1A) and the mesopore (Re2A) are each disordered between two equivalent positions (**Figure 2.6a** and **b**). The average O–Re–O angles are 110 and 109° in the small and mesopores, respectively, and are consistent with the traditional tetrahedral angle of the anion of 109.5°. The non-chelating perrhenate ions were found to be disordered over 3 positions surrounding each terminal –OH group on the Zr<sub>6</sub>-node (**Figure 2.6**), with two crystallographically nonequivalent positions in both the small pore (Re1B, Re1C) and the mesopore (Re2B, Re2C) (**Figure 2.6**). The terminal oxygen positions of the non-chelating perrhenate ions could not be resolved given the highly disordered structure and the surrounding solvent. The average O–Re bond lengths for the non-chelating perrhenate were 1.84 and 1.77 Å, respectively. They are observed to be slightly elongated compared to the traditional ~1.72 Å, possibly resultant of their highly disordered structure and low site occupancies (~0.2). The number of crystallographically determined perrhenate was *ca.* 0.7 and 2.2 per Zr<sub>6</sub>-node for chelating and non-chelating positions, respectively, which indicates that at room temperature, the non-chelating coordination mode contributes heavily to the capture of perrhenate by NU-1000.

## 2.9 Post-Adsorption Characterization

Full post-adsorption characterization of NU-1000 was performed to confirm the retention of both crystallinity and porosity. From powder X-ray diffraction patterns, it is apparent that NU-1000 remains crystalline throughout adsorption (**Figure 2.10**). Zirconium concentrations were monitored in all ICP-OES experiments and indicate no leaching, further verifying the stability of NU-1000. Additionally, N<sub>2</sub> isotherms before and after adsorption are nearly identical in shape with

Brunauer-Emmett-Teller (BET) surface areas of  $2140 \pm 5 \text{ m}^2 \text{ g}^{-1}$  ( $1010 \pm 5 \text{ m}^2 \text{ cm}^{-3}$ ) and  $1640 \pm 5 \text{ m}^2 \text{ g}^{-1}$  ( $1040 \pm 5 \text{ m}^2 \text{ cm}^{-3}$ ), respectively (**Figure 2.11**). The decrease in surface area is consistent with the increase in mass due to adding perrhenate to the framework and is in agreement with surface area reductions we have seen when capturing sulfate and selenate in NU-1000 and when installing catalysts in NU-1000 via post-synthetic modification.<sup>74, 75, 89</sup> The associated pore size distribution further corroborates the existence of binding motifs within both pores as shown by the SCXRD data (**Figure 2.12**). Diffuse reflectance infrared Fourier transform spectroscopy further elucidates the binding motifs of perrhenate within NU-1000. Neat NU-1000 exhibits a strong peak at  $3674 \text{ cm}^{-1}$  corresponding to non-H-bonding  $-\text{OH}$  stretches and this peak is diminished after perrhenate capture confirming the exchange of hydroxyl groups on the node for perrhenate anions (**Figure 2.13**).

## 2.10 Chapter Conclusions

In summary, the water stable,  $\text{Zr}_6$ -MOF NU-1000 was evaluated as a sorbent for aqueous perrhenate and found to have an adsorption capacity for  $\text{ReO}_4^-$  of 210 mg/g. Over a range of concentrations, NU-1000 was found to reach its maximum capacity within five minutes of exposure, presumably due to its large pores that facilitate diffusion and easy access to the nodes that contain substitutionally labile  $\text{Zr}-\text{OH}$  sites. Importantly, screening with pertechnetate further indicates NU-1000 is an effective sorbent and confirms that perrhenate is a suitable simulant for pertechnetate. Additionally, the presence of competing anions including chloride, bromide, iodide, and nitrate did not inhibit the adsorption of  $\text{ReO}_4^-$ ; while sulfate only slightly reduced  $\text{ReO}_4^-$  adsorption. Furthermore, NU-1000 can be regenerated after  $\text{ReO}_4^-$  adsorption by washing with dilute HCl and the MOF consistently adsorbs 1.8  $\text{ReO}_4^-$  ions per node through 5 cycles of exposure

and washing. Single-crystal X-ray diffraction was used to elucidate the  $\text{ReO}_4^-$  binding motifs which include a unique chelating mode in both the small pore and the mesopore, and two additional unique non-chelating modes in each pore. The facile, large scale preparation of NU-1000, large pores and high concentration of accessible nodes, and our recently garnered understanding of perrhenate binding at the node make this material a promising candidate for pertechnetate remediation.

## **2.11 Additional Information**

### *2.11.1 Materials*

All chemicals were used as received from the supplier. In these experiments, water is Milli-Q (Milli-pore). All gases were Ultra High Purity Grade 5 gases from Airgas Specialty Gases. Fisher Chemical Trace Metal Grade nitric acid was used for all ICP-OES and ICP-MS experiments. All ICP standards were purchased from Sigma-Aldrich. As-purchased Re and Na ICP standards were 1000 mg/g in 2% nitric acid, TraceCERT, and the Zr ICP standard was 1000 mg/g in 2% nitric acid and 0.2% hydrofluoric acid.

### *2.11.2 Physical Methods and Instrumentation*

NU-1000 was prepared according to literature procedure.<sup>77</sup> All MOF samples were thermally activated under ultra-high vacuum at 120 °C for 18 h on a Micromeritics Smart VacPrep. Nitrogen adsorption and desorption isotherm measurements were performed on a Micromeritics Tristar II at 77K. Powder X-ray diffraction measurements were collected on a STOE STADI MP equipped with  $\text{K}\alpha_1$  source and a 1D strip detector over a range of  $2^\circ < 2\theta < 37^\circ$ . DRIFTS measurements were obtained using a Nicolet 6700 FTIR spectrometer equipped with a liquid nitrogen cooled MCT detector. The spectra were collected in a KBr mixture and the pure KBr background was

subtracted. ICP-OES data were obtained using a Thermo iCAP 7600 ICP Spectrometer. ICP-MS data were collected on a ThermoFisher X Series II instrument equipped with an autodiluter and Collision Cell Technology (CCT). ICP-OES standards (0.0625 - 10 ppm) were prepared via serial dilution in 3% nitric acid. An ICP-MS standard (200 ppb) was similarly prepared for use with the autodiluter. All uptake experiments were performed in triplicate at a minimum.

Single-crystal X-ray diffraction measurements were performed on a Bruker Kappa APEX II CCD equipped with a Cu  $K\alpha$  ( $\lambda = 1.54178 \text{ \AA}$ ) microsource with MX optics. Single crystals of NU-1000 were immersed in an aqueous sodium perrhenate solution (0.1 M) at room temperature for two days. A single crystal was mounted on MicroMesh (MiTeGen) with paratone oil. The structure was solved by direct methods (SIR2014)<sup>90</sup> and refined by full-matrix least-squares refinement on  $F^2$  (SHELXL-2014/7)<sup>91</sup> using the Yadokari-XG software package.<sup>92</sup> The disordered non-coordinated solvents were removed using the PLATON SQUEEZE program.<sup>93</sup> The rhenium site occupancies were determined by structural refinement, and the total rhenium content is in moderate agreement with data obtained from ICP-OES analysis of digested perrhenate loaded MOF samples. Refinement results are summarized in **Table 2.1**. The associated CIF data file has been deposited in the Cambridge Crystallographic Data Centre (CCDC) under deposition numbers CCDC-1579219. The data can be obtained free of charge via [www.ccdc.cam.ac.uk/data\\_request/cif](http://www.ccdc.cam.ac.uk/data_request/cif) (or from the Cambridge Crystallographic Data Centre, 12 Union Road, Cambridge CB2 1EZ, U.K.).

Initial perrhenate uptake experiments were performed by exposing 5 mg ( $2.3 \times 10^{-6}$  mol) of NU-1000 to 15 mL of an aqueous sodium perrhenate solution in a 15 mL polypropylene centrifuge tube. Perrhenate solutions with Re concentrations of 57, 85, 114, 1142, 171, and 199 ppm

corresponding to 2 – 7 ions per MOF node ( $Zr_6$ -cluster) were used. Solutions were centrifuged for 1 min to allow the MOF to settle. A 1 mL aliquot of the supernatant was removed after 1 h, 18 h, and 24 h of exposure, and diluted to 10 mL in 3% nitric acid. The concentration of Re, Zr, and Na in each sample was determined by ICP-OES. These were compared to the concentrations of an identical analyte solution without MOF to determine the amount of  $ReO_4^-$  captured per node.

The maximum amount of perrhenate adsorbed per gram of NU-1000 was determined by exposing 5 mg ( $2.3 \times 10^{-6}$  mol) of MOF to 15 mL of an aqueous sodium perrhenate solution in a 15 mL polypropylene centrifuge tube. Solutions with rhenium concentrations of 28, 43, 57, 71, and 85 ppm corresponding to 1.0, 1.5, 2.0, 2.5, and 3.0 perrhenate ions per node were used. Each sample was centrifuged for 30 s to allow the MOF to settle. A 0.5 mL aliquot of the supernatant was removed at 1, 2, 3, 4, 5, 10, 15, 30, 60, 90, 120, and 180 min and diluted to 10 mL in 3% nitric acid. The concentration of Re, Zr, and Na in each solution was determined by ICP-OES. Similarly, these were compared to the concentrations of identical analyte solutions without MOF to determine the amount of  $ReO_4^-$  adsorbed ( $q$ ) in mg/g of NU-1000 where  $q = (C_i - C_f) \times V/m$ ,  $C_i$  = initial concentration (mg/L),  $C_f$  = final concentration (mg/L),  $V$  = volume of solution exposed to NU-1000 (L), and  $m$  = mass of NU-1000 (g).

Competition experiments were performed by exposing 5 mg ( $2.3 \times 10^{-6}$  mol) of NU-1000 to 15 mL of an aqueous equimolar ( $3.82 \times 10^{-5}$  M) solution of sodium perrhenate and sodium chloride, potassium bromide, potassium iodide, potassium nitrate, or sodium sulfate in a 15 mL polypropylene centrifuge tube. Samples were centrifuged for 30 s to allow MOF to settle and an aliquot of the supernatant was removed at 1, 5, 10, 15, 30, and 180 min. The concentration of Re

and Zr in each sample solution was determined by ICP-OES and compared to the concentrations of identical analyte solutions without MOF to determine the amount of  $\text{ReO}_4^-$  captured.

A low concentration kinetic study was performed by exposing 5 mg ( $2.3 \times 10^{-6}$  mol) of NU-1000 to 15 mL of an aqueous sodium perrhenate solution with a rhenium concentration of 1 ppm ( $5.4 \times 10^{-6}$  M). Samples were centrifuged for 30 s and aliquots of the supernatant were removed at 5, 10, 15, 30, 60 and 180 min and diluted in 3% nitric acid. The concentration of Re, Zr, and Na in each sample was determined by ICP-MS and compared to the concentration of an identical analyte solution without MOF to determine the amount of  $\text{ReO}_4^-$  captured.

Regeneration experiments were generally performed by exposing MOF to an aqueous sodium perrhenate solution, washing with a hydrochloric acid solution, and washing with water. The full exposure and washing cycle was repeated 4 additional times. Specifically, a glass microanalysis vacuum filter apparatus equipped with an Anodisc filter membrane was washed with 10 mL of water three times. A slurry of 10 mg ( $4.6 \times 10^{-6}$  mol) of NU-1000 in 10 mL of water was poured onto the membrane. Once the MOF had been brought to dryness under vacuum, 10 mL of an aqueous sodium perrhenate solution with a rhenium concentration of 255 ppm corresponding to 3 ions per  $\text{Zr}_6$ -node was poured into the apparatus. The entire solution passed through the MOF in less than one minute and was collected in a clean 6 dram vial. Once the MOF was returned to dryness, 10 mL of a 5% hydrochloric acid solution was passed through the MOF (again the solution passed through the MOF in less than one minute and the filtrate was collected in a clean 6 dram vial). Then, 10 mL of water was passed through the MOF (again the water was passed through the MOF in under one minute and the filtrate was collected in a clean 6 dram vial). This cycle was repeated for a total of 5 perrhenate exposures. An aliquot from each vial was removed and diluted

in 3% nitric acid. The concentrations of Re, Zr, and Na in each sample were determined by ICP-OES and compared to concentrations of identical analyte solutions without MOF to determine the amount of  $\text{ReO}_4^-$  captured.

Uptake experiments were performed according to a reported procedure.<sup>62</sup> In a typical experiment, 10 mg ( $4.6 \times 10^{-6}$  mol) of MOF was soaked in 10 mL of an aqueous pertechnetate solution ( $1.455 \times 10^{-4}$  M). The mixture was stirred for a selected time (5, 10, 30, 60, 90 min) followed by separation with a 0.22  $\mu\text{m}$  nylon membrane filter. The concentration of  $\text{TcO}_4^-$  was determined by UV-vis absorption spectroscopy and liquid scintillation spectrometry. A similar method was employed to examine the effect of competing nitrate on pertechnetate capture using an equimolar ( $1.94 \times 10^{-4}$  M)  $\text{TcO}_4^-$  and  $\text{NO}_3^-$  solution. Separation and concentration analysis were performed identically.

### 2.11.3 Single-Crystal X-Ray Diffraction Data for NU-1000- $\text{ReO}_4$

**Table 2.1** Crystallographic data for NU-1000- $\text{ReO}_4$ .

<b>Formula</b>	C88 H44 O36.4 Zr6 Re2.96
<b>Formula Weight</b>	2782.18
<b>Temperature (K)</b>	100(2)
<b>Wavelength (Å)</b>	1.54178
<b>Crystal system</b>	Hexagonal
<b>Space group</b>	<i>P6/mmm</i> (no.191)
<b><i>a</i> (Å)</b>	39.633(3)
<b><i>b</i> (Å)</b>	39.633(3)
<b><i>c</i> (Å)</b>	16.416(1)
<b><i>V</i> (Å<sup>3</sup>)</b>	22331(3)
<b><i>Z</i></b>	3
<b>Calcd Density (g/cm<sup>3</sup>)</b>	0.633
<b><math>\mu</math> (mm<sup>-1</sup>)</b>	4.181

<b><i>F</i>(000)</b>	4062
<b>Crystal size (mm<sup>3</sup>)</b>	0.06 × 0.03 × 0.03
<b><i>θ</i><sub>min</sub>, <i>θ</i><sub>max</sub> (°)</b>	2.70, 61.3
<b>Total reflection</b>	60572
<b>Unique reflection</b>	6409
<b>Parameter number</b>	224
<b><i>R</i><sub>int</sub></b>	0.1542
<b>Goodness-of-fit</b>	1.028
<b><i>R</i><sub>1</sub> [<i>I</i> &gt; 2σ(<i>I</i>)]</b>	0.0589
<b>w<i>R</i><sub>2</sub> (all reflection)</b>	0.1910

#### 2.11.4 Perrhenate Adsorption Measurements

**Table 2.2** Perrhenate adsorption per Zr<sub>6</sub>-node of NU-1000 when exposed to aqueous sodium perrhenate solutions with concentrations of 2 to 7 ReO<sub>4</sub><sup>-</sup> ions per node.

Exposure per Node	Uptake per Node	
	1 Hr	26 Hr
2	1.0	1.1
3	1.3	1.4
4	1.5	1.6
5	1.6	1.7
6	1.6	1.8
7	1.8	2.0

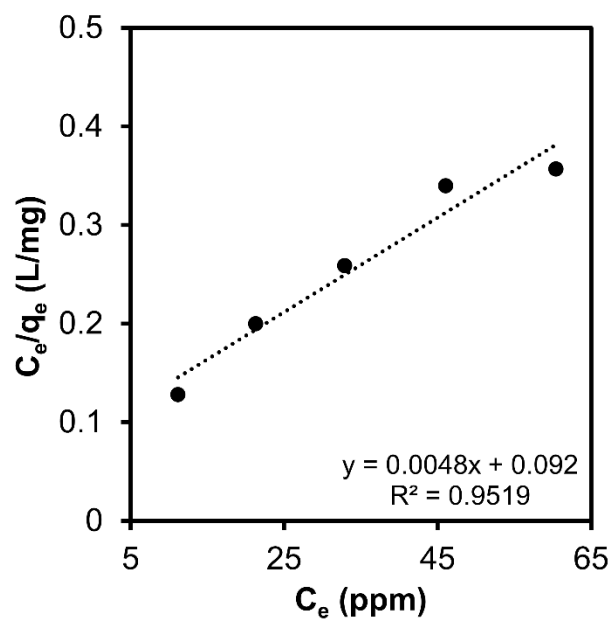


**Figure 2.7** The Type I, linear Langmuir plot (Table 2.3) for perhenate capture by NU-1000.

**Table 2.3** Langmuir Equation and Parameters

$$\frac{C_e}{q_e} = \left(\frac{1}{Q}\right)C_e + \frac{1}{K_L Q}$$

where  $C_e$  is the equilibrium concentration (mg/L),  $q_e$  is the equilibrium uptake (mg/g),  $Q$  is maximum uptake capacity (mg/g), and  $K_L$  is the Langmuir constant (L/mg).

Q	210 mg/g
$K_L$	0.052 L/mg
$K_d = q_e/C_e$	2,800 – 7,800 mL/g

**Table 2.4** Perrhenate uptake Capacities of several previously examined sorbents.

Material	Uptake ( $\text{ReO}_4^-$ )	Ref.
NU-1000	210 mg/g	this work
Na-Bentonite	2.9 mg/g	78
Modified Bentonite	8.5 mg/g	78
ZrCX-1	13.85 mg/g	88
32-Cascade (dendrimer)	93 mg/g ( $\text{TcO}_4^-$ )	79
UiO-66- $\text{NH}_3^+$	159 mg/g, 1 day	59
SCU-101	217 mg/g	63
PAF-1- $\text{NR}_3^+\text{X}^-$	420 mg/g, 1 day	58
SLUG-21	602 mg/g	80
SCU-100	541 mg/g	62
SBN	786 mg/g	81
PC2vimBr (ionic liquid gel)	860 mg/g, 4 hr	82
NU-1000	2,800 – 7,800 mL/g	this work
NDTB-1	72%, 36 hrs & 3,800 – 11,000 mL/g ( $\text{TcO}_4^-$ )	83, 84
Silica-supported nanoiron	95% (290L/kg phase ratio)	85
$\text{Ni}_6\text{Al}_2(\text{OH})_{16}\text{NO}_3 \cdot n\text{H}_2\text{O}$	1,390 mL/g	86
Various chalcogen materials	1,500 – 3,600 mL/g	87

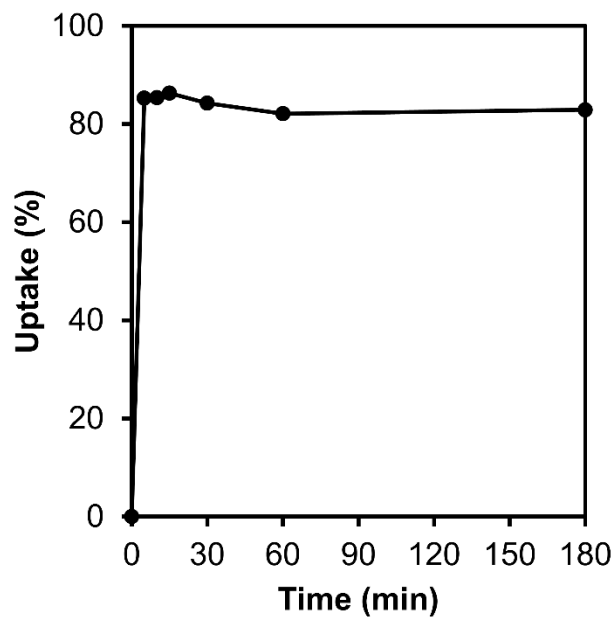


**Figure 2.8** Capture of  $\text{ReO}_4^-$  as a percentage vs time by NU-1000 (2 mg) from an aqueous solution with Re concentration of 1 ppm.

## 2.11.5 Residual Electron Density Plots

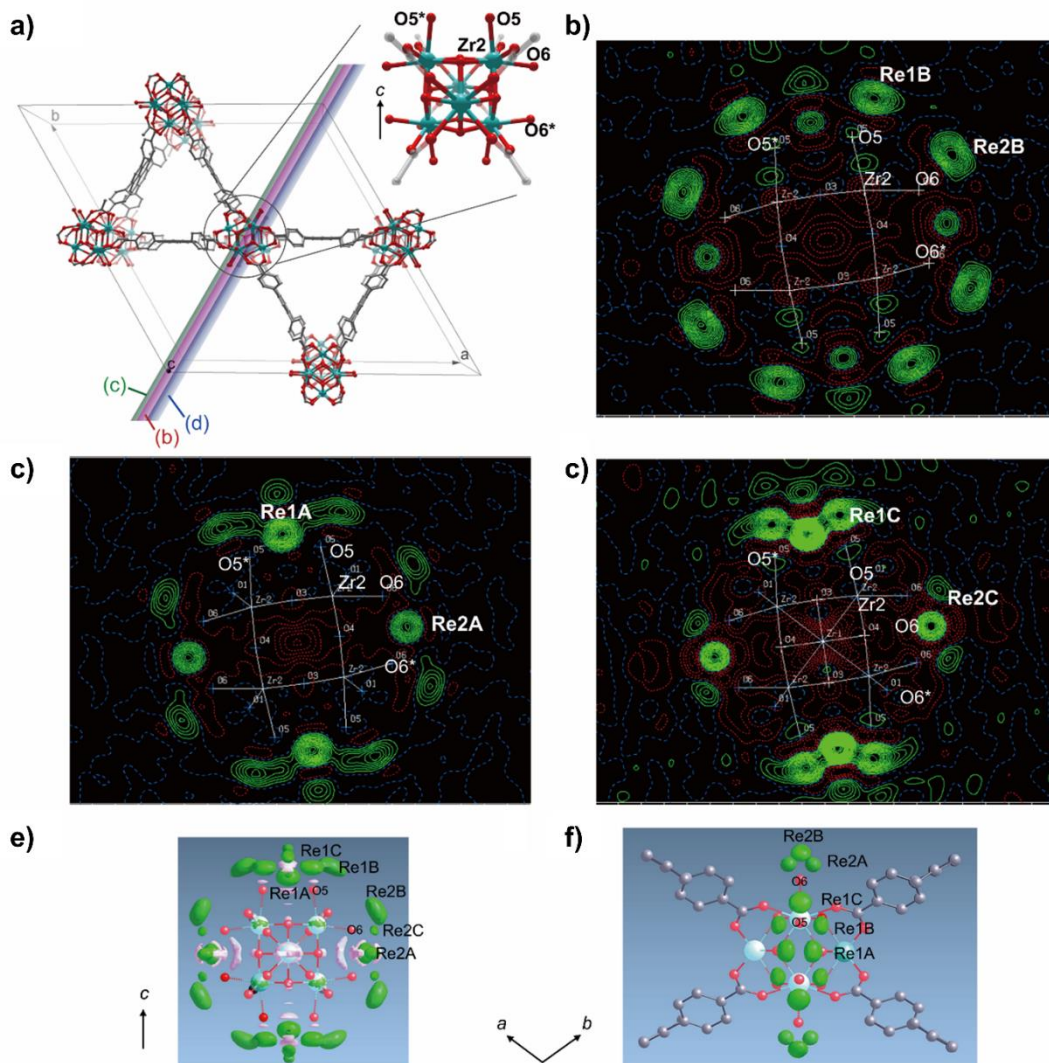


**Figure 2.9**  $F_o - F_c$  contoured Fourier maps around the  $Zr_6$ -node calculated when Re atoms are omitted from the crystallographic information file. PLATON software (b–d) and Shelxle software (e–f) were used for the calculations. (a) The crystal structure of NU-1000 and the (110) plane (red color). Gray, red, and cyan spheres represent carbon, oxygen, and zirconium atoms, respectively. The O5 and O6 oxygen atoms belong to the hydroxyl groups that point toward the small pore and the mesopore, respectively. (b) The contoured map in the (110) plane (contours are from  $-2.40$  to  $4.80 \text{ e } \text{Å}^{-3}$  in steps of  $0.40 \text{ e } \text{Å}^{-3}$ ). The residual electron densities correspond to the non-chelating Re1B and Re2B. (c) The contoured map in the green-colored plane parallel to the (110) plane and shifted  $0.06 \text{ Å}$  (contours are from  $-2.40$  to  $4.80 \text{ e } \text{Å}^{-3}$  in steps of  $0.40 \text{ e } \text{Å}^{-3}$ ). The residual electron densities correspond to the chelating Re1A and Re2A. (d) The contoured map in the blue-colored plane parallel to the (110) plane and shifted  $0.10 \text{ Å}$  (contours are from  $-2.40$  to  $5.80 \text{ e } \text{Å}^{-3}$  in steps of  $0.20 \text{ e } \text{Å}^{-3}$ ). The electron densities correspond to the non-chelating Re1C and Re2C. (e) The 3D contoured map with contours from  $-0.90$  to  $0.90 \text{ e } \text{Å}^{-3}$ . (f) The 3D contoured map with contours from  $-2.40$  to  $2.40 \text{ e } \text{Å}^{-3}$ .

## 2.11.6 Post-Adsorption Characterization

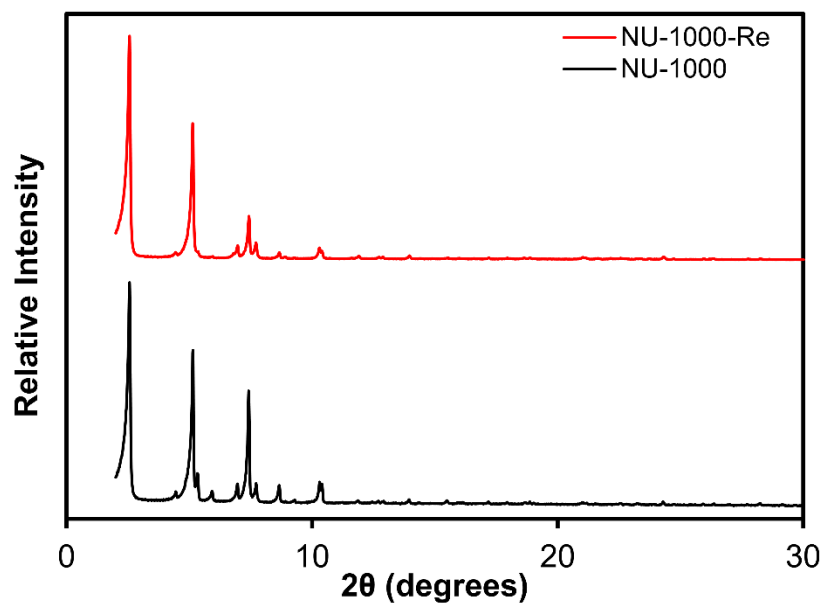


**Figure 2.10** Powder X-ray diffraction patterns for neat NU-1000 and NU-1000-Re loaded with  $\sim 1.8 \text{ ReO}_4^-$  ions per  $\text{Zr}_6$ -node indicate the MOF retains its crystallinity throughout adsorption.

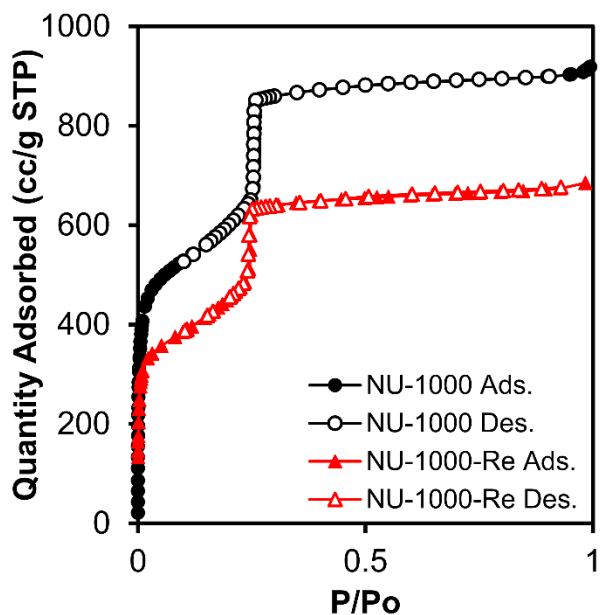


**Figure 2.11**  $\text{N}_2$  isotherms of NU-1000 and NU-1000-Re containing  $\sim 1.8 \text{ ReO}_4^-$  per  $\text{Zr}_6$ -node show a surface area decrease consistent with the installation of anions at the node.

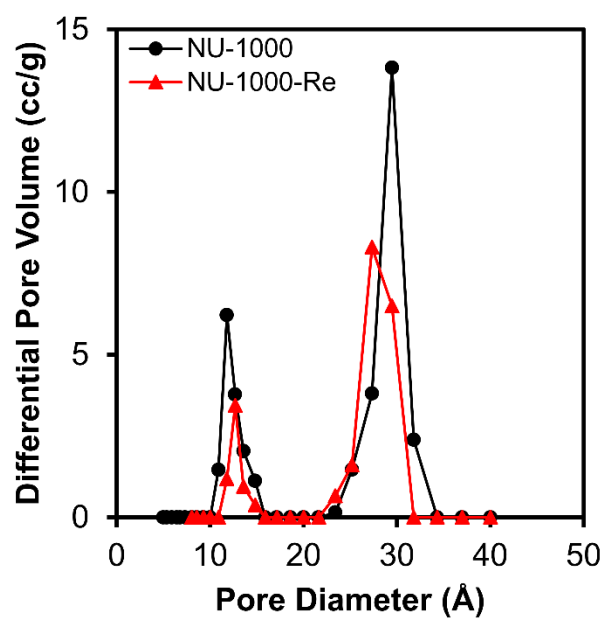


**Figure 2.12** Pore size distributions of NU-1000 and NU-1000-Re containing  $\sim 1.8 \text{ ReO}_4^-$  per node confirm the binding of perrhenate in the framework.

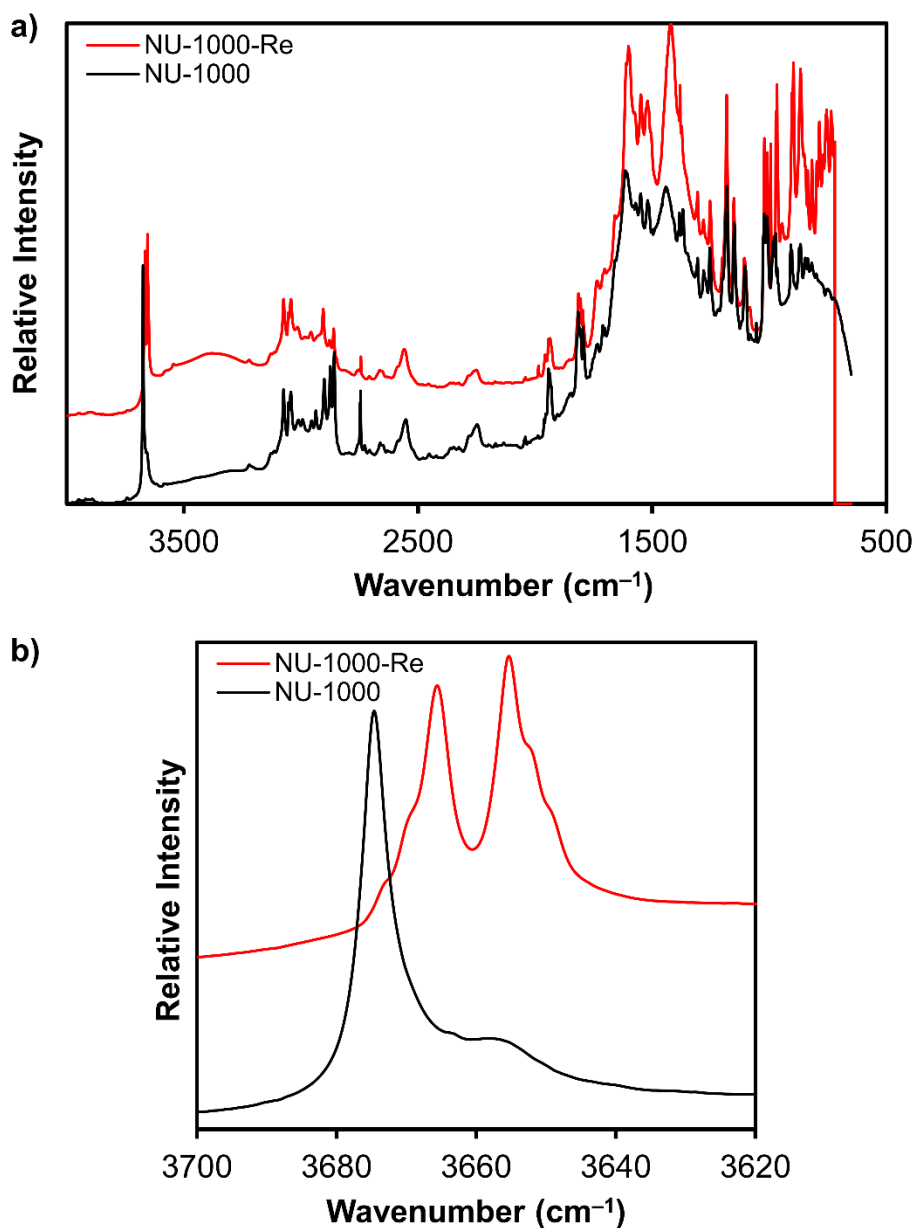


**Figure 2.13** (a) Full DRIFTS spectra for NU-1000 and NU-1000-Re containing  $\sim 1.8$   $\text{ReO}_4^-$  per node. (b) DRIFTS spectra for NU-1000 and NU-1000-Re containing  $1.8$   $\text{ReO}_4^-$  per node highlighting the reduced intensity and splitting of the non-hydrogen bonding  $-\text{OH}$  stretching peak at  $3674$   $\text{cm}^{-1}$ .

## Chapter 3. Efficient Extraction of Inorganic Selenium from Water by a Zr Metal–Organic Framework: Investigation of Volumetric Uptake Capacity and Binding Motifs

Portions of this chapter appear in the following manuscript:

**Drout, R.J.**; Howarth, A.J.; Otake, K.; Islamoglu, T.; Farha, O.K., Efficient Extraction of Inorganic Selenium from Water by a Zr Metal–Organic Framework: Investigation of Volumetric Uptake Capacity and Binding Motifs. *CrystEngComm*, **2018**, *20* (40), 6140-6145.

### 3.1 Chapter Summary

Strict monitoring and control of selenium concentrations in freshwater supplies is critical to safeguarding human health and aquatic life. A handful of previously investigated sorbents exhibit noteworthy gravimetric ( $\text{mg g}^{-1}$ ) Se uptake capacities; however, often display insufficient volumetric ( $\text{mg cm}^{-3}$ ) capacities, thereby requiring large volumes of material for commercial implementation. In pursuit of mitigating this material inefficiency, we investigated the selenite ( $\text{SeO}_3^{2-}$ ) and selenate ( $\text{SeO}_4^{2-}$ ) affinity of MOF-808, a Zr-based metal–organic framework with a high density of potential Se oxyanion binding sites. MOF-808 recorded exceptional volumetric and gravimetric Se oxyanion capacities of  $133 \text{ mg g}^{-1}$  ( $127 \text{ mg cm}^{-3}$ ) and  $118 \text{ mg g}^{-1}$  ( $112 \text{ mg cm}^{-3}$ ) for aqueous selenite and selenate, respectively. Single-crystal X-ray diffraction studies revealed that selenite and selenate can bind at the MOF node via two distinct binding motifs, an  $\eta_2\mu_2$  motif in which the oxyanion coordinates to two different metal atoms in a single node, and a  $\mu_2$  motif in which the oxyanion interacts with only a single metal atom. Furthermore, powder X-ray diffraction (PXRD) patterns and  $\text{N}_2$  adsorption/desorption isotherms confirm the retention of bulk crystallinity and porosity after the uptake of Se oxyanions.

### 3.2 Selenium Oxyanion Pollution

In the preceding decades, researchers have uncovered the vital role of selenium as an essential trace element for human life. Selenium, of all trace essential elements, displays the most confined window of exposure between dietary deficiency ( $<40 \text{ }\mu\text{g/day}$ ) and selenosis, acute Se toxicity, ( $>400 \text{ }\mu\text{g/day}$ ).<sup>94</sup> As such, the rigid maintenance of the selenium concentration in drinking water is paramount. Selenium, which is present naturally in rocks, coal, and soil, can enter the freshwater supply via erosion.<sup>95, 96</sup> Several anthropogenic activities such as coal and fossil fuel combustion, mining, and metal refining, further increase the degree of selenium contamination in freshwater

supplies.<sup>95,96</sup> To protect both aquatic and human health, the U.S. Environmental Protection Agency (EPA) has mandated a maximum contaminant level (MCL) of 50 ppb selenium in drinking water.<sup>97</sup> While organoselenides exist, most selenium pollution remediation efforts focus on capturing inorganic selenium species including selenite ( $\text{SeO}_3^{2-}$ ) and selenate ( $\text{SeO}_4^{2-}$ ) because their high solubility enhances their bioavailability and thereby increases the risk of exposure.<sup>95</sup>

Several strategies to remove selenite and selenate from aqueous media have been investigated including chemical reduction,<sup>98</sup> bioremediation using bacteria and fungi,<sup>99-103</sup> and adsorption.<sup>104-106</sup> Unfortunately, immense startup expenses and continuing operational costs have forestalled the large-scale use of bioremediation techniques.<sup>103</sup> Conversely, implementation of sorbent-based water decontamination technologies in industry is often impeded by insufficient uptake capacities presumed to partially result from low porosity and binding site density. Industrial application obligates that a technique be both financially lucrative and demonstrate exceptional uptake, both gravimetrically ( $\text{mg g}^{-1}$ ) and volumetrically ( $\text{mg cm}^{-3}$ ).<sup>107</sup>

Metal-organic frameworks (MOFs) integrate the properties of ideal sorbents, namely high porosity, surface area, and binding site density, and have already demonstrated promise in removing toxic species from aqueous media.<sup>63, 108-112</sup> MOFs are crystalline, multidimensional lattices comprised of inorganic metal oxide nodes and organic multitopic ligands assembled through coordination bonds.<sup>7, 68</sup> Judicious selection of the node and linker during synthesis has yielded materials displaying an extensive array of chemical and physical properties.<sup>113, 114</sup> Additionally, post-synthetic modification techniques can further tailor MOF properties through installation of chemical functionality at the nodes or linkers or by doping the framework pores.<sup>9</sup> The vast assortment of chemical and physical properties expressed by MOFs has prompted their

application in gas storage<sup>12, 70</sup> and separation,<sup>13, 71</sup> catalysis,<sup>14</sup> chemical sensing,<sup>10</sup> drug delivery,<sup>72</sup> and water remediation.<sup>15, 109</sup>

Howarth *et al.* reported that NU-1000, an 8-connected MOF composed of Zr<sub>6</sub>-based nodes and tetratopic H<sub>4</sub>TBAPy linkers, exhibits exceptional gravimetric uptake of both selenite (95 mg g<sup>-1</sup>) and selenate (85 mg g<sup>-1</sup>).<sup>74</sup> Unfortunately, the corresponding volumetric uptake capacities are merely 45 mg cm<sup>-3</sup> and 40 mg cm<sup>-3</sup>, meaning that a substantial volume of material (i.e. larger column) would be required for water treatment. We anticipated that by increasing the density of potential binding sites, through use of a smaller linker and thus higher density MOF, we should increase the volumetric uptake capacities of the Se oxyanions. Herein, we investigate both the gravimetric and volumetric uptake capacities of selenite and selenate in MOF-808. This MOF, comprised of 6-connected Zr<sub>6</sub>-based nodes and tritopic trimesic acid linkers, has smaller pores (~17 Å) compared to NU-1000 (~30 Å and 10 Å) and a higher density (0.955 g cm<sup>-3</sup> vs. 0.473 g cm<sup>-3</sup>) and should thereby exhibit a higher volumetric Se uptake capacity given that the pores are still large enough to permit diffusion of the Se oxyanions (**Figure 3.1**). Furthermore, we capitalize on the crystalline nature of the MOF to characterize the selenite/selenate binding motif via single-crystal X-ray diffraction.

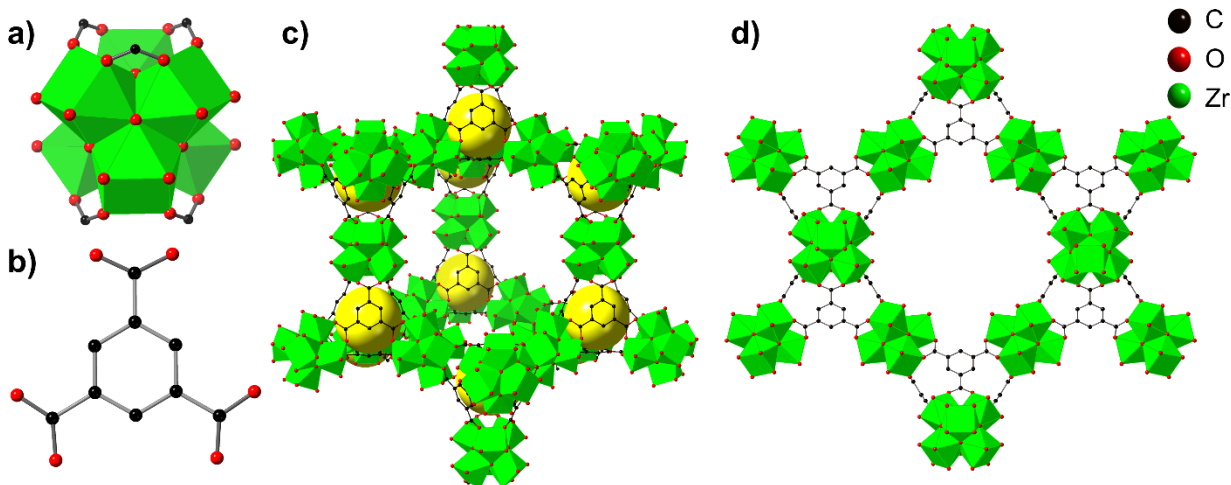


**Figure 3.1** MOF-808 is comprised of a) Zr<sub>6</sub>-nodes and b) tritopic trimesic acid linkers. The framework consists of c) large adamantane cages and exhibits the d) **spn** topology.

### 3.3 Preliminary Investigation of SeO<sub>3</sub><sup>2-</sup> and SeO<sub>4</sub><sup>2-</sup> Uptake

Initial experiments were performed to garner an understanding of the affinity of MOF-808 for selenite (SeO<sub>3</sub><sup>2-</sup>) and selenate (SeO<sub>4</sub><sup>2-</sup>). MOF-808 samples were exposed to aqueous solutions with SeO<sub>3</sub><sup>2-</sup> or SeO<sub>4</sub><sup>2-</sup> concentrations corresponding to 2 – 7 ions per Zr<sub>6</sub>-node with Se concentrations of 61 ppm to 212 ppm (**Table 3.3** and **Table 3.4**). After 24 h, MOF-808 was found to capture up to 1.6 SeO<sub>3</sub><sup>2-</sup> and 1.4 SeO<sub>4</sub><sup>2-</sup> ions per Zr<sub>6</sub>-node. These promising results prompted us to further investigate the kinetics and capacity of SeO<sub>3</sub><sup>2-</sup> and SeO<sub>4</sub><sup>2-</sup> uptake in MOF-808.

### 3.4 Examination of Uptake Kinetics

Large scale sorbent use requires a material rapidly capture the target species. To examine the kinetics of SeO<sub>3</sub><sup>2-</sup> and SeO<sub>4</sub><sup>2-</sup> uptake in MOF-808, we exposed MOF-808 samples to aqueous selenite and selenate solutions with Se concentrations ranging from 15 ppm to 71 ppm corresponding to 0.5, 1.0, 1.5, 2.0, and 2.5 ions per MOF node. To monitor the adsorption of Se oxyanions by MOF-808, an aliquot of the supernatant was removed after 5, 10, 15, 30, 60, 90, and

120 min. The amount  $q$  in mg of Se oxyanion per gram of MOF-808 was determined using **Eqn 1.1** as reproduced below:

$$q = \frac{(C_i - C_f) \times V}{m} \quad (1.1)$$

where  $C_i$  is the initial concentration (mg/L) of Se oxyanion in the solution exposed to MOF-808,  $C_f$  is the final Se oxyanion concentration (mg/L) after exposure to MOF-808,  $V$  is the volume of solution exposed to MOF-808, and  $m$  is the mass (g) of MOF-808. By monitoring  $q$  as a function of time, adsorption isotherms could be constructed for each exposure concentration (**Figure 3.2**). These isotherms reveal that within 5 min, MOF-808 reaches its maximum Se oxyanion uptake. We attribute the rapid capture kinetics to the framework's large pores ( $\sim 17 \text{ \AA}$ ) and the substitutionally labile water ( $-\text{OH}_2$ ) and hydroxyl ( $-\text{OH}$ ) groups on the MOF node.

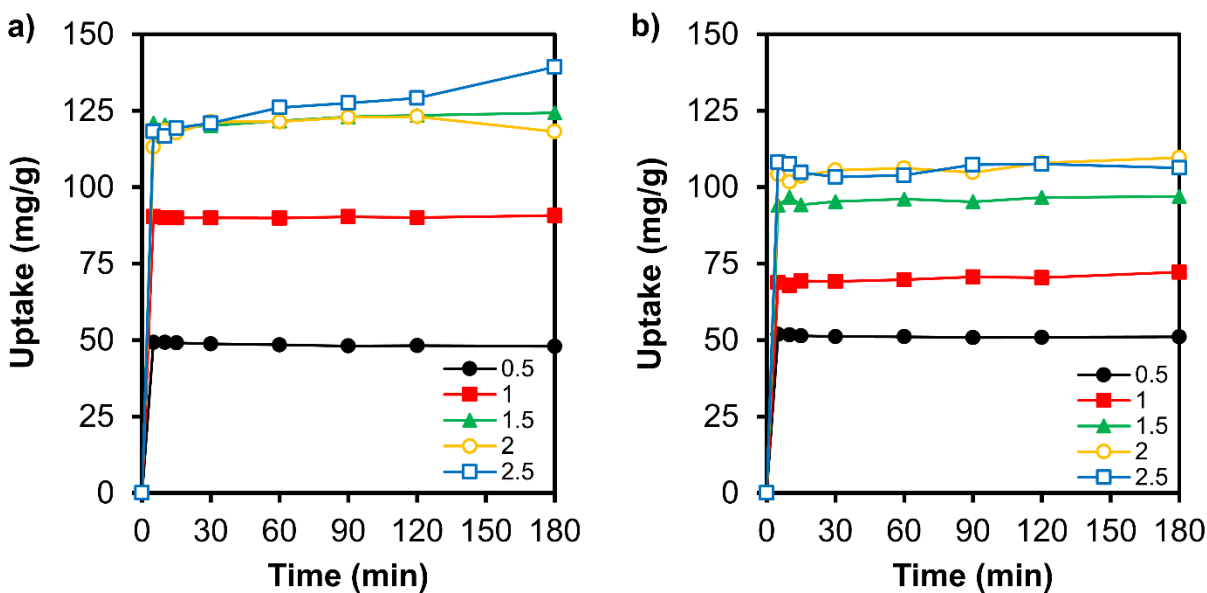


**Figure 3.2** Uptake isotherms of aqueous a) selenite and b) selenate at various exposure concentrations corresponding to 0.5, 1.0, 1.5, 2.0, and 2.5 ions per node.

### 3.5 Determination of Gravimetric and Volumetric Uptake Capacity

In addition to rapid kinetics, it is also critical that a material exhibit high uptake capacity for the target contaminant. Predominantly, gravimetric uptake capacities (mg/g) are reported; however, commercial application requires exceptional volumetric uptake capacities to minimize the size of purification columns. To this end, we evaluated both the gravimetric and volumetric uptakes capacities of  $\text{SeO}_3^{2-}$  and  $\text{SeO}_4^{2-}$  in MOF-808. The Type I shape of the Se sorption isotherms prompted us to employ a Linear Type I Langmuir Fit to determine the maximum uptake capacities (**Figure 3.5**, **Figure 3.6**, and **Table 3.5**). MOF-808 recorded gravimetric uptake capacities of  $133 \text{ mg g}^{-1}$  and  $118 \text{ mg g}^{-1}$  for  $\text{SeO}_3^{2-}$  and  $\text{SeO}_4^{2-}$ , respectively. The corresponding volumetric uptake capacities for selenite and selenate are  $127 \text{ mg cm}^{-3}$  and  $112 \text{ mg cm}^{-3}$ , respectively. These capacities are exceptional in comparison to other materials, and also noteworthy given that many materials exhibit a high affinity for only one of either selenite and selenate (**Table 3.8**).<sup>74, 106, 115-121</sup> Furthermore, we see that MOF-808 records *higher* gravimetric and volumetric capacities for  $\text{SeO}_3^{2-}$  and  $\text{SeO}_4^{2-}$  than NU-1000 as initially predicted (

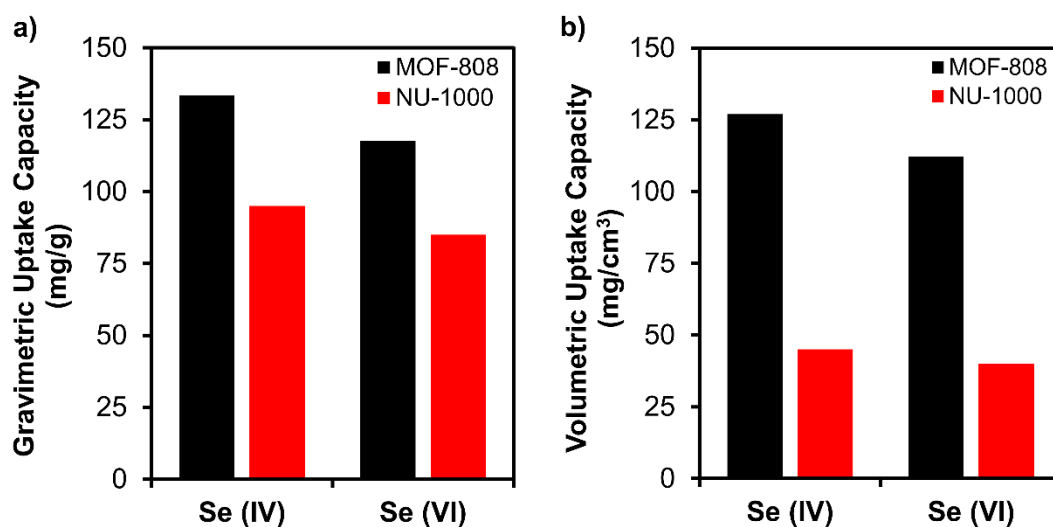


**Figure 3.3**, **Table 3.6**, and **Table 3.7**.

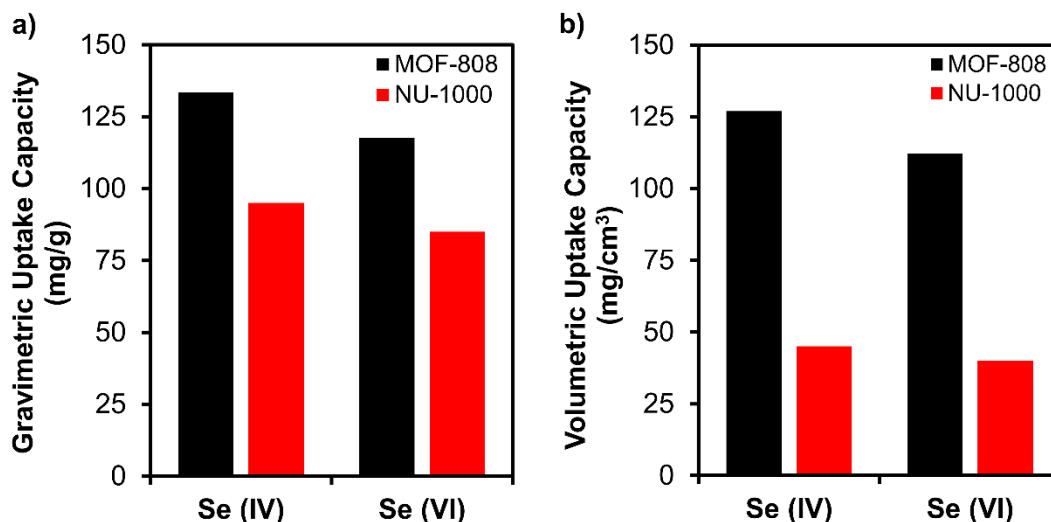


**Figure 3.3** Selenite (Se(IV)) and selenate (Se(VI)) a) gravimetric uptake capacities and b) volumetric uptake capacities in MOF-808 and NU-1000.

### 3.6 Crystallographic Investigation of Binding Motifs

The amorphous nature of many commonly used sorbents renders them difficult to characterize throughout a sorption process. Advantageously, MOF crystallinity offers a unique opportunity to investigate the ion binding motifs via single-crystal X-ray diffraction analysis. To this end, single crystals of Hf-MOF-808 were prepared and analyzed after exposure to an aqueous solution of  $\text{SeO}_3^{2-}$  and  $\text{SeO}_4^{2-}$ . The Hf derivative, which exhibits a PXRD pattern and  $\text{N}_2$  adsorption/desorption isotherm shape consistent with Zr-MOF-808, was utilized to improve the quality of the single-crystal X-ray diffraction measurement.<sup>122</sup>

Both selenite and selenate were observed to bind at the  $\text{Hf}_6$ -node via two distinct motifs. In the first, an  $\eta_2\mu_2$  motif directed into the large cages, two oxygen atoms of selenite bind to two different Hf atoms within a single node (**Figure 3.4a and b, Table 3.1, Table 3.2**). The Se–O(node) bond lengths of 1.684 Å and 1.826 Å suggest a slight distortion of the selenite ion upon binding in comparison to the accepted selenite Se–O bond length of 1.709 Å.<sup>123</sup> The O(node)–Se–O(node)

bond angle of  $111.7^\circ$  is slightly larger than the accepted  $107^\circ$  for an ideal trigonal pyramid. Due to the disorder and low occupancy of this binding motif, the terminal oxygen atom could not be resolved.<sup>124</sup> Selenite can also bind to the node via a  $\mu_2$  motif directed into the cage in which two of the selenite oxygen atoms coordinate to a single Hf atom (**Figure 3.4c** and **d**). The Se–O(node) and the Se–O(terminal) bond lengths are  $1.853 \text{ \AA}$  and  $\sim 1.727 \text{ \AA}$ , respectively. The slight elongation of the bonds may be due to the binding event itself or the disordered nature of the binding event. The bond angles of  $89.99^\circ$  and  $101.9^\circ$  for O(node)–Se–O(node) and O(node)–Se–O(terminal) also suggest significant distortion of the ion upon binding.

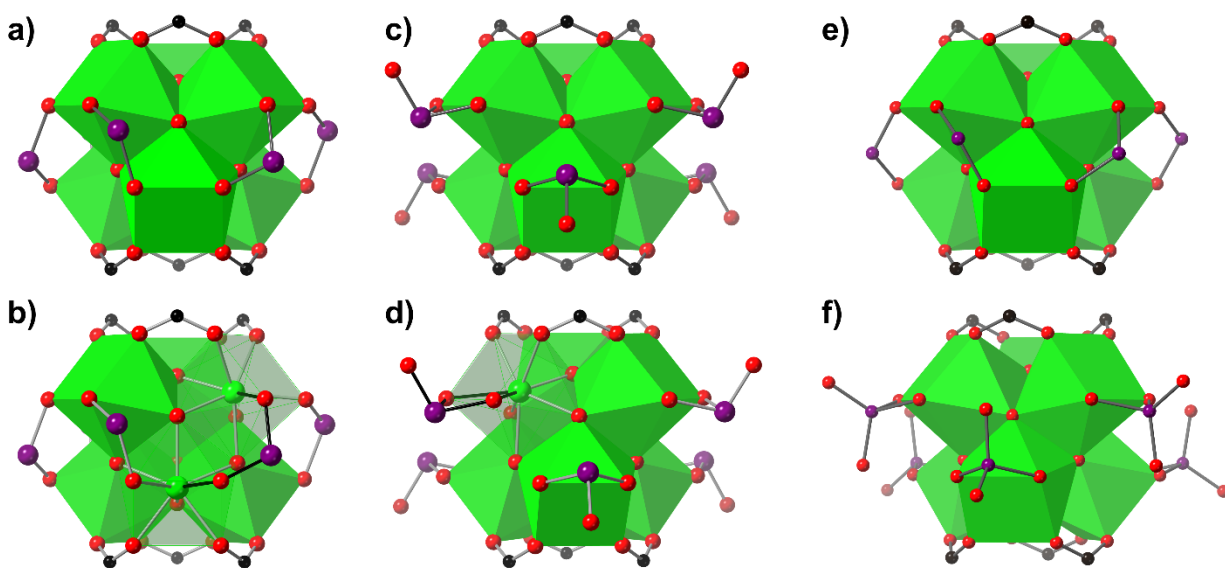


**Figure 3.4** Visualizations of selenite and selenate binding at the Hf-MOF-808 node. a) Selenite  $\eta_2\mu_2$  binding motif in which two of selenite oxygen atoms coordinate to two different Hf atoms of a single node. Due to disorder, the terminal oxygen atom could not be resolved. b) Selenite  $\eta_2\mu_2$  with two transparent Hf polyhedrons to demonstrate binding to two different Hf atoms. c) Selenite  $\mu_2$  binding motif in which two oxygen atoms coordinate the same Hf atom in the node. d) Selenite  $\mu_2$  binding motif with transparent Hf polyhedron to demonstrate binding at a single Hf atom. e) Selenate  $\eta_2\mu_2$  binding motif. f) Selenate  $\mu_2$  binding motif. The green, red, black, and purple spheres represent Hf, O, C, and Se atoms, respectively.

Similarly, selenate ( $\text{SeO}_4^{2-}$ ) binds via both  $\eta_2\mu_2$  and  $\mu_2$  motifs. In the  $\eta_2\mu_2$  motif, the Se–O(node) bond lengths are  $1.610 \text{ \AA}$  and  $1.669 \text{ \AA}$  (**Figure 3.4e**) and are moderately consistent with the  $1.64$

Å Se–O bond length recorded for hydrated selenate in aqueous media.<sup>123</sup> The O(node)–Se–O(node) bond angle is 117.6°, larger than anticipated (109.5°) for an ideal tetrahedral ion. In comparison, the Se–O(node) bond lengths of the  $\mu_2$  motif are significantly elongated to 1.767 Å; however, the Se–O(terminal) bond lengths of 1.603 Å and 1.649 Å are consistent (**Figure 3.4f**). The O(node)–Se–O(node) bond angle is significantly contracted to 92.39° possibly as a result of the aforementioned Se–O(node) bond elongation. The bond angles between terminal and node-based oxygen atoms differ only slightly from the ideal tetrahedral bond angle.

The majority of the bound selenite was found in the  $\mu_2$  motif (69%) in comparison to the  $\eta_2\mu_2$  motif (31%). Similarly, selenate primarily binds via the  $\mu_2$  motif (75%) suggesting that coordinating to a single Hf atom is more stable as compared to coordinating to two Hf atoms in the  $\eta_2\mu_2$  motif (25%). We suspect this favorability stems from the distribution of terminal hydroxyl and water groups on the node and charge balancing requirements; however, the proton topology of MOF-808 requires further investigation.<sup>125</sup>

### 3.7 Post-Adsorption Characterization

To confirm the retention of crystallinity and porosity, selenite- and selenate-loaded MOF-808 samples were fully characterized. As monitored by ICP-OES, no zirconium leaching was observed during the sorption process. Powder X-ray diffraction (PXRD) patterns verify that bulk purity and crystallinity of MOF-808 are preserved during the sorption of selenite and selenate (**Figure 3.7**). Nitrogen adsorption/desorption isotherms for native MOF-808 and MOF-808 loaded with selenite or selenate are nearly identical in shape and yield Brunauer–Emmett–Teller (BET) surface areas of 1930 m<sup>2</sup> g<sup>-1</sup> (1840 m<sup>2</sup> cm<sup>-3</sup>), 1680 m<sup>2</sup> g<sup>-1</sup> (1880 m<sup>2</sup> cm<sup>-3</sup>), and 1790 m<sup>2</sup> g<sup>-1</sup> (2010 m<sup>2</sup> cm<sup>-3</sup>), respectively (**Figure 3.8**). The observed decrease in gravimetric surface area is consistent with the increase of the framework mass when chemical moieties are captured or installed at the MOF

node.<sup>19, 74, 126</sup> Additionally, the associated pore size distributions further support the capture of  $\text{SeO}_3^{2-}$  and  $\text{SeO}_4^{2-}$  at the MOF node (**Figure 3.9**). Finally, scanning electron microscopy (SEM) images and the associated energy dispersive X-ray spectroscopy (EDS) spectra verify the uniform distribution of Se throughout MOF-808 crystals exposed to aqueous selenite and selenate solutions (**Figure 3.10**).

### 3.8 Chapter Conclusions

In summary, the suitability of MOF-808 as a sorbent for selenite and selenate was thoroughly investigated. Post-adsorption characterization of MOF-808 loaded with selenite and selenate confirms the framework retains its crystallinity and porosity throughout the uptake process. Notably, MOF-808 was found to have exceptional gravimetric and volumetric Se oxyanion uptake capacities of  $133 \text{ mg g}^{-1}$  ( $127 \text{ mg cm}^{-3}$ ) and  $118 \text{ mg g}^{-1}$  ( $112 \text{ mg cm}^{-3}$ ) for  $\text{SeO}_3^{2-}$  and  $\text{SeO}_4^{2-}$ , respectively. Additionally, diffusion is facilitated by the framework pores and results in rapid saturation in  $<5$  min. Furthermore, single-crystal X-ray diffraction studies reveal that selenite and selenate both coordinate at the MOF node via two distinct binding motifs. In the  $\eta_2\mu_2$  motif, the ion binds through two oxygen atoms to two Hf atoms in the node; whereas, in the  $\mu_2$  motif, the Se oxyanion oxygen atoms are bound to a single Hf atom in the node. We are hopeful that the exceptional volumetric Se uptake capacity and the illuminating crystallographic investigation reported here will prompt researchers to thoroughly examine the potential of MOFs in the water decontamination effort.

### 3.9 Additional Information

#### 3.9.1 Materials

All chemicals were used as received from the supplier. In these experiments, water is Milli-Q (Milli-pore). All gases were Ultra High Purity Grade 5 gases from Airgas Specialty Gases. Fisher

Chemical Trace Metal Grade nitric acid was used for all ICP-OES experiments. All ICP standards were purchased from Sigma-Aldrich. As-purchased Se and Na ICP standards were 1000 mg/g in 2% nitric acid, TraceCERT, and the Zr ICP standard was 1000 mg/g in 2% nitric acid and 0.2% hydrofluoric acid.

### *3.9.2 Physical Methods and Instrumentation*

MOF-808 was prepared solvothermally. In a typical procedure, zirconyl chloride octahydrate (282 mg, 0.875 mmol) and trimesic acid (216 mg, 1.029 mmol) were dissolved in a solution of DMF (40 mL) and formic acid (40 mL) and allowed to react for 48 h in an oven preheated to 120 °C. The MOF crystals were then washed 3 times with DMF (40 mL) and 3 times with acetone (40 mL). The MOF was soaked overnight in acetone and then dried in an 80 °C vacuum oven for 2 h. At this point the MOF was soaked in dilute hydrochloric acid (0.1 M, 40 mL) overnight. The MOF was washed 3 times with water (40 mL) and 3 times with acetone (40 mL). Again, the MOF was soaked in acetone (40 mL) overnight before drying in the vacuum oven for 2 h. All native MOF samples were thermally activated under ultra-high vacuum at 120 °C for 18 h on a Micromeritics Smart VacPrep. Selenium loaded samples were activated using the same technique, but at 80 °C. Nitrogen adsorption and desorption isotherm measurements were performed on a Micromeritics Tristar II at 77K. Powder X-ray diffraction measurements were collected on a STOE STADI MP equipped with  $K\alpha_1$  source and a 1D strip detector over a range of  $2^\circ < 2\theta < 45^\circ$ . ICP-OES data were obtained using a Thermo iCAP 7600 ICP Spectrometer. ICP-OES standards (0.5 - 20 ppm) were prepared via serial dilution in 2% nitric acid. All uptake experiments were performed in triplicate at a minimum.

Single-crystal X-ray diffraction measurements were performed on a Bruker Kappa APEX II CCD equipped with a Cu  $K\alpha$  ( $\lambda = 1.54178 \text{ \AA}$ ) microsource with MX optics. Single crystals of

MOF-808(Hf) were immersed in an aqueous sodium selenite or sodium selenate solution (0.1 M) at room temperature for 24 h. A single crystal was mounted on MicroMesh (MiTeGen) with paratone oil. The structure was solved by direct methods (SHELXT-2014/5)<sup>127</sup> and refined by full-matrix least-squares refinement on  $F^2$  (SHELXL-2014/7)<sup>91</sup> using the Yadokari-XG software package.<sup>128</sup> The disordered non-coordinated solvents were removed using the PLATON SQUEEZE program.<sup>93</sup> The selenium site occupancies were determined by structural refinement, and the total selenium content agrees well with data obtained from ICP-OES analysis of digested selenite- and selenate-loaded MOF samples. Refinement results are summarized in **Table 3.1** and **Table 3.2**. The associated CIF data file has been deposited in the Cambridge Crystallographic Data Centre (CCDC) under deposition numbers CCDC-1843055 and CCDC-1843056. The data can be obtained free of charge via [www.ccdc.cam.ac.uk/data\\_request/cif](http://www.ccdc.cam.ac.uk/data_request/cif) (or from the Cambridge Crystallographic Data Centre, 12 Union Road, Cambridge CB2 1EZ, U.K.).

Initial selenite and selenate uptake experiments were performed by exposing 5 mg ( $3.8 \times 10^{-6}$  mol) of MOF-808 to 10 mL of an aqueous sodium selenite or sodium selenate solution in a 15 mL polypropylene centrifuge tube. Selenite and selenate solutions with Se concentrations of 61, 91, 121, 151, 182, and 212 ppm corresponding to 2–7 ions per MOF node ( $Zr_6$ -cluster) were used. Solutions were centrifuged for 3 min to allow the MOF to settle. A 0.5 mL aliquot of the supernatant was removed after 1 h, 3 h, and 24 h of exposure, and diluted to 7 mL in 2% nitric acid. The concentration of Se, Zr, and Na in each sample was determined by ICP-OES. These concentrations were compared to the concentrations of an identical analyte solution without MOF to determine the amount of selenium captured per node.

The maximum amount of selenite and selenate adsorbed per gram of MOF-808 was determined by exposing 5 mg ( $3.8 \times 10^{-6}$  mol) of MOF to 10 mL of an aqueous sodium selenite or sodium selenate solution in a 15 mL polypropylene centrifuge tube. Solutions with selenium concentrations of 15, 30, 45, 61, and 76 ppm corresponding to 0.5, 1.0, 1.5, 2.0, and 2.5 selenite or selenate ions per MOF node were used. Each sample was centrifuged for 3 min to allow the MOF to settle. A 0.5 mL aliquot of the supernatant was removed at 5, 10, 15, 30, 60, 90, 120, and 180 min and diluted to 7 mL in 2% nitric acid. The concentration of Se, Zr, and Na in each solution was determined by ICP-OES. These were compared to the concentrations of identical analyte solutions without MOF to determine the amount of selenium adsorbed  $q$  in mg of selenium per g of MOF-808 using **Eqn. 1.1**,  $q = (C_i - C_f) \times V/m$ , where  $C_i$  = initial concentration (mg/L),  $C_f$  = final concentration (mg/L),  $V$  = volume of solution exposed to MOF-808 (L), and  $m$  = mass of MOF-808 (g). The volumetric uptake capacity of MOF-808 for selenium in the form of selenite and selenate was easily calculated by considering the framework density.

### 3.9.3 Single-Crystal X-Ray Diffraction Data

**Table 3.1** Crystallographic data for Hf-MOF-808- SeO<sub>3</sub>.

<b>Formula</b>	C18 H6 Hf6 O33.08 Se1.56
<b>Formula Weight</b>	1945.95
<b>Temperature (K)</b>	100(2)
<b>Wavelength (Å)</b>	1.54178
<b>Crystal system</b>	Cubic
<b>Space group</b>	$Fd\bar{3}m$ (no.227)
<b><math>a</math> (Å)</b>	35.286(9)
<b><math>b</math> (Å)</b>	35.286(9)
<b><math>c</math> (Å)</b>	35.286(9)
<b><math>V</math> (Å<sup>3</sup>)</b>	43936(34)
<b>Z</b>	16

<b>Calcd Density (g/cm<sup>3</sup>)</b>	1.177
<b><math>\mu</math> (mm<sup>-1</sup>)</b>	11.073
<b><math>F(000)</math></b>	13821
<b>Crystal size (mm<sup>3</sup>)</b>	0.025 × 0.025 × 0.025
<b><math>\theta_{min}, \theta_{max}</math> (°)</b>	6.52, 58.49
<b>Total reflection</b>	10188
<b>Unique reflection</b>	1502
<b>Parameter number</b>	68
<b><math>R_{int}</math></b>	0.2229
<b>Goodness-of-fit</b>	0.944
<b><math>R_1 [I &gt; 2\sigma(I)]</math></b>	0.0636
<b><math>wR_2</math> (all reflection)</b>	0.1722

---

**Table 3.2** Crystallographic data for Hf-MOF-808- $\text{SeO}_4$ .

Formula	C18 H6 Hf6 O34.16 Se1.44
<b>Formula Weight</b>	1953.43
<b>Temperature (K)</b>	100(2)
<b>Wavelength (Å)</b>	1.54178
<b>Crystal system</b>	Cubic
<b>Space group</b>	$Fd\bar{3}m$ (no.227)
$a$ (Å)	35.087(1)
$b$ (Å)	35.087(1)
$c$ (Å)	35.087(1)
$V$ (Å <sup>3</sup> )	43196(4)
<b>Z</b>	16
<b>Calcd Density (g/cm<sup>3</sup>)</b>	1.201
$\mu$ (mm <sup>-1</sup> )	11.228
$F(000)$	13892
<b>Crystal size (mm<sup>3</sup>)</b>	0.03 × 0.03 × 0.03
$\theta_{min}, \theta_{max}$ (°)	2.18, 58.81
<b>Total reflection</b>	11057
<b>Unique reflection</b>	1515
<b>Parameter number</b>	68
$R_{int}$	0.0473
<b>Goodness-of-fit</b>	1.125
$R_1 [I > 2\sigma(I)]$	0.0363
$wR_2$ (all reflection)	0.1134

### 3.9.4 Bulk Adsorption Measurements

**Table 3.3** Selenite adsorption per  $Zr_6$ -node of MOF-808 when exposed to aqueous sodium selenite solutions with concentrations of 2 to 7  $SeO_3^{2-}$  ions per node.

Exposure	Time		
	1 Hr	3 Hr	24 Hr
2	1.5	1.5	1.5
3	1.6	1.5	1.6
4	1.5	1.4	1.6
5	1.1	1.2	1.2
6	0.9	1.0	1.1
7	1.2	1.2	1.4

**Table 3.4** Selenate adsorption per  $Zr_6$ -node of MOF-808 when exposed to aqueous sodium selenate solutions with concentrations of 2 to 7  $SeO_4^{2-}$  ions per node.

Exposure	Time		
	1 Hr	3 Hr	24 Hr
2	1.1	1.1	1.1
3	1.2	1.2	1.2
4	1.2	1.2	1.2
5	1.1	1.0	1.1
6	1.4	1.3	1.4
7	1.4	1.4	1.3

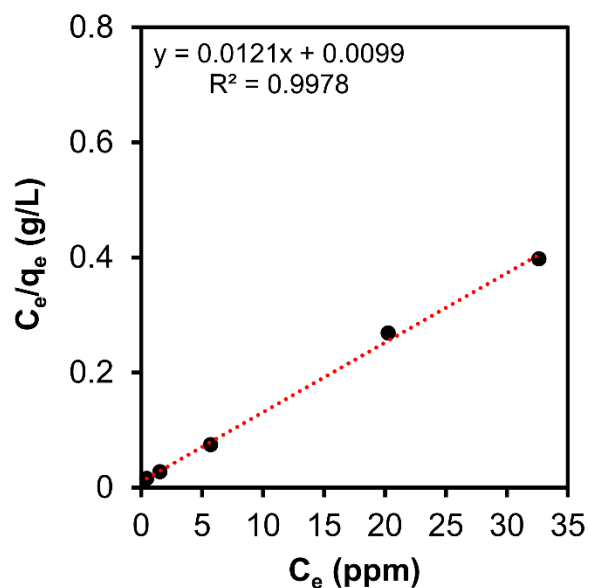


**Figure 3.5** The Type I, linear Langmuir plot of  $C_e/q_e$  versus  $C_e$  for selenite capture in MOF-808 at various equilibrium concentrations according to **Eqn. 1.2** reproduced below, in **Table 3.5**, for convenience.

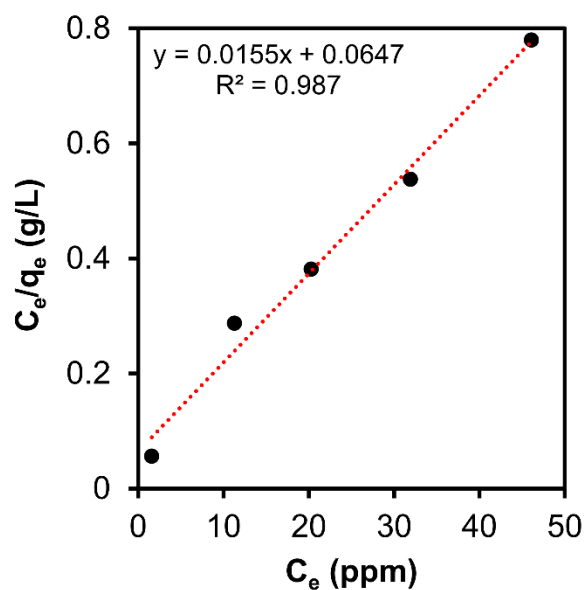


**Figure 3.6** The Type I, linear Langmuir plot of  $C_e/q_e$  versus  $C_e$  for selenate capture in MOF-808 at various equilibrium concentrations according to **Eqn. 1.2** reproduced below, in **Table 3.5**, for convenience.

**Table 3.5** The selenite and selenate uptake isotherms (**Figure 3.2**) and the Langmuir equation (**Eqn. 1.2** as reproduced below):

$$\frac{C_e}{q_e} = \left(\frac{1}{Q}\right) C_e + \frac{1}{K_L Q} \quad (1.2)$$

where  $C_e$  is the equilibrium concentration (mg/L),  $q_e$  is the equilibrium uptake (mg/g),  $Q$  is maximum uptake capacity (mg/g), and  $K_L$  is the Langmuir constant (L/mg) were employed to determine the maximum selenium uptake capacity of MOF-808 in the form of selenite or selenate as summarized below.

	mg/g	mg/cm <sup>3</sup>
<b>SeO<sub>3</sub><sup>2-</sup></b>	133	127
<b>SeO<sub>4</sub><sup>2-</sup></b>	118	112

**Table 3.6** Comparison of the gravimetric and volumetric selenite uptake capacity of MOF-808 and NU-1000. The shaded box indicates the greater capacity.

	mg/g	mg/cm <sup>3</sup>
<b>MOF-808</b>	133	127
<b>NU-1000</b>	95	45

**Table 3.7** Comparison of the gravimetric and volumetric selenate uptake capacity of MOF-808 and NU-1000. The shaded box indicates the greater capacity.

	mg/g	mg/cm <sup>3</sup>
<b>MOF-808</b>	118	112
<b>NU-1000</b>	85	40

**Table 3.8** Comparison of gravimetric uptake capacities for selenite and selenate in various materials.

<b>Material</b>	<b>Selenite Gravimetric Uptake Capacity (mg/g)</b>	<b>Selenate Gravimetric Uptake Capacity (mg/g)</b>	<b>Ref.</b>
Al <sub>2</sub> O <sub>3</sub> Impregnated Chitosan Beads	11	20	106
Fe(III) on Silica	20	2	115
Al(III) on Silica	33	11	115
NU-1000	62	102	74
MOF-808	133	118	This Work
Y <sub>2</sub> (OH) <sub>5</sub> Cl•1.5H <sub>2</sub> O	150	102	116
MgAl-MoS <sub>4</sub> -LDH	294	85	117
Thiourea-formaldehyde (TUF) Resin	833	526	118
MgAl <sub>2</sub> O <sub>4</sub> (cLDH)	180	N/A	119
Cu <sup>2+</sup> /diaminofunctionalized-MCM-41	N/A	83	120
UiO-66-HCl	N/A	86.8	121
Fe <sup>2+</sup> /diaminofunctionalized-MCM-41	N/A	117	120
H <sup>+</sup> /diaminofunctionalized-MCM-41	N/A	123	120

### 3.9.5 Post-Adsorption Characterization

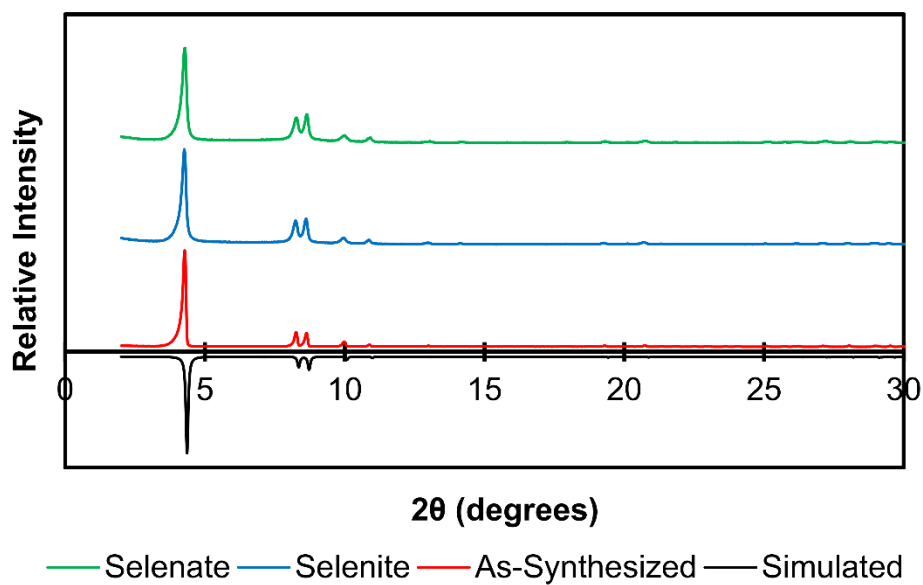


**Figure 3.7** Powder X-ray diffraction (PXRD) patterns of neat MOF-808 and MOF-808 loaded with 1.8  $\text{SeO}_3^{2-}$  ions per node or 1.6  $\text{SeO}_4^{2-}$  ions per node confirm the retention of bulk crystallinity and purity.

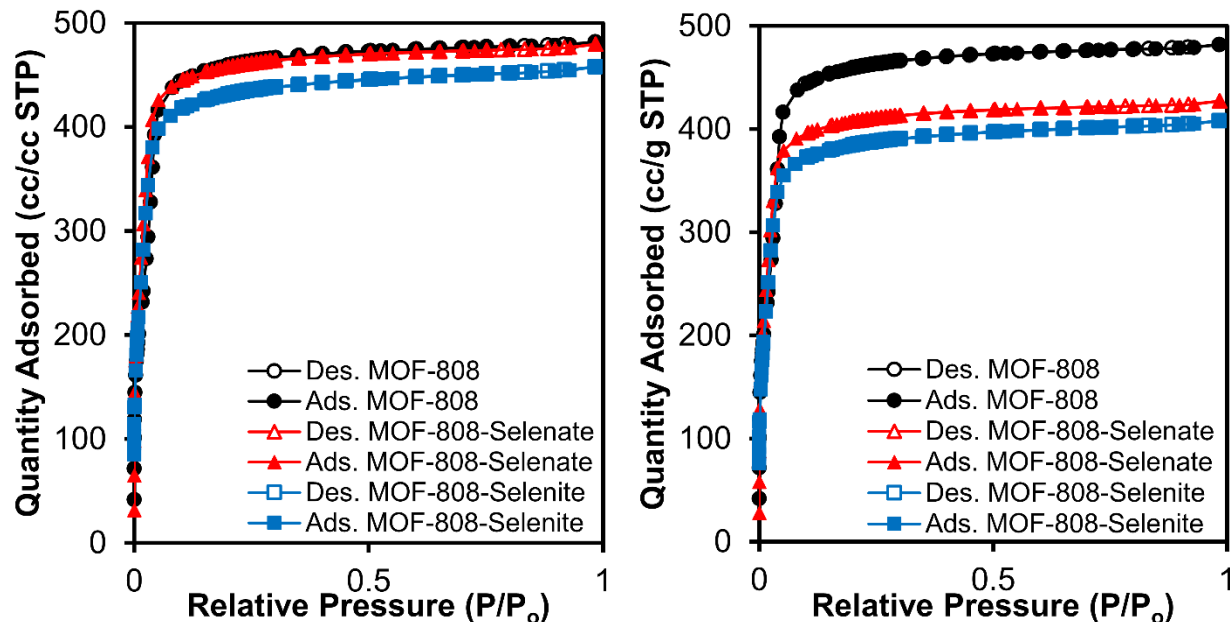


**Figure 3.8** a) Volumetric  $N_2$  adsorption/desorption isotherms of neat MOF-808 and MOF-808 loaded with 1.8  $SeO_3^{2-}$  ions per node or 1.6  $SeO_4^{2-}$  ions per node confirm the retention of porosity throughout the adsorption process. b) The associated gravimetric  $N_2$  adsorption/desorption isotherms show a surface area reduction consistent with the installation of functionality at the MOF node.

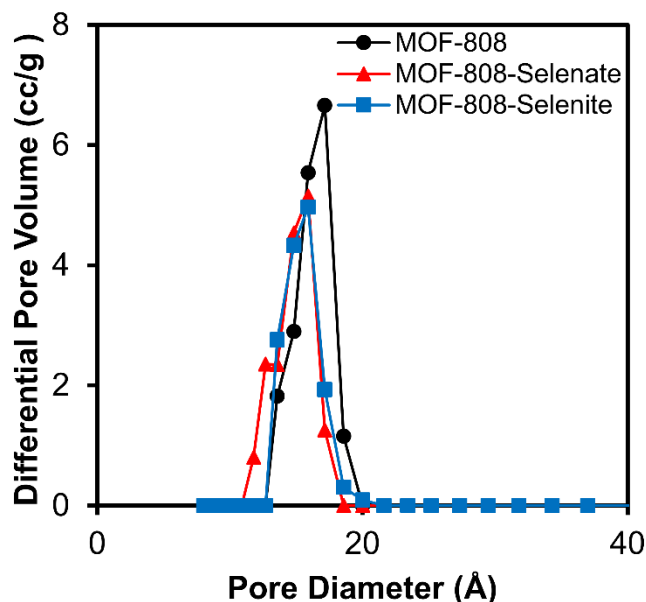


**Figure 3.9** DFT pore size distributions for neat MOF-808 and MOF-808 loaded with 1.8  $SeO_3^{2-}$  ions per node or 1.6  $SeO_4^{2-}$  ions per node reveal a decrease in the pore volume which supports the capture of selenite and selenate within the framework.

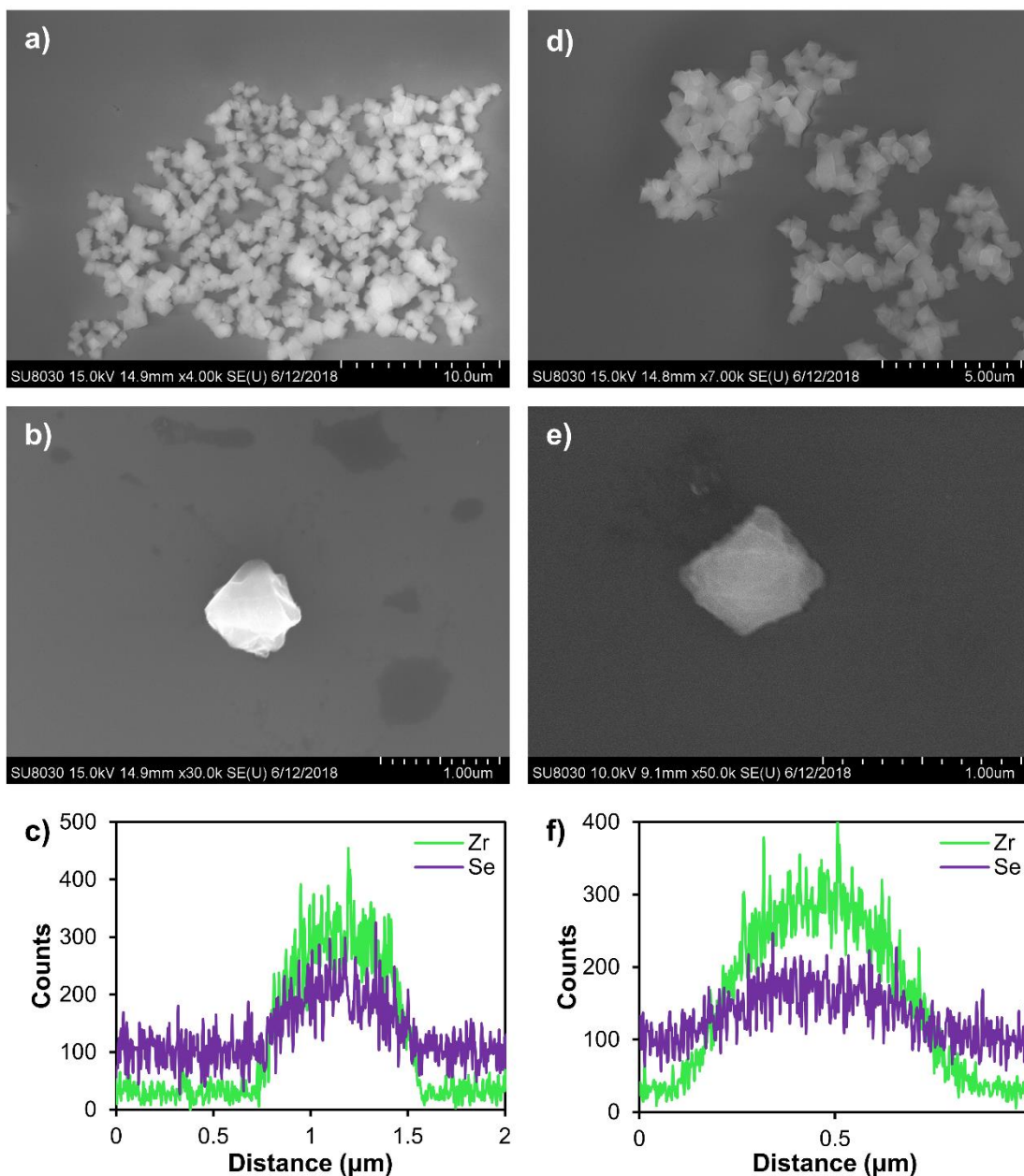


**Figure 3.10** SEM images of a) the bulk sample and b) an individual crystal of MOF-808 loaded with 1.8  $\text{SeO}_3^{2-}$  ions per node, and c) the EDS linescan of the crystal in b. SEM images of d) the bulk sample and e) an individual crystal of MOF-808 loaded with 1.6  $\text{SeO}_4^{2-}$  ions per node, and f) the EDS linescan of the crystal in e. Both EDS linescans confirm the uniform distribution of selenium throughout the MOF-808 crystals.

## Chapter 4. Capitalizing on $\pi$ - $\pi$ Interactions to Design an Efficient Sorbent for Atrazine Removal from Water

Portions of this chapter appear in the following manuscript:

Akpinar, I.;\* **Drout, R.J.**;\* Islamoglu, T.; Kato, S.; Lyu, J.; Farha, O.K., Exploiting  $\pi$ - $\pi$  Interactions to Design an Efficient Sorbent for Atrazine Removal from Water. *ACS Appl. Mater. Interfaces*. **2019**, *11* (6), 6097-6103.

## 4.1 Chapter Summary

The United States Environmental Protection Agency (EPA) recognizes atrazine, a commonly used herbicide, as an endocrine disrupting compound. Excessive use of this agrochemical results in contamination of surface and ground water supplies via agricultural runoff. Efficient removal of atrazine from contaminated water supplies is paramount. Here, the mechanism governing atrazine adsorption in  $Zr_6$ -based MOFs has been thoroughly investigated by studying the effects of MOF linker and topology on atrazine uptake capacity and uptake kinetics. We found that the mesopores of NU-1000 facilitated rapid atrazine uptake saturating in  $< 5$  min and that the pyrene-based linkers offered sufficient sites for  $\pi$ - $\pi$  interactions with atrazine as demonstrated by the near 100% uptake. Without the presence of a pyrene-based linker, NU-1008, a MOF similar to NU-1000 with respect to surface area and pore size, removed  $< 20\%$  of the exposed atrazine. These results suggest that the atrazine uptake capacity demonstrated by NU-1000 stems from the presence of a pyrene core in the MOF linker, affirming that  $\pi$ - $\pi$  stacking is responsible for driving atrazine adsorption. Furthermore, NU-1000 displays an exceptional atrazine removal capacity through 3 cycles of adsorption-desorption. Powder X-ray diffraction (PXRD) and Brunauer–Emmett–Teller (BET) surface area analysis confirmed the retention of MOF crystallinity and porosity throughout the adsorption-desorption cycles.

## 4.2 Pollution of Fresh Water Sources with Atrazine

Atrazine, recognized by U.S. Environmental Protection Agency (EPA) as an endocrine disrupting compound and a possible human carcinogen,<sup>129, 130</sup> is the second most used herbicide in the United States. Annually, the agricultural industry uses approximately 80 million pounds of atrazine to treat farmland across the nation.<sup>131</sup> Due to its widespread use, persistency, and

environmental mobility, atrazine ultimately contaminates surface and ground water supplies. To safeguard aquatic life and human health, the EPA has imposed a maximum contaminant level (MCL) for atrazine in drinking water of 0.003 ppm (3 ppb).<sup>132</sup> Therefore, development of an effective method for removing atrazine from water sources is of utmost importance.

A number of atrazine removal strategies have been reported. Many methods such as coagulation, chlorination, clarification, and filtration are highly inefficient atrazine removal processes.<sup>133-135</sup> Other methods including ozonation,<sup>134</sup> advanced electrochemical,<sup>136</sup> and UV-based<sup>130</sup> oxidation processes display moderate atrazine removal capacity; however, formation of more toxic oxidation by-products and high operational energy costs limit the widespread implementation of these techniques. Alternatively, adsorption is an effective, relatively less expensive, and harmless method, that demonstrates promise in resolving atrazine contamination.<sup>137, 138</sup> Specifically, activated carbon,<sup>139</sup> zeolites,<sup>140</sup> resins,<sup>141</sup> clay materials,<sup>142</sup> and biochar<sup>143</sup> have been examined as sorbents for atrazine removal. Unfortunately, though widely used, activated carbon is a moderately expensive strategy for water treatment because the low volumetric capacities necessitate the use of excessive amounts of sorbent.<sup>144, 145</sup> Regeneration of porous carbons also remains challenging.<sup>146</sup> Further, carbon-based materials, including carbon nanotubes and porous carbons, often require long exposure times to reach saturation capacity.<sup>147, 148</sup> Therefore, a recyclable, high capacity material to remove organic contaminants from water must be designed to ensure cost efficiency. We anticipate that the hierarchical porous structure and dense chemical functionality characteristic of metal–organic frameworks (MOFs) will afford both rapid uptake kinetics and high uptake capacity, respectively.

The properties displayed by MOFs, namely porosity and crystallinity, make them potential candidates for atrazine sorption. MOFs are comprised of inorganic nodes and organic linkers that assemble into multidimensional periodic lattices through coordination bonds.<sup>149, 150</sup> Through judicious choice of node and linker and/or *via* a host of post-synthetic modification techniques, these crystalline materials can be chemically and structurally tuned to yield various pore sizes and shapes, surface areas, and chemical functionality.<sup>151-153</sup> Because of their tailorable properties, MOFs have been utilized for numerous applications including, but not limited to, gas storage and separation,<sup>13, 154-157</sup> catalysis,<sup>158-163</sup> drug delivery,<sup>164, 165</sup> chemical separation,<sup>166, 167</sup> detoxification of chemical warfare agents,<sup>15, 168</sup> and water remediation.<sup>74, 75, 169</sup>

Importantly, Zr<sub>6</sub>-based MOFs demonstrate exceptional water stability owing to their strong Zr(IV)–O bonds.<sup>151, 170</sup> Therefore, such materials have been investigated for the capture of arsenic, rhenium, and selenium oxyanions.<sup>19, 73, 74</sup> Given MOF crystallinity, single-crystal X-ray diffraction can be utilized to elucidate the binding motif; for example, perrhenate binds at the Zr<sub>6</sub>-node of NU-1000 through displacement of the terminal water (–OH<sub>2</sub>) and hydroxyl (–OH) groups. Further, MOF linkers can also serve as potential adsorption sites. For example, sorption of aldehyde- over carboxylic acid-functionalized phenolics in NU-1000 has been attributed to  $\pi$ - $\pi$  interactions between the analyte and the pyrene-based linker.<sup>171</sup> Herein, we capitalize on the precise synthetic designability of MOFs to systematically tune MOF structure and chemical functionality to investigate the mechanism driving atrazine adsorption from water.

To this end, we chose to investigate atrazine sorption in Zr<sub>6</sub>-based MOFs with a variety of pore sizes and linker functionalities. We hypothesized that  $\pi$ - $\pi$  interactions govern atrazine sorption and therefore investigated a series of MOFs comprised of linkers with increasingly large conjugated

$\pi$ -systems (**Figure 4.1**). Considering the assortment of linkers, NU-1000 and NU-901, both of which contain the pyrene-based linker, H<sub>4</sub>TBAPy, were expected to display the highest atrazine uptakes. While consisting of the same node and linker, the larger pores of NU-1000 compared to NU-901 were predicted to facilitate diffusion and afford faster atrazine uptake. Though similar to NU-1000 with respect to surface area and pore size, NU-1008 does not contain a pyrene-based linker and is expected to exhibit a lower atrazine affinity. Following a preliminary screening, NU-1000 was fully analyzed to determine its maximum atrazine uptake capacity, selectivity in the presence of salt, recyclability, and stability to the adsorption-desorption process.

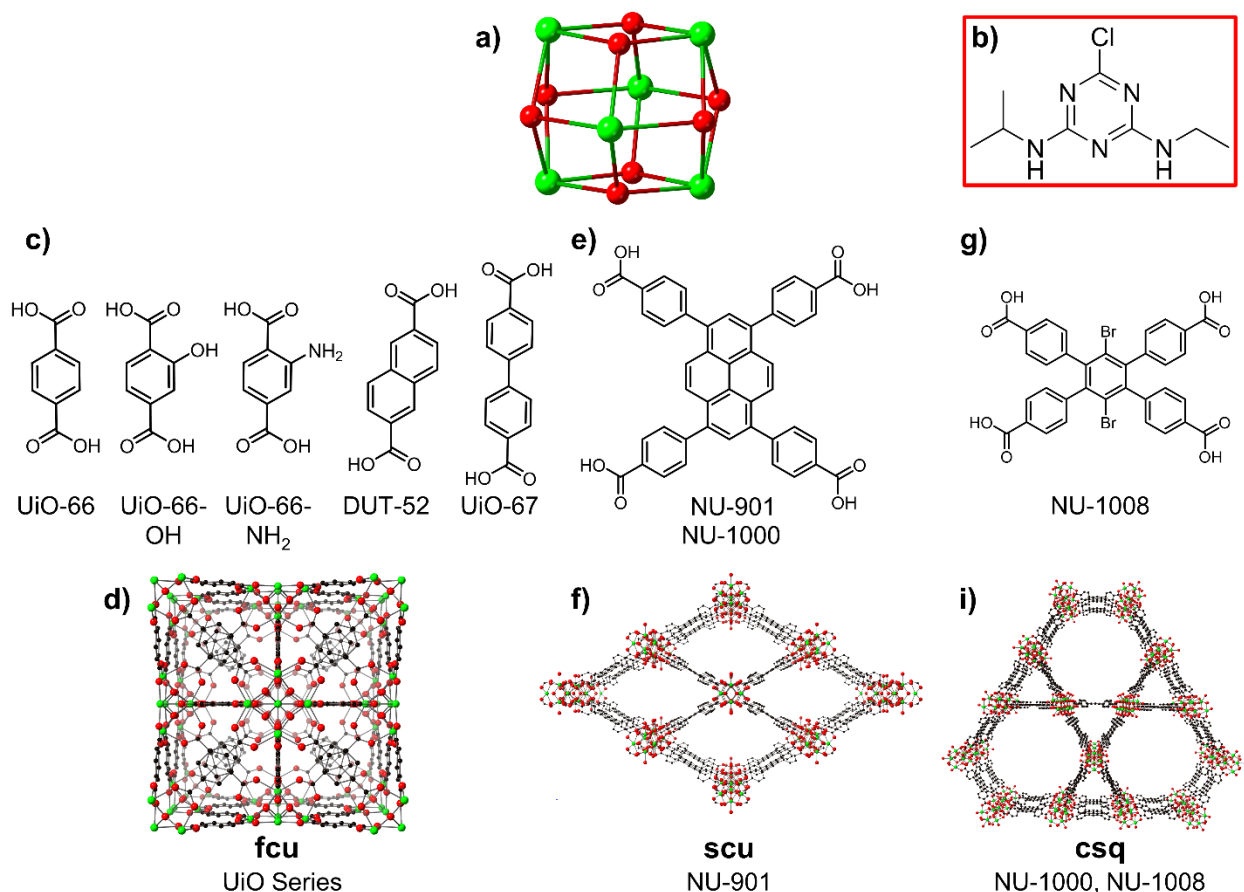


**Figure 4.1** The structures of a) the Zr<sub>6</sub>-node, b) atrazine, c) linkers for UiO-66, UiO-66-OH, UiO-66-NH<sub>2</sub>, DUT-52, and UiO-67, d) UiO series topology, e) linker for NU-1000 and NU-901 and f) NU-901 topology, g) linker for NU-1008, and h) NU-1000 and NU-1008 topology.

### 4.3 Screening of Atrazine Affinity

Preliminary studies were performed to investigate the atrazine affinity of several  $Zr_6$ -based MOFs (Table 4.1, Figure 4.1, Figure 4.2, Figure 4.6, Figure 4.7, Figure 4.8, Figure 4.9). UiO-66, and its derivatives, UiO-67, and DUT-52 are composed of 12-connected  $Zr_6$ -nodes and dicarboxylate organic linkers (Figure 4.1). The linkers in UiO-66, UiO-66-OH, and UiO-66-NH<sub>2</sub> are 1,4-benzenedicarboxylate (BDC), 2-hydroxy-1,4 benzenedicarboxylate (BDC-OH), and 2-amino-1,4 benzenedicarboxylate (BDC-NH<sub>2</sub>), respectively. These derivatives of UiO-66 were synthesized to evaluate the effect of linker functional groups on atrazine uptake. Additionally, UiO-67 and DUT-52, which feature the extended linkers biphenyl-4,4'-dicarboxylate (BPDC) and 2,6 naphthalenedicarboxylate (NDC), respectively, were chosen because their linkers contain larger  $\pi$ -systems compared to the UiO-66 series which may contribute to greater atrazine uptake. To further investigate the role of  $\pi$ - $\pi$  interactions in the adsorption process, NU-1000 and NU-901 which consist of  $Zr_6$ -nodes and the pyrene-based linker, 1,3,6,8-tetrakis(p-benzoic acid)pyrene (H<sub>4</sub>TBAPy), were examined (Figure 4.1). The framework of NU-1000 is characterized by 12 Å triangular and 31 Å hexagonal 1D channels connected by small windows ( $\sim 8$  Å);<sup>172</sup> whereas NU-901 displays diamond-shaped 1D channels with an aperture of 12 Å.

In a traditional screening experiment, an activated MOF sample was exposed to an aqueous atrazine solution. UiO-66 and UiO-66-NH<sub>2</sub> were found to adsorb a mere 2% of the total atrazine in solution, and UiO-66-OH adsorbed only 3% (Figure 4.2). Such low uptake amounts suggest that atrazine is unable to diffuse into the small pores of UiO-66 and its derivatives and could only adsorb to the particle surface. Additionally, the hydrogen bonding potential of the functional groups did not increase the atrazine adsorption capacity likely because atrazine cannot displace the

water molecules hydrogen bonding to the functional groups on the linkers (i.e.  $-\text{NH}_2$ ,  $-\text{OH}$ ) while the MOFs are submersed in water. The extended linker of UiO-67 increases the pore size facilitating diffusion and offers more atrazine adsorption sites as demonstrated by a moderate atrazine removal efficiency of 40%. While the pores of DUT-52 are slightly smaller than those of UiO-67, the MOF displays a higher atrazine removal capacity (54%) presumably due to the increased  $\pi$ - $\pi$  interaction potential of the naphthalene linker.

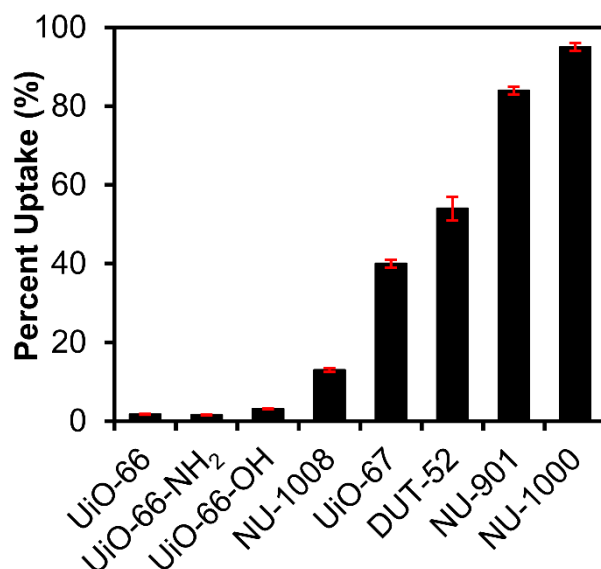


**Figure 4.2** Atrazine adsorption uptake as a percentage of the total amount of atrazine exposed to MOF samples (3.5 mg of MOF exposed to 10 mL of 10 ppm atrazine solution under ambient conditions for 24h).

Upon incorporation of a pyrene-based linker, the atrazine removal capacity dramatically increased. NU-901, while it has smaller pores than both UiO-67 and DUT-52, removed 84% of the atrazine in the solution to which it was exposed. This high atrazine removal efficiency can be attributed to the pyrene core of the H<sub>4</sub>TBAPy linker which enhances the removal capacity through the increased availability of  $\pi$ - $\pi$  interactions. Of all MOFs investigated, NU-1000 demonstrated the most efficient atrazine adsorption behavior removing 95% of the atrazine in solution. In

comparison to the pores of NU-901, the hexagonal pores of NU-1000 are larger further enhancing diffusion and increasing the atrazine capacity per pore. To confirm pore size was not the primary factor contributing to the enhanced atrazine uptake in NU-901 and NU-1000 compared to the UiO MOFs, NU-1008 was examined. NU-1008 has similar pore size and surface area to NU-1000; however, its linker does not contain a pyrene moiety. The low atrazine removal capacity of NU-1008 (13%) reinforces that  $\pi$ - $\pi$  interactions between atrazine and the pyrene-based linker present in NU-1000 and NU-901 are the primary interactions driving atrazine adsorption.

**Table 4.1** The surface areas, pore sizes, and approximate pore apertures of  $Zr_6$ -based MOFs screened for atrazine adsorption. <sup>a</sup>Reported pore aperture sizes of UiO series MOFs are measured for the node-to-node distance of the tetrahedral pore.<sup>173</sup>

MOF	Surface Area ( $m^2 g^{-1}$ )	Pore Size ( $\text{\AA}$ )	Pore Aperture ( $\text{\AA}$ ) <sup>a</sup>
UiO-66	1690	12 and 16	7.5
UiO-66-NH <sub>2</sub>	1410	13	7.5
UiO-66-OH	1210	11	7.5
UiO-67	2510	13 and 23	12
DUT-52	1960	12 and 20	9
NU-1008	1400	14 and 30	14 and 30
NU-901	2110	12	12
NU-1000	2210	12 and 30	12 and 30

#### 4.4 Kinetic Studies

Rapid uptake of the target contaminant is critical in evaluating the feasibility of water purification methods given that large amounts of liquid must be treated efficiently. To this end, the kinetics of atrazine adsorption in DUT-52, NU-1008, NU-901 and NU-1000 were investigated. Specifically, MOF samples were exposed to identical 10 ppm atrazine solutions and the concentration of atrazine in solution was analyzed at several time points (**Figure 4.3**). Within 1

min, NU-1000 captures 93% of the atrazine in the test solution equivalent to 98% of its saturation uptake. The rapid atrazine uptake kinetics are most likely attributed to the periodicity of the MOF lattice, the large pores of NU-1000 that facilitate diffusion, and the easily accessible and highly abundant pyrene-based linkers. NU-901 displays slightly slower kinetics than NU-1000, reaching 85% of its saturation uptake within 1 min to capture 75% of the exposed atrazine. While NU-901 displays rather efficient uptake, the slower saturation is believed to stem from the framework's smaller pores in comparison to NU-1000. Similarly, within 1 min, DUT-52 removes 44% of the exposed atrazine, and while this is a relatively low uptake amount, it is equivalent to 82% of the atrazine saturation capacity of DUT-52. Of the MOFs investigated, NU-1008 exhibits the slowest kinetics capturing only 69% after its saturation capacity within 1 min equivalent to a mere 9% of the exposed atrazine. If pore size was the main contributing factor, the kinetics of atrazine uptake in NU-1008 should exceed those of both DUT-52 and NU-901; however, this is not the case. Comparing NU-1000 and NU-901 suggests that pore size contributes slightly to rapid uptake saturation; however, the availability of  $\pi$ - $\pi$  interactions present in NU-1000, NU-901, and DUT-52 are primarily responsible for driving rapid atrazine uptake given the pore sizes vary dramatically between the three MOFs. These results suggest that pore size and the availability of  $\pi$ - $\pi$  interactions at adsorption sites concomitantly influence atrazine capture kinetics.

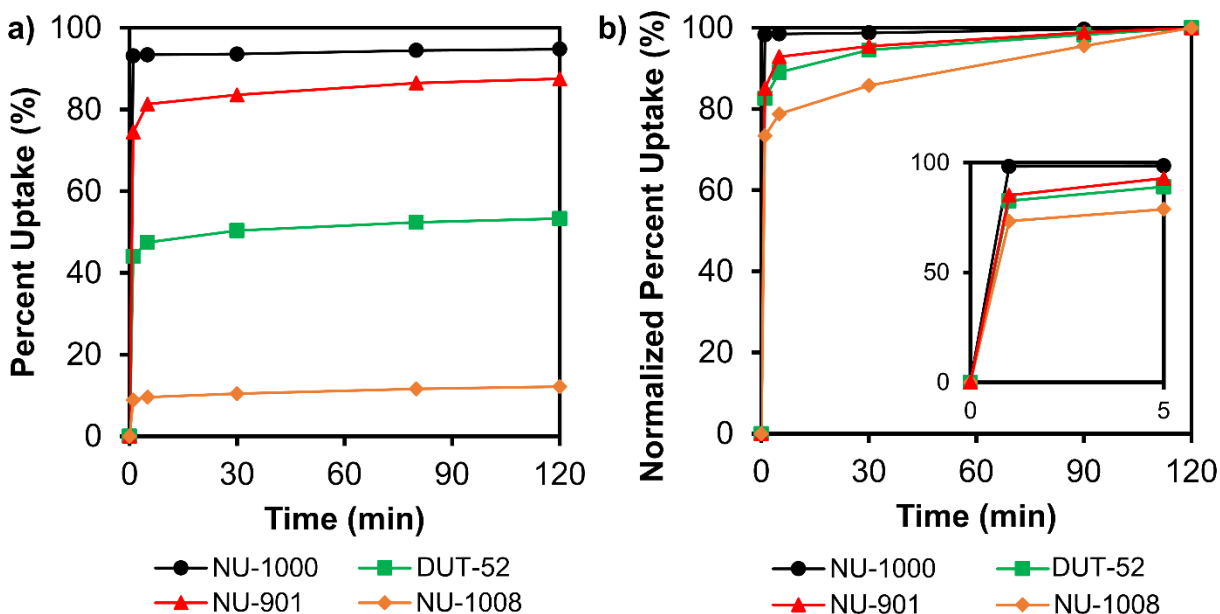


**Figure 4.3** a) Atrazine adsorption isotherms as percent (%) uptake of atrazine exposed versus time for various MOFs. b) Atrazine adsorption isotherms as normalized percent (%) of respective saturation uptake versus time for various MOFs. Insets show the uptake between 0 and 5 min.

#### 4.5 Adsorption Capacity of NU-1000

The exceptional and rapid atrazine adsorption demonstrated by NU-1000 prompted us to determine its maximum atrazine uptake capacity. To do so, MOF samples were exposed to aqueous solutions with various atrazine concentrations. Adsorption isotherms were constructed for each exposure concentration by determining the amount  $q$  of atrazine (mg) adsorbed by the MOF (g) at various time points using eq 1. The equilibrium atrazine concentration in solution was determined by HPLC-DAD and used to calculate the amount of atrazine adsorbed at equilibrium. A Type-I Langmuir fit () revealed a maximum atrazine uptake capacity of 36 mg of atrazine per gram of NU-1000 (Figure 4.10, Table 4.3, and Table 4.4).<sup>148,174-180</sup> The associated Langmuir constant ( $K_L$ ) value of 1.78 L mg<sup>-1</sup> low time to saturation for atrazine adsorption in NU-1000 indicates that NU-1000 displays a greater affinity for atrazine and more favorable sorption kinetics than most materials reported for atrazine adsorption (Table 4.2).

**Table 4.2** Comparison of Langmuir constant values reported for atrazine adsorption on various materials reveals that NU-1000 outperforms most reported materials with respect to uptake capacity and sorption kinetics.

Adsorbents	$K_L$ Langmuir Constant ( $L\ mg^{-1}$ )	Time to Saturation	Ref.
NU-1000	1.78	< 1 min	This work
Carbon nanotube – r-MWNT	1.47 (at 25°C)	6 h	175
Carbon nanotube - SMWNT20	0.96 (at 25°C)	6 h	175
Multiwalled carbon nanotubes	0.7710	7 h	148
Biochar - CS450	0.618 (at 25°C)	N/A	176
Polyacrylic acid-functionalized magnetic ordered mesoporous carbon (P-MMC)	0.2058	24 h	178
Biochar - ADPCS450	0.196 (at 25°C)	N/A	176
Treated banana peels	0.12 (at 25°C)	15 h	179
Ordered mesoporous carbon (OMC)	0.1130	24 h	178
Magnetic ordered mesoporous carbon (MMC)	0.1089	24 h	178
Sludge-based activated carbon-like material	0.05	10 h	180

#### 4.6 Effect of Ionic Strength on Adsorption

Equally important as rapid saturation and high uptake capacity is selectivity for the target contaminant even in the presence of competing interferents. Given their abundance in water sources, sodium chloride, sodium nitrate, sodium sulfate, and calcium chloride were used to investigate the selectivity of NU-1000 for atrazine in the presence of competing ions (**Figure 4.4**). As such, MOF samples were exposed to a 10 ppm aqueous atrazine solution or a 10 ppm aqueous atrazine solution in 0.1 M NaCl, NaNO<sub>3</sub>, Na<sub>2</sub>SO<sub>4</sub>, or CaCl<sub>2</sub>. NU-1000 was found to remove 94% of the atrazine from pure water and 93%, 92%, 97%, and 97% of the total exposed atrazine from the 0.1 M NaCl, 0.1 M NaNO<sub>3</sub>, 0.1 M Na<sub>2</sub>SO<sub>4</sub>, and 0.1 M CaCl<sub>2</sub> solutions, respectively. Therefore, the presence of competing salts does not significantly affect the atrazine affinity of NU-1000 suggesting NU-1000 may be a promising material for adsorptive atrazine removal.

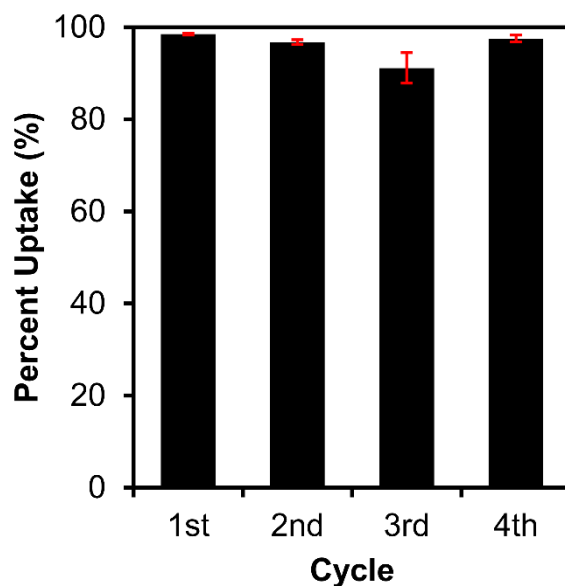


**Figure 4.4** NU-1000 maintains its atrazine affinity in the presence of competing salt ions.

#### **4.7 Regeneration and Stability of NU-1000**

A sorbent's cost efficiency can be significantly enhanced if the material can be regenerated after adsorption and reused for many additional adsorption-desorption cycles. Atrazine is highly soluble in acetone ( $31 \text{ g L}^{-1}$  at  $25 \text{ }^\circ\text{C}$ ); therefore, this solvent was chosen to study the recyclability of NU-1000.<sup>181</sup> In a typical experiment, a MOF sample was loaded with atrazine and then treated with acetone at room temperature. NMR spectra of regenerated MOF samples demonstrate the presence of no residual atrazine (**Figure 4.11** and **Figure 4.12**). Through three cycles of the adsorption-desorption process, NU-1000 efficiently removed atrazine without significant decrease in efficiency (**Figure 4.5a**). Moreover, through this process, the structural integrity and porosity of NU-1000 are retained as demonstrated by powder X-ray diffraction patterns (PXRD) (**Figure 4.5b**) and  $\text{N}_2$  adsorption-desorption isotherms (**Figure 4.13**), respectively.

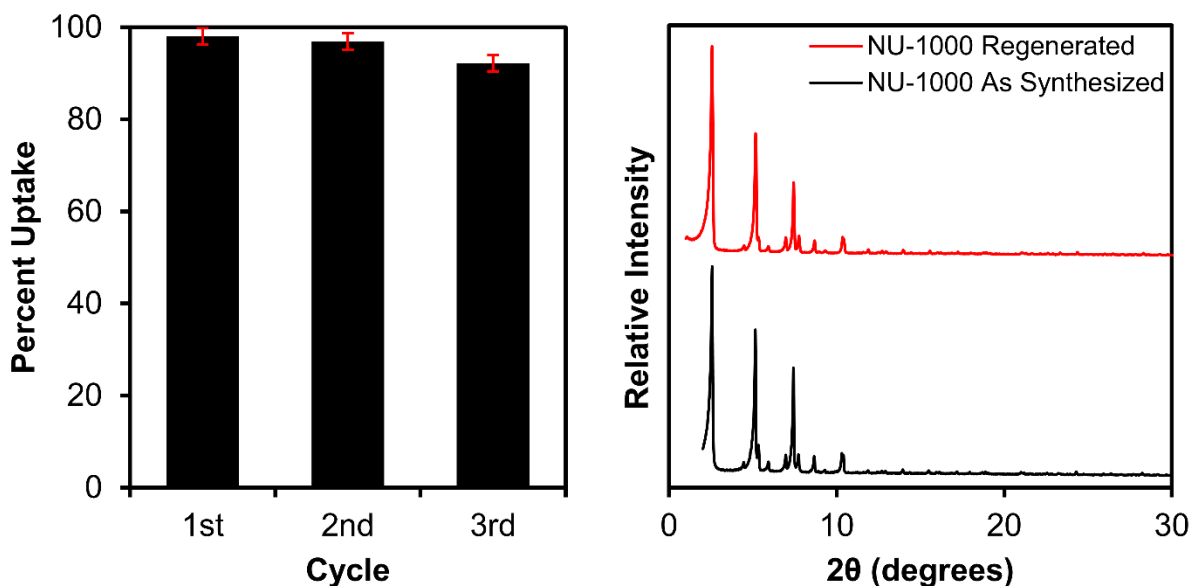


**Figure 4.5** Through three cycles of atrazine adsorption and regeneration with acetone, a) NU-1000 shows only a slight decrease in atrazine uptake and b) retains its bulk structural integrity as demonstrated by PXRD.

#### 4.8 Chapter Conclusions

In summary, we capitalized on the synthetic tunability of MOFs to systematically investigate the role of chemical functionality, specifically  $\pi$ -system size, in the adsorptive removal of atrazine from water. In preliminary screenings, the atrazine affinity of a selection of Zr-based MOFs with various linker  $\pi$ -system sizes and chemical functionality, framework topologies, and pore sizes was assessed. NU-1000, NU-901, and DUT-52 displayed the highest atrazine affinities suggesting that  $\pi$ - $\pi$  interactions are the primary contributor to atrazine adsorption. A thorough investigation of atrazine uptake kinetics in DUT-52, NU-901, NU-1008, and NU-1000 further corroborated that the presence of linkers with extended  $\pi$ -systems, rather than large pores results in the exceptional atrazine uptake demonstrated by NU-1000. Additionally, NU-1000 was found to reach its maximum capacity within 1 min likely due to the framework's large pores which facilitate diffusion and the abundance of potential  $\pi$ - $\pi$  interaction sites at the pyrene-based linkers. NU-1000

was fully evaluated for atrazine adsorption and found to have a maximum adsorption capacity of 36 mg of atrazine per g of NU-1000. Although this capacity is comparable to that of other sorbents that have been used for atrazine adsorption, 98% of its saturation atrazine uptake is attained within 1 min, again because of rapid diffusion through the hierarchically porous MOF structure. Moreover, in the presence of competing salt ions, NU-1000 maintains its atrazine affinity. Furthermore, after atrazine adsorption, NU-1000 can be easily regenerated by acetone washing while retaining at least 99% of its original atrazine uptake. Given that its large pores and pyrene-based linkers facilitate rapid and exceptionally high atrazine uptake, NU-1000 is a promising candidate for adsorptive atrazine removal.

## **4.9 Additional Information**

### *4.9.1 Materials*

All chemicals were purchased from commercial suppliers and used as received. Specifically, atrazine was purchased from Sigma-Aldrich. Water in all experiments is Milli-Q (milli-pore). In all HPLC-diode array detector (DAD) experiments, HPLC-grade acetone was used. All gases were Ultra High Purity grade 5 gases from Airgas Specialty Gases.

### *4.9.2 Physical Methods & Instrumentation*

UiO-66, UiO-66-OH, UiO-66-NH<sub>2</sub>, UiO-67, DUT-52, NU-901, NU-1008 and NU-1000 were prepared according to reported protocols.<sup>182-184</sup> Detailed syntheses are provided in the Supporting Information for convenience.

Synthesis of UiO-66: 125 mg of ZrCl<sub>4</sub> (0.54 mmol), 123 mg of 1,4 benzene dicarboxylic acid (0.75 mmol), and 15 ml of DMF were placed in an 8-dram vial and sonicated until the solution was clear. Afterwards, 1 mL of concentrated HCl was added to the solution and the solution was

further sonicated for 5 min. The resultant mixture was heated at 80 °C in a preheated oven for 18 h. After cooling to room temperature, the solid was separated from the mother solution by centrifugation. The MOF powder was washed with 15 mL of DMF (3 times) and 15 mL of acetone (3 times) and finally soaked in 15 mL of acetone for 18 h before activation under vacuum at 120 °C.<sup>182</sup>

Synthesis of UiO-66-OH: 125 mg of ZrCl<sub>4</sub> (0.54 mmol), 135 mg of 2-hydroxy-1,4 benzenedicarboxylic acid (0.75 mmol), and 15 mL of DMF were placed in an 8-dram vial and sonicated until the solution was clear. Afterward, 1 mL of concentrated HCl was added to the solution and the mixture was further sonicated for 5 min. The resultant mixture was heated at 80 °C in a preheated oven for 18h. After cooling to room temperature, the solid was separated from the mother solution by centrifugation and the powder was washed with 15 mL of DMF (3 times) and 15 mL of acetone (3 times) and finally soaked in 15 mL of acetone for 18h prior to activation under vacuum at 120 °C.<sup>182</sup>

Synthesis of UiO-66-NH<sub>2</sub>: 125 mg of ZrCl<sub>4</sub> (0.54 mmol), 134 mg of 2-amino-1,4 benzenedicarboxylic acid (0.75 mmol), and 15 mL of DMF were added to an 8-dram vial and sonicated. Afterward, 1 mL of concentrated HCl was added to the solution and the mixture was further sonicated for 5 min. The consequent mixture was then heated at 80 °C in a preheated oven for 18 h. After cooling down to room temperature, the solid was separated from the mother solution by centrifugation and the powder was washed with 15 mL of DMF (3 times) and 15 mL of acetone (3 times) and finally soaked in 15 mL of acetone for 18 h before being activated under vacuum 120 °C.<sup>182</sup>

Synthesis of UiO-67: 67 mg of  $ZrCl_4$  (0.27 mmol), 90 mg 4,4' biphenyl dicarboxylic acid (0.38 mmol), and 15 mL of DMF were placed in an 8-dram vial and sonicated. To the milky solution, 0.5 mL of concentrated HCl was added and the mixture was further sonicated. The resultant mixture was then heated at 80 °C in a preheated oven for 18 h. After cooling down to room temperature, the solid was separated from the mother solution by centrifugation and washed with 15 mL of DMF (3 times) and 15 mL of acetone (3 times) and finally soaked in 15 mL of acetone for 18 h prior to activation under vacuum at 120 °C .<sup>182</sup>

Synthesis of DUT-52: 67 mg of  $ZrCl_4$  (0.27 mmol), 80 mg of 2,6 naphthalene- dicarboxylic acid (0.38 mmol), and 15 mL of DMF were placed in an 8-dram vial and sonicated. Afterward, 0.5 mL of concentrated HCl was added to the solution and the mixture was further sonicated for 5 min. The resultant mixture was then heated at 80 °C in a preheated oven for 18 h. After cooling down to room temperature, the solid was separated from the mother solution by centrifugation and the powder was washed with 15 mL of DMF (3 times) and 15 mL of acetone (3 times) prior to activation under vacuum at 120 °C.

Synthesis of NU-1000: 4.85 g (15mmol) of  $ZrOCl_2 \cdot 8H_2O$ , 100 g (0.8 mol) of benzoic acid, and 300 mL of DMF were placed in a 1000 mL glass bottle and sonicated until clear. The clear mixture was heated in an oven at 100 °C for 1 h. 2 g (3 mmol) of 1,3,6,8-tetrakis (p-benzoic acid) pyrene ( $H_4TBAPy$ ) and 100 mL of DMF were mixed and heated at 100 °C for 1 h. After both solutions had cooled to room temperature, the yellow linker solution was added into the 1000 mL bottle containing the zirconium precursor and 2 ml of trifluoroacetic acid (TFA) was added into the solution. The solution was heated at 120 °C overnight. After cooling to room temperature, the yellow material was separated from the mother solution by centrifugation and washed 3 times with

DMF. The resulting light-yellow material was returned to the 1000 mL bottle and 650 mL of DMF and 25 mL of 8 M HCl were added to the solution. The resultant mixture was heated at 100 °C in a preheated oven overnight. After cooling to room temperature, the yellow powder was separated from the mother solution by centrifugation. The material was subsequently washed three times with DMF followed by 4 acetone washes. The material was dried in the vacuum oven at 80 °C overnight and activated at 120 °C.<sup>183</sup>

Synthesis of NU-901: 97 mg zirconium acetylacetonate ( $Zr(acac)_4$ ), 3.02 g of 4-aminobenzoic acid, and 8 mL of DMF were added to an 8-dram vial and sonicated until clear. The mixture was then placed in a preheated oven at 80 °C for 1 h. After the mixture was cooled to room temperature, 40 mg of  $H_4TBAPy$  linker were added and the resultant solution was heated at 100 °C overnight. The yellow material was separated from the mother solution by centrifugation and the material was washed with 10 mL of DMF (2 times). For HCl activation, 40 mg of MOF, 12 mL of DMF, and 0.5 mL of 8M HCl were added to an 8-dram vial and heated at 100 °C overnight. Again, the yellow material was separated from the mother solution via centrifugation. The material was subsequently washed three times with 15 mL of DMF followed by 4 acetone washes (15 mL). The material was dried overnight in a vacuum oven at 70 °C before being activated at 120 °C.

Synthesis of NU-1008: 66.4 mg of zirconium oxynitrate hydrate (0.267 mmol) and 1 mL of formic acid were added to 1.5 mL of DMF to prepare the  $Zr_6$ -node solution by heating the mixture in a preheated oven at 80 °C for 1 h. After the mixture cooled to the room temperature, 38.2 mg 3,6-dibromo-1,2,4,5-tetrakis(4-carboxyphenyl)benzene (TPhB-Br<sub>2</sub>) (0.0533 mmol) was dissolved in 1.5 mL of DMF and this solution was added into the prepared node solution. The mixture was placed in a preheated oven at 100°C for 16 h. After cooling down to the room temperature, the

white powder was separated from the mother solution by centrifugation and washed with 5 mL of DMF (3 times) and 5 mL of acetone (3 times). The material was dried under vacuum at 80 °C for 1 h. After washed with DMF and acetone, three fresh-synthesized MOFs were activated by heating at 120 °C overnight under high vacuum on a Micromeritics Smart Vacprep.<sup>184</sup>

Nitrogen adsorption and desorption isotherm measurements were collected at 77 K on a Micromeritics Tristar II. Powder X-ray diffraction measurements were obtained using a STOE STADI MP equipped with a  $K\alpha 1$  source and a 1D strip detector over a range of  $2^\circ \leq 2\theta \leq 30^\circ$ . Scanning electron microscopy (SEM) samples were prepared by drop casting and coated with a ~9 nm thick layer of OsO<sub>4</sub> using a Denton Desk III TSC Sputter Coater. SEM images were collected on a Hitachi SU8030. HPLC experiments were performed on an HPLC Agilent 1100 series system coupled with a diode-array detector (DAD). The reverse phase HPLC column, C18 (Supelco, Ascentis® C18, 150 mm x 4.6 mm, 5  $\mu$ m particle) was used with a water/acetonitrile mobile phase (50:50 v/v) at a flow rate of 1 mL min<sup>-1</sup>. The detector was set to a wavelength of 223 nm and the column temperature was set to 25°C. HPLC standards were prepared via serial dilution in water. All experiments were performed in triplicate.

Initial experiments were performed to evaluate the atrazine affinity of Zr<sub>6</sub>-based MOFs, namely, UiO-66 UiO-66-OH, UiO-66-NH<sub>2</sub>, UiO-67, DUT-52, NU-1008, NU-901 and NU-1000. In a typical experiment, an activated MOF sample (3.5 mg) was exposed to 10 mL of a 10 ppm aqueous atrazine solution in a 4-dram glass vial. The vials were agitated at ambient temperature for 24 h to ensure constant mixing and to allow sufficient time to reach saturation uptake. After 24 h, an aliquot (1 mL) of the solution was removed using a disposable syringe equipped with a 0.45  $\mu$ m PDVF syringe filter. The atrazine concentration was quantified by HPLC-DAD. The amount

of atrazine adsorbed by the MOF was determined by comparing these concentrations to the concentration of a 10 ppm atrazine solution without MOF. Percent adsorption uptake was calculated using **Eqn. 4.1**:

$$\text{Uptake (\%)} = \frac{C_i - C_e}{C_i} \times 100 \quad (4.1)$$

where  $C_i$  and  $C_e$  ( $\text{mg L}^{-1}$ ) are the initial and equilibrium concentrations, respectively.

To investigate the kinetics of atrazine adsorption, samples of NU-1000 (3.5 mg) were exposed to 10 mL of an aqueous 10 ppm atrazine solution in 4-dram glass vials. After a designated time (1, 5, 30, 60 and 120 min), 1 mL aliquots were removed with a disposable syringe equipped with a  $0.45 \mu\text{m}$  PDVF syringe filter. The initial and equilibrium atrazine concentrations in each solution were determined as previously described via HPLC-DAD. The amount of atrazine uptake  $q$  in mg of atrazine per gram of MOF was determined at each time point according to **Eqn. 1.1** reproduced below:

$$q = \frac{(C_i - C_f)V}{m} \quad (1.1)$$

where  $C_i$  is the initial concentration ( $\text{mg L}^{-1}$ ),  $C_f$  is the final concentration ( $\text{mg L}^{-1}$ ),  $V$  is the volume of solution exposed to sorbent (L), and  $m$  is the mass of sorbent (g).

To determine the maximum atrazine adsorption capacity of NU-1000, MOF samples (3.5 mg) were exposed to 10 mL of aqueous atrazine solutions with atrazine concentrations of 1, 2, 4, 6, or 8 ppm in 4-dram glass vials. After 2 h, aliquots of the supernatant were removed using a disposable syringe equipped with a  $0.45 \mu\text{m}$  PDVF syringe filter and analyzed by HPLC-DAD. The amount of atrazine adsorbed by the MOF was determined again by comparing these concentrations to the concentration of control solutions without MOF.

To investigate the effect of ionic strength on atrazine adsorption, NU-1000 samples (3.5 mg) were exposed to 10 mL of a 10 ppm aqueous atrazine solution in 0.1 M sodium chloride, 0.1 M sodium nitrate, 0.1 M sodium sulfate, or 0.1 M calcium chloride. After 1 h, an aliquot (1 mL) was removed with a disposable syringe equipped with a 0.45  $\mu\text{m}$  PDVF syringe filter. The initial and equilibrium atrazine concentrations were determined by HPLC-DAD.

The regeneration of NU-1000 was explored first by exposing a MOF sample (10 mg) to 10 mL of an aqueous 10 ppm atrazine solution in a 4-dram glass vial. The mixture was agitated at ambient temperature for 24 h. The slurry was then centrifuged to allow the MOF to settle and the supernatant was decanted. The atrazine-saturated NU-1000 sample was then soaked in 1 mL of acetone and agitated for 12 h. Similarly, this sample was centrifuged to settle the MOF and the supernatant was decanted. NU-1000 was then soaked again in 1 mL of acetone for 12 h and then centrifuged to settle the MOF and the supernatant was decanted. Finally, NU-1000 was dried in a vacuum oven at 80 °C for 12 h. This adsorption-desorption cycle was performed a total of three cycles.

## 4.9.3 MOF Characterization

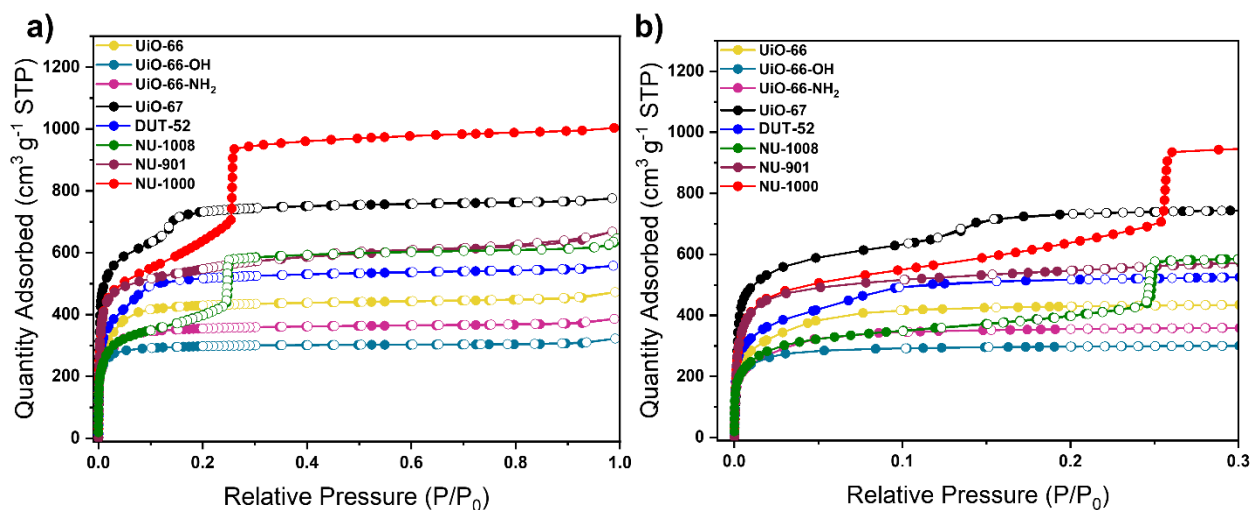


**Figure 4.6** a) Nitrogen adsorption-desorption isotherms at 77 K of all MOFs used in this study and b) nitrogen adsorption-desorption isotherms of MOFs at 77 K over the  $P/P_0$  range from 0 to 0.3.

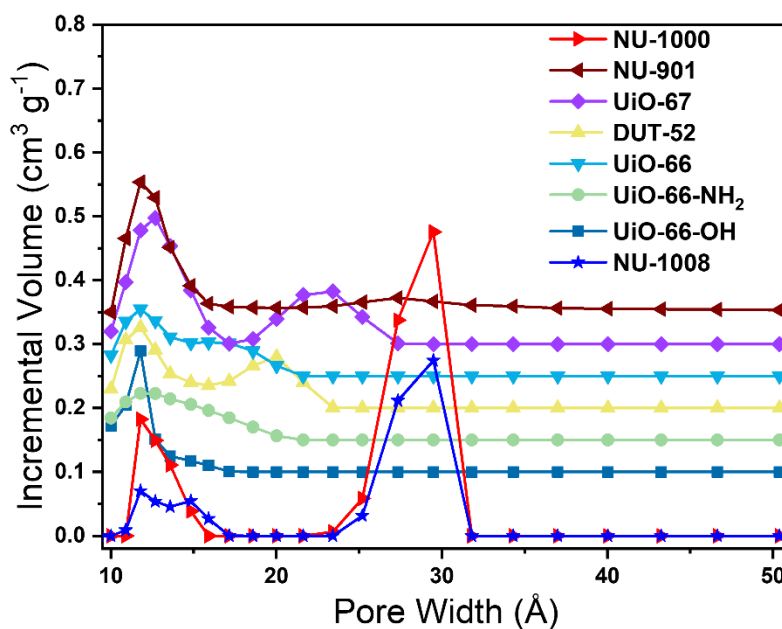


**Figure 4.7** DFT calculated pore size distributions for all MOFs used in this study.

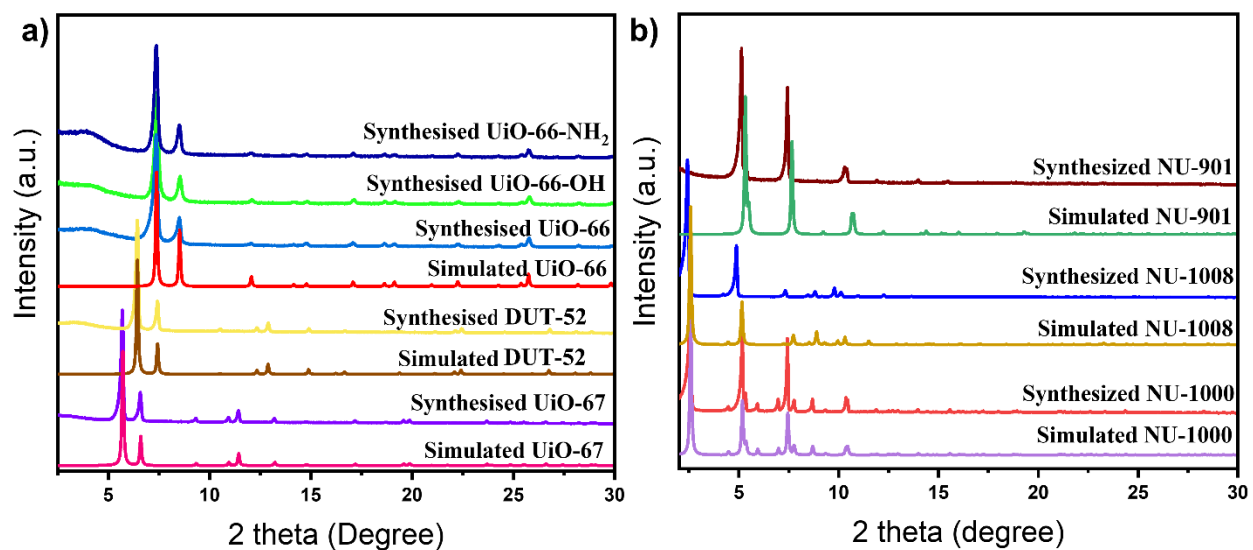


**Figure 4.8** Powder X-ray diffraction (PXRD) patterns of simulated and as-synthesized a) UiO-66, UiO-66-OH, UiO-66-NH<sub>2</sub>, DUT-52 and UiO-67 and b) NU-901, NU-1000 and NU-1008.

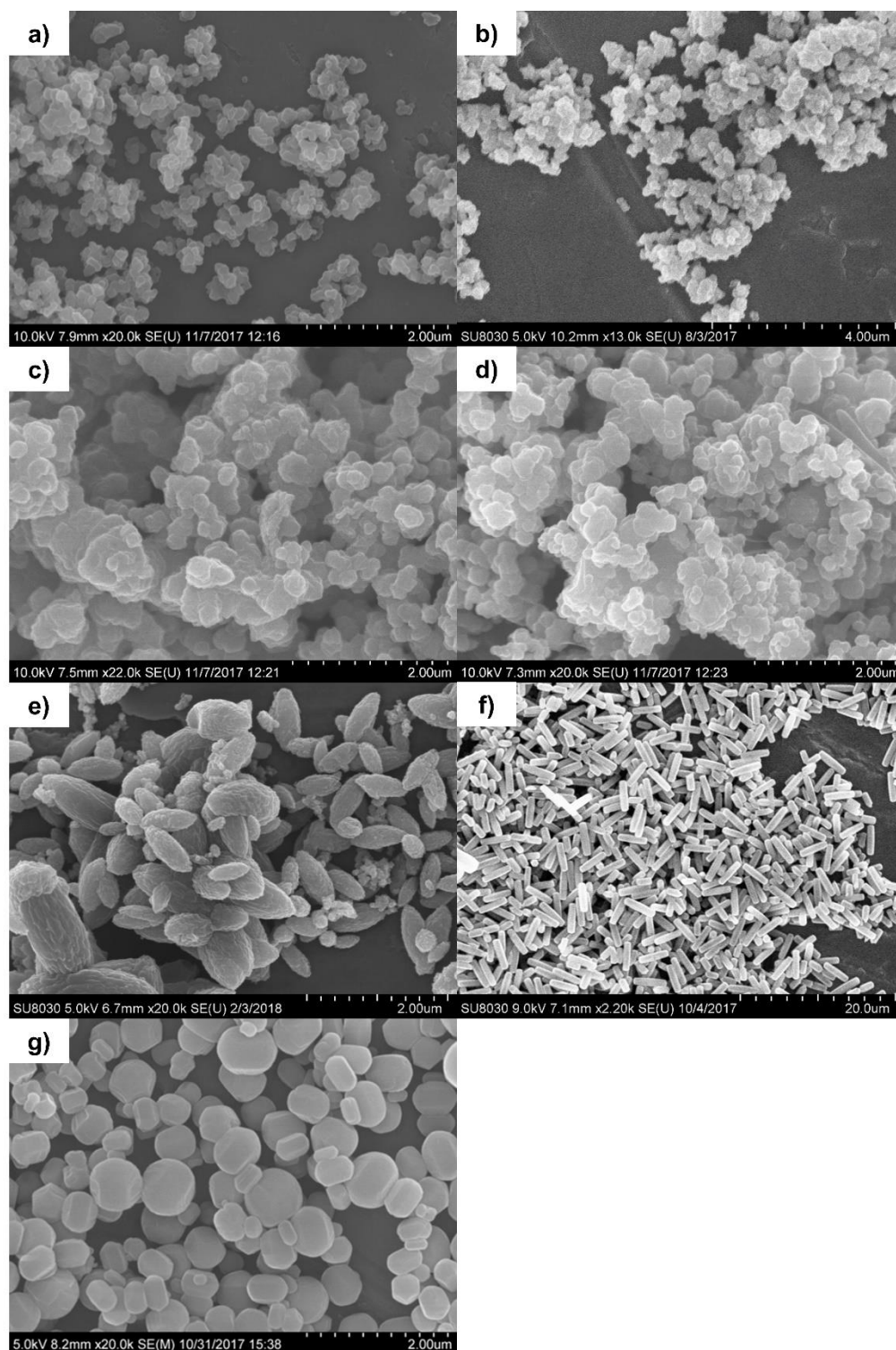


**Figure 4.9** Scanning Electron Microscopy (SEM) images of all Zr<sub>6</sub>-based MOFs used in this study: a) UiO-66, b) UiO-66-OH, c) UiO-67, d) DUT-52, e) NU-901, f) NU-1000 and g) NU-1008.

## 4.9.4 Atrazine Adsorption Measurements

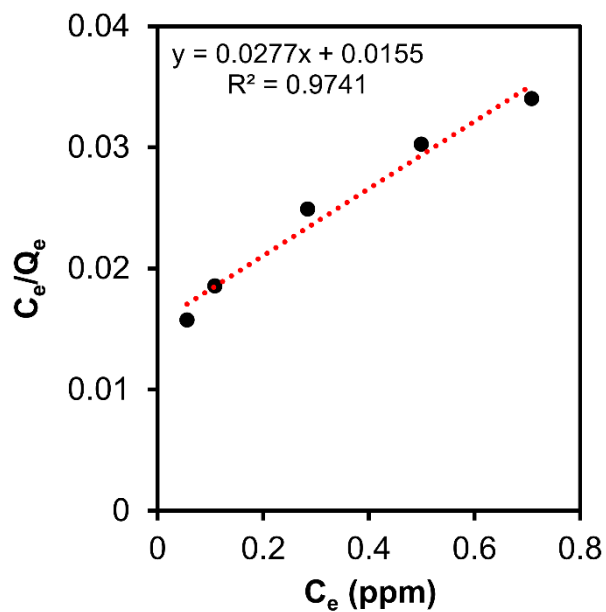


**Figure 4.10** Type I Linear Langmuir Fit to determine the maximum uptake capacity of atrazine in mg per g of NU-1000.

**Table 4.3** Langmuir Fitting Parameters for atrazine adsorption in NU-1000.

	$K_L$ (L mg <sup>-1</sup> )	Q (mg g <sup>-1</sup> )	$R^2$
NU-1000 (3.5 mg)	1.78	36	0.96

**Table 4.4** Atrazine adsorption capacities of various sorbents.

Material	Q (mg g <sup>-1</sup> )	Time to Saturation	Ref
Carbon nanotube - SMWNT20	31.37	6 h	175
Carbon nanotube - r-MWNT	100.43	6 h	175
Treated banana peels	14	15 h	179
Multiwalled carbon nanotubes	40.16	7 h	148
Activated Carbon (commercial)	0.240	N/A	177
Biochar - CS450	7.842	N/A	176
Biochar - ADPCS450	53.85	N/A	176
Sludge-based activated carbon-like material	45.49	10 h	180
Polyacrylic acid-functionalized magnetic ordered mesoporous carbon (P-MMC)	76.51	24 h	178
Magnetic ordered mesoporous carbon (MMC)	62.19	24 h	178
Ordered mesoporous carbon (OMC)	49.74	24 h	178
Porous poly(divinylbenzene)	32.6	2 h	174

#### 4.9.5 Regeneration and Stability of NU-1000

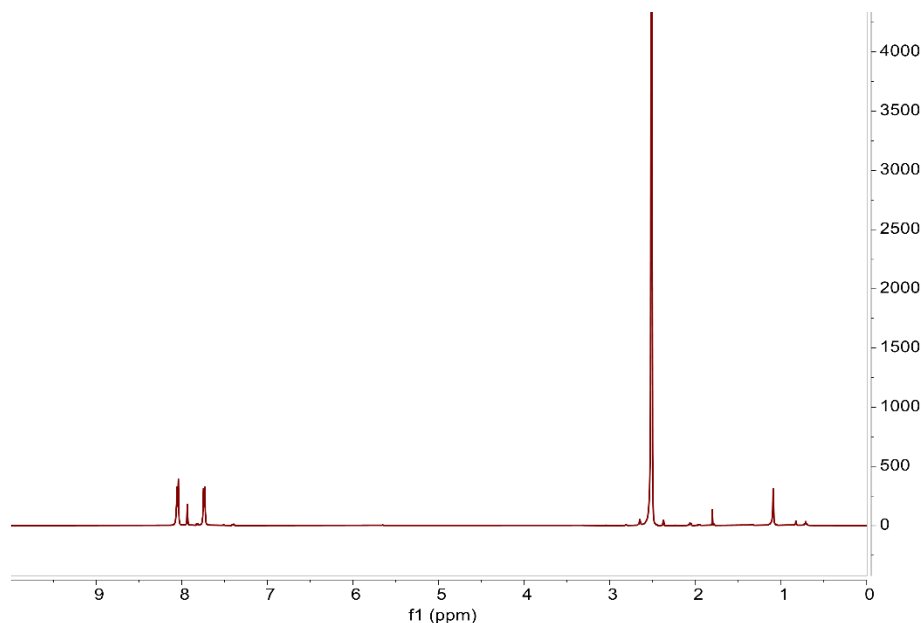


**Figure 4.11** <sup>1</sup>H NMR spectrum of digested NU-1000 after atrazine adsorption and regeneration with acetone (1 mL) shows only H<sub>4</sub>TBAPy (NU-1000 linker) and residual solvent peaks. No atrazine peaks are observed demonstrating that NU-1000 can be regenerated with acetone (1 mL) after atrazine adsorption. [MOF digestion protocol: ~1.5 mg of NU-1000 is digested in 6 drops of concentrated D<sub>2</sub>SO<sub>4</sub> and diluted in 700 microliters of DMSO for NMR analysis].

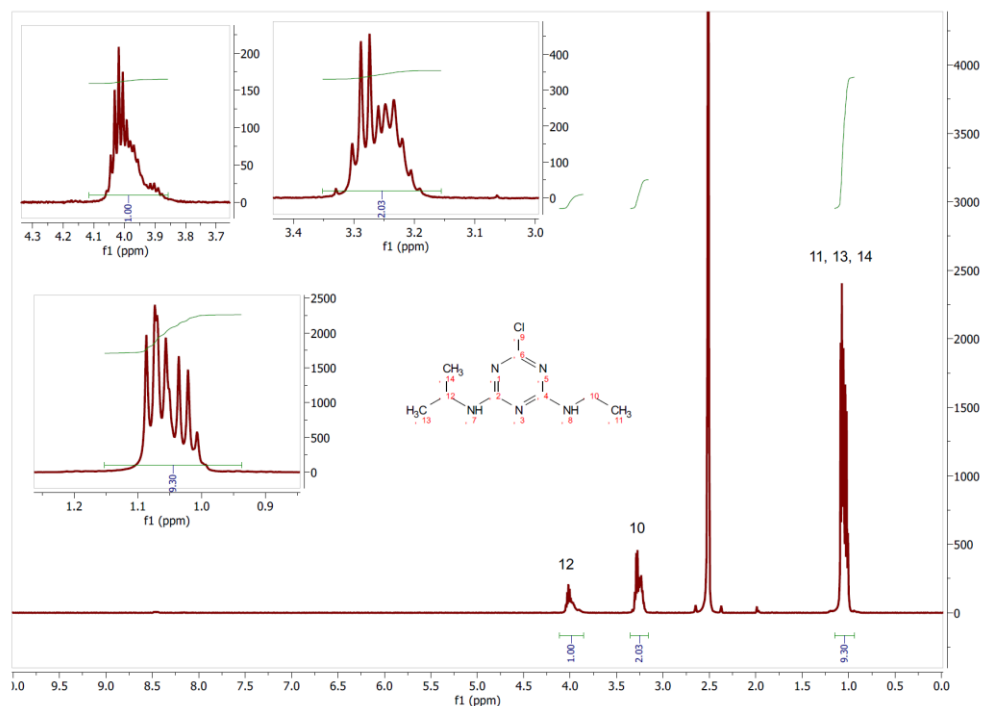


**Figure 4.12** Control  $^1\text{H}$  NMR spectrum of atrazine in the  $\text{DMSO}/\text{D}_2\text{SO}_4$  solution used for MOF digestion.

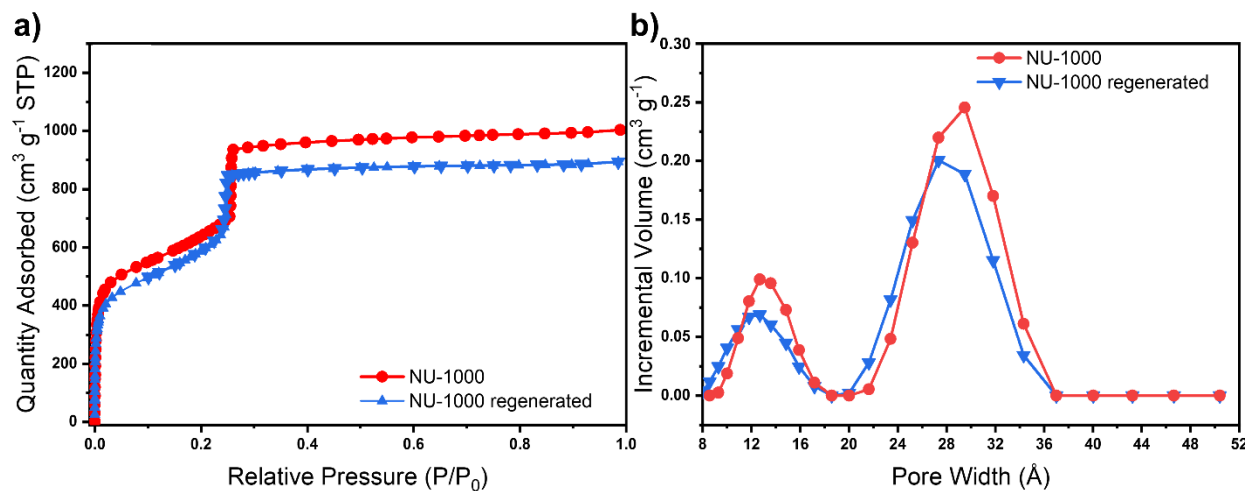


**Figure 4.13** a)  $\text{N}_2$  adsorption isotherms of pristine NU-1000 and NU-1000 after atrazine adsorption and regeneration with acetone (1 mL) show a slight decrease in surface area. b) The associated DFT calculated pore size distributions.

## Chapter 5. Isothermal Titration Calorimetry to Explore the Parameter Space of Organophosphorus Agrochemical Adsorption in MOFs

Portions of this chapter appear in the following manuscript:

**Drout, R.J.**; Kato, S.; Chen, H.; Son, F.A.; Otake, K-i.; Islamoglu, T.; Snurr, R.Q.; Farha, O.K. Isothermal Titration Calorimetry to Explore the Parameter Space of Organophosphorus Agrochemical Adsorption in MOFs. *J. Am. Chem. Soc.* **2020**, *142* (28), 12357-12366.

## 5.1 Chapter Summary

The expansion of manufacturing and commercial agriculture alongside rapid globalization have resulted in the widespread contamination of freshwater supplies with chemical toxins including persistent organic pollutants. Effective mitigation of such pollution is paramount to safeguarding human health, animal and aquatic life, and the environment. Currently, adsorption is the most economically viable water purification strategy. Owing to their crystallinity and modular nature, metal–organic frameworks (MOFs) are an excellent platform material for systematically investigating the physical and chemical properties which govern adsorption processes. X-ray diffraction techniques provide atomically precise descriptions of toxin-MOF interactions, while liquid-phase adsorption isotherms readily allow for the determination of uptake capacity and kinetics; however, determination of the thermodynamics of toxin-MOF interactions in aqueous media remains tedious. Herein, we add isothermal titration calorimetry (ITC) to our arsenal of techniques for characterizing adsorption mechanisms in MOFs. With this method, we are able to directly quantify the full thermodynamic profile of a chemical process ( $K_a$ ,  $\Delta G$ ,  $\Delta H$ ,  $T\Delta S$ ), providing critical details to support the rational design of next-generation sorbents. We demonstrate the suitability of ITC through our exploration of the parameter space of organophosphorus agrochemical adsorption in zirconium-based MOFs.

## 5.2 Adsorption of Agrochemical Pollutants

During the last 200 years, anthropogenic activities and globalization have pervaded Earth's freshwater sources with chemical toxins.<sup>185, 186</sup> Briefly, Cold War era weapons development notoriously released radioactive species<sup>187</sup> and mining operations continue to leach heavy metals.<sup>188</sup> Currently, commercial-scale farms apply excessive amounts of agrochemicals (e.g. fertilizers, pesticides, herbicides, etc.),<sup>189</sup> and healthcare providers dramatically overprescribe

pharmaceuticals.<sup>190</sup> While we understand the effects of heavy metal<sup>191</sup> and radiation exposure,<sup>192,</sup><sup>193</sup> longitudinal studies to examine the effects of continued exposure to agrochemicals and pharmaceuticals are lacking. Therefore, to adequately safeguard human health as well as Earth's threatened ecosystems, we rely on adsorption technologies including activated carbon,<sup>194, 195</sup> polymer-based resins,<sup>196</sup> and zeolites<sup>197</sup> to remove these species from water prior to human consumption. These porous materials often record moderate to high uptake capacities and are economically viable for commercial implementation; however, researchers are largely unable to define the specific adsorption sites and mechanisms governing adsorption in porous carbons and polymeric materials due to the materials' amorphous natures. Toward this end, recent efforts have sought to explore adsorption processes in porous crystalline materials in which binding interactions can be defined via X-ray diffraction.

Metal-organic frameworks (MOFs) are a class of porous, crystalline materials consisting of metal oxide nodes and organic linkers which assemble through coordination bonds into multidimensional lattices.<sup>198-203</sup> MOFs embody several features that make them an ideal platform material for exploring favorable binding interactions en route to designing next-generation adsorbents. Specifically, the nodes and linkers offer a high density of potential binding sites which may promote high adsorption capacities, while high framework porosity facilitates diffusion, affording rapid saturation. Moreover, the inherent diversity of structural building blocks (i.e. nodes and linkers) allows for the preparation of MOFs with a range of chemical and physical properties.<sup>204</sup> Most importantly, the intrinsic periodic nature of these materials allows for the atomically-precise characterization of toxin-sorbent interactions using powder and single-crystal X-ray diffraction.

### 5.3 Monitoring Adsorption Events Using Isothermal Titration Calorimetry

Recently, the exploration of MOF-based sorbents for the extraction of chemical toxins from water has expanded to include zirconium-based MOFs (Zr-MOFs) because of their unique chemical and thermal stability, which arises from the abundance of strong Zr(IV)–O bonds.<sup>21, 160, 205-209</sup> Researchers have screened MOFs as sorbents for radioactive species,<sup>83, 210</sup> heavy metals,<sup>17, 211, 212</sup> and persistent organic pollutants.<sup>25, 213-215</sup> Using bulk adsorption methods, researchers have demonstrated that node and linker structure as well as framework topology influence toxin uptake capacity and kinetics. Additionally, crystallographic investigations occasionally paired with computational modeling have precisely characterized specific analyte binding motifs.<sup>19, 20</sup> While these efforts have dramatically expanded our understanding of structural and chemical features that influence adsorption, they yield minimal information about the thermodynamic parameters of the adsorption processes in the liquid phase. To better inform our design of next-generation sorbents, it is imperative that we understand the affinity of binding interactions and the enthalpic and entropic changes arising from those interactions.

Fortunately, isothermal titration calorimetry (ITC) allows for the direct quantification of the binding association constant ( $K_a$ ), enthalpy change ( $\Delta H$ ), entropy change ( $\Delta S$ ) and Gibbs free energy change ( $\Delta G$ ) of a chemical process.<sup>216-218</sup> Most commonly, researchers in the biological sciences use this technique to investigate substrate-active site interactions.<sup>219, 220</sup> Similarly, we envisioned the value of this technique for illuminating adsorptive processes in MOFs. Only recently have materials chemists begun exploring the applicability of this technique for the study of porous sorbents.<sup>221-225</sup> Therefore, we undertook a proof-of-concept study using ITC to explore the parameter space of glyphosate adsorption in Zr-MOFs (**Figure 5.1**). Glyphosate, the active ingredient of the widely used pesticide Roundup, possesses both a carboxylic acid and a

phosphonic acid.<sup>226</sup> Herein, we examine the influence of analyte structure, MOF structure, and buffer composition on the thermodynamic parameters of adsorption.

#### 5.4 Glyphosate Binding in NU-1000

We elected to begin our exploration by examining the adsorption of glyphosate in NU-1000. This MOF consists of  $Zr_6$ -nodes and tetratopic pyrene-based linkers assembled into the **csq** topology, which features 1D hexagonal (31 Å) and triangular (12 Å) channels connected by orthogonal windows ( $10 \times 8$  Å) referred to as the c-pores (**Figure 5.1** and **Figure 5.16**).<sup>183</sup> Eight linkers coordinate to each node, while four terminal hydroxyl (–OH) and water (–H<sub>2</sub>O) ligands balance the node's overall charge. The lability of these ligands allows for pseudo-ion-exchange processes to occur at the node, whereby a hydroxyl and/or water ligand are exchanged for an oxyanion such as perrhenate or a phosphate containing species.<sup>19, 227-229</sup> We hypothesized that glyphosate could similarly coordinate to the node.<sup>230-232</sup> While the carboxylic acid ( $pK_a \approx 2.6$ ) can coordinate to the node, binding through the phosphonic acid ( $pK_a \approx 2.0$ ) is more probable, as it is more likely to be in the deprotonated form.<sup>233</sup>

To ensure the heat absorbed or released during an isothermal titration calorimetry (ITC) experiment results from the chemisorption process rather than the ionization of the aqueous media, both the sorbent (MOF) and titrant (analyte) solutions must be prepared in equivalent buffer matrices. Therefore, we sought to verify that no enthalpic peaks resulted from interactions between the analyte or MOF and buffer matrix. To this end, we first verified that NU-1000 retained its structural integrity after soaking in acetate buffer for 3 days (**Figure 5.8**, **Figure 5.9**, **Figure 5.13**). Blank titrations of a glyphosate solution (10 mM in 50 mM acetate buffer, pH 4) into acetate buffer (50 mM, pH 4) and acetate buffer (10 mM, pH 4) into an NU-1000 suspension (1 mM, 50 mM acetate, pH 4) displayed no substantial enthalpy peaks (**Figure 5.21**). Therefore, we were confident

that enthalpy peaks arising from the titration of NU-1000 (1 mM, 50 mM acetate, pH 4) with a glyphosate solution (10 mM, 50 mM acetate, pH 4) arose from the chemisorption of glyphosate to the NU-1000 node (**Figure 5.2**).

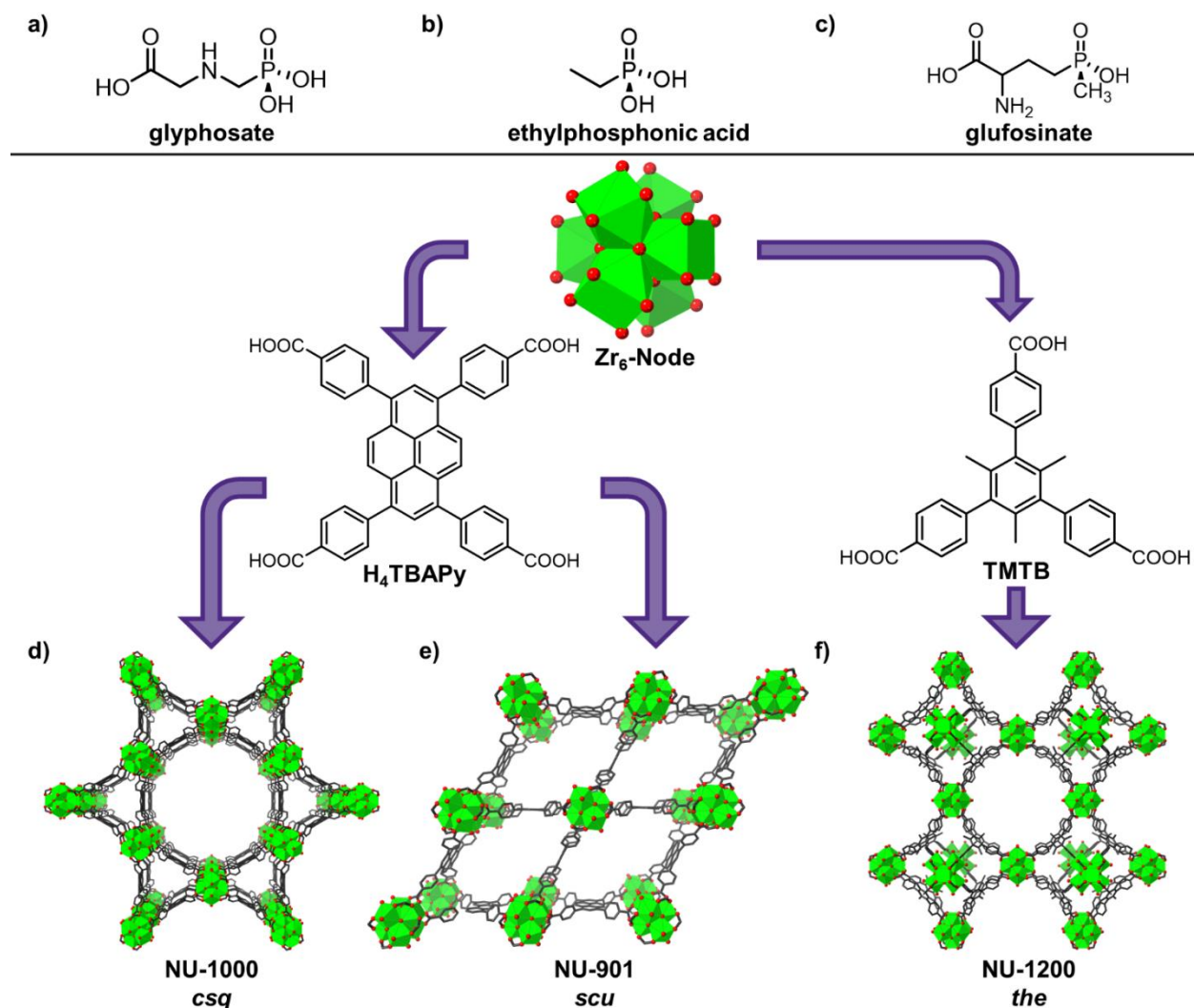


**Figure 5.1** Structures of a) glyphosate, b) ethylphosphonic acid, and c) glufosinate and structures of d) NU-1000, e) NU-901, and f) NU-1200. The structural properties of these MOFs are summarized in **Table 5.3**.

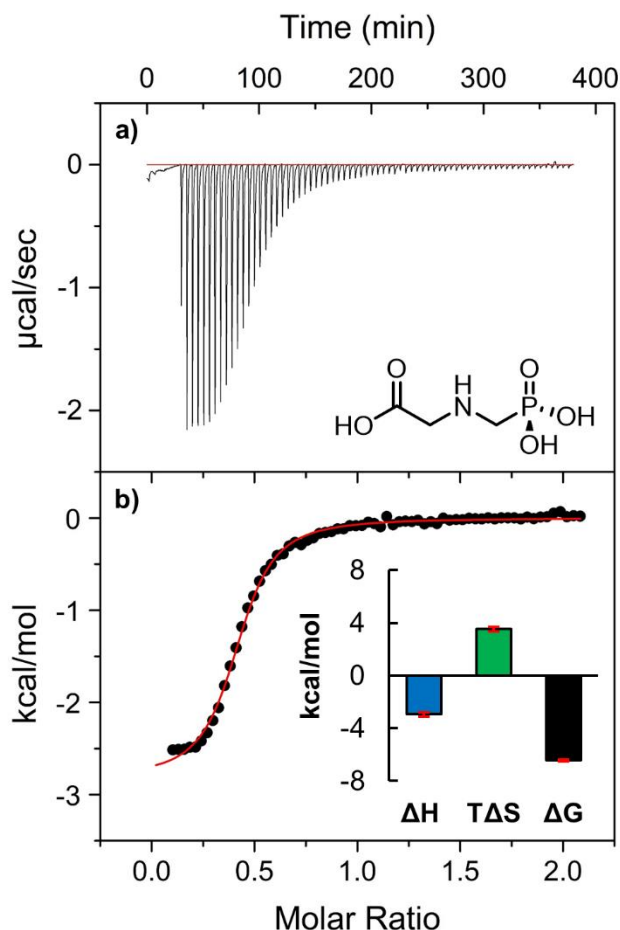


**Figure 5.2** a) ITC thermogram resulting from titration of a NU-1000 suspension (1 mM, 1.4 mL, 50 mM acetate buffer, pH 4) with a glyphosate solution (10 mM, 50 mM acetate, 4  $\mu\text{L}$  injections) exhibits exothermic peaks and b) fitting with a single site model demonstrates a highly favorable binding affinity ( $\Delta G$ , black bar). The inset depicts the magnitude of the calculated thermodynamic parameters. Error bars represent the standard deviations of triplicate measurements.

Thermograms resulting from the titration of a suspension of NU-1000 with a glyphosate solution displayed strong, negative peaks meaning glyphosate chemisorption proceeds via an exothermic pathway (**Figure 5.2** and **Table 5.1**). Preliminary crystallographic studies confirmed that glyphosate molecules coordinated to the node through two of the phosphonic acid's oxygen atoms (**Figure 5.16**). Moreover, we observed no interactions between multiple glyphosate molecules at a single binding site and therefore elected to fit the data using a single site model.<sup>225</sup> Chemisorption of glyphosate is both favorable and spontaneous as demonstrated by the large

positive binding association constant ( $K_a = 5.3 \times 10^4 \text{ M}^{-1}$ ) and negative Gibbs free energy change ( $\Delta G = -6.44 \pm 0.07 \text{ kcal mol}^{-1}$ ) (**Table 5.1**). The negative enthalpic term indicates that the interactions between the substrate (glyphosate) and sorbent (NU-1000) are more favorable than the combined interactions between both species and the buffer matrix.<sup>234</sup> The positive entropic term ( $\Delta S$ ) also suggests that upon glyphosate coordination, the environment immediately surrounding the binding site becomes more disordered, which we attribute to the reorganization of solvent molecules (water and buffer).<sup>234</sup>

### 5.5 Effect of Analyte Structure on Binding Thermodynamics

Confident that ITC was suitable for studying chemisorption processes at MOF nodes, we sought to further explore how analyte structure influences the thermodynamic parameters of adsorption. To our study we added two other organophosphorus agrochemicals, ethylphosphonic acid and glufosinate (**Figure 5.1**). Ethylphosphonic acid resembles glyphosate but is significantly smaller and does not contain a polar group besides the phosphonic acid. Alternatively, glufosinate is approximately the same size as glyphosate; however, unlike glyphosate, glufosinate possesses a carboxylic acid, a primary amine, and a methylphosphonate. For all analytes, binding through the phosphonic acid is most probable; however, the carboxylic acids may be able to interact with the framework through hydrogen bonding.

Initial bulk adsorption measurements allowed for the quantification of the maximum uptake capacity of the three analytes in NU-1000 (**Figure 5.17**). According to linear Langmuir fits of the equilibrium uptake amounts and residual analyte concentrations in solution, NU-1000 attained the highest molar capacity ( $Q_m$ ) of ethylphosphonic acid followed by glufosinate and glyphosate (**Table 5.1, Figure 5.19**); however, these molar capacities are quite similar as one might expect given the analytes' similar chemical functionality. Alternatively, examination of the associated

partition coefficients (PCs), which reflect the ratio of analyte adsorbed compared to the residual analyte in solution, reveals that NU-1000 most readily adsorbs glyphosate followed by ethylphosphonic acid and glufosinate when exposed to low initial analyte concentrations (**Table 5.4, Table 5.5, Table 5.6, Figure 5.18**).<sup>235</sup> Paralleling the similar equilibrium molar adsorption capacities, NU-1000 obtains nearly equivalent PCs across the three organophosphorus species when exposed to higher initial concentrations. The Langmuir constants ( $K_L$ ), which reflect the affinity of the binding interactions, indicate that glyphosate coordinates most strongly and glufosinate most weakly. Similarly, the binding association constants ( $K_a$ ) and thereby Gibbs free energy changes ( $\Delta G$ ) extracted from the relevant ITC thermograms, show that coordination to the NU-1000 node is most favorable for glyphosate followed by ethylphosphonic acid and finally, glufosinate (**Table 5.1** Uptake capacity ( $Q_m$ ) of NU-1000 and thermodynamic parameters of adsorption for various analytes. Errors are calculated as the standard deviations of triplicate measurements.). In fact, the binding association constants ( $K_a$ ) determined from the ITC thermograms and Langmuir constants ( $K_L$ ) extracted from bulk adsorption data display excellent linear correlation (**Figure 5.3**). This relationship demonstrates that ITC experiments complement bulk adsorption studies by allowing for the efficient quantification of the thermodynamic parameters of a chemisorption process.

**Table 5.1** Uptake capacity ( $Q_m$ ) of NU-1000 and thermodynamic parameters of adsorption for various analytes. Errors are calculated as the standard deviations of triplicate measurements.

Analyte	$Q_m$ (mol/mol)	$Q_m$ (mg/g)	$K_L$ (L/mg)	$\Delta H$ (kcal/mol)	T $\Delta S$ (kcal/mol)	$\Delta G$ (kcal/mol)
Glyphosate	2.17	168	1.76	$-2.9 \pm 0.2$	$3.5 \pm 0.2$	$-6.44 \pm 0.07$
Ethylphosphonic Acid	2.36	119	0.418	$2.0 \pm 0.1$	$7.7 \pm 0.1$	$-5.74 \pm 0.09$
Glufosinate	2.28	183	0.230	$1.1 \pm 0.1$	$5.4 \pm 0.1$	$-4.35 \pm 0.03$

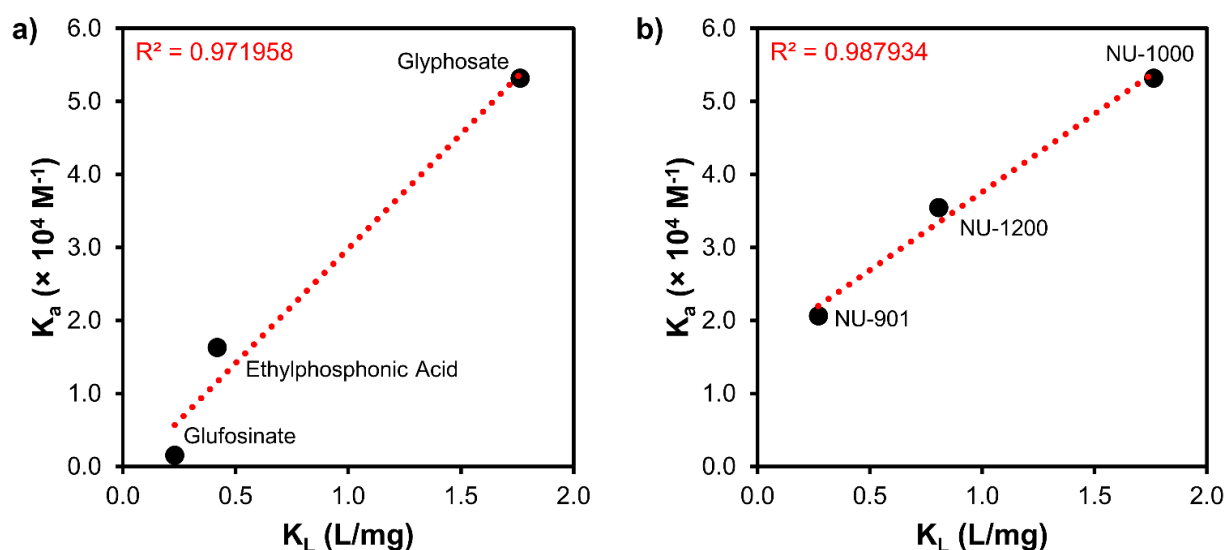


**Figure 5.3** Linear relationship of Langmuir constants ( $K_L$ ) and binding association constants ( $K_a$ ) for a) glyphosate, ethylphosphonic acid, and glufosinate chemisorption in NU-1000 and b) glyphosate chemisorption in NU-1000, NU-901, and NU-1200 verify that ITC and bulk adsorption experiments yield comparable and complementary data.

Beyond the association constants, the enthalpic and entropic terms also display interesting details. Different from glyphosate, the chemisorption of both ethylphosphonic acid and glufosinate in NU-1000 was entropically-driven and enthalpically-opposed (**Table 5.1**). Interactions with the solvent serve as the reference point for the overall enthalpic term, which embodies the energetics

of electrostatic interactions, hydrogen bonding, van der Waals forces, and polar/dipolar interactions.<sup>234</sup> Therefore, these positive enthalpic terms indicate that the desolvation penalty exceeds the favorable interactions between either ethylphosphonic acid or glufosinate and NU-1000. Moreover, the entropic terms for chemisorption of ethylphosphonic acid and glufosinate are both positive and greater than that of glyphosate. Given that the MOF framework is rigid and that the trends do not follow the analyte size, we suspect that conformational entropy and rotational entropy contribute only slightly to the overall entropy term and anticipate that the entropy of solvation is likely the largest contributor.<sup>234</sup> Therefore, we sought additional characterization of the analyte-MOF interactions to better explain the influence of analyte structure on chemisorption thermodynamics.

Single-crystal X-ray diffraction provides an excellent strategy for characterizing analyte-MOF interactions with atomic precision. While significant disorder of glyphosate's alkyl chain prohibited complete resolution of the crystal structure, the incomplete structure verified that glyphosate coordinated to the  $Zr_6$ -node of NU-1000 through two of the phosphonic acid's oxygen atoms and demonstrated that most (>60%) of the glyphosate bound within the framework occupied binding sites directed into the c-pore, the orthogonal windows between the hexagonal and triangular channels (**Figure 5.16**). Further investigation of the glyphosate molecule's possible orientations suggested that the carboxylic acid may be able to hydrogen bond with the terminal water and/or hydroxyl ligands on the adjacent node in the c-pore. Under the assumption that glyphosate coordinates to NU-1000 through the phosphonic acid, density functional theory (DFT) calculations illustrated that the lowest energy conformation of glyphosate in the NU-1000 c-pore involved two distinct hydrogen bonds ( $\sim 1.65 \text{ \AA}$  and  $\sim 2.01 \text{ \AA}$ ) between the carboxylic acid and the

ligands on the adjacent node (**Figure 5.4b** and **c**). Conversely, at sites directed into the mesopore, the DFT optimized structure does not feature any noncovalent interactions between glyphosate and the MOF framework besides van der Waals interactions (**Figure 5.4a**). We attribute the negative enthalpic term resulting from glyphosate chemisorption to strong electrostatic interactions between the analyte and MOF node and the aforementioned hydrogen bonding in the c-pore which overcome glyphosate and MOF solvation. As anticipated based on the size and structure of ethylphosphonic acid, the lowest energy conformations of this analyte bound at sites directed into the c-pore and mesopore showed no hydrogen bonding or particularly strong noncovalent interactions (**Figure 5.27**). Optimized structures of glufosinate coordinating to the node of NU-1000 in the c-pore showed multiple possible hydrogen bond sites similar to those of glyphosate and no such interactions when coordinated at a site directed into the mesopore (**Figure 5.28**). The smaller entropic terms for glyphosate and glufosinate chemisorption compared to that of ethylphosphonic acid indicate fewer degrees of freedom of the coordinated species which agrees well with the greater number of favorable interactions between the molecule and the MOF framework.

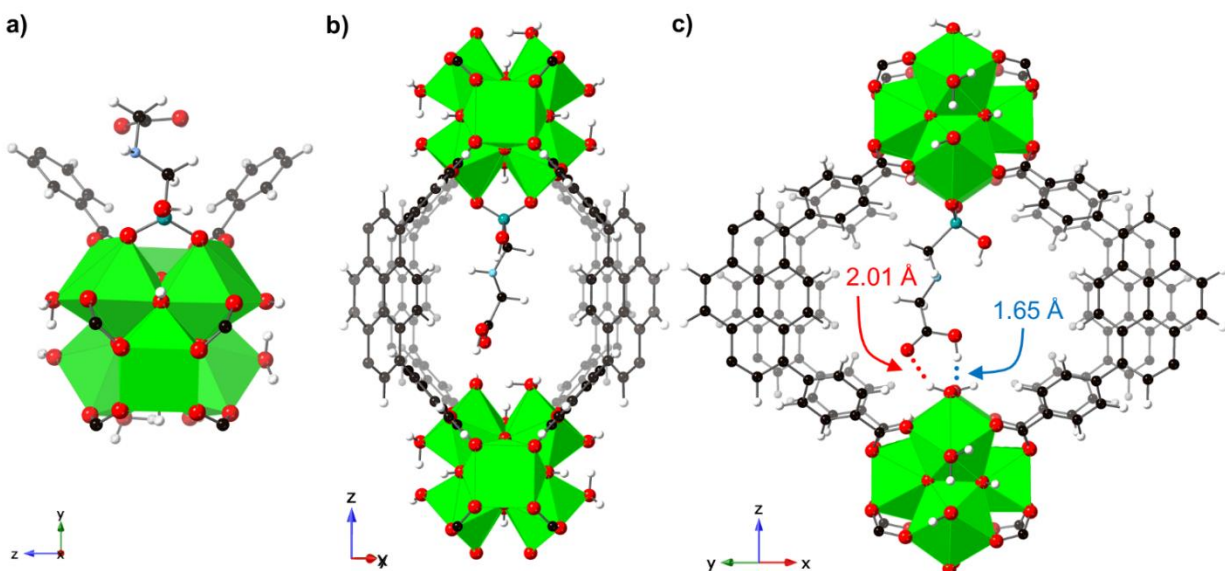


**Figure 5.4** Lowest energy conformation of glyphosate binding in a) the mesopore of NU-1000 shows minimal non-covalent interactions with the surrounding framework environment. Conversely, when coordinating in the c-pore of NU-1000 (b and c), glyphosate coordinates at one node through the phosphonic acid and H-bonds to the terminal ligands on the adjacent node through the carboxylic acid.

Moving forward, we sought to use ITC to experimentally assess how altering the accessibility of the NU-1000 c-pore influenced the thermodynamic parameters of glyphosate chemisorption. Numerous strategies exist to post-synthetically modify a parent MOF framework.<sup>9</sup> Specifically, solvent-assisted ligand incorporation offers a facile route to installing 2,6-naphthalene dicarboxylic (NDC) acid across the c-pores of NU-1000 without sacrificing the structural integrity or porosity of the framework (**Figure 5.8**, **Figure 5.9**, and **Figure 5.14**).<sup>236</sup> By blocking the c-pore with NDC, we anticipated that the enthalpic term associated with glyphosate sorption would become less negative due to occupation of the strongest binding sites and that the overall chemisorption process would also become less favorable. ITC thermograms resulting from the titration of NU-1000-NDC with glyphosate demonstrated that chemisorption was both less exothermic and less favorable compared to the same process in NU-1000 (**Figure 5.5**). This experimental evidence corroborates the DFT-optimized structures as well. Moreover, the entropic

term for chemisorption in NU-1000-NDC contributes more significantly than the enthalpic term to the overall change in Gibbs free energy compared to that for sorption in the parent framework suggesting that without the availability of noncovalent interaction sites in the c-pore, bound glyphosate has more degrees of freedom. Conversely, the thermodynamic profile resulting from chemisorption of ethylphosphonic acid in NU-1000-NDC is nearly identical to that for its binding in NU-1000 (**Figure 5.24**). This demonstrates that binding of ethylphosphonic acid in the c-pore is no more favorable than binding in the mesopore because the molecule is unable to interact with the adjacent node. In summary, DFT calculations and ITC experiments demonstrated that glyphosate binding in the c-pore of NU-1000 is more favorable than coordination at sites directed into the mesopore due to the molecule's ability to hydrogen bond with the terminal water and hydroxyl ligands on the adjacent node.

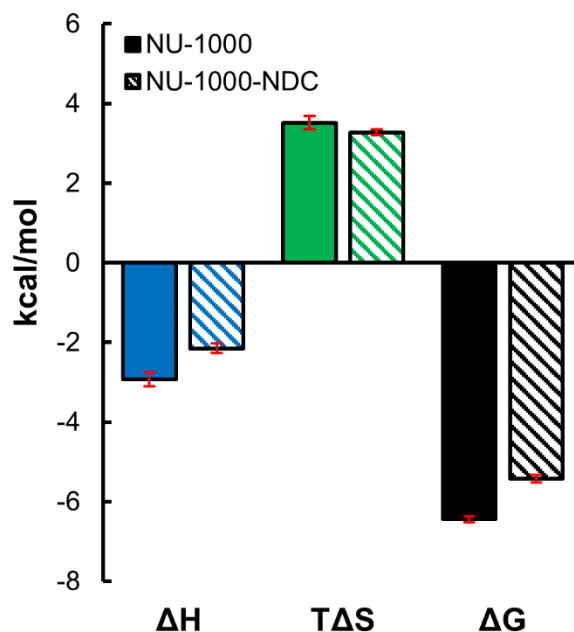


**Figure 5.5** Thermodynamic parameters of glyphosate binding in NU-1000 (solid) and NU-1000-NDC (hatched) demonstrate that glyphosate chemisorption in NU-1000-NDC is less favorable and less exothermic than glyphosate chemisorption in native NU-1000.

## 5.6 Effect of MOF Structure on Analyte Uptake

Inspired by glyphosate's unique coordination in the c-pore of NU-1000, we sought to further investigate the effects of MOF structure on chemisorption thermodynamics. To this end, we explored chemisorption in two additional 8-connected Zr-MOFs. Specifically, NU-901, a structural polymorph of NU-1000 with a **scu** net, features diamond pores (12 Å across) and c-pores approximately the same size as those in NU-1000,<sup>237</sup> and NU-1200, a MOF comprising tritopic linkers and Zr<sub>6</sub>-nodes assembled in the **the** topology with both cages (14 Å across) and mesoporous channels (22 Å across) (**Figure 5.1**).<sup>238</sup> Bulk adsorption experiments demonstrated NU-1200 attained the highest glyphosate uptake capacity followed by NU-901 and NU-1000 (**Table 5.2**, **Figure 5.17** and **Figure 5.20**). At low exposure concentrations, the partition coefficients (PCs) vary widely, with NU-1200 adsorbing significantly more analyte (PC = 9.25 L g<sup>-1</sup>) than either NU-1000 (PC = 5.13 L g<sup>-1</sup>) or NU-901 (PC = 3.11 L g<sup>-1</sup>); however, the three MOFs yield nearly equivalent PCs at higher glyphosate exposures (**Table 5.4**, **Table 5.7**, **Table 5.8**, and **Figure 5.18**). The Langmuir fit of adsorption in NU-1000 produces the greatest Langmuir constant (K<sub>L</sub>) followed by those of NU-1200 and NU-901 (**Table 5.2**). The binding association constants (K<sub>a</sub>) extracted from ITC experiments, and therefore the Gibbs free energy changes, associated with these adsorption processes follow the same trend and the two constants display strong linear correlation (**Figure 5.3**). This linear relationship again establishes the suitability of ITC for studying chemisorption in MOFs and demonstrates its complementarity to bulk adsorption studies.

**Table 5.2** Glyphosate uptake capacities ( $Q_m$ ), Langmuir constants ( $K_L$ ), and thermodynamic parameters of glyphosate chemisorption in NU-1000, NU-901, and NU-1200.

MOF	$Q_m$ (mol/mol)	$Q_m$ (mg/g)	$K_L$ (L/mg)	$\Delta H$ (kcal/mol)	$T\Delta S$ (kcal/mol)	$\Delta G$ (kcal/mol)
NU-1000	2.17	168	1.76	$-2.9 \pm 0.2$	$3.5 \pm 0.2$	$-6.44 \pm 0.07$
NU-901	2.48	192	0.207	$-3.0 \pm 0.2$	$2.9 \pm 0.1$	$-5.88 \pm 0.07$
NU-1200	2.53	205	0.806	$-1.3 \pm 0.1$	$4.9 \pm 0.1$	$-6.2 \pm 0.2$

ITC thermograms resulting from the titration of NU-901 with glyphosate yielded a similar enthalpic term, a smaller entropic term, and a less favorable binding association constant compared to those of NU-1000. Given NU-901 comprises a c-pore resembling that of NU-1000, the similar enthalpic term is reasonable. Conversely, the diamond pores of NU-901 are smaller than the hexagonal mesopores in NU-1000 and therefore may inhibit the molecule's free rotation resulting in the smaller entropic contribution. The chemisorption of ethylphosphonic acid in NU-901 similarly reflects the analogous process in NU-1000 but with a smaller entropic contribution (

**Table 5.10, Figure 5.25**). Due to the unique orientation of the linker's benzoate arms in NU-901 compared to NU-1000,<sup>183, 239, 240</sup> the framework environment surrounding the binding site may be slightly more disordered than that of NU-1000. Therefore, chemisorption of either species does not dramatically increase the system's overall disorder, ultimately resulting in a less favorable processes compared to those in NU-1000. Surprisingly, the chemisorption of glyphosate and ethylphosphonic acid in NU-901-NDC yield nearly identical parameters to those processes in parent NU-901 (**Figure 5.25**). Further DFT calculations to determine the lowest energy conformations of glyphosate coordinated to NU-901 revealed slight differences compared to NU-1000. In the diamond pore of NU-901, glyphosate does not significantly interact with the surrounding linkers just as in the hexagonal mesopore of NU-1000; however, the hydroxyl on the phosphonic acid is able to hydrogen bond to the node (**Figure 5.29**). When chemisorbed in the NU-901 c-pore, glyphosate is also able to hydrogen bond with a terminal ligand on the adjacent

node resembling the analogous site in NU-1000 (**Figure 5.6**). Accordingly, we suspect that noncovalent interactions available to glyphosate in the NU-901 c-pore play a less dominant role in the chemisorption because similar interactions are available in the mesopore, meaning that installing NDC minimally affects the overall thermodynamic profile of the process.

Interested in further understanding the role of linkers in the vicinity of the binding sites, we investigated the chemisorption of glyphosate and ethylphosphonic acid in NU-1200. The binding of glyphosate in NU-1200 is nearly as favorable as in NU-1000 as demonstrated by the very similar Gibbs free energy terms (**Table 5.2**). The significantly larger entropic contribution compared to NU-1000 compensates for the enthalpic penalty and corroborates the DFT-optimized structure that shows glyphosate and the surrounding linkers are too far apart to interact favorably (**Figure 5.6**). The chemisorption of ethylphosphonic acid in NU-1200 showed similar differences in thermodynamic parameters compared to NU-1000 (

**Table 5.10**). Exploration of chemisorption in different Zr-MOFs revealed that slight variations in structure can significantly impact the thermodynamics of the chemical process.

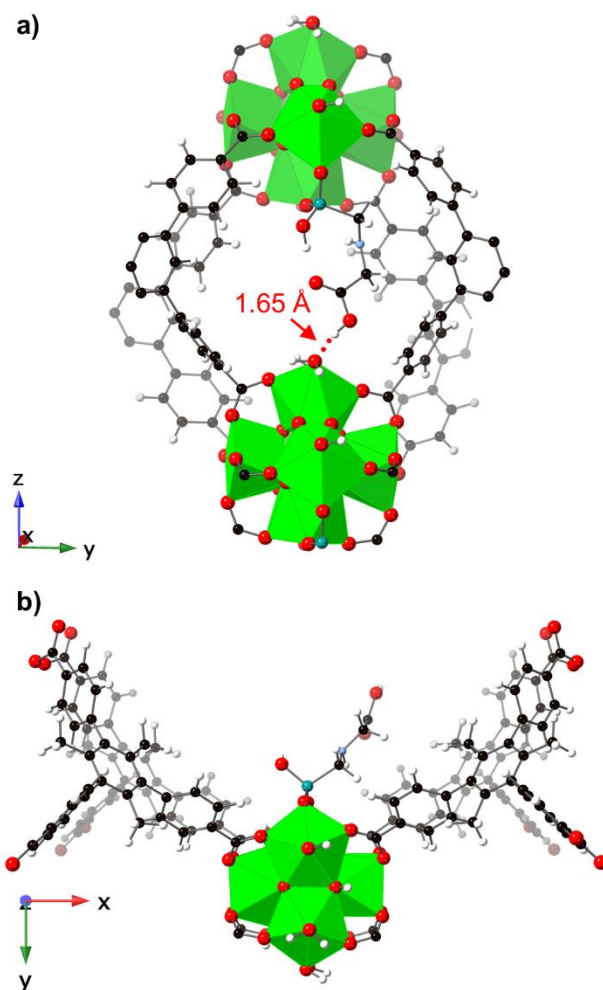


**Figure 5.6** Lowest energy conformations of glyphosate binding in a) the NU-901 c-pore and b) NU-1200.

### 5.7 Influence of Buffer Composition on Binding Thermodynamics

To more thoroughly investigate the suitability of ITC for the study of chemisorption in MOFs, we examined how the concentration of the buffer matrix influenced the thermodynamic parameters.<sup>241</sup> Specifically, we anticipated the acetate ions in the buffer may also coordinate to  $Zr_6$ -nodes thereby interfering with the desired chemisorption process. Upon increasing the acetate buffer concentration, the glyphosate chemisorption process became less favorable and the magnitude of the enthalpic contribution increased while the entropic contribution decreased (**Figure 5.7**). Each parameter correlates linearly with buffer concentration suggesting the buffer

molecules do interact with the MOF nodes (**Figure 5.26**). The binding association constant ( $K_a$ ) decreases with increasing buffer concentration primarily because glyphosate must compete with an increasing number of acetate ions for binding sites at the  $Zr_6$ -nodes. Similarly, the increased buffer concentration increases the overall disorder of the system; therefore, the increased disorder resulting from the ion-exchange processes occurring represents a smaller fraction of the system's total disorder. Moreover, in more concentrated media, the coordinating species on the node of NU-1000 likely include more acetate, and the more exothermic nature of the chemisorption process suggests displacing an acetate is easier energetically than displacing a water/hydroxyl pair. These results demonstrate that researchers must use the same buffer media if they want to confidently compare the thermodynamic parameters of adsorption for different analyte-MOF pairs.

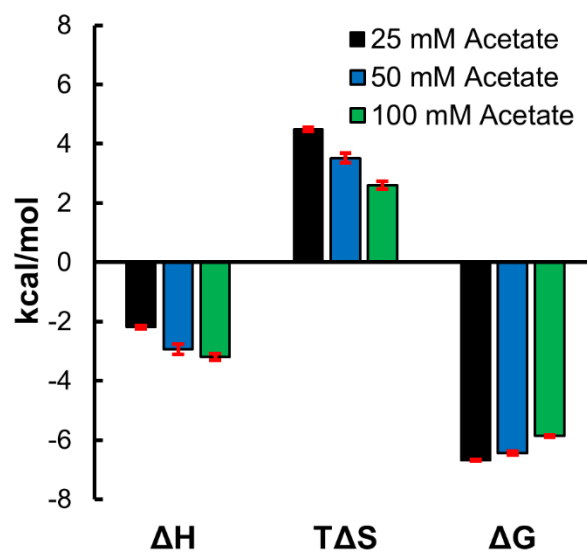


**Figure 5.7** Thermodynamic parameters of glyphosate (10 mM) binding to NU-1000 (1 mM) in various buffer concentrations. Error bars represent the standard deviation of triplicate measurements.

## 5.8 Chapter Conclusions

In summary, we have demonstrated the relevance of isothermal titration calorimetry (ITC) in characterizing liquid-phase chemisorption in MOFs. Specifically, our exploration of agrochemical sorption revealed that glyphosate coordinates to the node of Zr-MOFs through the phosphonic acid. Depending on the pore structure of the MOF, glyphosate's carboxylic acid may also be able to hydrogen bond to terminal ligands on adjacent nodes, thereby strengthening the analyte-MOF interaction and increasing the overall favorability of the chemisorption process. This work demonstrated that by blocking certain adsorption sites, we are able to evaluate the thermodynamic contributions from other sites and that slight variations in the framework environment surrounding a binding site influence affinity. Both of these results have implications in an array of MOF applications, particularly heterogeneous catalysis. ITC provides researchers with a more comprehensive description of adsorption thermodynamics and learnings from similar efforts will contribute to the rational design of next-generation sorbents. We envision the application of this technique in the MOF field will extend far beyond examining chemisorption to explore other valuable chemical processes.

## 5.9 Additional Information

### 5.9.1 Materials

All chemicals were purchased from commercial suppliers and used as received. In all experiments, water was Milli-Q (Millipore). Ethylphosphonic acid was purchased from Sigma, and glyphosate and ammonium glufosinate were purchased from ThermoFisher Scientific. Alfa Aesar™ 1M Acetate Buffer (pH 4.0) was purchased from ThermoFisher Scientific. The as-purchased P ICP standard was 1001 mg/g in 2% nitric acid, TraceCERT, and the Zr ICP standard

was 1000 mg/g in 2% nitric acid and 0.2% hydrofluoric acid. All gases were ultrahigh purity grade 5 gases from Airgas Specialty Gases.

### 5.9.2 MOF Syntheses

To synthesize NU-1000, 4,4',4'',4'''-(pyrene-1,3,6,8-tetrayl)tetrabenzoate (H<sub>4</sub>TBAPy) was synthesized according to the reported procedure.<sup>77</sup> The MOF was prepared according to an established procedure.<sup>183</sup> Briefly, ZrOCl<sub>2</sub>·8H<sub>2</sub>O (9.7 g, 30 mmol) and benzoic acid (200 g, 1.6 mol) were added to 600 mL of DMF in a 2 L glass bottle. The mixture was sonicated until clear and then heated for 1 h in a preheated oven at 100 °C. Similarly, H<sub>4</sub>TBAPy (4 g, 6 mmol) was added to 200 mL of DMF in a 500 mL glass bottle and heated for 1 h in a preheated oven at 100 °C. After cooling to room temperature, trifluoroacetic acid (TFA) (4 mL, 52 mmol) was added to the prepared Zr-solution. After sonicating for 15 min, the linker solution was added to the Zr-solution and then heated at 120 °C for 18 h. After cooling down to room temperature, the yellow powder was isolated by centrifugation (5 min, 7500 rpm) and washed with fresh DMF (~300 mL) three times for 2 h each. The resulting yellow powder was suspended in 1300 mL DMF in a 2 L glass jar and 50 mL of 8 M aqueous HCl was added. The mixture was heated in an oven at 100 °C for 18 h. After cooling to room temperature, the powder was washed with fresh DMF (~300 mL) three times for 2 h each and acetone (~300 mL) three times for 2 h each and soaked in acetone for additional 18 h. The NU-1000 powder was collected by centrifugation and dried in a vacuum oven at 80 °C for 2 h, and then thermally activated on a Smart VacPrep at 120 °C for 18 h.

To synthesize NU-901, 4,4',4'',4'''-(pyrene-1,3,6,8-tetrayl)tetrabenzoate (H<sub>4</sub>TBAPy) was synthesized according to the reported procedure.<sup>77</sup> NU-901 was synthesized according to an established procedure with slight modifications.<sup>242</sup> To a clean 100 mL glass jar, 4-aminobenzoic

acid (15.1 g, 0.110 mol) and DMF (40 mL) were added. After sonicating for 5 min, the jar was placed in an oven preheated to 80 °C for 30 min to fully dissolve the modulator. To the clear solution,  $\text{Zr}(\text{acac})_4$  (acac = acetylacetonate) (0.485 g, 0.995 mmol) was added. The mixture was sonicated for 5 min and placed in an oven preheated to 80 °C for 1 h. After cooling the solution to room temperature,  $\text{H}_4\text{TBAPy}$  (0.200 g, 0.3 mmol) was added to the jar. The solution was sonicated for 10 min and then distributed equally between five 8-dram vials. The vials were capped and placed in an oven preheated to 100 °C for 18 h. After cooling down to room temperature, the yellow powder was isolated by centrifugation (5 min, 7500 rpm) and washed with fresh DMF (~30 mL) three times for 2 h each. To remove monotonically bound 4-aminobenzoic acid, the resulting yellow powder (from all 5 vials) was suspended in 20 mL of DMF in a 250 mL glass jar. In a separate jar, a mixture of 8 M HCl (2.5 mL) and DMF (40 mL) was prepared. After swirling this solution, it was poured into the 250 mL jar containing the MOF. The mixture was sonicated for 5 min and then placed in an oven preheated to 80 °C for 18 h. After cooling to room temperature, the powder was washed with fresh DMF (~30 mL) three times for 2 h each and acetone (~30 mL) three times for 2 h each and soaked in acetone (30 mL) for additional 18 h. The NU-901 powder was collected by centrifugation and dried in a vacuum oven at 80 °C for 2 h, and then thermally activated on a Smart VacPrep at 120 °C for 18 h.

To synthesize NU-1200, 4,4',4''-(2,4,6-trimethylbenzene-1,3,5-triyl)tribenzoic acid (TMTB) was synthesized according to a reported procedure.<sup>243</sup> The MOF was synthesized as follows: TMTB linker (0.02 mmol, 10 mg) and  $\text{ZrOCl}_2 \cdot 8\text{H}_2\text{O}$  (17 mg, 0.07 mmol) were added to a 4 dram vial and dissolved in 2 mL of DMF. The mixture was then sonicated for 10 min. Then, TFA (150  $\mu\text{L}$ ) was added to the solution. After sonicating for 5 min, the solution was placed in an oven

preheated to 120 °C for 24 h. After cooling to room temperature, the MOF powder was isolated by centrifugation and washed three times with DMF (12 mL) for 10 min. The MOF powder was then dispersed in 12 mL of DMF in an 8-dram vial and 500  $\mu$ L of 4 M HCl was added. After sonicating the mixture for 5 min, the vial was placed in an oven preheated to 100 °C for 24 h. After cooling to room temperature, the MOF was isolated by centrifugation and washed three times with DMF (12 mL) for 1 h and three times with acetone (12 mL) for 1 h. The MOF powder was then soaked in acetone (12 mL) for 18 h overnight. The NU-1200 powder was collected by centrifugation and dried in a vacuum oven at 80 °C for 2 h, and then thermally activated on a Smart VacPrep at 120 °C.

SALI experiments were performed according to an established procedure.<sup>236</sup> Briefly, activated MOF (200 mg, 0.091 mmol) and 2,6-naphthalenedicarboxylic acid (79 mg, 0.37 mmol) were dispersed in 10 mL of DMF in an 8-dram glass vial. The mixture was sonicated for 15 min and then heated for 18 h in an oven at 80 °C. After cooling to room temperature, the powder was isolated by centrifugation (5 min, 7500 rpm). The powder was soaked three times in fresh DMF (12 mL) for 2 h. The yellow powder was then dispersed in 48 mL of fresh DMF and 2 mL of 8 M HCl were added to the mixture. After sonicating for 15 min, the vial was heated for 18 h in an oven at 60 °C. The powder was soaked three times in fresh DMF (40 mL) for 2 h and three times in acetone (40 mL) for 2 h. After soaking for 18 h in acetone, the MOF powder was isolated by centrifugation (5 min, 7500 rpm), dried in a vacuum oven at 80 °C, and finally thermally activated on a Smart VacPrep at 100 °C for 18 h. The NDC loading was determined by nuclear magnetic resonance (NMR) spectroscopy.

### 5.9.3 Physical Methods and Instrumentation

NU-901, NU-1000, and NU-1200 were prepared according to established procedures and as described above.<sup>183, 238, 242</sup> All MOFs were dried in an 80 °C vacuum oven for 2 h and then thermally activated at 120 °C under dynamic vacuum for 18 h on a Micromeritics Smart VacPrep instrument. Nitrogen adsorption-desorption isotherms were measured at 77 K on a Micromeritics TriStar II instrument. A carbon slit-pore model with a kernel, based on a molecular statistical approach, was used in the calculation of density functional theory (DFT)-calculated pore size distributions. Powder X-ray diffraction (PXRD) patterns were collected using a STOE STADI P diffractometer equipped with a CuK $\alpha$ 1 source and a 1D strip detector over the range of  $2^\circ \leq \theta \leq 30^\circ$ . ICP-OES data were obtained using a Thermo iCAP 7600 ICP Spectrometer. Standards (1 ppm–50 ppm) were prepared via serial dilution in 50 mM acetate buffer (pH 4) and 2% nitric acid.

Isothermal titration calorimetry (ITC) experiments were performed using a VP-ITC titration microcalorimeter (Malvern, MicroCal Inc.). All blank and sample solutions were degassed on a vacuum pump for 20 min. In an example titration, a solution of analyte (e.g. glyphosate) in aqueous buffer was titrated into the ITC sample cell containing a MOF suspension. All titration experiments were performed in aqueous buffer solutions with a pH of  $4.0 \pm 0.1$  under the following experimental conditions: reference power ( $10 - 15 \mu\text{cal s}^{-1}$ ), initial injection delay (600 s), stirring speed (697 rpm), feedback mode gain (high feedback), spacing between injections (300 s), and filter period (10 s). Individual experimental conditions are described in **Table 5.9**. Each titration experiment was performed in triplicate. The thermodynamic profile of each binding process was calculated by fitting the data with a single-site interaction model.

The maximum amount of phosphorus adsorbed per gram of NU-1000 was determined by exposing 4 mg ( $1.8 \times 10^{-6}$  mol) of MOF to 10 mL of an aqueous solution of glyphosate,

ethylphosphonic acid, or ammonium glufosinate (10 mM acetate buffer, pH 4).<sup>19</sup> Solutions with varying phosphorus concentrations were exposed to the MOF samples (**Table 5.4**, **Table 5.5**, **Table 5.6**). Samples were sonicated and allowed to soak for a designated time. Samples were then centrifuged to separate the MOF from the liquid, and 1 mL aliquots of supernatant were removed from the samples after 10, 30, 60 and 90 min and 24 h. MOF particulate which did not settle during centrifugation was removed from each sample by filtration using a 0.45  $\mu\text{M}$  PDVF syringe filter. To each sample, 6 mL of 2% nitric acid were added. The residual phosphorus concentration was determined by ICP-OES. The amount of phosphorus adsorbed by the MOF was determined by comparing the residual concentrations to the concentrations of identically prepared solutions not exposed to MOF. The amount of phosphorus uptake  $q$  in mg of phosphorus per gram of MOF was determined at each concentration and time point according to **Eqn. 1.1** as reproduced below:

$$q = \frac{(C_i - C_f)V}{m} \quad (1.1)$$

where  $C_i$  is the initial concentration ( $\text{mg L}^{-1}$ ),  $C_f$  is the final concentration at the time ( $\text{mg L}^{-1}$ ),  $V$  is the volume of solution exposed to sorbent (L), and  $m$  is the mass of the sorbent (g). The maximum uptake capacity,  $Q_m$  ( $\text{mg g}^{-1}$ ), and the Langmuir constant,  $K_L$  ( $\text{L mg}^{-1}$ ), which describes the overall affinity of the analyte for the binding site, were determined using a linear Langmuir fit as reported in **Eqn. 1.2**:

$$\frac{C_e}{q_e} = \left(\frac{1}{Q}\right) C_e + \frac{1}{K_L Q} \quad (1.2)$$

where  $C_e$  is the final equilibrium concentration after 24 h of exposure ( $\text{mg L}^{-1}$ ) and  $q_e$  is the equilibrium uptake after 24 h of exposure ( $\text{mg g}^{-1}$ ). All measurements were performed in duplicate.

The maximum amount of phosphorus adsorbed per gram of Zr-MOF (e.g. NU-1000, NU-901, NU-1200) was determined by exposing 4 mg of MOF to 10 mL of an aqueous solution of

glyphosate (10 mM acetate buffer, pH 4). Samples were exposed to solutions with various phosphorus concentrations (**Table 5.4**, **Table 5.7**, **Table 5.8**). Samples were sonicated and allowed to soak for a designated time. Samples were then centrifuged to separate the MOF from the liquid, and 1 mL aliquots of supernatant were removed from the samples after 10, 30, 60 and 90 min and 24 h. MOF particulate which did not settle during centrifugation was removed from each sample by filtration using a 0.45  $\mu\text{m}$  PDVF syringe filter. To each sample, 6 mL of 2% nitric acid were added. The residual phosphorus concentration was determined by ICP-OES. The amount of phosphorus adsorbed by the MOF was determined by comparing the residual concentrations to the concentrations of identically prepared solutions not exposed to MOF. The amount of phosphorus uptake  $q$  in mg of phosphorus per gram of MOF was determined at each concentration as previously described. Similarly, the maximum uptake capacity was determined using a linear Langmuir fit. All measurements were performed in duplicate.

Isothermal titration calorimetry (ITC) was used to explore the thermodynamic profile associated with the chemisorption of organophosphorus agrochemicals in Zr-MOFs in aqueous media. In all experiments, unless otherwise noted, solutions were prepared in 50 mM acetate buffer and adjusted to pH 4 using 0.1 M NaOH. Blank thermograms were collected for 1) the titration of buffer with an analyte solution and 2) the titration of a MOF suspension with buffer to confirm the buffer matrix did not interact with either of the titration components. Additionally, the enthalpy of dilution could then be subtracted from the thermograms collected for the titration of MOF with analyte. In a model experiment, a sample of NU-1000 (10.9 mg,  $5.0 \times 10^{-6}$  mol) was suspended in 5 mL of acetate buffer (50 mM, pH 4) and sonicated for 10 min. Similarly, glyphosate (67.6 mg,  $4.0 \times 10^{-4}$  mol) was dissolved in 50 mM acetate buffer (40 mL) and sonicated for 1 hr. The

glyphosate solution was then adjusted to  $\text{pH } 4.0 \pm 0.1$  with 0.1 M NaOH. All solutions were degassed for 20 min prior to loading in the instrument to remove all air bubbles.

To set up an experimental run, the reference cell was filled with a degassed acetate buffer solution (50 mM, pH 4) and the sample cell was filled with the MOF suspension. During the filling process, it is critical to avoid injecting an air bubble into either cell as this dramatically reduces the quality of the enthalpic data. Once the temperature of both cells equilibrated, the automatic syringe was filled with the degassed analyte solution, purged and refilled, and the outside rinsed three times with the buffer matrix. Before inserting the syringe into the sample cell, a Kimwipe was used to dab dry the outside. Upon completion of an experimental run the instrument was comprehensively cleaned according to the following procedure. The reference cell was rinsed with water three times and with the buffer matrix three times. The sample cell was cleaned with a Contrad 70 detergent solution (10% in water) three times for 10 min each. The sample cell was then rinsed five times with water or until no soap bubbles were observed in the syringe. Finally, the sample cell was rinsed three times with the matrix buffer solution.

To explore the effect of buffer composition on glyphosate chemisorption, we collected ITC thermograms in triplicate for the titration of glyphosate (10 mM) into NU-1000 (1 mM) in 25, 50, and 100 mM acetate buffer (pH 4). Additionally, to verify the stability of NU-1000 in these media, samples (40 mg) were soaked in 20 mL of 25, 50, and 100 mM acetate buffer solutions (pH 4) for 3 days. At the designated time, the MOFs were isolated by centrifugation and washed 3 times with water (20 mL) and three times with acetone (20 mL) for 30 min each. All samples were allowed to soak in acetone (20 mL) overnight. The samples were isolated by centrifugation and activated according to the procedure. Nitrogen adsorption-desorption isotherms were also collected at 77 K.

When performing DFT calculations, the initial structure of each MOF-adsorbate complex was generated using the MBAI tool ([github.com/snurr-group/mof-big-adsorbate-initializer](https://github.com/snurr-group/mof-big-adsorbate-initializer)), which was developed as part of this work and which extends the previous MAI tool ([github.com/snurr-group/mof-adsorbate-initializer](https://github.com/snurr-group/mof-adsorbate-initializer)) to work for bigger adsorbate molecules.<sup>244</sup> MBAI places the adsorbate in a reasonable location using classical molecular mechanics and Monte Carlo algorithms to avoid laborious and error-prone manual editing of the structures. In each case, two ligands (one water and one hydroxide) on two neighboring Zr atoms were replaced by the adsorbate (anion). Then, periodic density functional theory (DFT) calculations in the Vienna Ab initio Simulation Package (VASP, version 5.4.4)<sup>245, 246</sup> were employed to refine the structures. The Perdew-Burke-Ernzerhof (PBE)<sup>247</sup> density functional with D3 dispersion corrections (Becke-Johnson damping),<sup>248, 249</sup> a 520 eV plane-wave kinetic energy cutoff, the gamma-point for Brillouin-zone integration and the VASP-recommended projector-augmented wave (PAW)<sup>250</sup> potentials were used to describe the electronic structure. The atomic positions were relaxed using the conjugate gradient method until all forces were smaller than 0.05 eV/Å. The cell parameters were held fixed.

## MOF Characterization

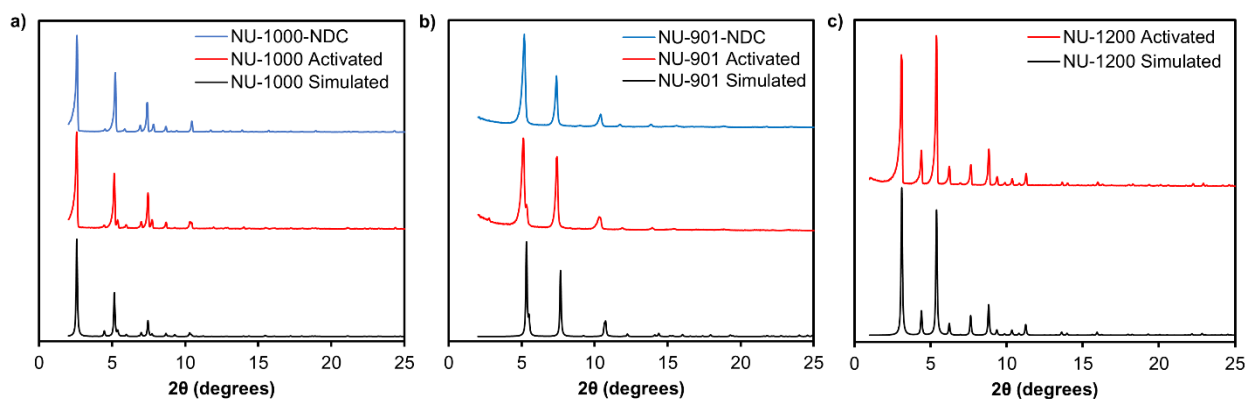


**Figure 5.8** PXR D patterns of a) NU-1000 and NU-1000-NDC, b) NU-901 and NU-901-NDC, and c) NU-1200.

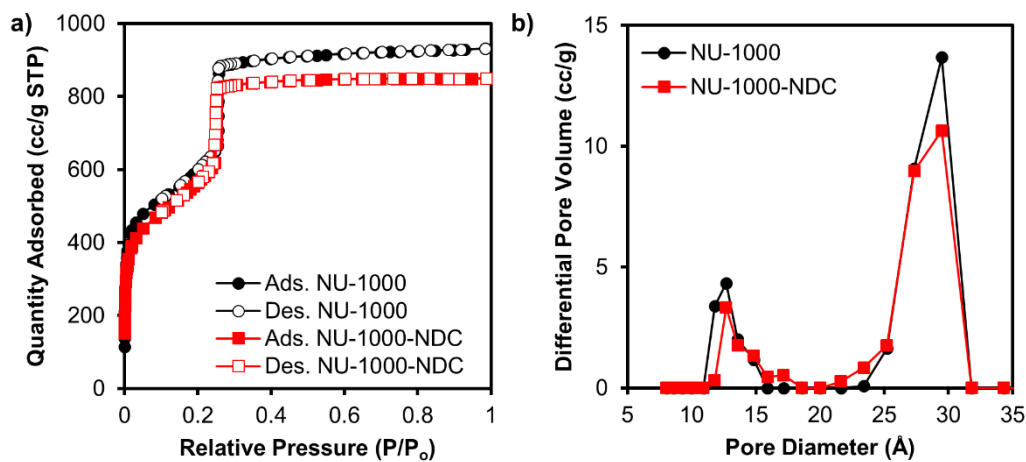


**Figure 5.9** a) Nitrogen adsorption-desorption isotherms at 77 K and b) DFT-calculated pore size distribution of NU-1000 and NU-1000-NDC.

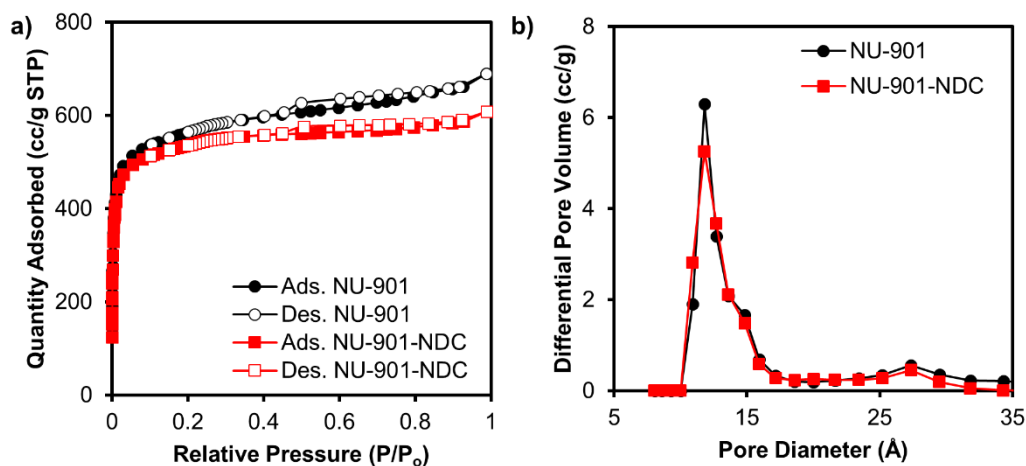


**Figure 5.10** a) Nitrogen adsorption-desorption isotherms at 77 K and b) DFT-calculated pore size distribution of NU-901 and NU-901-NDC.

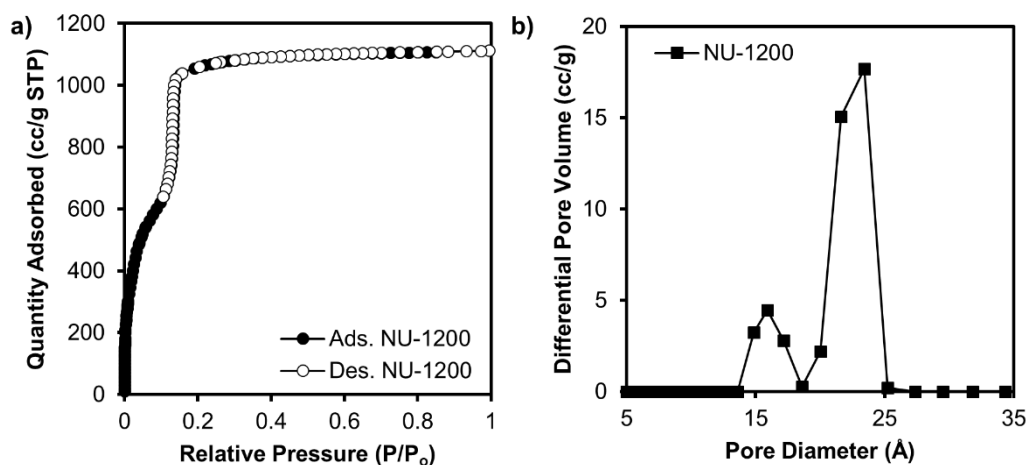


**Figure 5.11** a) Nitrogen adsorption-desorption isotherms at 77 K and b) DFT-calculated pore size distribution of NU-1200.

**Table 5.3** Nitrogen isotherm data, topologies, and node connectivity for  $Zr_6$ -MOFs.

MOF	Surface Area $m^2 g^{-1}$	Pore Size(s) $\text{\AA}$	Node Connectivity	Topology
NU-1000	2050	13, 30	8	csq
NU-1000-NDC	1870	13, 30	10	csq
NU-901	2180	12	8	scu
NU-901-NDC	2090	12	10	scu
NU-1200	2710	16, 23	8	the

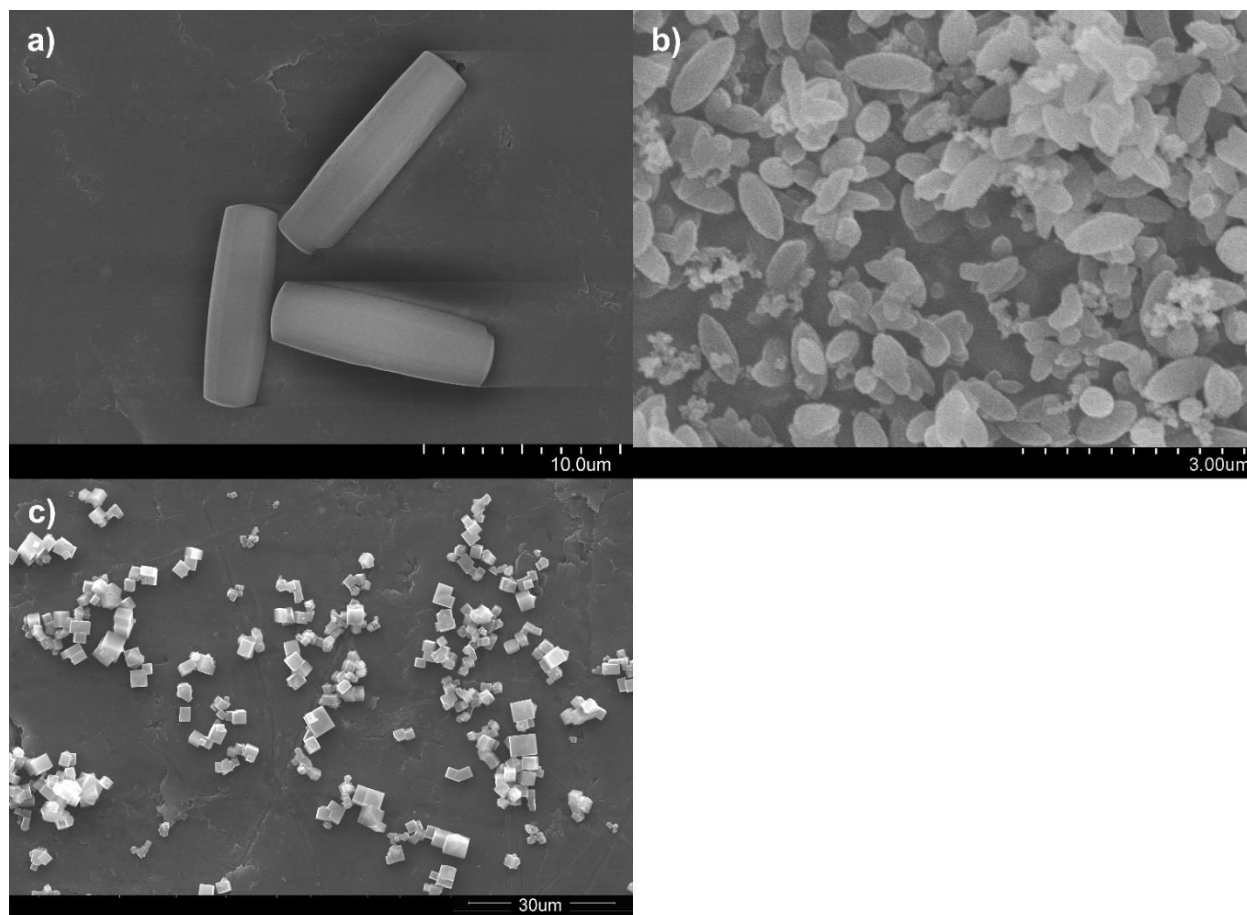


**Figure 5.12** SEM images of a) NU-1000, b) NU-901, and c) NU-1200.

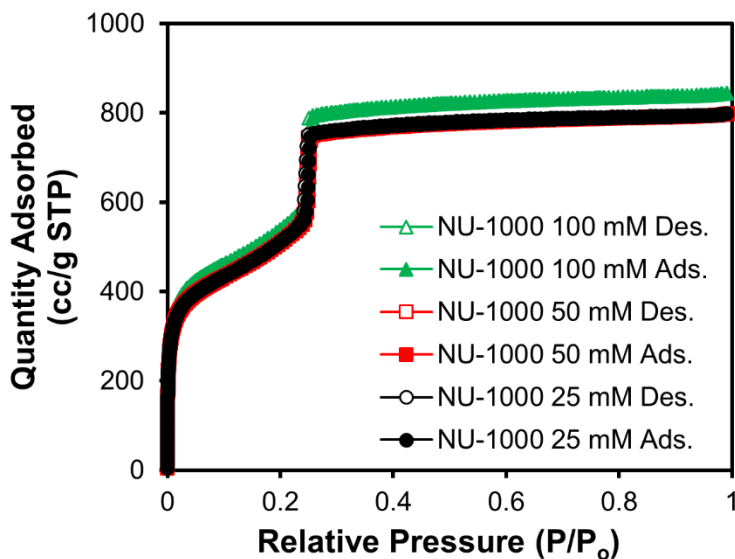


**Figure 5.13** Nitrogen adsorption-desorption isotherms at 77 K for NU-1000 soaked in 25 mM (black, BET area:  $1740 \text{ m}^2 \text{ g}^{-1}$ ), 50 mM (red, BET surface area:  $1740 \text{ m}^2 \text{ g}^{-1}$ ), and 100 mM (green, BET area:  $1850 \text{ m}^2 \text{ g}^{-1}$ ) acetate buffer (pH 4) for 3 days.

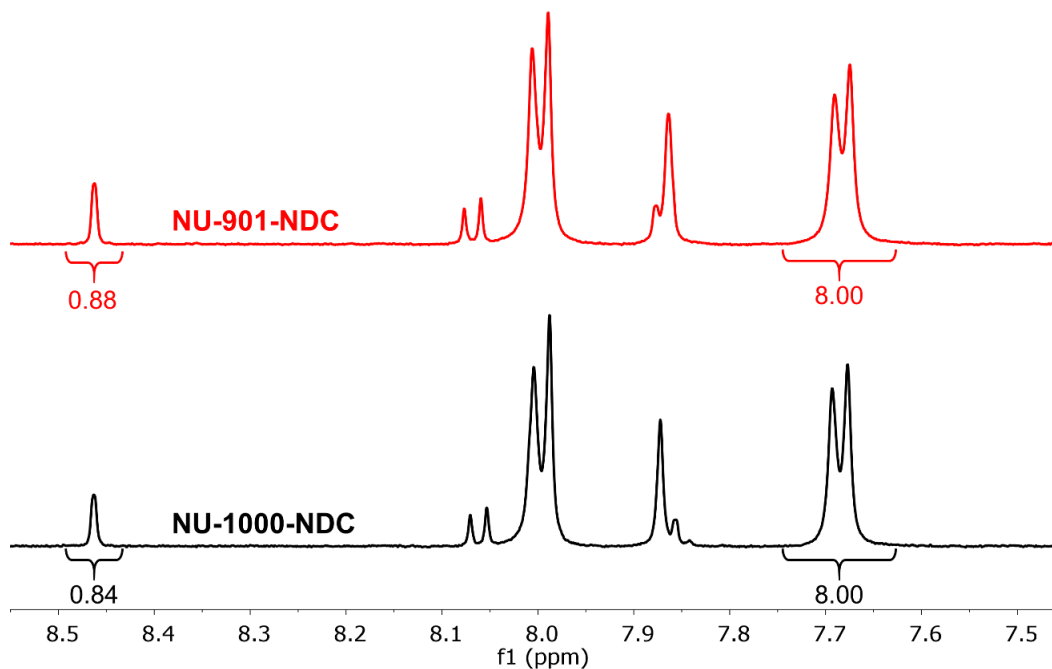


**Figure 5.14**  $^1\text{H}$  NMR spectra depicting the incorporation of 2,6-naphthalene dicarboxylic acid into the c-pores of NU-1000 (black trace) and NU-901 (red trace).

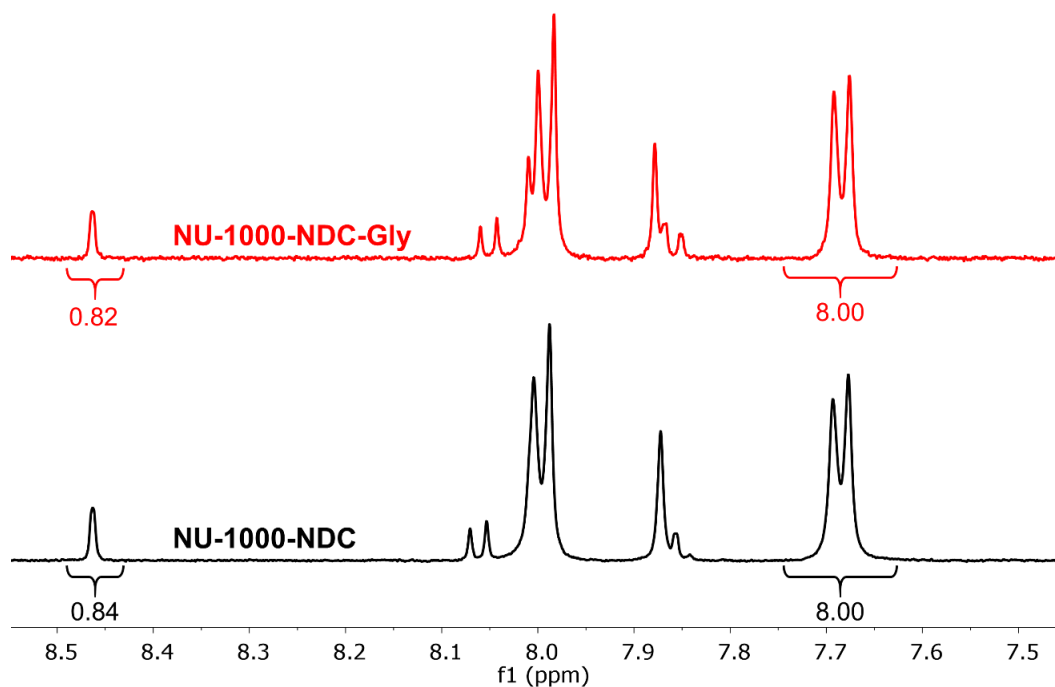


**Figure 5.15**  $^1\text{H}$  NMR spectra of NU-1000-NDC before (black trace) and after (red trace) exposure to glyphosate verifying that glyphosate does not substantially displace the 2,6-naphthalene dicarboxylic acid installed in the c-pores.

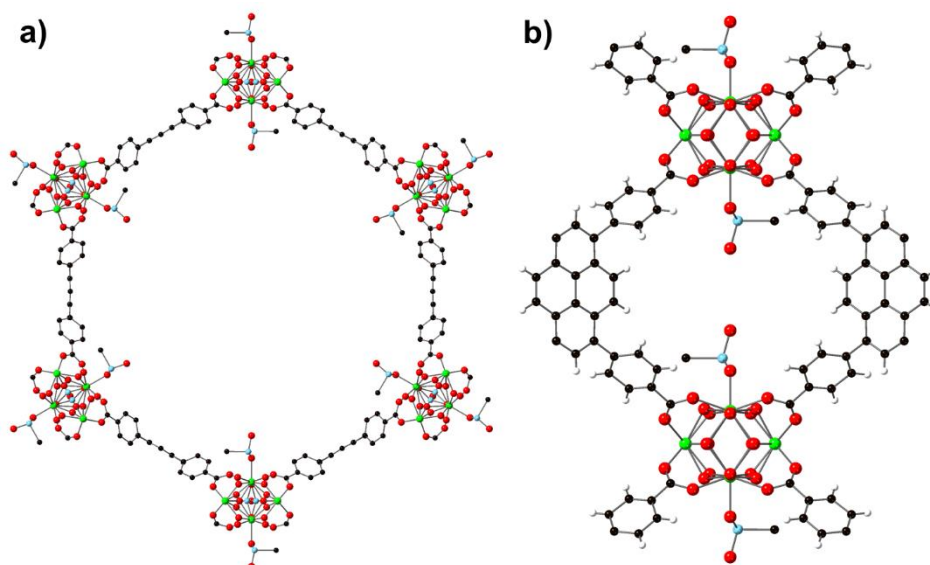


**Figure 5.16** Preliminary crystallographic data suggested 35% of the coordinated glycosate binds at sites directed into the a) hexagonal mesopore, while the remaining 65% binds at sites directed into the b) c-pore. Green, black, red, white, and blue spheres represent Zr, C, O, H, and P atoms, respectively.

## 5.9.4 Bulk Adsorption Experimental Data

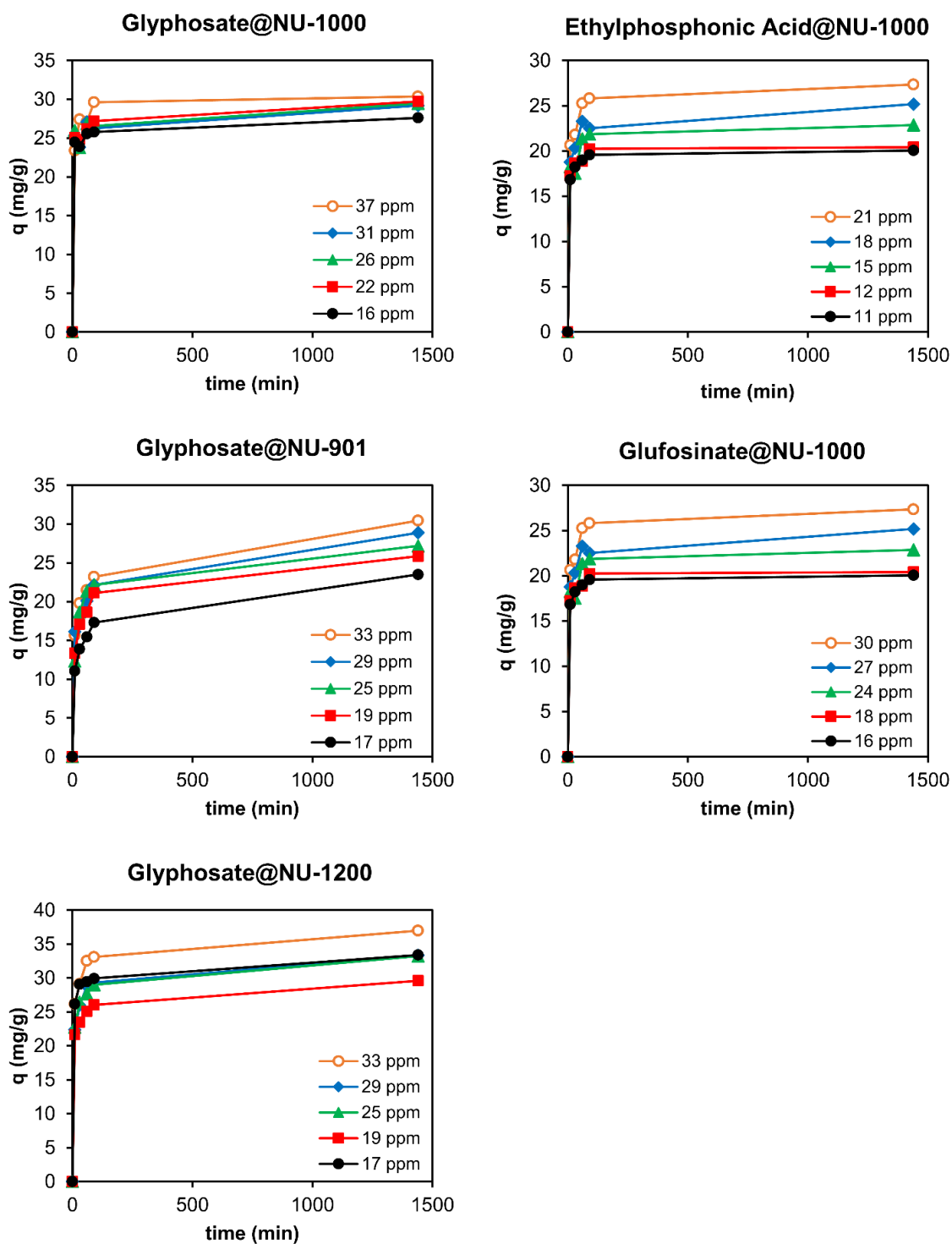


Figure 5.17 Plots of phosphorus uptake (mg/g) vs. time for each analyte-MOF pair.

**Table 5.4** Initial and final concentrations of glyphosate, uptake capacity of NU-1000, and respective partition coefficients.

Initial Concentration P (mg/L)	Final Concentration, C <sub>e</sub> P (mg/L)	Uptake, q <sub>e</sub> (mg/g)	Partition Coefficient, q <sub>e</sub> /C <sub>e</sub> (L/g)
16.4	5.39	27.6	5.13
21.7	9.85	29.7	3.02
25.9	14.1	29.5	2.10
30.7	19.0	29.2	1.54
36.5	24.4	30.4	1.25

**Table 5.5** Initial and final concentrations of ethylphosphonic acid, uptake capacity of NU-1000, and respective partition coefficients.

Initial Concentration P (mg/L)	Final Concentration, C <sub>e</sub> P (mg/L)	Uptake, q <sub>e</sub> (mg/g)	Partition Coefficient, q <sub>e</sub> /C <sub>e</sub> (L/g)
11.1	3.08	20.1	6.53
12.2	4.01	20.4	5.10
15.0	5.83	22.9	3.92
17.8	7.66	25.2	3.29
20.7	9.80	27.4	2.79

**Table 5.6** Initial and final concentrations of glufosinate, uptake capacity of NU-1000, and respective partition coefficients.

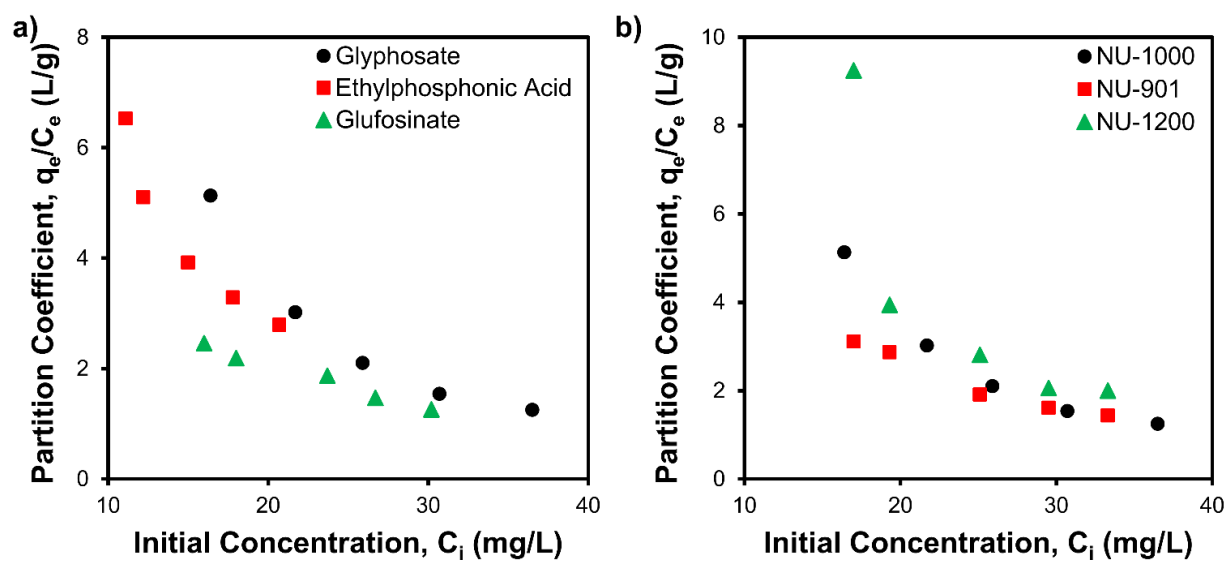
Initial Concentration P (mg/L)	Final Concentration, C <sub>e</sub> P (mg/L)	Uptake, q <sub>e</sub> (mg/g)	Partition Coefficient, q <sub>e</sub> /C <sub>e</sub> (L/g)
16.0	8.07	19.9	2.46
18.0	9.59	21.0	2.19
23.7	13.6	25.4	1.87
26.7	16.8	24.7	1.47
30.2	20.0	25.3	1.26

**Table 5.7** Initial and final concentrations of glyphosate, uptake capacity of NU-901, and respective partition coefficients.

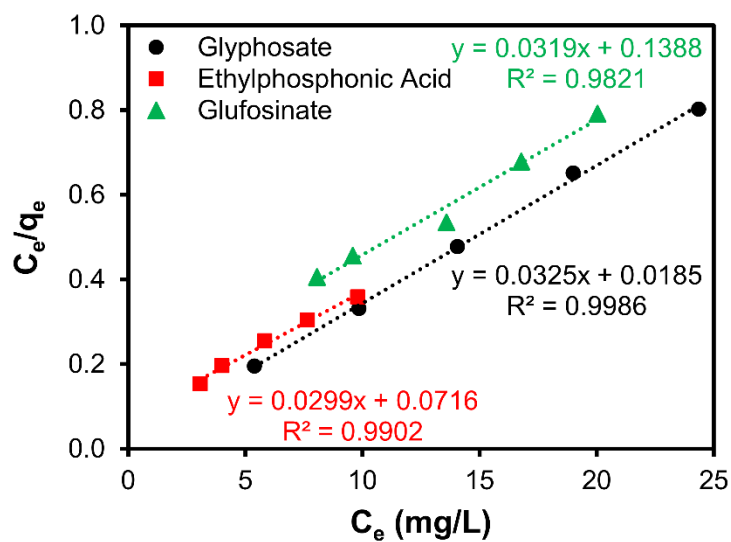
Initial Concentration P (mg/L)	Final Concentration, C <sub>e</sub> P (mg/L)	Uptake, q <sub>e</sub> (mg/g)	Partition Coefficient, q <sub>e</sub> /C <sub>e</sub> (L/g)
17.0	7.57	23.5	3.11
19.3	9.00	25.9	2.87
25.1	14.2	27.2	1.91
29.5	17.9	28.9	1.61
33.3	21.1	30.5	1.44

**Table 5.8** Initial and final concentrations of glyphosate, uptake capacity of NU-1200, and respective partition coefficients.

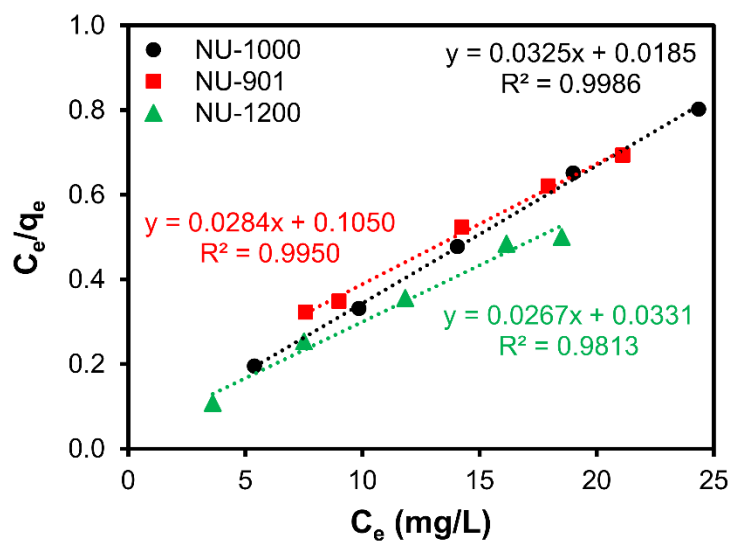
Initial Concentration P (mg/L)	Final Concentration, $C_e$ P (mg/L)	Uptake, $q_e$ (mg/g)	Partition Coefficient, $q_e/C_e$ (L/g)
17.0	3.61	33.4	9.25
19.3	7.51	29.6	3.94
25.1	11.8	33.2	2.81
29.5	16.2	33.4	2.06
33.3	18.5	37.0	2.00



**Figure 5.18** Relationship between initial phosphorus concentrations and partition coefficients for a) adsorption of analytes on NU-1000 and b) adsorption of glyphosate on NU-1000, NU-901, and NU-1200.



**Figure 5.19** Langmuir fits for the capture of various analytes by NU-1000.

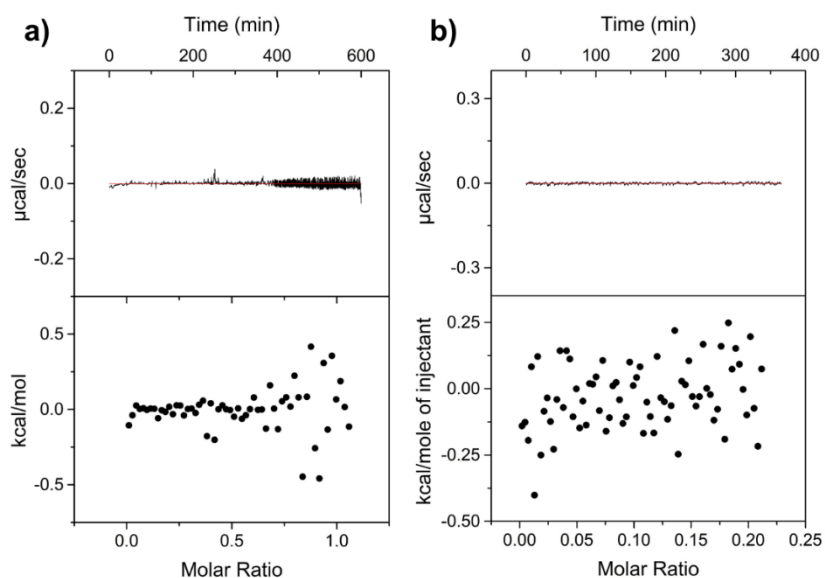


**Figure 5.20** Langmuir fits for the capture of glyphosate by NU-1000, NU-901, and NU-1200.

## 5.9.5 Isothermal Titration Calorimetry Experiments

**Table 5.9** Isothermal titration calorimetry measurement conditions.

Analyte	Analyte Concentration (mM)	MOF	MOF Concentration (mM)	Injection Volume ( $\mu\text{L}$ )	Acetate Buffer Matrix (pH 4)
glyphosate	10	NU-1000	1.0	4	50 mM
glyphosate	10	NU-1000	1.0	4	25 mM
glyphosate	10	NU-1000	1.0	4	100 mM
glyphosate	20	NU-1000-NDC	1.0	4	50 mM
glyphosate	10	NU-901	0.5	5	50 mM
glyphosate	20	NU-901-NDC	1.0	4	50 mM
glyphosate	20	NU-1200	1.0	4	50 mM
ethylphosphonic acid	10	NU-1000	1.0	5	50 mM
ethylphosphonic acid	20	NU-1000-NDC	1.0	4	50 mM
ethylphosphonic acid	10	NU-901	1.0	5	50 mM
ethylphosphonic acid	20	NU-901-NDC	1.0	5	50 mM
ethylphosphonic acid	20	NU-1200	1.0	4	50 mM
glufosinate	20	NU-1000	1.0	5	50 mM

**Figure 5.21** ITC thermograms for injections of a) glyphosate (10 mM, 50 mM acetate buffer, pH 4) into acetate buffer (50 mM, pH 4) and b) acetate buffer (50 mM, pH 4) into a NU-1000 suspension (1 mM, 50 mM acetate buffer, pH 4).

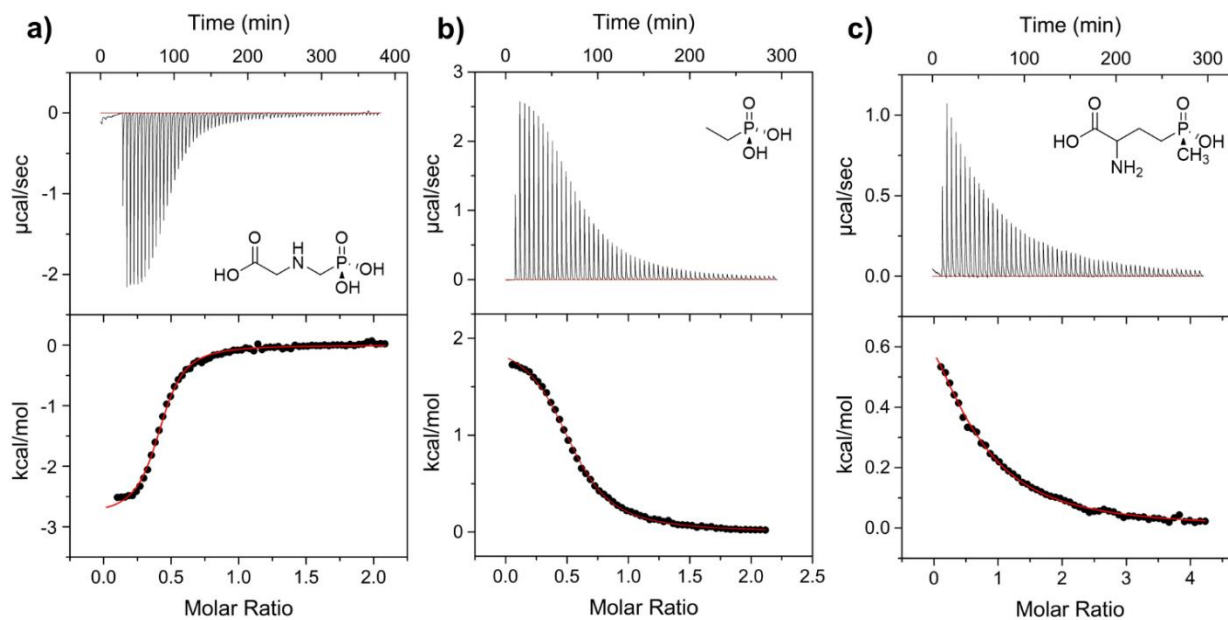


**Figure 5.22** ITC thermograms resulting from injections of a) glyphosate, b) ethylphosphonic acid, and c) glufosinate into a NU-1000 suspension (1 mM, 1.4 mL, 50 mM acetate buffer, pH 4).

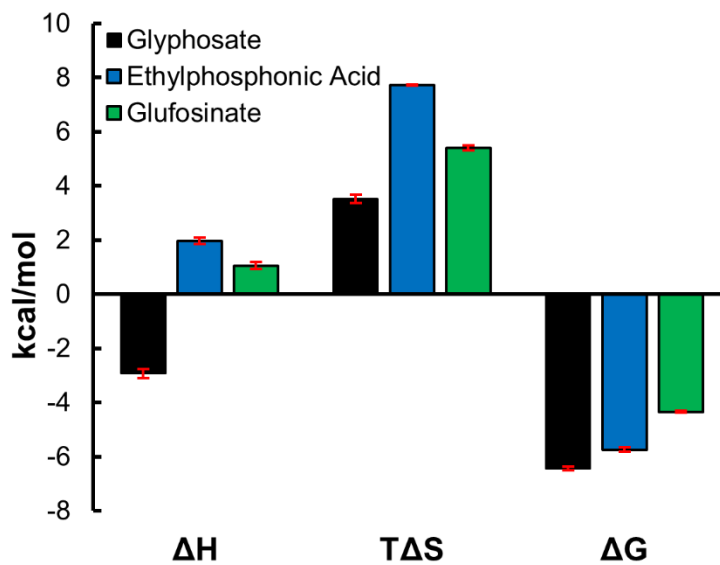


**Figure 5.23** Graphical representation of thermodynamic parameters of adsorption for various analytes in NU-1000.

**Table 5.10** The thermodynamic parameters of ethylphosphonic acid binding in NU-1000, NU-901, and NU-1200.

MOF	$\Delta H$ (kcal/mol)	$T\Delta S$ (kcal/mol)	$\Delta G$ (kcal/mol)
NU-1000	$2.0 \pm 0.1$	$7.72 \pm 0.03$	$-5.74 \pm 0.09$
NU-901	$1.4 \pm 0.1$	$6.8 \pm 0.1$	$-5.44 \pm 0.02$
NU-1200	$4.1 \pm 0.50$	$9.3 \pm 0.5$	$-5.18 \pm 0.07$

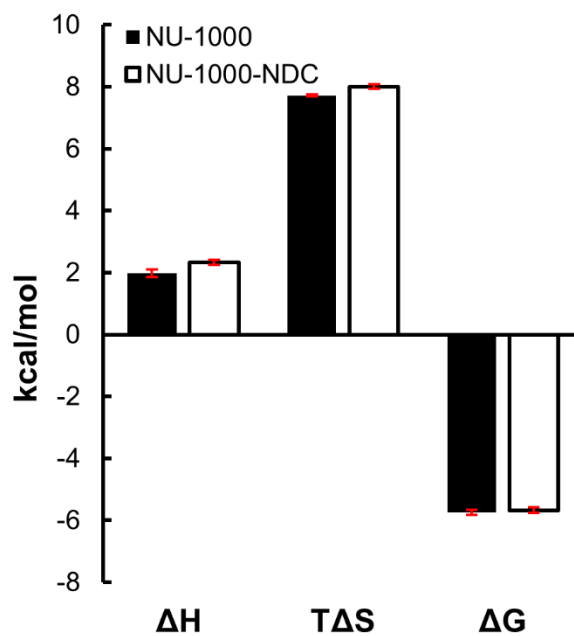


**Figure 5.24** Thermodynamic parameters of ethylphosphonic acid binding in NU-1000 and NU-1000-NDC.

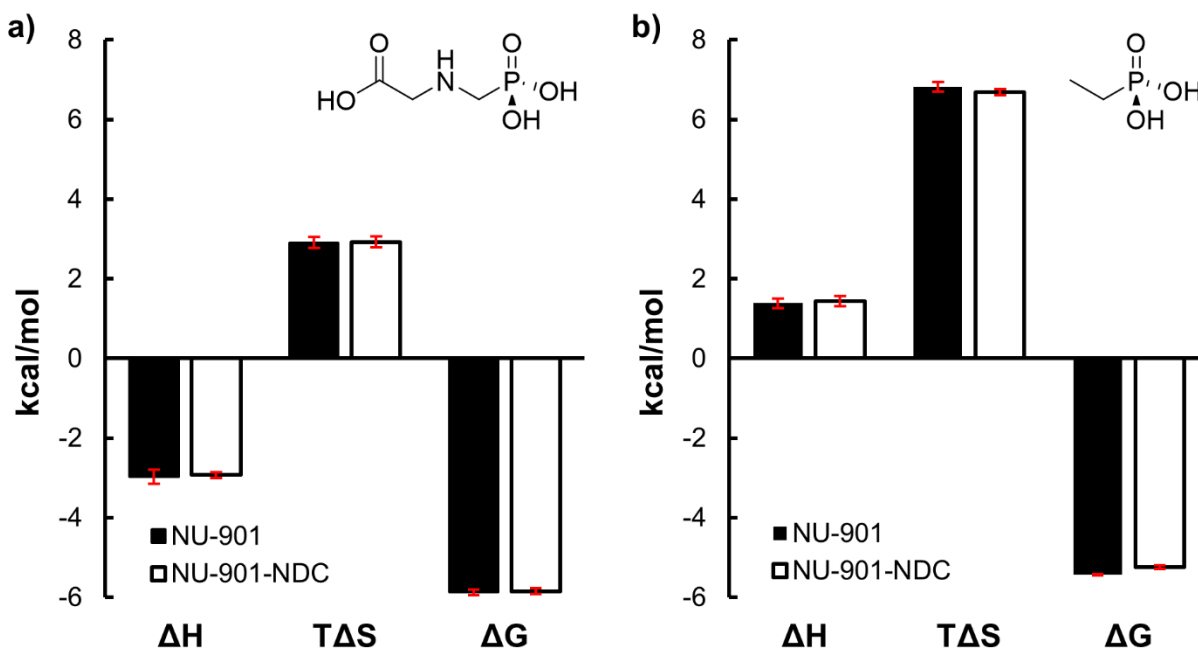


**Figure 5.25** Thermodynamic parameters of a) glyphosate and b) ethylphosphonic acid binding in NU-901 and NU-901-NDC.

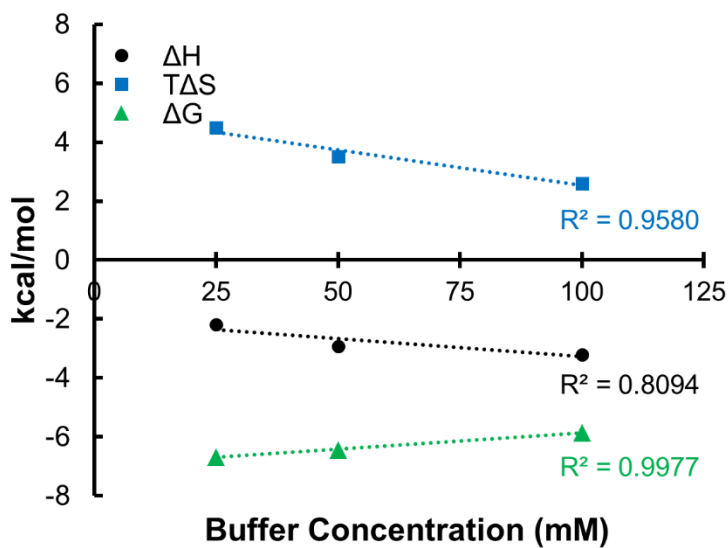


**Figure 5.26** Scatter plot demonstrating the linear relationship between the thermodynamic parameters ( $\Delta H$ ,  $T\Delta S$ , and  $\Delta G$ ) of glyphosate binding in NU-1000 and buffer concentration.

### 5.9.6 DFT Energy-Minimized Structures

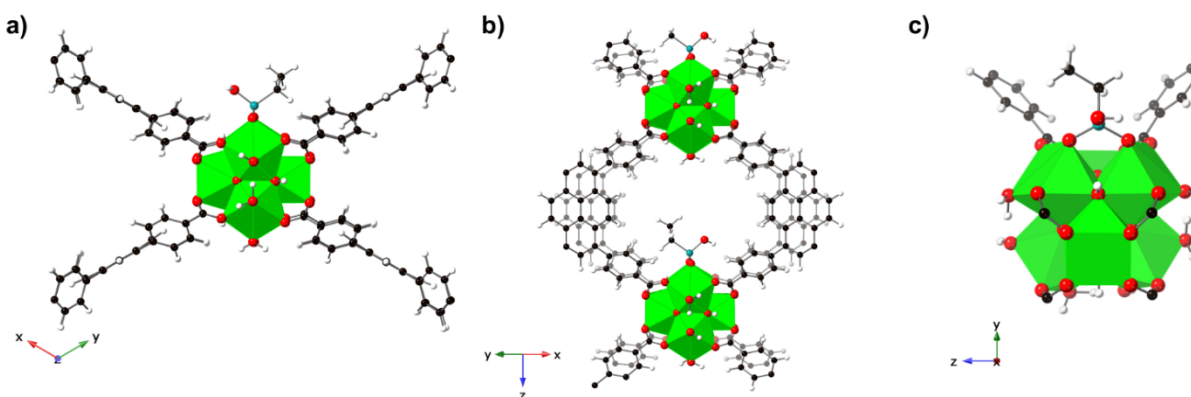


**Figure 5.27** Lowest energy structural conformations of ethylphosphonic acid binding in a) the NU-1000 mesopore and b and c) the NU-1000 c-pore.

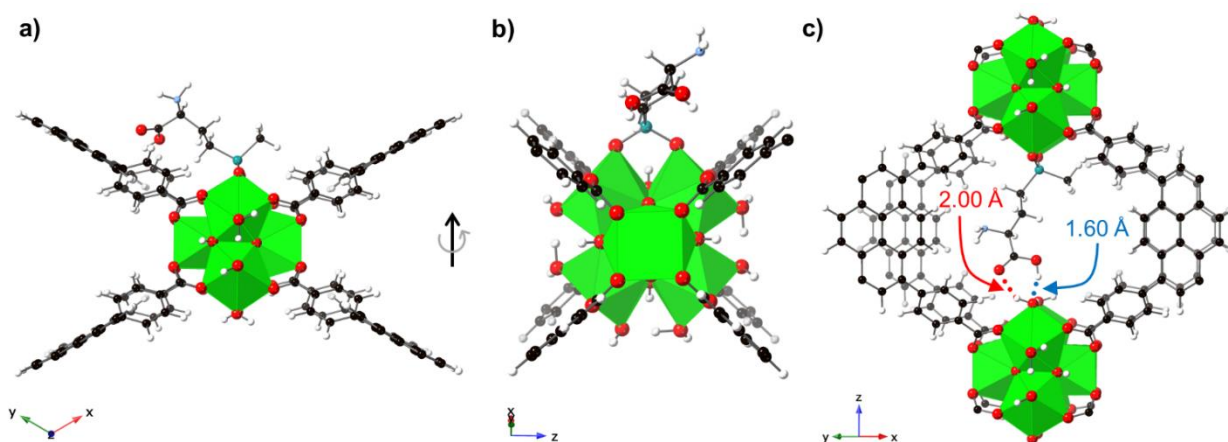


**Figure 5.28** Lowest energy structural conformations of glufosinate binding in the NU-1000 mesopore a) looking down the c-axis and b) rotated 90° around the axis shown and c) in the NU-1000 c-pore.

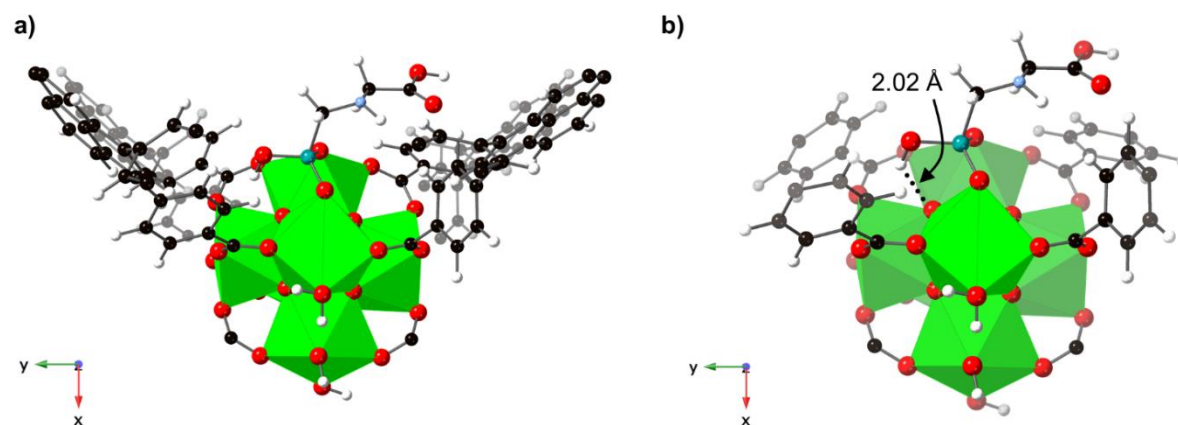


**Figure 5.29** Lowest energy structural conformation of a) glyphosate binding in the diamond pore of NU-901 and b) trimmed figure of same conformation to show hydrogen bonding.

## Chapter 6. Thermochemical Investigation of Oxyanion Coordination in a Zirconium-based Metal–Organic Framework

Portions of this chapter appear in the following manuscript:

**Drout, R.J.**; Gaidimas, M.A.; Farha, O.K. Thermochemical Investigation of Oxyanion Coordination in a Zirconium-based Metal–Organic Framework. *submitted*.

## 6.1 Chapter Summary

Porous materials possess high internal surface areas and void fractions that make them valuable in several applications including gas storage, heterogeneous catalysis, and water purification. Despite the plentiful effort allocated to porous materials research annually, few methods exist to directly monitor and characterize chemical events occurring within a pore's confines. The crystalline nature of zeolites, covalent organic frameworks (COFs), and metal–organic frameworks (MOFs) permit structural characterization by X-ray diffraction; yet, quantifying the thermodynamics of chemical processes and transformations remains tedious and error-ridden. Herein, we employ isothermal titration calorimetry (ITC) to determine the full thermodynamic profile of oxyanion adsorption in a zirconium-based MOF, NU-1000. To further validate this method, which we recently introduced to the field, we replicated ITC experiments as bulk adsorption measurements to demonstrate the correlation between the extracted stoichiometric parameter from ITC thermograms and the MOF uptake capacity. Moreover, based on the calculated association constants, we accurately predicted which analytes might be able to displace others and monitored the exchange processes by titrating oxyanion-functionalized MOF samples with a more strongly binding analyte.

## 6.2 Evolution of Studying Adsorption in Porous Materials

Humans have leveraged the properties of porous materials for millennia. The ancient Greeks, including Hippocrates (b. 460 BC d. 370 BC), demonstrated the therapeutic properties of activated carbon, and during World War I, this same material was the active component of gas masks protecting armed forces from chlorine, phosgene, and mustard gas exposure.<sup>251</sup> Today, consumers find activated carbon in their Brita filters,<sup>252</sup> kitty litters,<sup>253</sup> and even in their cosmetics.<sup>254</sup> In parallel with their adsorptive properties, the extensive surface areas of porous materials also

provide abundant anchoring sites for catalytically active species.<sup>255</sup> Such heterogeneous catalysts dominate the catalyst industry owning greater than 70% of the global market which facilitates nearly 90% of all commercial chemical transformations.<sup>256</sup> Such myriad applications evidence the value of intrinsic porosity, yet the chemical events occurring within these cavities remain largely veiled.

The discovery of natural and synthetic zeolites,<sup>257-260</sup> and more recently, metal–organic frameworks (MOFs),<sup>261, 262</sup> covalent organic frameworks (COFs),<sup>263</sup> porous organic polymers,<sup>264, 265</sup> and hydrogen-bonded organic frameworks (HOFs),<sup>266-268</sup> introduced permanently porous materials that were also crystalline. Bulk analyses, applicable in the study of both amorphous and crystalline samples, can reveal details regarding a material’s adsorption capacity, adsorption kinetics, and catalytic activity and kinetics; however, precise atomic-level structural characterization is only possible for crystalline materials.<sup>269</sup> When researchers can isolate diffraction-quality single-crystals, they can precisely determine the atomic connectivity of the parent lattice and, in many instances, subsequent host-guest interactions (e.g., adsorbate-sorbent, active center-support, etc.).<sup>270-272</sup> Moreover, methods such as Rietveld refinement<sup>273, 274</sup> and difference envelope density<sup>275</sup> rely on powder X-ray diffraction data and allow for the structural examination of a broader set of powder crystalline materials, while in-sequence PXRD may permit structural characterization of guest loaded samples.<sup>276</sup> Beyond their facile characterization, MOFs, comprised of inorganic nodes and organic linkers, offer unprecedented pre- and post-synthetic tunability owing to the wide variety of building blocks available.<sup>153, 261, 262, 277-279</sup> Moreover, exchangeable structural motifs afford a platform material useful for systematically exploring structure-property relationships.<sup>280-282</sup>

Since their advent, MOFs have shown promise for a range of applications including gas storage and delivery,<sup>283</sup> heterogeneous catalysis,<sup>284, 285</sup> and liquid phase adsorption<sup>110, 286</sup> among others.<sup>287</sup> The well-defined pores and spatially isolated binding sites inherent to these frameworks often directly influence a material's performance in a targeted application. Specifically, several teams have demonstrated that interactions at MOF nodes are relevant in the extraction of analytes from aqueous media<sup>73, 74, 288</sup> and in the post-synthetic modification of parent frameworks primarily for the installation of catalytic species.<sup>9, 124, 289-293</sup> Despite the importance of chemical events occurring at MOF nodes, researchers have validated few techniques beyond crystallographic methods for the study of such interactions.

With the aim of filling this gap, we recently demonstrated the use of isothermal titration calorimetry (ITC) for studying adsorption processes in MOFs from aqueous media.<sup>225, 294</sup> ITC allows for the direct quantification of the enthalpy, entropy, and Gibbs free energy changes associated with an adsorption event in a single experiment.<sup>295</sup> Briefly, an isothermal titration calorimeter consists of two cells, a reference cell and a sample cell, and following each injection of titrant, the instrument records the heat change required to bring the sample cell back into thermal equilibrium with the reference cell. In a typical experiment, a MOF suspension occupies the sample cell, and the syringe titrates the desired analyte while stirring at a fixed speed. Our previous work demonstrated that slight changes in the adsorbate chemical structure in addition to the microenvironment surrounding the binding site produced small, but distinguishable differences in the thermodynamic profiles of adsorption.<sup>225, 294</sup> Drawing on that work and our extensive collection of studies exploring adsorption in MOFs using bulk methods, we became interested in evaluating how the identity of an oxyanion's central atom influences its adsorption thermodynamic profile

when coordinating to a MOF node. Broadly, we sought to draw parallels between the thermodynamic parameters quantified by ITC and those extracted from bulk adsorption.

Owing to the recent implementation of ITC for the study of binding events in MOFs,<sup>225, 294, 296</sup> we elected to focus our study on NU-1000, a chemically and thermally robust zirconium MOF, comprising  $Zr_6O_8$ -nodes and tetratopic pyrene-based linkers (**Figure 6.1** and **Figure 6.5**).<sup>183, 297</sup> The framework displays the **csq** topology and features a mesoporous one-dimensional (1D) hexagonal channel ( $\sim 30$  Å) and a microporous 1D triangular channel ( $\sim 12$  Å). Between two adjacent nodes, parallel to the 1D channels, is a micropore often termed the c-pore ( $\sim 10$  Å, **Figure 6.5**). Each  $Zr_6$ -node coordinates to carboxylate groups from eight distinct linkers. Four pairs of labile water/hydroxyl ligands ( $-OH_2$ ,  $-OH$ ) balance the charge on each node. Our research group and several others have demonstrated that these ligands can be displaced by oxyanions and carboxylates among other functionalities demonstrating the adsorption capabilities of MOFs as well as their facile and valuable post-synthetic tunability. In this work, we assess the thermodynamic parameters of oxyanions of sulfur, selenium, phosphorus, and arsenic coordinating to the  $Zr_6$ -node of NU-1000.

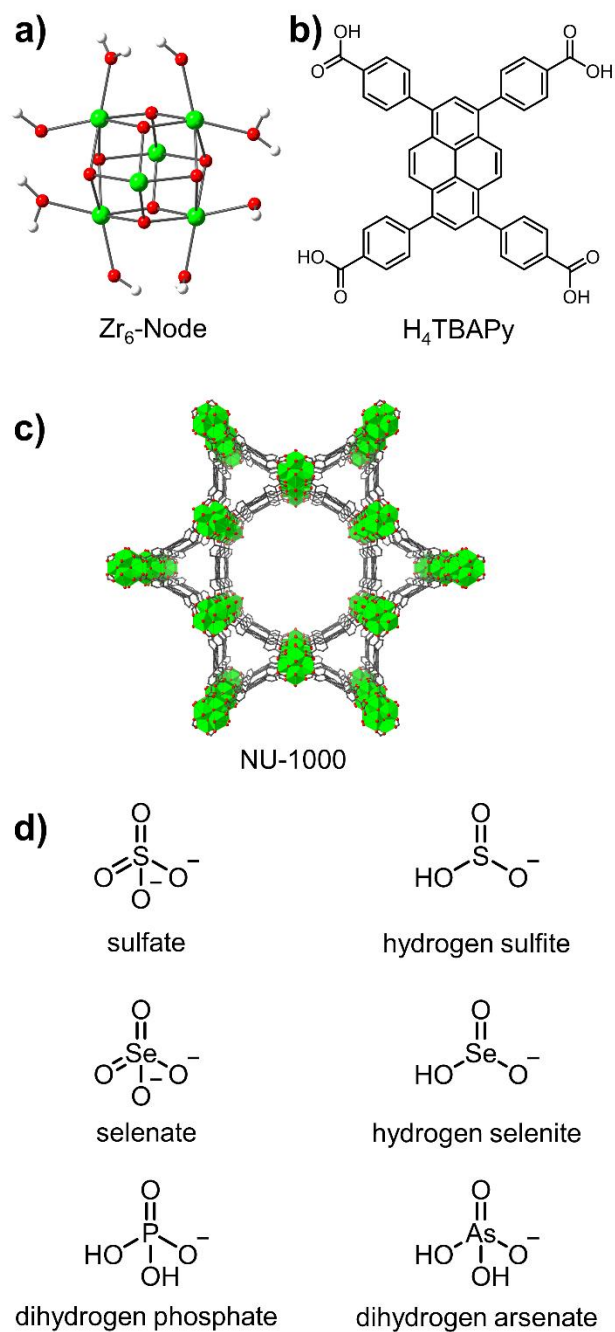


**Figure 6.1** Structures of a) the Zr<sub>6</sub>-node showing the proton topology, b) the tetratropic pyrene-based linker H<sub>4</sub>TBAPy, c) the **csq** topology characteristic of NU-1000, and d) the sulfur, selenium, phosphorus, and arsenic oxyanions present in aqueous media (pH 5) examined in this thermochemical investigation.

### 6.3 NU-1000 Characterization

We first synthesized NU-1000 according to our established procedure.<sup>183</sup> To ensure the availability of coordination sites, we performed an additional acid activation (two in total) to remove all residual benzoic acid modulator coordinated to the node. Acid digested samples analyzed by NMR demonstrated the complete removal of residual benzoic acid, while analysis of samples digested in base indicated ~2.4 formate ions coordinated to each node (**Figure 6.6** and **Figure 6.7**). Powder X-ray diffraction patterns confirmed the phase purity of the bulk MOF powder (**Figure 6.8**) and N<sub>2</sub> adsorption-desorption isotherms and the associated DFT-calculated pore size distributions demonstrated the MOF possessed the characteristic porosity of NU-1000 (**Figure 6.9**).

Considering isothermal titration calorimetry (ITC) measurements are highly sensitive to even minor pH mismatches between solutions, we elected to perform our experiments in acetate buffer (10 mM, pH 5) which has one of the smallest ionization enthalpies recorded.<sup>298</sup> Extensive research has demonstrated that NU-1000 retains its crystallinity and porosity when exposed to aqueous media, therefore we were confident we could proceed.<sup>206, 294</sup> Iterative parameter optimization experiments revealed that adsorption enthalpies were distinguishable and reproducible for 1 mM NU-1000 suspensions. We envisioned that acetate ions may be able to coordinate to the MOF node and determined via NMR that on average 1.4 ( $\pm 0.3$ ) acetate ions coordinated to each node after soaking overnight in buffer. This suggests that each node could accommodate approximately two additional oxyanions, assuming no acetate ions are displaced; however, we hypothesized that strongly coordinating ions would likely displace bound acetate and formate ions.

## 6.4 Adsorption of Sulfur Oxyanions

Previous research has demonstrated that sulfur- and phosphorus-containing oxyanions readily coordinate to the  $Zr_6$ -node offering a reasonable starting point for this work.<sup>74, 75, 124, 299</sup> In aqueous media at pH 5, the sulfur(VI) oxyanion exists as the divalent  $SO_4^{2-}$  species, while S(IV) exists as hydrogen sulfite or  $HSO_3^-$ . These charge differences led us to hypothesize that sulfate would interact more strongly with the node and therefore, record a higher association constant and stoichiometric parameter. We however, observed that adsorption of both anions produces nearly identical thermograms from which we extracted quite similar thermodynamic parameters (**Table 6.1**, **Figure 6.2**, **Figure 6.11**, and **Figure 6.12**). In both instances, adsorption was thermodynamically favored as demonstrated by the negative Gibbs free energy term calculated from the positive association constants ( $K_a$ ), and proceeded via exothermic processes, therefore, yielding positive entropic terms. To further explore these results, we replicated the titration conditions in the bulk and analyzed the supernatant of the solution exposed to MOF with inductively coupled plasma optical emission spectroscopy (ICP-OES). By comparing the concentration of sulfur in the supernatant to that in a solution not exposed to MOF, we determined the sulfur uptake per  $Zr_6$ -node. Indeed, we found the sulfite and sulfate loadings quantified by ICP-OES were nearly identical paralleling those extracted from ITC (**Table 6.3**). This correlation between parameters determined via ITC and bulk adsorption experiments further supports our previous observation of the near linear relationship between the respective association constants calculated from the two methods and advances our understanding of the applicability of ITC for studying adsorption in porous materials.<sup>294</sup>

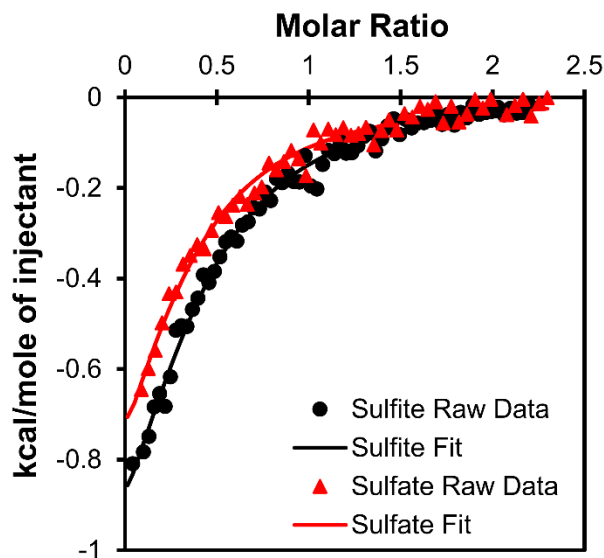


**Figure 6.2** Single-site model fitting of integrated heats of adsorption for each injection of hydrogen sulfite ( $\text{HSO}_3^-$ , black) and sulfate ( $\text{SO}_4^{2-}$ , red) demonstrate that adsorption of both analytes on NU-1000 produces similar thermodynamic profiles.

**Table 6.1** Thermodynamic parameters of adsorption for various analytes in NU-1000.

MOF	Analyte	n	$K_a$ ( $\times 10^3 \text{ M}^{-1}$ )	$\Delta G$ (kcal/mol)	$\Delta H$ (kcal/mol)	$T\Delta S$ (kcal/mol)
NU-1000	hydrogen sulfite	0.35 ( $\pm 0.06$ )	3.44 ( $\pm 0.07$ )	-4.82 ( $\pm 0.01$ )	-1.6 ( $\pm 0.1$ )	3.2 ( $\pm 0.1$ )
NU-1000	sulfate	0.35 ( $\pm 0.05$ )	3.2 ( $\pm 0.2$ )	-4.77 ( $\pm 0.04$ )	-1.3 ( $\pm 0.2$ )	3.5 ( $\pm 0.3$ )
NU-1000	hydrogen selenite	0.64 ( $\pm 0.07$ )	12.8 ( $\pm 0.8$ )	-5.59 ( $\pm 0.04$ )	-1.55 ( $\pm 0.06$ )	4.05 ( $\pm 0.03$ )
NU-1000	selenate	0.45 ( $\pm 0.04$ )	4.5 ( $\pm 0.4$ )	-4.98 ( $\pm 0.06$ )	-0.63 ( $\pm 0.04$ )	4.36 ( $\pm 0.03$ )
NU-1000	dihydrogen phosphate	0.60 ( $\pm 0.09$ )	9.5 ( $\pm 0.2$ )	-5.41 ( $\pm 0.01$ )	1.27 ( $\pm 0.08$ )	6.7 ( $\pm 0.1$ )
NU-1000	dihydrogen arsenate	0.22 ( $\pm 0.01$ )	200 ( $\pm 20$ )	-7.2 ( $\pm 0.1$ )	-0.22 ( $\pm 0.07$ )	6.99 ( $\pm 0.01$ )
		0.40 ( $\pm 0.01$ )	7 ( $\pm 1$ )	-5.2 ( $\pm 0.1$ )	0.60 ( $\pm 0.07$ )	5.81 ( $\pm 0.06$ )
NU-1000-Se	dihydrogen phosphate	0.31 ( $\pm 0.01$ )	18.0 ( $\pm 0.3$ )	-5.81 ( $\pm 0.01$ )	0.94 ( $\pm 0.07$ )	6.75 ( $\pm 0.06$ )
NU-1000-S	dihydrogen phosphate	0.20 ( $\pm 0.04$ )	7.1 ( $\pm 0.5$ )	-5.22 ( $\pm 0.04$ )	2.80 ( $\pm 0.01$ )	8.05 ( $\pm 0.06$ )

## 6.5 Adsorption of Selenium Oxyanions

Surprised that we did not observe significant differences in the uptake of sulfate and hydrogen sulfite, despite their difference in charge, we elected to examine the analogous selenium oxyanions, selenate ( $\text{SeO}_4^{2-}$ ) and hydrogen selenite ( $\text{HSeO}_3^-$ ). Significant research, including work in our lab, has focused on regulating selenium levels in freshwater and drinking water given this essential nutrient has the narrowest intake window between deficiency and toxicity in humans. In this study, we collected thermograms for hydrogen selenite and selenate adsorption in NU-1000 and observed reproducible differences in the stoichiometric terms, yet relatively similar thermodynamic parameters (**Figure 6.3**). NU-1000 records a higher uptake of hydrogen selenite compared to selenate in both ITC and bulk adsorption measurements (**Table 6.1** and **Table 6.3**, **Figure 6.3**, **Figure 6.13**, and **Figure 6.14**). The calculated association constant for hydrogen selenite is three times that of selenate and nearly four times that of sulfate and hydrogen sulfite (**Table 6.1**). Previous reports of Se(IV) and Se(VI) capture in Zr-MOFs similarly indicated higher uptake of selenite compared to selenate; however, this work revealed more dramatic differences.<sup>74</sup>

<sup>299</sup> We suspect that these larger discrepancies arose because we used a fixed pH ( $\text{pH} = 5.00 \pm 0.05$ ) across all experiments, which ensured the Se(IV) oxyanion (hydrogen selenite) carried a charge of  $-1$  while the Se(VI) oxyanion (selenate) carried a charge of  $-2$ . To further rationalize these observations, we must consider the proton topology of the  $\text{Zr}_6$ -node in addition to the projected selenium oxyanion binding motifs. First, rigorous computational and experimental studies have led researchers to believe that the NU-1000 node is charge balanced by four pairs of water/hydroxyl ions ( $-\text{OH}_2$ ,  $-\text{OH}$ ) and that adjacent ions have different identities meaning hydroxyl and water ligands are neighbors rather than two hydroxyl or two water ligands.<sup>300</sup>

Additionally, pair distribution function (PDF) analyses of X-ray diffraction data collected for NU-

1000 samples loaded with selenite or selenate found that both selenium oxyanions coordinated through an  $\eta_2\mu_2$  motif whereby two of the anion's oxygen atoms coordinate to two adjacent Zr atoms in the node.<sup>74</sup> Thus, adsorption of a  $-1$  oxyanion, such as hydrogen selenite, occurs via the displacement of one  $-\text{OH}_2/-\text{OH}$  ligand pair without necessitating adsorption of a counterion as would be required for binding a  $-2$  anion, such as selenate. Alternatively, adsorption of a  $-2$  anion could proceed via the displacement of two hydroxyl groups without requiring simultaneous adsorption of a counterion; however, calculations predict the configuration with adjacent hydroxyls to be less favorable.<sup>300</sup> Therefore, we are confident that these ITC measurements allow us to draw meaningful conclusions regarding the thermodynamics of selenium oxyanion binding events.

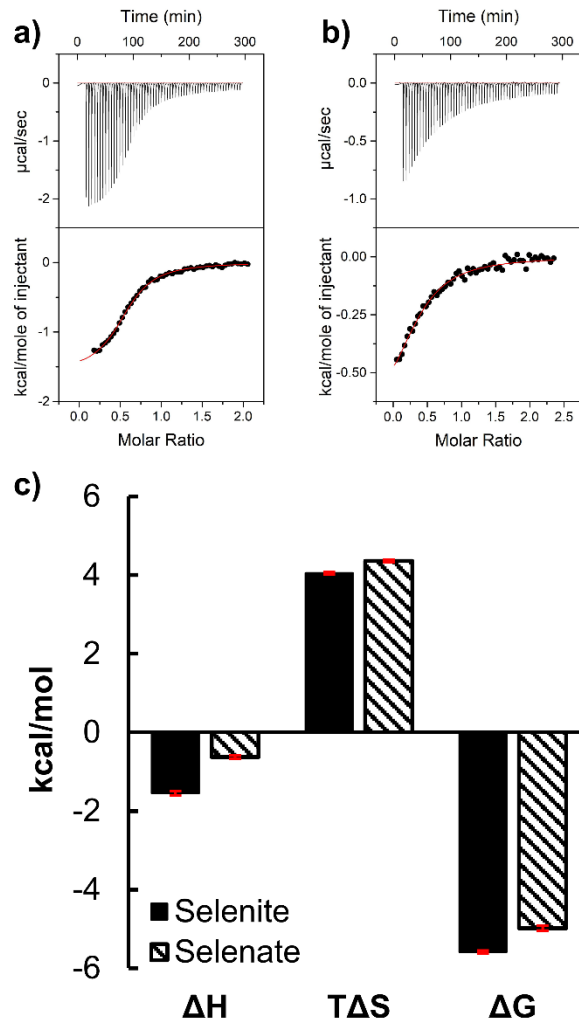


**Figure 6.3** ITC thermograms and integrated heat data for adsorption on NU-1000 of a) hydrogen selenite ( $\text{HSeO}_3^-$ ) and b) selenate ( $\text{SeO}_4^{2-}$ ) indicate that NU-1000 achieves a higher uptake of hydrogen selenite compared to selenate. The extracted thermodynamic parameters for adsorption of hydrogen selenite (c, solid) and selenate (c, slashed) suggest that hydrogen selenite adsorption is more thermodynamically favorable ( $\Delta G$ ) and exothermic ( $\Delta H$ ) compared to selenate adsorption.

## 6.6 Adsorption of Group 15 Oxyanions

Intrigued by the differences we observed between hydrogen selenite and selenate adsorption, we elected to also examine the adsorption of dihydrogen phosphate ( $\text{H}_2\text{PO}_4^-$ ) and dihydrogen arsenate ( $\text{H}_2\text{AsO}_4^-$ ), both of which are singly charged and whose central atoms are adjacent to sulfur and selenium on the Periodic Table, respectively. Extensive work in the MOF field has

demonstrated that Zr-MOFs achieve relatively high adsorption capacities for phosphorus oxyanions,<sup>227, 229, 294, 301</sup> and similar work has highlighted the extraction of arsenic-based oxyanions from water.<sup>73</sup> Therefore, we were confident we would observe binding events and were particularly interested in determining if NU-1000 could attain a higher loading of dihydrogen arsenate compared to the analogous phosphate ion as hydrogen selenite recording a higher loading than the analogous hydrogen sulfite. The thermograms associated with dihydrogen phosphate (**Figure 6.15**) and dihydrogen arsenate (**Figure 6.16**) adsorption resemble each other in shape; however, a two-site model fits the arsenate titration as compared to the single-site model which was appropriate for all other anions studied here. Despite multiple attempts to collect analogous data for phosphate adsorption, we did not observe an initial exothermic binding event. The sum of the stoichiometric terms for dihydrogen arsenate adsorption ( $n_1 = 0.22$  and  $n_2 = 0.40$ ) agrees well with that of dihydrogen phosphate adsorption ( $n = 0.60$ ) and correlate with the amount adsorbed as determined by ICP-OES for bulk samples (**Table 6.3**). We also observed that the association constant for the second dihydrogen arsenate binding event aligns well with that of dihydrogen phosphate adsorption, suggesting similarities between the two endothermic processes, which seems reasonable owing to the analytes' similar structures. Moreover, only these two species coordinated to NU-1000 through endothermic pathways suggesting these processes were entropically driven, likely owing to the additional release of weakly sorbed species surrounding the binding site.

### 6.7 Displacement of Adsorbed Oxyanions

Having demonstrated we could quantify adsorption events occurring at the MOF node using ITC, we wanted to propel this work farther and explore if we could observe the displacement of oxyanions adsorbed to the framework. Thus, we selected three candidate analytes: sulfate,

selenate, and dihydrogen phosphate. Given dihydrogen phosphate's larger association constant compared to selenate and sulfate ( $\Delta G_{\text{phosphate}} = -5.41$  kcal/mol;  $\Delta G_{\text{selenate}} = -4.98$  kcal/mol;  $\Delta G_{\text{sulfate}} = -4.77$  kcal/mol), we elected to load NU-1000 samples with sulfate and selenate and titrate these samples with dihydrogen phosphate. Adsorption of dihydrogen phosphate on NU-1000 samples loaded with 0.7 selenate ions per  $\text{Zr}_6$ -node, which we will denote as NU-1000-Se, produced a similar thermodynamic profile to those generated from the adsorption of dihydrogen phosphate on unmodified NU-1000 (**Figure 6.4**, **Figure 6.15**, **Figure 6.17**). The extracted enthalpic and entropic terms are quite similar and overall, adsorption on the selenate functionalized MOF yields a slightly larger association constant; however, the curve of integrated heats of adsorption is shifted left to lower molar ratios for the selenate loaded sample ( $n = 0.31$  vs.  $n = 0.60$ ; **Table 6.1**, **Figure 6.4**). To determine if the dihydrogen phosphate ions were displacing selenate or binding in addition to selenate, we separated the MOF from the solution following titration and analyzed digested samples via ICP-OES. We found that nearly all of the selenate ions had been displaced (loading  $< 0.1$  per  $\text{Zr}_6$  node) by dihydrogen phosphate which achieved a loading of  $1.09 (\pm 0.04)$  ions per node. This dihydrogen phosphate is less than that quantified for the parent NU-1000 material ( $1.6 \pm 0.1$  ions per  $\text{Zr}_6$ -node), yet it surpasses the initial selenate loading. To explore a similar system, we also assessed adsorption on samples of NU-1000 loaded with 0.6 sulfate ions per node, which we can denote as NU-1000-S. Similarly, the adsorption of dihydrogen phosphate adsorption on the sulfate loaded sample generated a lower stoichiometric parameter than that recorded for the unmodified framework ( $n = 0.20$  vs.  $n = 0.60$ ; **Figure 6.15**, **Figure 6.18**, **Figure 6.19**). Considering the enthalpic terms, adsorption of phosphate on NU-1000-S required more heat input (i.e., was

more endothermic) presumably because sulfate coordination is enthalpically favorable (Table 6.1).

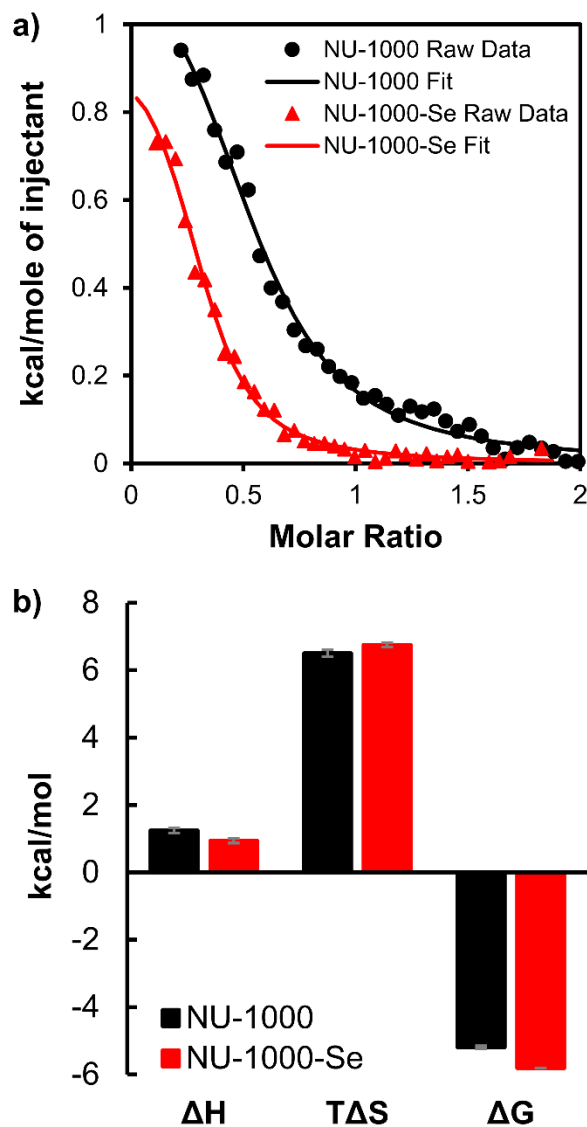


**Figure 6.4** Single-site model fitting of integrated heats of adsorption on NU-1000 (black, circle) and NU-1000-0.6 SeO<sub>4</sub> (red, triangle) for each injection of phosphate demonstrate that NU-1000 loaded with ~0.6 selenate ions per node records a stoichiometric parameter of only 0.31 ( $\pm 0.01$ ) while parent NU-1000 records a value of 0.60 ( $\pm 0.09$ ). In addition, the extracted thermodynamic parameters indicate that adsorption on NU-1000-0.6 SeO<sub>4</sub> is slightly more thermodynamically ( $\Delta G$ ) favorable.

Finally, we sought to examine displacement between two ions more evenly paired in terms of their association constants; thus, we elected to measure selenate adsorption on NU-1000-S because adsorption of both sulfate and selenate generate similar Gibbs free energy changes ( $\Delta G_{\text{selenate}} = -4.98$  kcal/mol;  $\Delta G_{\text{sulfate}} = -4.77$  kcal/mol). Thermograms resulting from the titration of NU-1000-S with a selenate solution produced enthalpies that were nearly irresolvable from the blank titration of selenate into the buffer matrix; therefore, we could not extract any thermodynamic parameters (**Figure 6.20**). However, analysis by ICP-OES indicated that, following titration with selenate,  $\sim 0.66$  selenate ions coordinated to each node of the MOF framework and sulfur could not be quantified in the sample owing to its low concentration ( $<20$  ppb). This result made us confident that adsorption of selenate occurs at least partially through the displacement of sulfate. When considering the adsorption enthalpies of the two ions independently on NU-1000, we suspect that the enthalpic penalty of displacing sulfate is balanced by the enthalpic benefit of coordinating selenate, thus the net heat change is nearly negligible. ITC measures the heats associated with binding events; thus, to study exchange-like processes, the enthalpies of adsorption of the species in question must be sufficiently different such that the enthalpy of displacement is resolvable. Despite the experimental challenges we encountered in analyzing displacement events, these titrations demonstrate that based on association constants we can reliably predict which ions might displace others and compete for finite binding sites.

## 6.8 Chapter Conclusions

In summary, we undertook a thermochemical investigation of oxyanion adsorption in NU-1000 using isothermal titration calorimetry (ITC). From a single titration, we can calculate the complete thermodynamic profile of adsorption. Despite differences in charge, sulfate and hydrogen sulfite display nearly identical thermodynamic profiles, while the analogous selenium oxyanions do not.

Hydrogen selenite adsorption is more enthalpically favorable compared to selenate adsorption and records a larger stoichiometric parameter, agreeing with previous work in the field and demonstrating the influence of charge during binding events at  $Zr_6$  MOF nodes capped with water and hydroxyl ligands. Adsorption of dihydrogen phosphate and the analogous arsenic-based species proceeded through endothermic pathways and generated association constants exceeding those of most of the sulfur and selenium oxyanions. In comparing the association constants, we accurately predicted which analytes could displace others and monitored the thermodynamics of these exchange processes. In future investigations of displacement or competitive binding events, research teams must assess if the individual adsorption enthalpies are sufficiently different to observe net heats of displacement in ITC titrations. Importantly, we observed that the stoichiometric parameters extracted from ITC thermograms correlated with analyte uptakes measured for bulk exposure experiments. We envision that the addition of ITC to our toolkit will facilitate our screening of MOFs for adsorption, but also for other applications including assessing a material's suitability as a catalyst support.

## 6.9 Additional Information

### 6.9.1 Materials

All chemicals were used as received from the supplier. In these experiments, all water is Milli-Q (Milli-pore). All gases were Ultra High Purity grade 5 gases from Airgas Specialty Gases. Fisher Chemical Trace Metal grade nitric acid was used for all ICP-OES measurements.

### 6.9.2 Physical Methods and Instrumentation

4,4',4'',4'''-(pyrene-1,3,6,8-tetrayl)tetrabenzoate ( $H_4TBAPy$ ) was synthesized according to the reported procedure.<sup>297</sup> The MOF was prepared according to an established procedure by Riki Drout at Northwestern University in Evanston, IL.<sup>183</sup> Briefly,  $ZrOCl_2 \cdot 8H_2O$  (9.7 g, 30 mmol) and

benzoic acid (200 g, 1.6 mol) were added to 600 mL of DMF in a 2 L glass bottle. The mixture was sonicated until clear and then heated for 1 h in a preheated oven at 100 °C. Similarly, H<sub>4</sub>TBAPy (4 g, 6 mmol) was added to 200 mL of DMF in a 500 mL glass bottle and heated for 1 h in a preheated oven at 100 °C. After cooling to room temperature, trifluoroacetic acid (TFA) (4 mL, 52 mmol) was added to the prepared Zr-solution. After sonicating for 15 min, the linker solution was added to the Zr-solution and then heated at 120 °C for 18 h. After cooling down to room temperature, the yellow powder was isolated by centrifugation (5 min, 7500 rpm) and washed with fresh DMF (~300 mL) three times for 2 h each. The resulting yellow powder was suspended in 1300 mL DMF in a 2 L glass jar and 50 mL of 8 M aqueous HCl was added. The mixture was heated in an oven at 100 °C for 18 h. After cooling to room temperature, the powder was washed with fresh DMF (~300 mL) three times for 2 h each and acetone (~300 mL) three times for 2 h each and soaked in acetone for additional 18 h. The NU-1000 powder was collected by centrifugation and dried in a vacuum oven at 80 °C for 2 h, and then thermally activated on a Smart VacPrep at 120 °C for 18 h. Nitrogen adsorption desorption isotherms were collected on a Micromeritics TriStar II 3020. Powder X-ray diffraction measurements were collected on a STOE STADI-P equipped with a CuK $\alpha$ 1 source and a 1D strip detector.

To prepare a sample for analysis by NMR, 2 strategies may be used. To digest a MOF sample under acidic conditions, ~1 mg of material was treated with 6-8 drops of deuterated sulfuric acid. After sonicating for 5 min, 0.6 mL of deuterated dimethyl sulfoxide were added. To digest a MOF sample under basic conditions, ~1 mg of material was treated with 6-8 drops of 0.1 M NaOD in D<sub>2</sub>O. After sonicating for 5 min, 0.6 mL of D<sub>2</sub>O were added.

To prepare a sample for analysis by ICP-OES, a MOF sample (2-4 mg) and nitric acid (67-70%, 2 mL) were added to a 5 mL Biotage microwave vial. After capping the vial, it was heated to 150 °C for 15 min in a microwave reactor. Once the vial contents cooled to room temperature, an aliquot (0.5 mL) was diluted to 12 mL in Millipore water. Metal analysis was performed on a Thermo iCap7600 ICP-OES and standard curves for constructed for each analyte (Zr, S, Se, P, As) based on at least four data points.

### *6.9.3 Isothermal Titration Calorimetry*

All ITC experiments were completed on a MicroCal VP-ITC microcalorimeter. In a typical ITC experiment, the reference cell is filled with deionized water, the sample cell is filled with a MOF suspension, and the syringe is loaded with an analyte solution. All MOF and analyte solutions were prepared in 10 mM acetate buffer and their pH values were adjusted to  $5.00 \pm 0.05$  as measured on a Metrohm Titrando 905. Prior to collecting thermograms, all solutions were degassed for 10 min using a MicroCal ThermoVac2. All thermograms were collected at a fixed stirring rate of 698 rpm. The first injection of each titration was fixed at 2  $\mu$ L. All analyte concentrations were determined by Thermo iCap7600 ICP-OES. At least two titrations for each analyte-MOF pair were collected. Data analysis was performed in MicroCal's Origin package. In all instances, the heats of injection for blank titrations (analyte into buffer) were subtracted from the heats of injection into MOF suspensions.

**Table 6.2** ITC experimental conditions for all analytes. All MOF suspensions were 1.0 mM in 10 mM acetate buffer.

MOF	Analyte	Analyte Concentration (mM)	Injection Volume ( $\mu\text{L}$ )	Equilibration Time (s)
NU-1000	Sulfite ( $\text{HSO}_3^-$ )	10.6	5 ( $\times 58$ )	300*
NU-1000	Sulfate ( $\text{SO}_4^{2-}$ )	10.9	4 ( $\times 70$ )	300
NU-1000	Selenite ( $\text{HSeO}_3^-$ )	9.8	5 ( $\times 58$ )	300
NU-1000	Selenate ( $\text{SeO}_4^{2-}$ )	11.2	5 ( $\times 58$ )	300
NU-1000	Phosphate ( $\text{H}_2\text{PO}_4^-$ )	18.0	4 ( $\times 70$ )	300*
NU-1000	Arsenate ( $\text{H}_2\text{AsO}_4^-$ )	20.0	4 ( $\times 70$ )	300*
NU-1000- $\text{SeO}_4$	Phosphate ( $\text{H}_2\text{PO}_4^-$ )	18.0	3.5 ( $\times 42$ )	300*
NU-1000- $\text{SO}_4$	Selenate ( $\text{SeO}_4^{2-}$ )	22.4	3.5 ( $\times 70$ )	300

\* First 11 injections had 600 s equilibration interval due to slow returns to baseline.

To explore the physical meaning of the stoichiometric ( $n$ ) parameter extracted from ITC thermograms, we elected to replicate the measurements conditions in the bulk phase. In a typical ITC experiment, the cell is filled with 1.8 mL of a MOF suspension. The automated syringe then titrates the suspension with 280  $\mu\text{L}$  of the loaded analyte solution. These conditions were replicated and after 6 h, the average length of an ITC experiment, samples were filtered through 0.45  $\mu\text{m}$  PVDF syringe filters before metal analysis on a Thermo iCap7600 ICP-OES.

## 6.9.4 NU-1000 Characterization

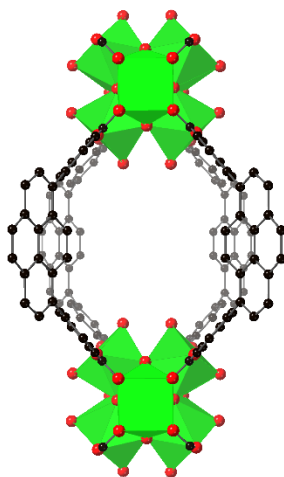


**Figure 6.5** Structure of the c-pore of NU-1000 which is parallel to the hexagonal 1D mesoporous channels and the triangular 1D microporous channels.

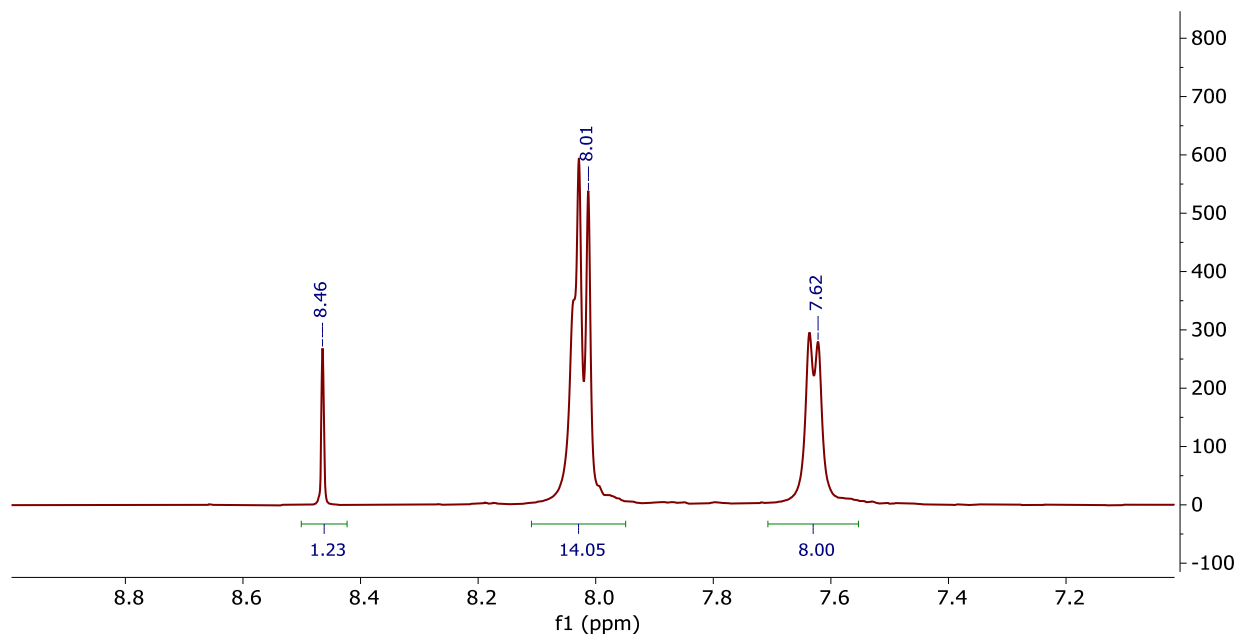


**Figure 6.6** NMR spectrum of NU-1000 digested by 0.1 M NaOD in D<sub>2</sub>O indicates each node is capped by ~2.4 formate ions after 2 consecutive acid washes.

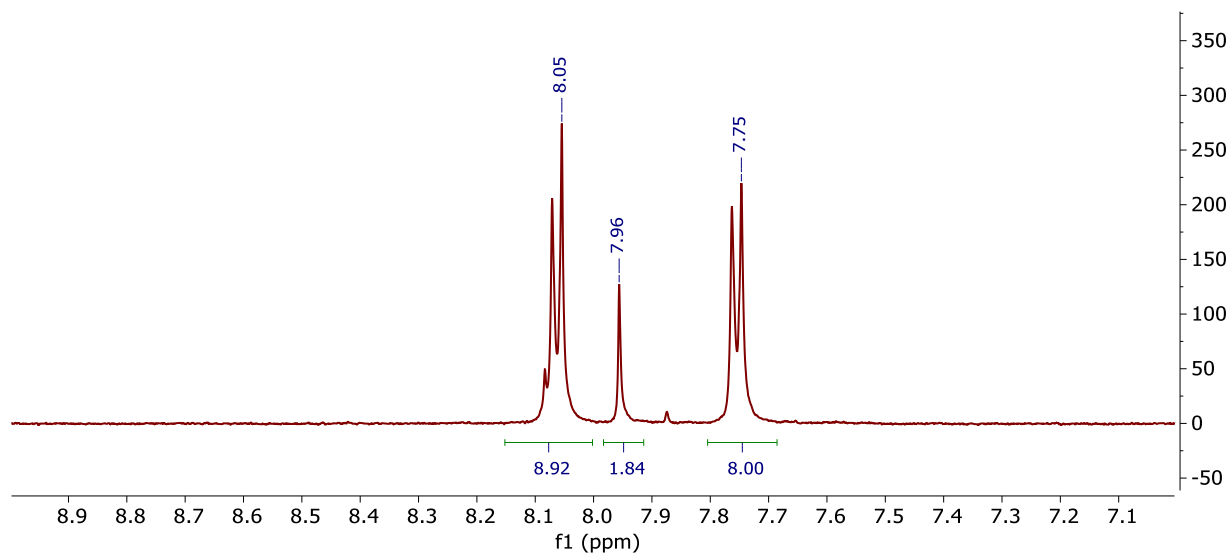


**Figure 6.7** NMR spectrum of NU-1000 digested by  $d_2SO_4$  in  $d_6$ -DMSO indicates the complete removal of the benzoic acid modulator.

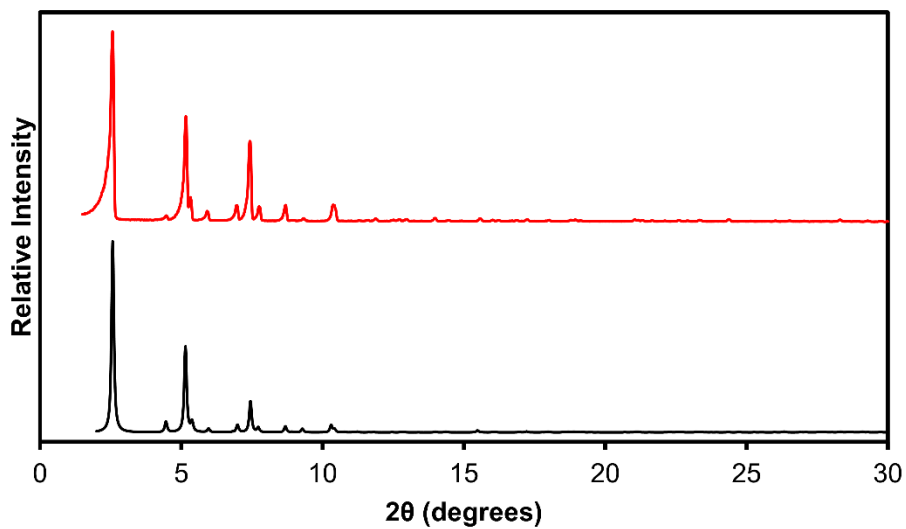


**Figure 6.8** Powder X-ray diffraction patterns of as-synthesized NU-1000 (red trace) compared to a simulated pattern (black trace).

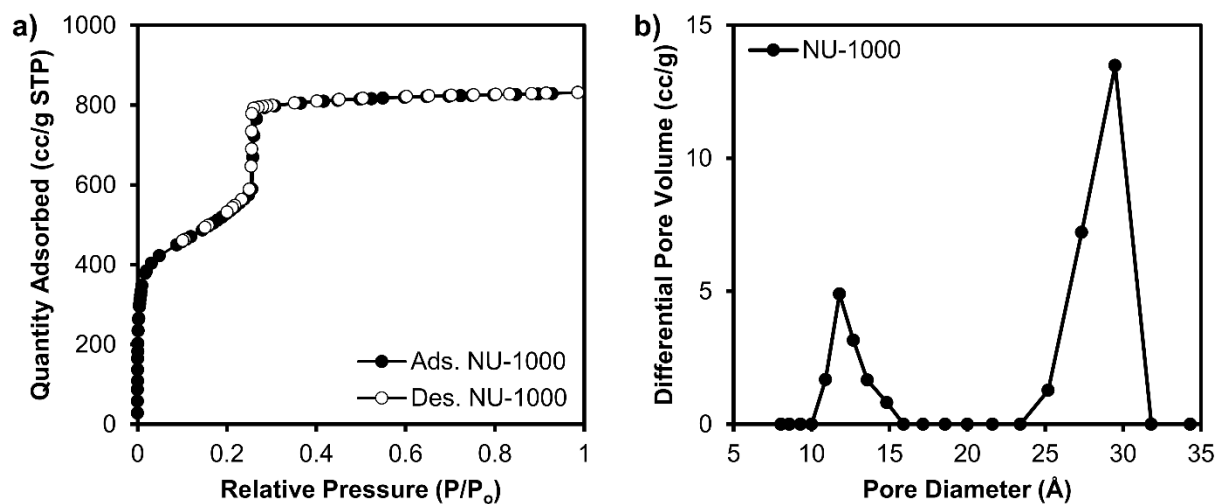


**Figure 6.9** a) Nitrogen adsorption and desorption isotherm of NU-1000 and b) DFT-calculated pore size distribution.

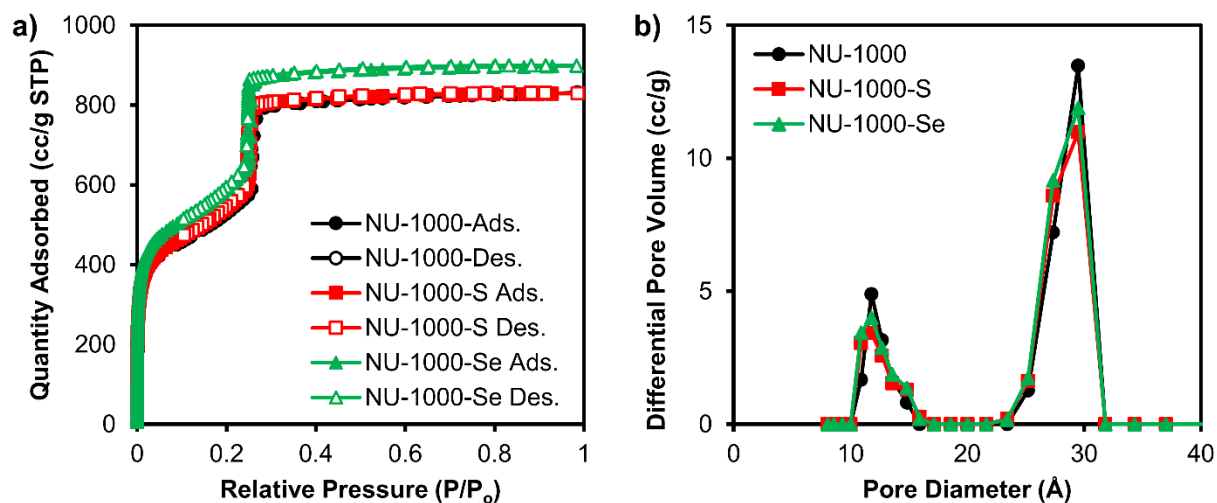


**Figure 6.10** a) Nitrogen adsorption and desorption isotherms of NU-1000, NU-1000-0.6 SO<sub>4</sub> (denoted NU-1000-S), and NU-1000-0.7 SeO<sub>4</sub> (denoted NU-1000-Se) and b) the associated DFT-calculated pore size distributions.

*6.9.5 Isothermal Titration Calorimetry Data*

**Table 6.3** Analyte uptake as determined by ICP-OES in bulk experiments replicating ITC conditions compared to the stoichiometric parameters extracted for each analyte from the respective ITC thermograms.

Analyte	Bulk Uptake	ITC Stoichiometric Parameter (n)
hydrogen sulfite	0.47	0.35
sulfate	0.47	0.30
hydrogen selenite	1.29	0.64
selenate	0.44	0.45
dihydrogen phosphate	1.44	0.65
dihydrogen arsenate	1.57	0.62

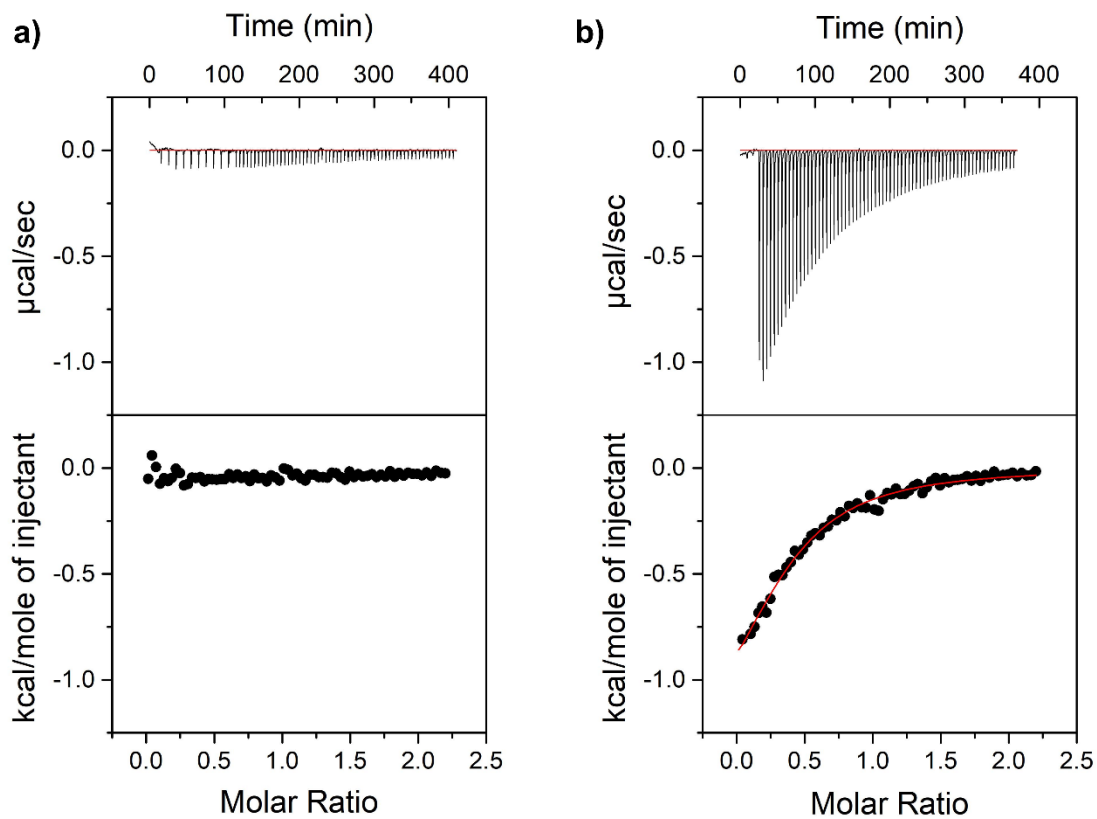


**Figure 6.11** a) Thermogram and integrated heat data for the titration of 10 mM acetate buffer (pH 5) with a 10.6 mM sodium sulfite solution. b) Thermogram and integrated heat data for the titration of a 1 mM NU-1000 suspension with a 10.6 mM sodium sulfite solution in a 10 mM acetate buffer matrix (pH 5).

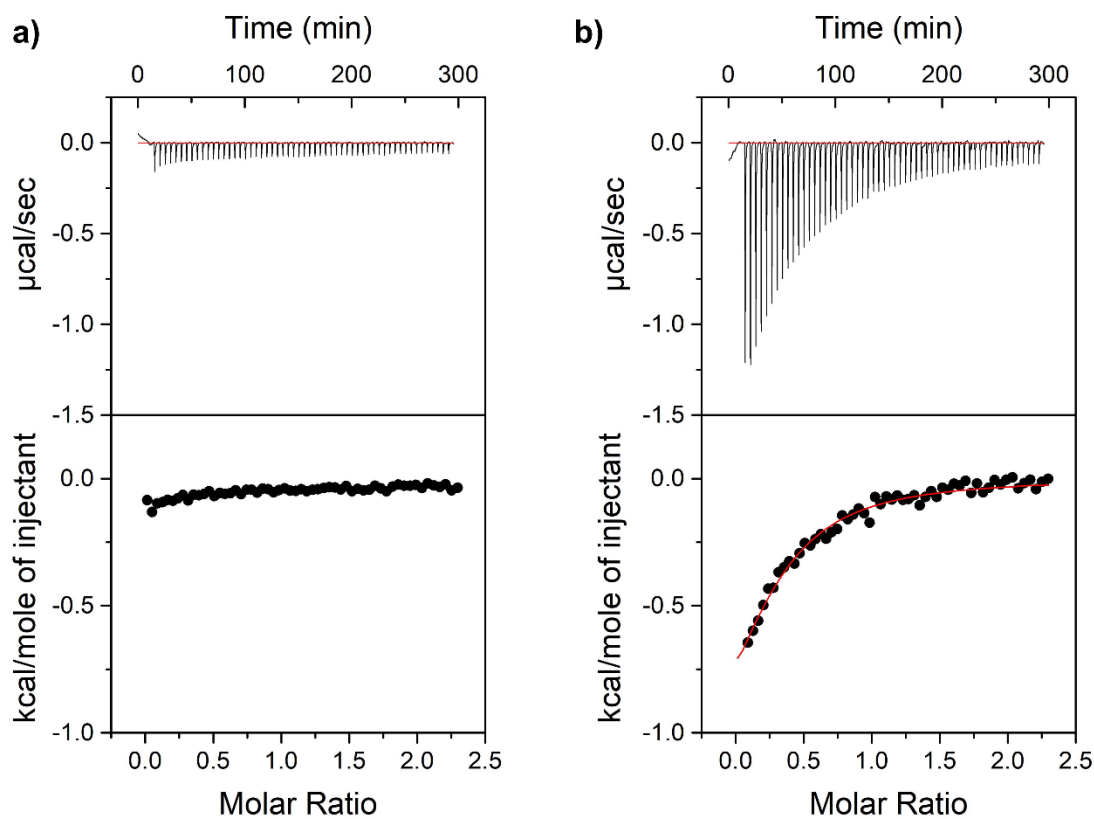


**Figure 6.12** a) Thermogram and integrated heat data for the titration of 10 mM acetate buffer (pH 5) with a 10.9 mM sodium sulfate solution. b) Thermogram and integrated heat data for the titration of a 1 mM NU-1000 suspension with a 10.9 mM sodium sulfate solution in a 10 mM acetate buffer matrix (pH 5).

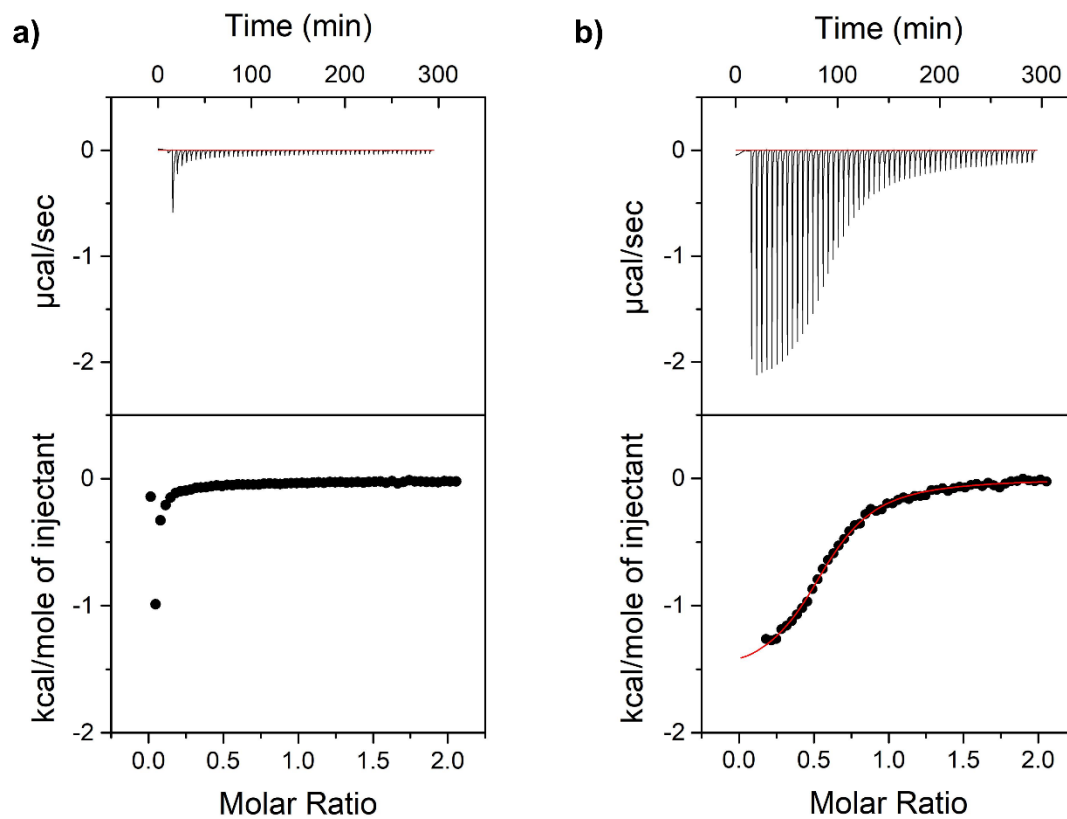


**Figure 6.13** a) Thermogram and integrated heat data for the titration of 10 mM acetate buffer (pH 5) with a 9.8 mM sodium selenite solution. b) Thermogram and integrated heat data for the titration of a 1 mM NU-1000 suspension with a 9.8 mM sodium selenite solution in a 10 mM acetate buffer matrix (pH 5).

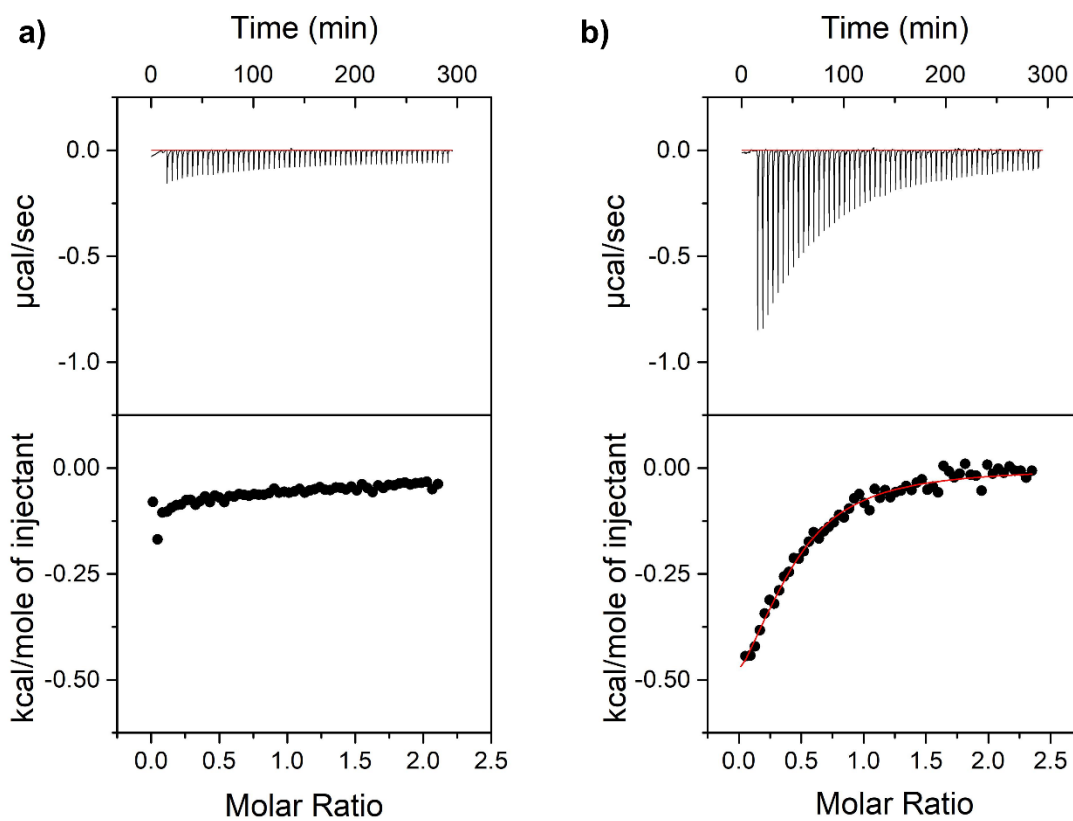


**Figure 6.14** a) Thermogram and integrated heat data for the titration of 10 mM acetate buffer (pH 5) with a 11.2 mM sodium selenate solution. b) Thermogram and integrated heat data for the titration of a 1 mM NU-1000 suspension with a 11.2 mM sodium selenate solution in a 10 mM acetate buffer matrix (pH 5).

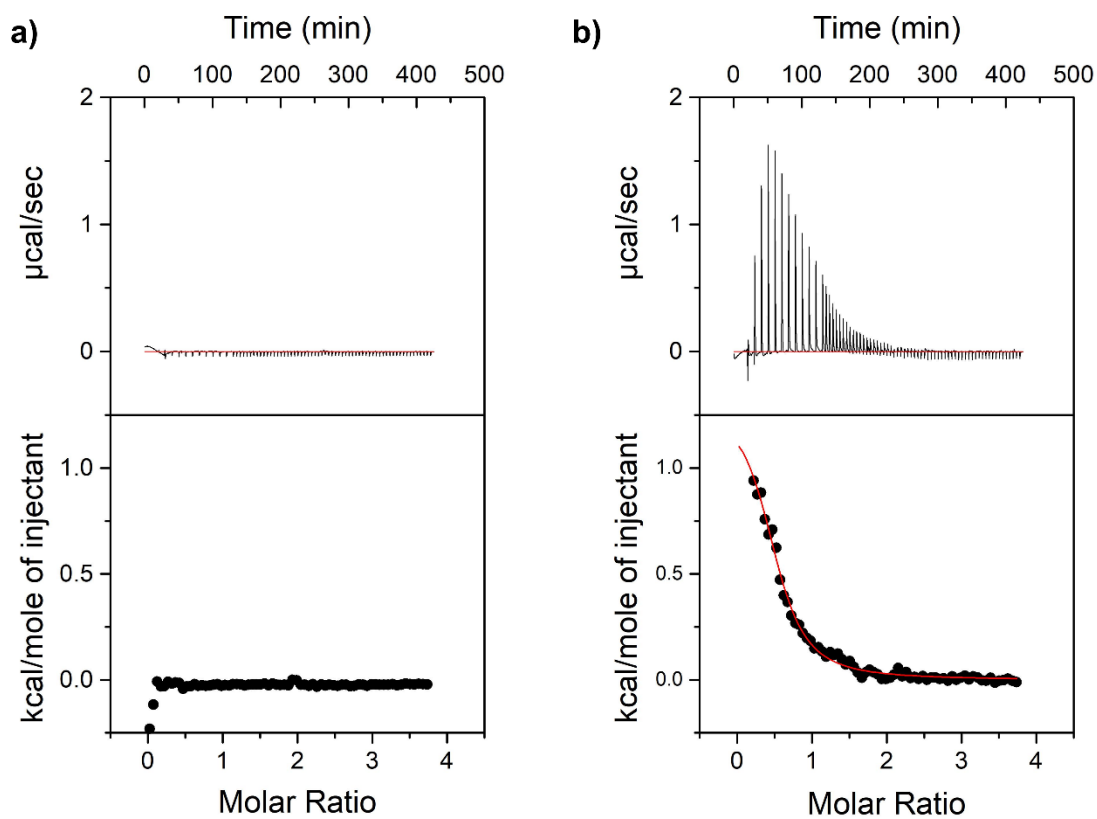


**Figure 6.15** a) Thermogram and integrated heat data for the titration of 10 mM acetate buffer (pH 5) with an 18.0 mM disodium phosphate solution. b) Thermogram and integrated heat data for the titration of a 1 mM NU-1000 suspension with an 18.0 mM disodium phosphate solution in a 10 mM acetate buffer matrix (pH 5).

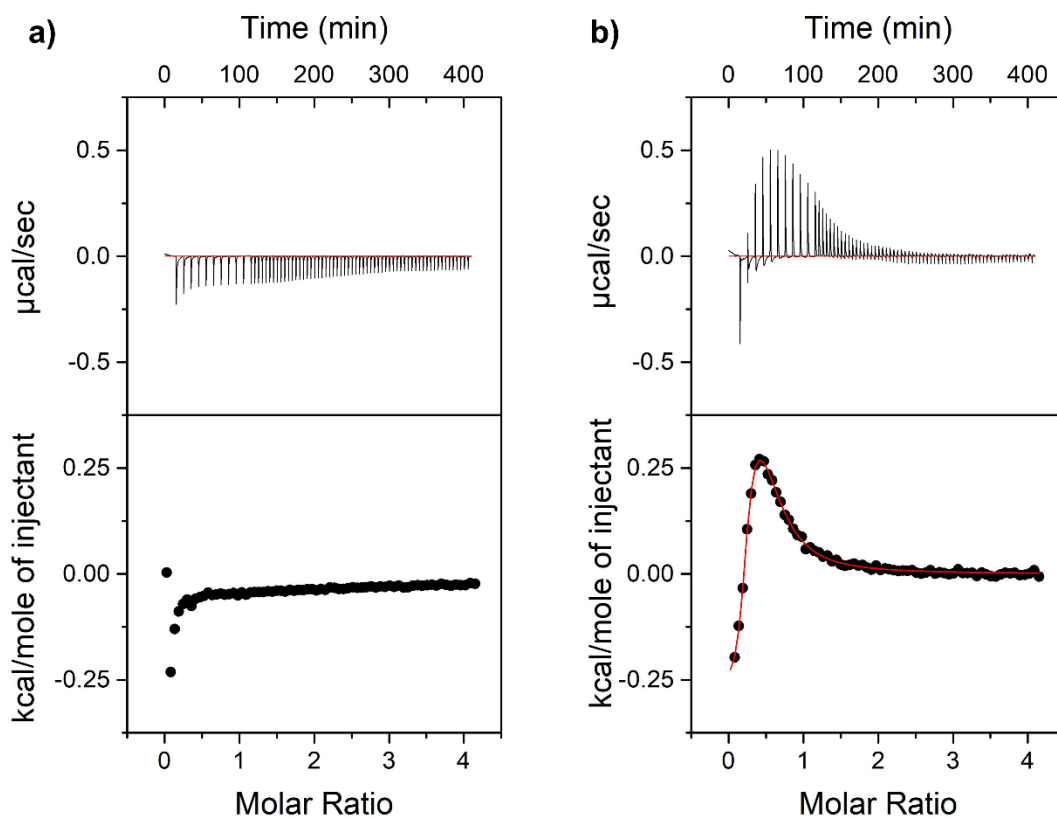


**Figure 6.16** a) Thermogram and integrated heat data for the titration of 10 mM acetate buffer (pH 5) with a 20.0 mM sodium arsenate dibasic solution. b) Thermogram and integrated heat data for the titration of a 1 mM NU-1000 suspension with a 20.0 mM sodium arsenate dibasic solution in a 10 mM acetate buffer matrix (pH 5).

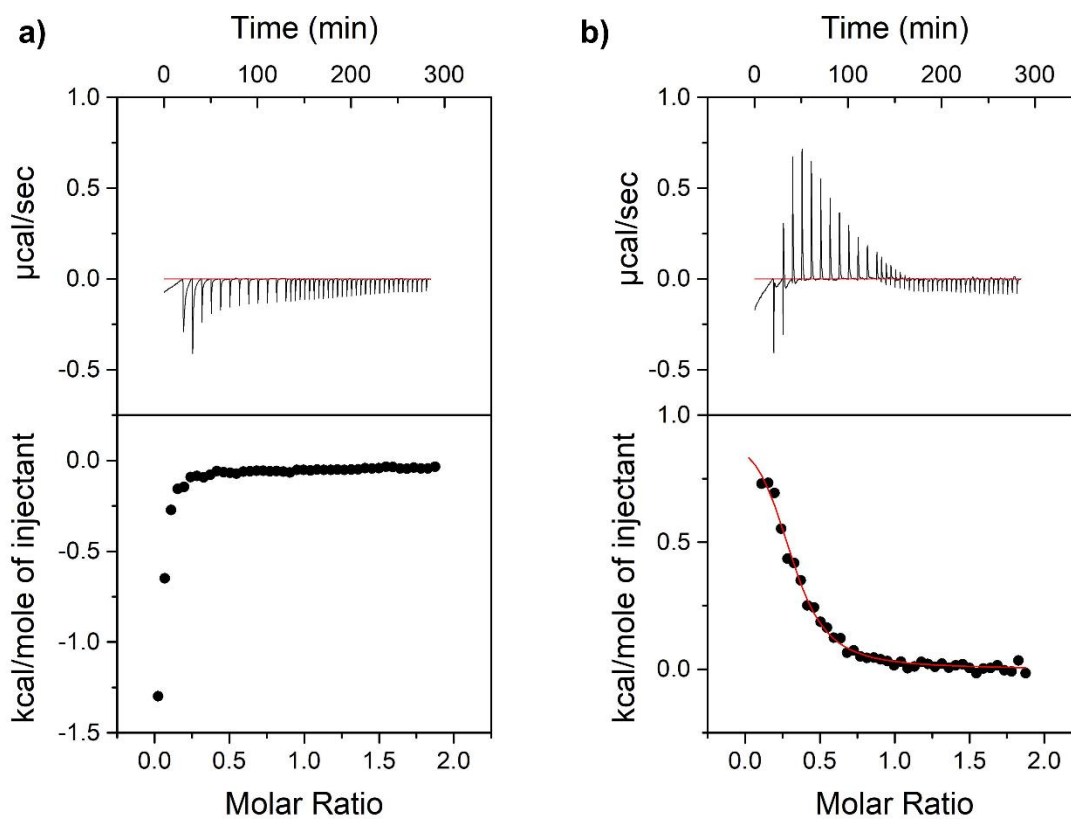


**Figure 6.17** a) Thermogram and integrated heat data for the titration of 10 mM acetate buffer (pH 5) with an 18.0 mM disodium phosphate solution. b) Thermogram and integrated heat data for the titration of a 1 mM NU-1000-0.7  $\text{SeO}_4$  (denoted NU-1000-Se) suspension with an 18.0 mM disodium phosphate solution in a 10 mM acetate buffer matrix (pH 5).

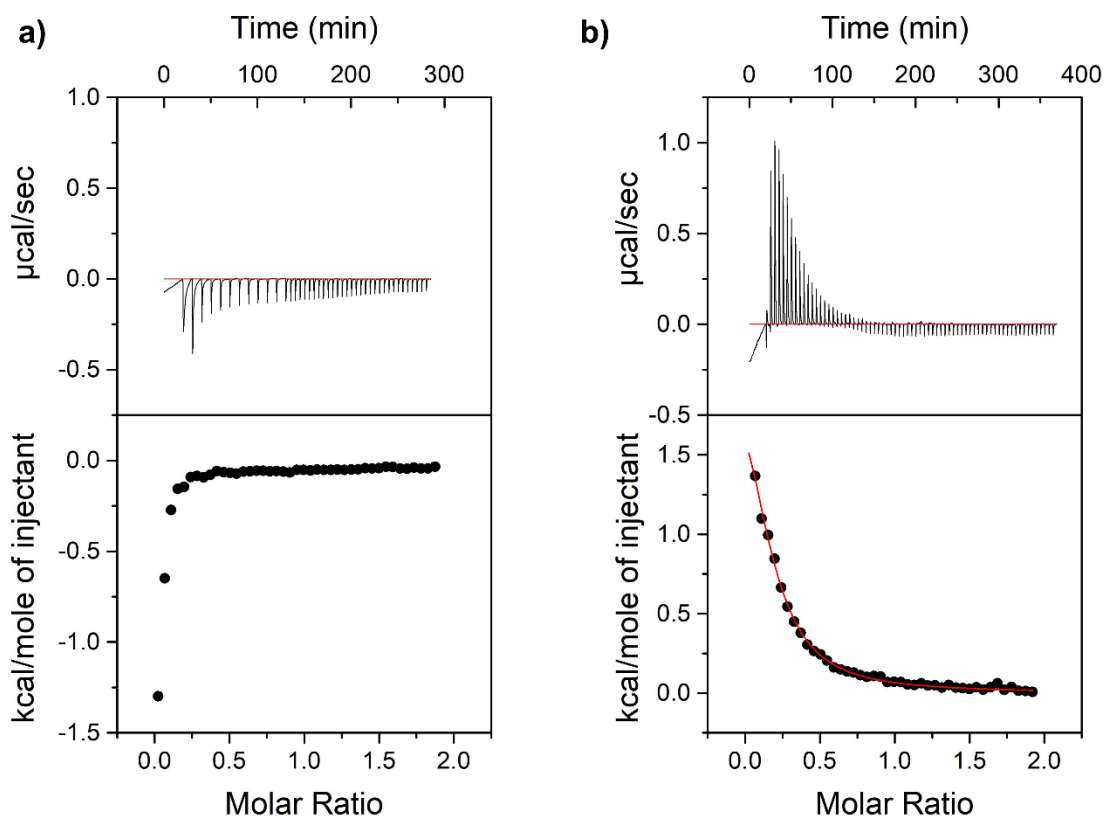


**Figure 6.18** a) Thermogram and integrated heat data for the titration of 10 mM acetate buffer (pH 5) with an 18.0 mM disodium phosphate solution. b) Thermogram and integrated heat data for the titration of a 1 mM NU-1000-0.6  $\text{SO}_4$  (denoted NU-1000-S) suspension with an 18.0 mM disodium phosphate solution in a 10 mM acetate buffer matrix (pH 5).

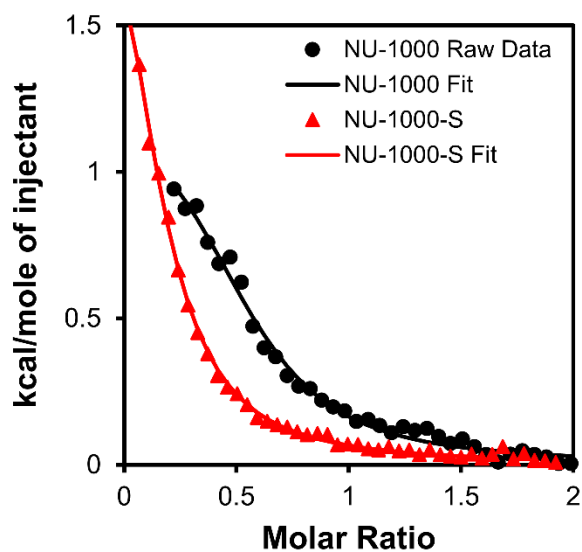


**Figure 6.19** Single site model fitting of integrated heats of adsorption for each injection of 18.0 mM phosphate into 1 mM suspensions of NU-1000 (black) and NU-1000-0.6 SO<sub>4</sub> (denoted NU-1000-S, red) demonstrate similar adsorption thermodynamic profiles; however, the sulfate loaded sample records a lower stoichiometric parameter as determined from the inflection point of the titration curve.

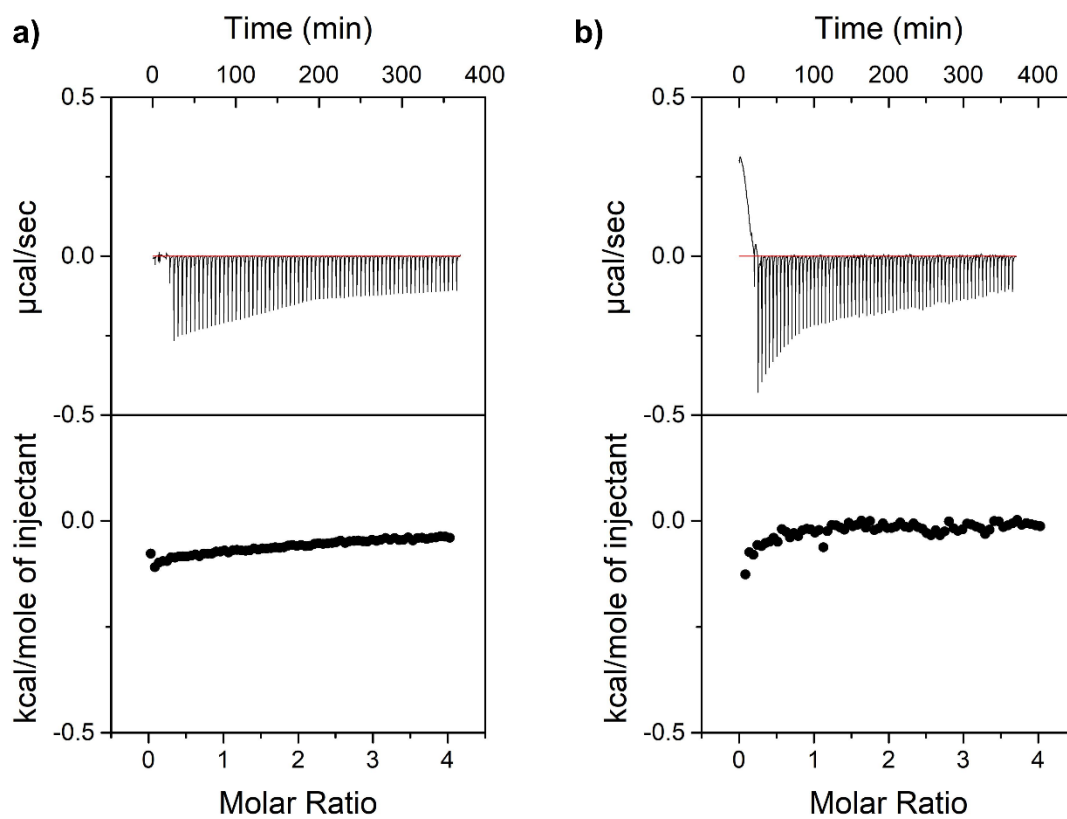


**Figure 6.20** a) Thermogram and integrated heat data for the titration of 10 mM acetate buffer (pH 5) with a 22.4 mM sodium selenate solution. b) Thermogram and integrated heat data for the titration of a 1 mM NU-1000-0.6  $\text{SO}_4$  (denoted NU-1000-S) suspension with a 22.4 mM sodium selenate solution in a 10 mM acetate buffer matrix (pH 5).

## Chapter 7. Conclusions and Outlook

In summary, this work showcases the recent advances in examining liquid-phase adsorption processes in metal–organic frameworks (MOFs). Initial work sought to explore the role of Zr-based MOF nodes in removing oxyanions from aqueous media. Bulk adsorption studies allowed for the quantification of the theoretical uptake capacity and the exploration of adsorption kinetics. Through single-crystal X-ray diffraction measurements, we directly observed the analyte binding motifs which indicated that the oxyanions displace the labile water and hydroxyl ligands on the  $Zr_6$ -node. Subsequent work went on to examine how the MOF linker influenced adsorption. Briefly, this work demonstrated that by increasing the size of a MOF linker's  $\pi$ -system, we can systematically increase the material's adsorption capacity for organic pollutants. While bulk adsorption measurements yield valuable insights, determining the thermodynamic profile of binding events using bulk methods remains largely tedious and error ridden.

Thus, we turned our attention to isothermal titration calorimetry (ITC) which allows for the direct quantification of the full thermodynamic profile of an adsorption process. From a single experiment, we can directly determine the association constant ( $K_a$ ), enthalpy change ( $\Delta H$ ), entropy change ( $\Delta S$ ) and Gibbs free energy change ( $\Delta G$ ) of a chemical process. In a proof-of-concept experimental and computational investigation of agrochemical adsorption in MOFs, we observed differences in the thermodynamic profiles of adsorption depending on MOF architecture and analyte structure. Importantly, we demonstrated that the association constants extracted from ITC experiments correlate quite well with the analogous parameters extracted from bulk adsorption experiments. ITC provides researchers with a more comprehensive description of

chemical processes occurring within the confines of a MOF pore, and learnings from similar efforts will contribute to the rational design of next-generation sorbents.

We anticipate the application of ITC in the MOF field will extend far beyond examining chemisorption to explore other chemical processes, particularly MOF assembly and the reactivity of heterogeneous, MOF-based catalyst systems. For example, our lab has demonstrated that installing an enzyme in a MOF enhances its catalytic activity compared to the native enzyme free in solution. To date, there is no clear experimental evidence to rationalize this observation. We envision that with ITC, we will be able to unveil the energetics of enzyme installation processes and the subsequent composite's catalytic activity.

## References

1. WWAP, The United Nations World Water Development Report 4: Managing Water under Uncertainty and Risk. UNESCO Paris: 2012.
2. Schwarzenbach, R. P.; Egli, T.; Hofstetter, T. B.; Gunten, U. v.; Wehrli, B., Global Water Pollution and Human Health. *Annu. Rev. Environ. Resour.* **2010**, *35* (1), 109-136.
3. Organization, W. H. *Guidelines for Drinking-Water Quality*; 2017.
4. Hinkebein, T. E.; Price, M. K., Progress with the Desalination and Water Purification Technologies Us Roadmap. *Desalination* **2005**, *182* (1), 19-28.
5. Shannon, M. A.; Bohn, P. W.; Elimelech, M.; Georgiadis, J. G.; Marinas, B. J.; Mayes, A. M., Science and Technology for Water Purification in the Coming Decades. In *Nanoscience and Technology: A Collection of Reviews from Nature Journals*, World Scientific: 2010; pp 337-346.
6. Van de Voorde, B.; Bueken, B.; Denayer, J.; De Vos, D., Adsorptive Separation on Metal–Organic Frameworks in the Liquid Phase. *Chem. Soc. Rev.* **2014**, *43* (16), 5766-5788.
7. Li, H.; Eddaoudi, M.; O'Keeffe, M.; Yaghi, O. M., Design and Synthesis of an Exceptionally Stable and Highly Porous Metal-Organic Framework. *Nature* **1999**, *402* (6759), 276-279.
8. H. Furukawa, K. E. C., M. O'Keeffe and O. M. Yaghi, *The Chemistry and Applications of Metal-Organic Frameworks*. Science: Science, 2013; Vol. 341.
9. Islamoglu, T.; Goswami, S.; Li, Z.; Howarth, A. J.; Farha, O. K.; Hupp, J. T., Postsynthetic Tuning of Metal-Organic Frameworks for Targeted Applications. *Acc. Chem. Res.* **2017**, *50* (4), 805-813.
10. Kreno, L. E.; Leong, K.; Farha, O. K.; Allendorf, M.; Van Duyne, R. P.; Hupp, J. T., Metal-Organic Framework Materials as Chemical Sensors. *Chem. Rev.* **2012**, *112* (2), 1105-25.
11. Gutov, O. V.; Bury, W.; Gomez-Gualdrón, D. A.; Krungleviciute, V.; Fairen-Jimenez, D.; Mondloch, J. E.; Sarjeant, A. A.; Al-Juaid, S. S.; Snurr, R. Q.; Hupp, J. T.; Yildirim, T.; Farha, O. K., Water-Stable Zirconium-Based Metal-Organic Framework Material with High-Surface Area and Gas-Storage Capacities. *Chemistry* **2014**, *20* (39), 12389-93.
12. Murray, L. J.; Dinca, M.; Long, J. R., Hydrogen Storage in Metal-Organic Frameworks. *Chem. Soc. Rev.* **2009**, *38* (5), 1294-314.
13. Li, J. R.; Kuppler, R. J.; Zhou, H. C., Selective Gas Adsorption and Separation in Metal-Organic Frameworks. *Chem. Soc. Rev.* **2009**, *38* (5), 1477-504.
14. Lee, J.; Farha, O. K.; Roberts, J.; Scheidt, K. A.; Nguyen, S. T.; Hupp, J. T., Metal-Organic Framework Materials as Catalysts. *Chem. Soc. Rev.* **2009**, *38* (5), 1450-9.
15. Bobbitt, N. S.; Mendonca, M. L.; Howarth, A. J.; Islamoglu, T.; Hupp, J. T.; Farha, O. K.; Snurr, R. Q., Metal-Organic Frameworks for the Removal of Toxic Industrial Chemicals and Chemical Warfare Agents. *Chem. Soc. Rev.* **2017**, *46* (11), 3357-3385.
16. Howarth, A. J.; Liu, Y. Y.; Hupp, J. T.; Farha, O. K., Metal-Organic Frameworks for Applications in Remediation of Oxyanion/Cation-Contaminated Water. *CrystEngComm* **2015**, *17* (38), 7245-7253.
17. Kobielska, P. A.; Howarth, A. J.; Farha, O. K.; Nayak, S., Metal–Organic Frameworks for Heavy Metal Removal from Water. *Coord. Chem. Rev.* **2018**, *358*, 92-107.

18. Ajoyan, Z.; Marino, P.; Howarth, A. J., Green Applications of Metal–Organic Frameworks. *CrystEngComm* **2018**.
19. Drout, R. J.; Otake, K.; Howarth, A. J.; Islamoglu, T.; Zhu, L.; Xiao, C.; Wang, S.; Farha, O. K., Efficient Capture of Perrhenate and Per technetate by a Mesoporous Zr Metal–Organic Framework and Examination of Anion Binding Motifs. *Chem. Mater.* **2018**, *30* (4), 1277-1284.
20. Kato, S.; Otake, K.-i.; Chen, H.; Akpınar, I.; Buru, C. T.; Islamoglu, T.; Snurr, R. Q.; Farha, O. K., Zirconium-Based Metal–Organic Frameworks for the Removal of Protein-Bound Uremic Toxin from Human Serum Albumin. *J. Am. Chem. Soc.* **2019**, *141* (6), 2568-2576.
21. Howarth, A. J.; Liu, Y. Y.; Li, P.; Li, Z. Y.; Wang, T. C.; Hupp, J.; Farha, O. K., Chemical, Thermal and Mechanical Stabilities of Metal-Organic Frameworks. *Nat. Rev. Mater.* **2016**, *1* (3), 15018.
22. Lindström, E. S.; Kamst-Van Agterveld, M. P.; Zwart, G., Distribution of Typical Freshwater Bacterial Groups Is Associated with Ph, Temperature, and Lake Water Retention Time. *Appl. Environ. Microbiol.* **2005**, *71* (12), 8201-8206.
23. Mondloch, J. E.; Katz, M. J.; Planas, N.; Semrouni, D.; Gagliardi, L.; Hupp, J. T.; Farha, O. K., Are Zr 6-Based Mofs Water Stable? Linker Hydrolysis Vs. Capillary-Force-Driven Channel Collapse. *Chem. Commun.* **2014**, *50* (64), 8944-8946.
24. Yuan, S.; Feng, L.; Wang, K.; Pang, J.; Bosch, M.; Lollar, C.; Sun, Y.; Qin, J.; Yang, X.; Zhang, P.; Wang, Q.; Zou, L.; Zhang, Y.; Zhang, L.; Fang, Y.; Li, J.; Zhou, H.-C., Stable Metal–Organic Frameworks: Design, Synthesis, and Applications. *Adv. Mater.* **2018**, *30* (37), 1704303.
25. Wang, B.; Lv, X.-L.; Feng, D.; Xie, L.-H.; Zhang, J.; Li, M.; Xie, Y.; Li, J.-R.; Zhou, H.-C., Highly Stable Zr(IV)-Based Metal–Organic Frameworks for the Detection and Removal of Antibiotics and Organic Explosives in Water. *J. Am. Chem. Soc.* **2016**, *138* (19), 6204-6216.
26. Hansen, L. D., Christensen, J. J., Izatt, R. M., Entropy Titration. A Calorimetric Method for the Determination of Dg (K), Dh and Ds. *Chem. Commun.* **1965**, *0*, 36-38.
27. B., R. L., Temperature Dependence of the Hydrophobic Interaction in Protein Folding. *Proc. Natl. Acad. Sci. U. S. A* **1986**, *83*, 8069-8072.
28. Spolar, R. S., Livingstone, J. R., Thomas Record, Jr. M., Use of Liquid Hydrocarbon and Amide Transfer Data to Estimate Contributions to Thermodynamic Functions of Protein Folding from the Removal of Nonpolar and Polar Surface from Water. *Biochemistry* **1992**, *31*, 3947-3955.
29. Christensen, J. J., I. R. M., Hansen, L. D., Patridge, J. A., Entropy Titration. A Calorimetric Method for the Determination of Dg, Dh, and Ds from a Single Thermometric Titration. *J. Phys. Chem.* **1966**, *70*, 2003-2010.
30. Holbrook, J. A., Capp, M. W., Saecker, R. M., Thomas Record, Jr. M., Enthalpy and Heat Capacity Changes for Formation of an Oligometric DNA Suplex: Interpretation in Terms of Coupled Processes of Formation and Association of Single-Stranded Helices. *Biochemistry* **1999**, *38*, 8409-8422.
31. Robert, B. R., (Extra)Thermodynamics of the Drug-Receptor Interaction. *Life Sci.* **1999**, *65* (10), 967-980.

32. Bradshaw, J. M.; Waksman, G., Calorimetric Investigation of Proton Linkage by Monitoring Both the Enthalpy and Association Constant of Binding: Application to the Interaction of the Src Sh2 Domain with a High-Affinity Tyrosyl Phosphopeptide. *Biochemistry* **1998**, *37* (44), 15400-15407.
33. Penn, C. J.; Gonzalez, J. M.; Chagas, I., Investigation of Atrazine Sorption to Biochar with Titration Calorimetry and Flow-through Analysis: Implications for Design of Pollution-Control Structures. *Front. Chem.* **2018**, *6*.
34. Moreno-Pirajan, J. C.; Giraldo, L., Design, Construction, and Calibration of an Isothermal Titration Calorimeter and Its Application in the Study of the Adsorption of Phenolic Compounds. *Rev Sci Instrum* **2012**, *83* (1).
35. Aykaç, A. N., M.; Malanga, M; Agostoni, V.; Casas-Solvas, J. M.; Fenyvesi, É.; Gref, R.; Vargas-Berenguel, A., A Non-Covalent “Click Chemistry” Strategy to Efficiently coat highly Porous Mof Nanoparticles with a Stable Polymeric Shell. *Biochim. Biophys. Acta* **2017**, *1861*, 1606-1616.
36. Agostoni, V. C., T.; Horcajada, P.; Willaime, H.; Anand, R.; Semiramoth, N.; Baati, T.; Hall, S.; Maurin, G.; Chacun, H.; Boushemal, K.; Martineau, C.; Taelle, F.; Couvreur, P.; Rogez-Kreuz, C.; Clayette, P.; Monti, S.; Serre, C.; Gref, R., Towards an Improved Anti-Hiv Activity of Nrti Via Metal–Organic Frameworks Nanoparticles *Adv. Healthcare Mater.* **2013**, *2*, 1630-1637.
37. Agostoni, V.; Anand, R.; Monti, S.; Hall, S.; Maurin, G.; Horcajada, P.; Serre, C.; Bouchemal, K.; Gref, R., Impact of Phosphorylation on the Encapsulation of Nucleoside Analogues within Porous Iron(Iii) Metal–Organic Framework Mil-100(Fe) Nanoparticles. *J. Mater. Chem. B* **2013**, *1* (34), 4231-4242.
38. Deria, P.; Mondloch, J. E.; Tyljanakis, E.; Ghosh, P.; Bury, W.; Snurr, R. Q.; Hupp, J. T.; Farha, O. K., Perfluoroalkane Functionalization of Nu-1000 Via Solvent-Assisted Ligand Incorporation: Synthesis and Co<sub>2</sub> Adsorption Studies. *J. Am. Chem. Soc.* **2013**, *135* (45), 16801-16804.
39. He, H. M.; Sun, Q.; Gao, W. Y.; Perman, J. A.; Sun, F. X.; Zhu, G. S.; Aguila, B.; Forrest, K.; Space, B.; Ma, S. Q., A Stable Metal–Organic Framework Featuring a Local Buffer Environment for Carbon Dioxide Fixation. *Angew Chem Int Edit* **2018**, *57* (17), 4657-4662.
40. Energy, U. S. D. o., *Plutonium: The First 50 Years ... Doe/Dp-0137 ... U.S. Department of Energy ... February 1996*. publisher not identified: 1998.
41. Offenbauer, P., Defense Nuclear Facilities Safety Board: The First Twenty Years. **2009**.
42. Gephart, R.; Lundgren, R. E. *Hanford Tank Clean Up: A Guide to Understanding the Technical Issues*; Pacific Northwest Lab., Richland, WA (United States): 1995.
43. Icenhower, J. P.; Qafoku, N. P.; Zachara, J. M.; Martin, W. J., The Biogeochemistry of Technetium: A Review of the Behavior of an Artificial Element in the Natural Environment. *Am J Sci* **2010**, *310* (8), 721-752.
44. Icenhower, J. P. Q., N.P.; Martin, W.J.; Zachara, J.M. U.S. Department of Energy, The Geochemistry of Technetium: A Summary of the Behavior of an Artificial Element in the Natural Environment. **2008**.

45. Childs, B. C.; Poineau, F.; Czerwinski, K. R.; Sattelberger, A. P., The Nature of the Volatile Technetium Species Formed During Vitrification of Borosilicate Glass. *J. Radioanal. Nucl. Chem.* **2015**, *306* (2), 417-421.
46. Darab, J. G.; Smith, P. A., Chemistry of Technetium and Rhenium Species During Low-Level Radioactive Waste Vitrification. *Chem. Mater.* **1996**, *8* (5), 1004-1021.
47. Pegg, I. L., Behavior of Technetium in Nuclear Waste Vitrification Processes. *J. Radioanal. Nucl. Chem.* **2015**, *305* (1), 287-292.
48. Banerjee, D.; Kim, D.; Schweiger, M. J.; Kruger, A. A.; Thallapally, P. K., Removal of Tco4(-) Ions from Solution: Materials and Future Outlook. *Chem. Soc. Rev.* **2016**, *45* (10), 2724-39.
49. Bonnesen, P. V.; Brown, G. M.; Alexandratos, S. D.; Bavoux, L. B.; Presley, D. J.; Patel, V.; Ober, R.; Moyer, B. A., Development of Bifunctional Anion-Exchange Resins with Improved Selectivity and Sorptive Kinetics for Per technetate: Batch-Equilibrium Experiments. *Environ. Sci. Technol.* **2000**, *34* (17), 3761-3766.
50. Sarri, S.; Misaelides, P.; Zamboulis, D.; Gaona, X.; Altmaier, M.; Geckeis, H., Rhenium(Vii) and Technetium(Vii) Separation from Aqueous Solutions Using a Polyethylenimine-Epichlorohydrin Resin. *J. Radioanal. Nucl. Chem.* **2016**, *307* (1), 681-689.
51. Zu, J. H.; Wei, Y. Z.; Ye, M. S.; Tang, F. D.; He, L. F.; Liu, R. Q., Preparation of a New Anion Exchanger by Pre-Irradiation Grafting Technique and Its Adsorptive Removal of Rhenium (Vii) as Analogue to Tc-99. *Nucl. Sci. Tech.* **2015**, *26* (1), 69-75.
52. Ding, Q. W.; Ding, F.; Qian, T. W.; Zhao, D. Y.; Wang, L. X., Reductive Immobilization of Rhenium in Soil and Groundwater Using Pyrite Nanoparticles. *Water Air Soil Poll.* **2015**, *226* (12), 10.
53. Lenell, B. A.; Arai, Y., Perrhenate Sorption Kinetics in Zerovalent Iron in High Ph and Nitrate Media. *J. Hazard. Mater.* **2017**, *321*, 335-343.
54. Levitskaia, T. G.; Chatterjee, S.; Pence, N. K.; Romero, J.; Varga, T.; Engelhard, M. H.; Du, Y. G.; Kovarik, L.; Arey, B. W.; Bowden, M. E.; Walter, E. D., Inorganic Tin Aluminophosphate Nanocomposite for Reductive Separation of Per technetate. *Environ. Sci. Nano* **2016**, *3* (5), 1003-1013.
55. Li, J.; Chen, C. L.; Zhang, R.; Wang, X. K., Reductive Immobilization of Re(Vii) by Graphene Modified Nanoscale Zero-Valent Iron Particles Using a Plasma Technique. *Sci. China Chem.* **2016**, *59* (1), 150-158.
56. Neeway, J. J.; Asmussen, R. M.; Lawter, A. R.; Bowden, M. E.; Lukens, W. W.; Sarma, D.; Riley, B. J.; Kanatzidis, M. G.; Qafoku, N. P., Removal of Tco4- from Representative Nuclear Waste Streams with Layered Potassium Metal Sulfide Materials. *Chem. Mater.* **2016**, *28* (11), 3976-3983.
57. Katayev, E. A.; Kolesnikov, G. V.; Sessler, J. L., Molecular Recognition of Per technetate and Perrhenate. *Chem. Soc. Rev.* **2009**, *38* (6), 1572-86.
58. Banerjee, D.; Elsaidi, S. K.; Aguila, B.; Li, B.; Kim, D.; Schweiger, M. J.; Kruger, A. A.; Doonan, C. J.; Ma, S.; Thallapally, P. K., Removal of Per technetate-Related Oxyanions from Solution Using Functionalized Hierarchical Porous Frameworks. *Chemistry* **2016**, *22* (49), 17581-17584.

59. Banerjee, D.; Xu, W.; Nie, Z.; Johnson, L. E.; Coghlan, C.; Sushko, M. L.; Kim, D.; Schweiger, M. J.; Kruger, A. A.; Doonan, C. J.; Thallapally, P. K., Zirconium-Based Metal-Organic Framework for Removal of Perrhenate from Water. *Inorg. Chem.* **2016**, *55* (17), 8241-3.
60. Colinas, I. R.; Silva, R. C.; Oliver, S. R., Reversible, Selective Trapping of Perchlorate from Water in Record Capacity by a Cationic Metal-Organic Framework. *Environ Sci Technol* **2016**, *50* (4), 1949-54.
61. Desai, A. V.; Manna, B.; Karmakar, A.; Sahu, A.; Ghosh, S. K., A Water-Stable Cationic Metal-Organic Framework as a Dual Adsorbent of Oxoanion Pollutants. *Angew. Chem.-Int. Edit.* **2016**, *55* (27), 7811-5.
62. Sheng, D.; Zhu, L.; Xu, C.; Xiao, C.; Wang, Y.; Wang, Y.; Chen, L.; Diwu, J.; Chen, J.; Chai, Z.; Albrecht-Schmitt, T. E.; Wang, S., Efficient and Selective Uptake of Tco<sub>4</sub><sup>-</sup> by a Cationic Metal-Organic Framework Material with Open Ag<sup>+</sup> Sites. *Environ Sci Technol* **2017**, *51* (6), 3471-3479.
63. Zhu, L.; Sheng, D.; Xu, C.; Dai, X.; Silver, M. A.; Li, J.; Li, P.; Wang, Y.; Wang, Y.; Chen, L.; Xiao, C.; Chen, J.; Zhou, R.; Zhang, C.; Farha, O. K.; Chai, Z.; Albrecht-Schmitt, T. E.; Wang, S., Identifying the Recognition Site for Selective Trapping of 99tco<sub>4</sub><sup>-</sup> in a Hydrolytically Stable and Radiation Resistant Cationic Metal-Organic Framework. *J. Am. Chem. Soc.* **2017**, *139* (42), 14873-14876.
64. Goh, K. H.; Lim, T. T.; Dong, Z., Application of Layered Double Hydroxides for Removal of Oxyanions: A Review. *Water Res.* **2008**, *42* (6-7), 1343-68.
65. Sheng, G.; Tang, Y.; Linghu, W.; Wang, L.; Li, J.; Li, H.; Wang, X.; Huang, Y., Enhanced Immobilization of Reo 4<sup>-</sup> by Nanoscale Zerovalent Iron Supported on Layered Double Hydroxide Via an Advanced Xafs Approach: Implications for Tco 4<sup>-</sup> Sequestration. *Appl. Catal. B* **2016**, *192*, 268-276.
66. Duffey, C.; King, W.; Hamm, L. *Determination of Perrhenate Adsorption Kinetics from Hanford Waste Simulants Using Superling 639 Resin*; SRS: 2002.
67. Nash, C.; Musall, B.; Morse, M.; McCabe, D., Characterization of Superlig 639 Rhenium and Technetium Resin with Batch Contact and Column Tests. *Sep Sci Technol* **2015**, *50* (18), 2881-2887.
68. Zhou, H. C.; Long, J. R.; Yaghi, O. M., Introduction to Metal-Organic Frameworks. *Chem. Rev.* **2012**, *112* (2), 673-4.
69. Farha, O. K.; Eryazici, I.; Jeong, N. C.; Hauser, B. G.; Wilmer, C. E.; Sarjeant, A. A.; Snurr, R. Q.; Nguyen, S. T.; Yazaydin, A. O.; Hupp, J. T., Metal-Organic Framework Materials with Ultrahigh Surface Areas: Is the Sky the Limit? *J. Am. Chem. Soc.* **2012**, *134* (36), 15016-21.
70. Eddaoudi, M.; Kim, J.; Rosi, N.; Vodak, D.; Wachter, J.; O'Keeffe, M.; Yaghi, O. M., Systematic Design of Pore Size and Functionality in Isoreticular Mofs and Their Application in Methane Storage. *Science* **2002**, *295* (5554), 469-72.
71. Sumida, K.; Rogow, D. L.; Mason, J. A.; McDonald, T. M.; Bloch, E. D.; Herm, Z. R.; Bae, T. H.; Long, J. R., Carbon Dioxide Capture in Metal-Organic Frameworks. *Chem. Rev.* **2012**, *112* (2), 724-81.
72. Horcajada, P.; Chalati, T.; Serre, C.; Gillet, B.; Sebrie, C.; Baati, T.; Eubank, J. F.; Heurtaux, D.; Clayette, P.; Kreuz, C.; Chang, J. S.; Hwang, Y. K.; Marsaud, V.; Bories,

- P. N.; Cynober, L.; Gil, S.; Ferey, G.; Couvreur, P.; Gref, R., Porous Metal-Organic-Framework Nanoscale Carriers as a Potential Platform for Drug Delivery and Imaging. *Nat. Mater.* **2010**, *9* (2), 172-8.
73. Audu, C. O.; Nguyen, H. G. T.; Chang, C. Y.; Katz, M. J.; Mao, L.; Farha, O. K.; Hupp, J. T.; Nguyen, S. T., The Dual Capture of Asv and Asiii by Uio-66 and Analogues. *Chem. Sci.* **2016**, *7* (10), 6492-6498.
74. Howarth, A. J.; Katz, M. J.; Wang, T. C.; Platero-Prats, A. E.; Chapman, K. W.; Hupp, J. T.; Farha, O. K., High Efficiency Adsorption and Removal of Selenate and Selenite from Water Using Metal-Organic Frameworks. *J. Am. Chem. Soc.* **2015**, *137* (23), 7488-94.
75. Howarth, A. J.; Wang, T. C.; Al-Juaid, S. S.; Aziz, S. G.; Hupp, J. T.; Farha, O. K., Efficient Extraction of Sulfate from Water Using a Zr-Metal-Organic Framework. *Dalton Trans.* **2016**, *45* (1), 93-7.
76. Mondloch, J. E.; Bury, W.; Fairen-Jimenez, D.; Kwon, S.; DeMarco, E. J.; Weston, M. H.; Sarjeant, A. A.; Nguyen, S. T.; Stair, P. C.; Snurr, R. Q.; Farha, O. K.; Hupp, J. T., Vapor-Phase Metalation by Atomic Layer Deposition in a Metal-Organic Framework. *J. Am. Chem. Soc.* **2013**, *135* (28), 10294-7.
77. Wang, T. C.; Vermeulen, N. A.; Kim, I. S.; Martinson, A. B.; Stoddart, J. F.; Hupp, J. T.; Farha, O. K., Scalable Synthesis and Post-Modification of a Mesoporous Metal-Organic Framework Called Nu-1000. *Nat. Protoc.* **2016**, *11* (1), 149-62.
78. Li, Y. M.; Bi, M. L.; Wang, Z. P.; Li, R.; Shi, K. L.; Wu, W. S., Organic Modification of Bentonite and Its Application for Perrhenate (an Analogue of Per technetate) Removal from Aqueous Solution. *J. Taiwan Inst. Chem. E* **2016**, *62*, 104-111.
79. Stephan, H.; Spies, H.; Johannsen, B.; Gloe, K.; Gorke, M.; Vögtle, F., Synthesis and Host-Guest Properties of Multi-Crown Dendrimers Towards Sodium Per technetate and Mercury(Ii) Chloride. *Eur. J. Inorg. Chem.* **2001**, *2001* (11), 2957-2963.
80. Fei, H.; Bresler, M. R.; Oliver, S. R., A New Paradigm for Anion Trapping in High Capacity and Selectivity: Crystal-to-Crystal Transformation of Cationic Materials. *J. Am. Chem. Soc.* **2011**, *133* (29), 11110-3.
81. Zhu, L.; Xiao, C. L.; Dai, X.; Li, J.; Gui, D. X.; Sheng, D. P.; Chen, L. H.; Zhou, R. H.; Chai, Z. F.; Albrecht-Schmitt, T. E.; Wang, S., Exceptional Perrhenate/Per technetate Uptake and Subsequent Immobilization by a Low-Dimensional Cationic Coordination Polymer: Overcoming the Hofmeister Bias Selectivity. *Environ. Sci. Technol. Lett.* **2017**, *4* (7), 316-322.
82. Han, D.; Li, X. X.; Peng, J.; Xu, L.; Li, J. Q.; Li, H. B.; Zhai, M. L., A New Imidazolium-Based Polymeric Ionic Liquid Gel with High Adsorption Capacity for Perrhenate. *RSC Adv.* **2016**, *6* (73), 69052-69059.
83. Wang, S.; Alekseev, E. V.; Diwu, J.; Casey, W. H.; Phillips, B. L.; Depmeier, W.; Albrecht-Schmitt, T. E., Ndtb-1: A Supertetrahedral Cationic Framework That Removes Tco4- from Solution. *Angew. Chem.-Int. Edit.* **2010**, *49* (6), 1057-60.
84. Wang, S.; Yu, P.; Purse, B. A.; Orta, M. J.; Diwu, J.; Casey, W. H.; Phillips, B. L.; Alekseev, E. V.; Depmeier, W.; Hobbs, D. T.; Albrecht-Schmitt, T. E., Selectivity, Kinetics, and Efficiency of Reversible Anion Exchange with Tco4- in a Supertetrahedral Cationic Framework. *Adv. Func. Mater.* **2012**, *22* (11), 2241-2250.

85. Darab, J. G.; Amonette, A. B.; Burke, D. S. D.; Orr, R. D.; Ponder, S. M.; Schrick, B.; Mallouk, T. E.; Lukens, W. W.; Caulder, D. L.; Shuh, D. K., Removal of Pertechnetate from Simulated Nuclear Waste Streams Using Supported Zerovalent Iron. *Chem. Mater.* **2007**, *19* (23), 5703-5713.
86. Wang, Y.; Gao, H., Compositional and Structural Control on Anion Sorption Capability of Layered Double Hydroxides (Ldhs). *J. Colloid Interface Sci.* **2006**, *301* (1), 19-26.
87. Riley, B. J.; Chun, J.; Um, W.; Lepry, W. C.; Matyas, J.; Olszta, M. J.; Li, X.; Polychronopoulou, K.; Kanatzidis, M. G., Chalcogen-Based Aerogels as Sorbents for Radionuclide Remediation. *Environ Sci Technol* **2013**, *47* (13), 7540-7.
88. Scales, N.; Chen, J.; Aughterson, R. D.; Karatchevtseva, I.; Stopic, A.; Lumpkin, G. R.; Luca, V., Porous Zr 2 Sc-Carbon Composite Microspheres: Possible Radiation Tolerant Sorbents and Transmutation Hosts for Technetium-99. *Microporous Mesoporous Mater.* **2017**.
89. Atilgan, A.; Islamoglu, T.; Howarth, A. J.; Hupp, J. T.; Farha, O. K., Detoxification of a Sulfur Mustard Simulant Using a Bodipy-Functionalized Zirconium-Based Metal-Organic Framework. *ACS Appl. Mater. Inter.* **2017**, *9* (29), 24555-24560.
90. Burla, M. C.; Caliendo, R.; Carrozzini, B.; Cascarano, G. L.; Cuocci, C.; Giacobazzo, C.; Mallamo, M.; Mazzone, A.; Polidori, G., Crystal Structure Determination and Refinement Viasir2014. *J. Appl. Cryst.* **2015**, *48* (1), 306-309.
91. Sheldrick, G. M., Crystal Structure Refinement with Shelxl. *Acta Crystallogr. C Struct. Chem.* **2015**, *71* (Pt 1), 3-8.
92. Kabuto, H.; Amakawa, M.; Mankura, M.; Yamanushi, T. T.; Mori, A., Docosahexaenoic Acid Ethyl Ester Enhances 6-Hydroxydopamine-Induced Neuronal Damage by Induction of Lipid Peroxidation in Mouse Striatum. *Neurochem. Res.* **2009**, *34* (7), 1299-303.
93. Spek, A. L., Structure Validation in Chemical Crystallography. *Acta Crystallogr. D Biol. Crystallogr.* **2009**, *65* (Pt 2), 148-55.
94. Organization, W. H., Guidelines for Drinking-Water Quality, Fourth Edition. *WHO chronicle* **2011**, *38* (4), 104-8.
95. Organization, W. H., Selenium in Drinking-Water. Background Document for Development of Who Guidelines for Drinking-Water Quality. *WHO/HSE/WSH/10.01/14* **2011**.
96. Lemly, A. D., Aquatic Selenium Pollution Is a Global Environmental Safety Issue. *Ecotox. Environ. Safe.* **2004**, *59* (1), 44-56.
97. Agency, U. S. E. P., National Primary Drinking Water Regulations. *EPA 816-F-09-004* **2009**.
98. Murphy, A. P., Removal of Selenate from Water by Chemical Reduction. *Ind. Eng. Chem. Res.* **1988**, *27* (1), 187-191.
99. Khalilian, M.; Zolfaghari, M. R.; Sole, M., Bacillus Sp. Strain Qw90, a Bacterial Strain with a High Potential Application in Bioremediation of Selenite. *Report of Health Care* **2015**.
100. Khalilian, M.; Zolfaghari, M. R.; Soleimani, M., High Potential Application in Bioremediation of Selenate by Proteus Hauseri Strain Qw4. *Iran J. Microbiol.* **2015**, *7* (2), 94.

101. Martin, U.; Katarína, B.; Marek, B.; Peter, M., Fungal Selenium(Vi) Accumulation and Biotransformation—Filamentous Fungi in Selenate Contaminated Aqueous Media Remediation. *CLEAN – Soil, Air, Water* **2016**, *44* (6), 610-614.
102. Adriano, D.; Wenzel, W.; Vangronsveld, J.; Bolan, N., Role of Assisted Natural Remediation in Environmental Cleanup. *Geoderma* **2004**, *122* (2-4), 121-142.
103. Wu, L., Review of 15 Years of Research on Ecotoxicology and Remediation of Land Contaminated by Agricultural Drainage Sediment Rich in Selenium. *Ecotox. Environ. Safe.* **2004**, *57* (3), 257-269.
104. Peak, D., Adsorption Mechanisms of Selenium Oxyanions at the Aluminum Oxide/Water Interface. *J. Colloid Interface Sci.* **2006**, *303* (2), 337-345.
105. Jegadeesan, G.; Mondal, K.; Lalvani, Selenate Removal from Sulfate Containing Aqueous Solutions. *Environ. Technol.* **2005**, *26* (10), 1181-1188.
106. Yamani, J. S.; Lounsbury, A. W.; Zimmerman, J. B., Adsorption of Selenite and Selenate by Nanocrystalline Aluminum Oxide, Neat and Impregnated in Chitosan Beads. *Water Res.* **2014**, *50*, 373-381.
107. Shannon, M. A.; Bohn, P. W.; Elimelech, M.; Georgiadis, J. G.; Marinas, B. J.; Mayes, A. M., Science and Technology for Water Purification in the Coming Decades. *Nature* **2008**, *452* (7185), 301.
108. Dias, E. M.; Petit, C., Towards the Use of Metal-Organic Frameworks for Water Reuse: A Review of the Recent Advances in the Field of Organic Pollutants Removal and Degradation and the Next Steps in the Field. *J. Mater. Chem. A* **2015**, *3* (45), 22484-22506.
109. Howarth, A. J.; Liu, Y.; Hupp, J. T.; Farha, O. K., Metal–Organic Frameworks for Applications in Remediation of Oxyanion/Cation-Contaminated Water. *CrystEngComm* **2015**, *17* (38), 7245-7253.
110. Kadhom, M.; Deng, B., Metal-Organic Frameworks (Mofs) in Water Filtration Membranes for Desalination and Other Applications. *Appl. Mater. Today* **2018**, *11*, 219-230.
111. Siqing, L.; Yifa, C.; Xiaokun, P.; Shenghan, Z.; Xiao, F.; Junwen, Z.; Bo, W., Water Purification: Adsorption over Metal-Organic Frameworks. *Chin. J. Chem.* **2016**, *34* (2), 175-185.
112. Sheng, D.; Zhu, L.; Xu, C.; Xiao, C.; Wang, Y.; Wang, Y.; Chen, L.; Diwu, J.; Chen, J.; Chai, Z.; Albrecht-Schmitt, T. E.; Wang, S., Efficient and Selective Uptake of Tco4– by a Cationic Metal–Organic Framework Material with Open Ag+ Sites. *Environ. Sci. Technol.* **2017**, *51* (6), 3471-3479.
113. Ma, L.; Falkowski, J. M.; Abney, C.; Lin, W., A Series of Isoreticular Chiral Metal–Organic Frameworks as a Tunable Platform for Asymmetric Catalysis. *Nat. Chem.* **2010**, *2* (10), 838.
114. Yuan, D.; Zhao, D.; Sun, D.; Zhou, H. C., An Isoreticular Series of Metal–Organic Frameworks with Dendritic Hexacarboxylate Ligands and Exceptionally High Gas-Uptake Capacity. *Angew. Chem.-Int. Edit.* **2010**, *49* (31), 5357-5361.
115. Chan, Y. T.; Kuan, W. H.; Chen, T. Y.; Wang, M. K., Adsorption Mechanism of Selenate and Selenite on the Binary Oxide Systems. *Water Res.* **2009**, *43* (17), 4412-4420.
116. Zhu, L.; Zhang, L.; Li, J.; Zhang, D.; Chen, L.; Sheng, D.; Yang, S.; Xiao, C.; Wang, J.; Chai, Z.; Albrecht-Schmitt, T. E.; Wang, S., Selenium Sequestration in a Cationic

- Layered Rare Earth Hydroxide: A Combined Batch Experiments and Exafs Investigation. *Environ. Sci. Technol.* **2017**, *51* (15), 8606-8615.
117. Ma, L.; Islam, S. M.; Xiao, C.; Zhao, J.; Liu, H.; Yuan, M.; Sun, G.; Li, H.; Ma, S.; Kanatzidis, M. G., Rapid Simultaneous Removal of Toxic Anions [Hseo3]<sup>-</sup>, [Seo3]<sup>2-</sup>, and [Seo4]<sup>2-</sup>, and Metals Hg<sup>2+</sup>, Cu<sup>2+</sup>, and Cd<sup>2+</sup> by Mos<sub>4</sub><sup>2-</sup> Intercalated Layered Double Hydroxide. *J. Am. Chem. Soc.* **2017**, *139* (36), 12745-12757.
  118. Nisa, G.; Mustafa, G.; Osman, A. A., Adsorption of Selenite and Selenate Ions onto Thiourea-Formaldehyde Resin. *J. Appl. Polym. Sci.* **2011**, *122* (2), 1134-1141.
  119. Tian, N.; Zhou, Z.; Tian, X.; Yang, C.; Li, Y., Superior Capability of MgAl<sub>2</sub>O<sub>4</sub> for Selenite Removal from Contaminated Groundwater During Its Reconstruction of Layered Double Hydroxides. *Sep. Purif. Technol.* **2017**, *176*, 66-72.
  120. Toshiyuki, Y.; Takashi, T.; Hideaki, Y., Selective Selenate Adsorption on Cationated Amino-Functionalized Mcm-41. *Bull. Chem. Soc. Jpn.* **2003**, *76* (11), 2225-2232.
  121. Li, J.; Liu, Y.; Wang, X.; Zhao, G.; Ai, Y.; Han, B.; Wen, T.; Hayat, T.; Alsaedi, A.; Wang, X., Experimental and Theoretical Study on Selenate Uptake to Zirconium Metal–Organic Frameworks: Effect of Defects and Ligands. *Chem. Eng. J.* **2017**, *330*, 1012-1021.
  122. Liu, Y.; Klet, R. C.; Hupp, J. T.; Farha, O., Probing the Correlations between the Defects in Metal–Organic Frameworks and Their Catalytic Activity by an Epoxide Ring-Opening Reaction. *Chem. Commun.* **2016**, *52* (50), 7806-7809.
  123. Eklund, L.; Persson, I., Structure and Hydrogen Bonding of the Hydrated Selenite and Selenate Ions in Aqueous Solution. *Dalton Trans.* **2014**, *43* (17), 6315-6321.
  124. Jiang, J.; Gándara, F.; Zhang, Y.-B.; Na, K.; Yaghi, O. M.; Klemperer, W. G., Superacidity in Sulfated Metal–Organic Framework-808. *J. Am. Chem. Soc.* **2014**, *136* (37), 12844-12847.
  125. Klet, R. C.; Liu, Y.; Wang, T. C.; Hupp, J. T.; Farha, O. K., Evaluation of Bronsted Acidity and Proton Topology in Zr- and Hf-Based Metal–Organic Frameworks Using Potentiometric Acid-Base Titration. *J. Mater. Chem. A* **2016**, *4* (4), 1479-1485.
  126. Rangwani, S.; Howarth, A. J.; DeStefano, M. R.; Malliakas, C. D.; Platero-Prats, A. E.; Chapman, K. W.; Farha, O. K., Adsorptive Removal of Sb(V) from Water Using a Mesoporous Zr-Based Metal–Organic Framework. *Polyhedron*.
  127. Sheldrick, G. M., Shelxt–Integrated Space-Group and Crystal-Structure Determination. *Acta Crystallogr. A* **2015**, *71* (1), 3-8.
  128. Kabuto, C.; Akine, S.; Nemoto, T.; Kwon, E., Release of Software (Yadokari-Xg 2009) for Crystal Structure Analyses. *Nihon Kessho Gakkaishi* **2010**, *51*, 218-224.
  129. Environmental Protection Agency, U. S. Edsp: Weight of Evidence Analysis of Potential Interaction with the Estrogen, Androgen or Thyroid Pathways. <https://www.epa.gov/endocrine-disruption/endocrine-disruptor-screening-program-tier-1-screening-determinations-and> (accessed 1 June 2018).
  130. Kong, X.; Jiang, J.; Ma, J.; Yang, Y.; Liu, W.; Liu, Y., Degradation of Atrazine by Uv/Chlorine: Efficiency, Influencing Factors, and Products. *Water Res.* **2016**, *90*, 15-23.
  131. Runes, H. B.; Bottomley, P. J.; Lerch, R. N.; Jenkins, J. J., Atrazine Remediation in Wetland Microcosms. *Environ. Toxicol. Chem.* **2001**, *20* (5), 1059-1066.

132. United States Environmental Protection Agency National Primary Drinking Water Regulations. <https://www.epa.gov/ground-water-and-drinking-water/national-primary-drinking-water-regulations> (accessed 16 June 2018).
133. Brown, N. W.; Roberts, E. P. L.; Chasiotis, A.; Cherdron, T.; Sanghrajka, N., Atrazine Removal Using Adsorption and Electrochemical Regeneration. *Water Res.* **2004**, *38* (13), 3067-3074.
134. Broseus, R.; Vincent, S.; Aboufadi, K.; Daneshvar, A.; Sauve, S.; Barbeau, B.; Prevost, M., Ozone Oxidation of Pharmaceuticals, Endocrine Disruptors and Pesticides During Drinking Water Treatment. *Water Res.* **2009**, *43* (18), 4707-4717.
135. Gomes, J.; Costa, R.; Quinta-Ferreira, R. M.; Martins, R. C., Application of Ozonation for Pharmaceuticals and Personal Care Products Removal from Water. *Sci. Total Environ.* **2017**, *586*, 265-283.
136. Komtchou, S.; Dirany, A.; Drogui, P.; Robert, D.; Lafrance, P., Removal of Atrazine and Its by-Products from Water Using Electrochemical Advanced Oxidation Processes. *Water Res.* **2017**, *125*, 91-103.
137. Ali, I.; Gupta, V. K., Advances in Water Treatment by Adsorption Technology. *Nat. Protoc.* **2007**, *1*, 2661-2667.
138. Ali, I., Water Treatment by Adsorption Columns: Evaluation at Ground Level. *Sep. Purif. Rev.* **2014**, *43* (3), 175-205.
139. Chingombe, P.; Saha, B.; Wakeman, R. J., Sorption of Atrazine on Conventional and Surface Modified Activated Carbons. *J. Colloid Interface Sci.* **2006**, *302* (2), 408-416.
140. Lemic, J.; Kovacevic, D.; Tomasevic-Canovic, M.; Kovacevic, D.; Stanic, T.; Pfend, R., Removal of Atrazine, Lindane and Diazinone from Water by Organo-Zeolites. *Water Res.* **2006**, *40* (5), 1079-1085.
141. Doulia, D.; Hourdakis, A.; Rigas, F.; Anagnostopoulos, E., Removal of Atrazine from Water by Use of Nonionic Polymeric Resins. *J. Environ. Sci. Health A* **2008**, *32* (9-10), 2635-2656.
142. Sanchez-Martin, M. J.; Rodriguez-Cruz, M. S.; Andrades, M. S.; Sanchez-Camazano, M., Efficiency of Different Clay Minerals Modified with a Cationic Surfactant in the Adsorption of Pesticides: Influence of Clay Type and Pesticide Hydrophobicity. *Appl. Clay Sci.* **2006**, *31* (3-4), 216-228.
143. Tan, G.; Sun, W.; Xu, Y.; Wang, H.; Xu, N., Sorption of Mercury (Ii) and Atrazine by Biochar, Modified Biochars and Biochar Based Activated Carbon in Aqueous Solution. *Bioresour. Technol.* **2016**, *211*, 727-735.
144. Mohan, D.; Pittman, C. U., Arsenic Removal from Water/Wastewater Using Adsorbents—a Critical Review. *J. Hazard. Mater.* **2007**, *142* (1), 1-53.
145. Xu, J.; Wang, L.; Zhu, Y., Decontamination of Bisphenol a from Aqueous Solution by Graphene Adsorption. *Langmuir* **2012**, *28* (22), 8418-8425.
146. Gupta, V. K.; Saleh, T. A., Sorption of Pollutants by Porous Carbon, Carbon Nanotubes and Fullerene- an Overview. *Environ. Sci. Poll. Res.* **2013**, *20* (5), 2828-2843.
147. Zhang, W.; Zheng, J.; Zheng, P.; Qiu, R., Atrazine Immobilization on Sludge Derived Biochar and the Interactive Influence of Coexisting Pb(Ii) or Cr(Vi) Ions. *Chemosphere* **2015**, *134*, 438-445.

148. Tang, W.-W.; Zeng, G.-M.; Gong, J.-L.; Liu, Y.; Wang, X.-Y.; Liu, Y.-Y.; Liu, Z.-F.; Chen, L.; Zhang, X.-R.; Tu, D.-Z., Simultaneous Adsorption of Atrazine and Cu (II) from Wastewater by Magnetic Multi-Walled Carbon Nanotube. *Chem. Eng. J.* **2012**, *211-212*, 470-478.
149. Hailian Li, M. E., M. O'Keeffe & O.M. Yaghi, Design and Synthesis of an Exceptionally Stable and Highly Porous Metal-Organic Framework. *Nature* **1999**, *402*, 276-279.
150. Furukawa, H.; Cordova, K. E.; O'Keeffe, M.; Yaghi, O. M., The Chemistry and Applications of Metal-Organic Frameworks. *Science* **2013**, *341*, 1230444.
151. Howarth, A. J.; Liu, Y.; Li, P.; Li, Z.; Wang, T. C.; Hupp, J. T.; Farha, O. K., Chemical, Thermal and Mechanical Stabilities of Metal-Organic Frameworks. *Nat. Rev. Mater.* **2016**, *1* (3), 1-15.
152. Susumu, K.; Ryo, K.; Shin-ichiro, N., Functional Porous Coordination Polymers. *Angew. Chem.-Int. Edit.* **2004**, *43* (18), 2334-2375.
153. Wang, Z.; Cohen, S. M., Postsynthetic Modification of Metal-Organic Frameworks. *Chem. Soc. Rev.* **2009**, *38* (5), 1315-1329.
154. Rosi, N. L.; Eckert, J.; Eddaoudi, M.; Vodak, D. T.; Kim, J.; O'Keeffe, M.; Yaghi, O. M., Hydrogen Storage in Microporous Metal-Organic Frameworks. *Science* **2003**, *300* (5622), 1127-1129.
155. Nugent, P.; Belmabkhout, Y.; Burd, S. D.; Cairns, A. J.; Luebke, R.; Forrest, K.; Pham, T.; Ma, S.; Space, B.; Wojtas, L.; Eddaoudi, M.; Zaworotko, M. J., Porous Materials with Optimal Adsorption Thermodynamics and Kinetics for CO<sub>2</sub> Separation. *Nature* **2013**, *495*, 80-84.
156. Xue, D.-X.; Cairns, A. J.; Belmabkhout, Y.; Wojtas, L.; Liu, Y.; Alkordi, M. H.; Eddaoudi, M., Tunable Rare-Earth Fcu-Mofs: A Platform for Systematic Enhancement of CO<sub>2</sub> Adsorption Energetics and Uptake. *J. Am. Chem. Soc.* **2013**, *135* (20), 7660-7667.
157. Alezi, D.; Belmabkhout, Y.; Suyetin, M.; Bhatt, P. M.; Weseliński, Ł. J.; Solovyeva, V.; Adil, K.; Spanopoulos, I.; Trikalitis, P. N.; Emwas, A.-H.; Eddaoudi, M., Mof Crystal Chemistry Paving the Way to Gas Storage Needs: Aluminum-Based Soc-Mof for CH<sub>4</sub>, O<sub>2</sub>, and CO<sub>2</sub> Storage. *J. Am. Chem. Soc.* **2015**, *137* (41), 13308-13318.
158. Schlichte, K.; Kratzke, T.; Kaskel, S., Improved Synthesis, Thermal Stability and Catalytic Properties of the Metal-Organic Framework Compound Cu<sub>3</sub>(Btc)<sub>2</sub>. *Microporous Mesoporous Mater.* **2004**, *73* (1), 81-88.
159. Lee, J.; Farha, O. K.; Roberts, J.; Scheidt, K. A.; Nguyen, S. T.; Hupp, J. T., Metal-Organic Framework Materials as Catalysts. *Chem. Soc. Rev.* **2009**, *38* (5), 1450-1459.
160. Bai, Y.; Dou, Y.; Xie, L. H.; Rutledge, W.; Li, J. R.; Zhou, H. C., Zr-Based Metal-Organic Frameworks: Design, Synthesis, Structure, and Applications. *Chem. Soc. Rev.* **2016**, *45* (8), 2327-2367.
161. Comito, R. J.; Fritzsche, K. J.; Sundell, B. J.; Schmidt-Rohr, K.; Dincă, M., Single-Site Heterogeneous Catalysts for Olefin Polymerization Enabled by Cation Exchange in a Metal-Organic Framework. *J. Am. Chem. Soc.* **2016**, *138* (32), 10232-10237.
162. Grigoropoulos, A.; Whitehead, G. F. S.; Perret, N.; Katsoulidis, A. P.; Chadwick, F. M.; Davies, R. P.; Haynes, A.; Brammer, L.; Weller, A. S.; Xiao, J.; Rosseinsky, M. J., Encapsulation of an Organometallic Cationic Catalyst by Direct Exchange into an Anionic Mof. *Chem. Sci.* **2016**, *7* (3), 2037-2050.

163. Islamoglu, T.; Ortuno, M. A.; Prousaloglou, E.; Howarth, A. J.; Vermeulen, N. A.; Atilgan, A.; Asiri, A. M.; Cramer, C. J.; Farha, O. K., Presence Versus Proximity: The Role of Pendant Amines in the Catalytic Hydrolysis of a Nerve Agent Simulant. *Angew. Chem. Int. Ed.* **2018**, *57* (7), 1949-1953.
164. Horcajada, P.; Serre, C.; Vallet-Regí, M.; Sebban, M.; Taulelle, F.; Férey, G., Metal–Organic Frameworks as Efficient Materials for Drug Delivery. *Angew. Chem. Int. Ed.* **2006**, *118* (36), 6120-6124.
165. Huxford, R. C.; Della Rocca, J.; Lin, W., Metal-Organic Frameworks as Potential Drug Carriers. *Curr. Opin. Chem. Biol.* **2010**, *14* (2), 262-268.
166. Bloch, E. D.; Queen, W. L.; Krishna, R.; Zadrozny, J. M.; Brown, C. M.; Long, J. R., Hydrocarbon Separations in a Metal-Organic Framework with Open Iron(II) Coordination Sites. *Science* **2012**, *335* (6076), 1606-1610.
167. DeCoste, J. B.; Peterson, G. W., Metal-Organic Frameworks for Air Purification of Toxic Chemicals. *Chem. Rev.* **2014**, *114* (11), 5695-727.
168. Islamoglu, T.; Atilgan, A.; Moon, S.-Y.; Peterson, G. W.; DeCoste, J. B.; Hall, M.; Hupp, J. T.; Farha, O. K., Cerium(IV) Vs Zirconium(IV) Based Metal–Organic Frameworks for Detoxification of a Nerve Agent. *Chem. Mater.* **2017**, *29* (7), 2672-2675.
169. Khan, N. A.; Jung, B. K.; Hasan, Z.; Jung, S. H., Adsorption and Removal of Phthalic Acid and Diethyl Phthalate from Water with Zeolitic Imidazolate and Metal-Organic Frameworks. *J. Hazard. Mater.* **2015**, *282*, 194-200.
170. Cavka, J. H.; Jakobsen, S.; Olsbye, U.; Guillou, N.; Lamberti, C.; Bordiga, S.; Lillerud, K. P., A New Zirconium Inorganic Building Brick Forming Metal Organic Frameworks with Exceptional Stability. *J. Am. Chem. Soc.* **2008**, *130* (42), 13850-13851.
171. Yabushita, M.; Li, P.; Durkin, K. A.; Kobayashi, H.; Fukuoka, A.; Farha, O. K.; Katz, A., Insights into Supramolecular Sites Responsible for Complete Separation of Biomass-Derived Phenolics and Glucose in Metal-Organic Framework Nu-1000. *Langmuir* **2017**, *33* (17), 4129-4137.
172. Wang, T. C.; Vermeulen, N. A.; Kim, I. S.; Martinson, A. B.; Stoddart, J. F.; Hupp, J. T.; Farha, O. K., Scalable Synthesis and Post-Modification of a Mesoporous Metal-Organic Framework Called Nu-1000. *Nat. Protoc* **2016**, *11* (1), 149-162.
173. Chavan, S.; Vitillo, J. G.; Gianolio, D.; Zavorotynska, O.; Civalleri, B.; Jakobsen, S.; Nilsen, M. H.; Valenzano, L.; Lamberti, C.; Lillerud, K. P.; Bordiga, S., H<sub>2</sub>storage in Isostructural Uio-67 and Uio-66 Mofs. *Phys. Chem. Chem. Phys.* **2012**, *14* (5), 1614-1626.
174. Kica, M.; Ronka, S., The Removal of Atrazine from Water Using Specific Polymeric Adsorbent. *Sep Sci Technol* **2014**, *49* (11), 1634-1642.
175. Yan, X. M.; Shi, B. Y.; Lu, J. J.; Feng, C. H.; Wang, D. S.; Tang, H. X., Adsorption and Desorption of Atrazine on Carbon Nanotubes. *J. Colloid Interface Sci.* **2008**, *321* (1), 30-38.
176. Zhao, X.; Ouyang, W.; Hao, F.; Lin, C.; Wang, F.; Han, S.; Geng, X., Properties Comparison of Biochars from Corn Straw with Different Pretreatment and Sorption Behaviour of Atrazine. *Bioresour. Technol.* **2013**, *147*, 338-344.
177. El-Sheikh, A. H.; Sweileh, J. A.; Al-Degs, Y. S.; Insisi, A. A.; Al-Rabady, N., Critical Evaluation and Comparison of Enrichment Efficiency of Multi-Walled Carbon Nanotubes,

- C18 Silica and Activated Carbon Towards Some Pesticides from Environmental Waters. *Talanta* **2008**, *74* (5), 1675-1680.
178. Zhou, Y.; Zhang, F.; Tang, L.; Zhang, J.; Zeng, G.; Luo, L.; Liu, Y.; Wang, P.; Peng, B.; Liu, X., Simultaneous Removal of Atrazine and Copper Using Polyacrylic Acid-Functionalized Magnetic Ordered Mesoporous Carbon from Water: Adsorption Mechanism. *Sci. Rep.* **2017**, *7*, 43831.
  179. Chaparadza, A.; Hossenlopp, J. M., Adsorption Kinetics, Isotherms and Thermodynamics of Atrazine Removal Using a Banana Peel Based Sorbent. *Water Sci. Technol.* **2012**, *65* (5), 940-947.
  180. Lladó, J.; Lao-Luque, C.; Ruiz, B.; Fuente, E.; Solé-Sardans, M.; Dorado, A. D., Role of Activated Carbon Properties in Atrazine and Paracetamol Adsorption Equilibrium and Kinetics. *Process Saf. Environ. Prot.* **2015**, *95*, 51-59.
  181. Iarc Working Group on the Evaluation of Carcinogenic Risk to Humans. Some Chemicals That Cause Tumours of the Kidney or Urinary Bladder in Rodents and Some Other Substances. Lyon (Fr): International Agency for Research on Cancer; 1999. (Iarc Monographs on the Evaluation of Carcinogenic Risks to Humans, No. 73.) 1, Exposure Data. <https://www.ncbi.nlm.nih.gov/books/NBK402084/> (accessed 16 June).
  182. Katz, M. J.; Brown, Z. J.; Colon, Y. J.; Siu, P. W.; Scheidt, K. A.; Snurr, R. Q.; Hupp, J. T.; Farha, O. K., A Facile Synthesis of UiO-66, UiO-67 and Their Derivatives. *Chemical Comm* **2013**, *49* (82), 9449-9451.
  183. Islamoglu, T.; Otake, K.-i.; Li, P.; Buru, C. T.; Peters, A. W.; Akpinar, I.; Garibay, S. J.; Farha, O. K., Revisiting the Structural Homogeneity of Nu-1000, a Zr-Based Metal–Organic Framework. *CrystEngComm* **2018**, *20* (39), 5913-5918.
  184. Lyu, J.; Zhang, X.; Otake, K.-i.; Wang, X.; Li, P.; Li, Z.; Chen, Z.; Zhang, Y.; Wasson, M. C.; Yang, Y.; Bai, P.; Guo, X.; Islamoglu, T.; Farha, O. K., Topology and Porosity Control of Metal–Organic Frameworks through Linker Functionalization. *Chem. Sci.* **2019**, 10.1039/C8SC04220A.
  185. The United Nations World Water Development Report 4: Managing Water under Uncertainty and Risk. World Water Assessment Programme-UNESCO: 2012.
  186. *Guidelines for Drinking-Water Quality: Fourth Edition Incorporating the First Addendum.* World Health Organization: Geneva, 2017.
  187. Rana, D.; Matsuura, T.; Kassim, M. A.; Ismail, A. F., Radioactive Decontamination of Water by Membrane Processes — a Review. *Desalination* **2013**, *321*, 77-92.
  188. Dean, J. G.; Bosqui, F. L.; Lanouette, K. H., Removing Heavy Metals from Waste Water. *Environ. Sci. Technol.* **1972**, *6* (6), 518-522.
  189. Hamilton, D.; Crossley, S., *Pesticide Residues in Food and Drinking Water: Human Exposure and Risks.* John Wiley & Sons: Hoboken, New Jersey, 2004.
  190. Watkinson, A.; Murby, E.; Kolpin, D. W.; Costanzo, S., The Occurrence of Antibiotics in an Urban Watershed: From Wastewater to Drinking Water. *Sci. Total Environ.* **2009**, *407* (8), 2711-2723.
  191. Järup, L., Hazards of Heavy Metal Contamination. *Br. Med. Bull.* **2003**, *68* (1), 167-182.
  192. Kamiya, K.; Ozasa, K.; Akiba, S.; Niwa, O.; Kodama, K.; Takamura, N.; Zaharieva, E. K.; Kimura, Y.; Wakeford, R., Long-Term Effects of Radiation Exposure on Health. *Lancet* **2015**, *386* (9992), 469-478.

193. Lyon, J. L.; Alder, S. C.; Mary Bishop, S.; Scholl, A.; Reading, J. C.; Holubkov, R.; Sheng, X.; White, G. L.; Hegmann, K. T.; Anspaugh, L.; Hoffman, F. O.; Simon, S. L.; Thomas, B.; Carroll, R.; Meikle, A. W., Thyroid Disease Associated with Exposure to the Nevada Nuclear Weapons Test Site Radiation: A Reevaluation Based on Corrected Dosimetry and Examination Data. *Epidemiology* **2006**, *17* (6), 604-614.
194. Çeçen, F.; Aktas, Ö., *Activated Carbon for Water and Wastewater Treatment: Integration of Adsorption and Biological Treatment*. John Wiley & Sons: Hoboken, New Jersey, 2011.
195. Kemp, K. C.; Seema, H.; Saleh, M.; Le, N. H.; Mahesh, K.; Chandra, V.; Kim, K. S., Environmental Applications Using Graphene Composites: Water Remediation and Gas Adsorption. *Nanoscale* **2013**, *5* (8), 3149-3171.
196. Pan, B.; Pan, B.; Zhang, W.; Lv, L.; Zhang, Q.; Zheng, S., Development of Polymeric and Polymer-Based Hybrid Adsorbents for Pollutants Removal from Waters. *Chem. Eng. J.* **2009**, *151* (1), 19-29.
197. Margeta, K.; Logar, N. Z.; Šiljeg, M.; Farkaš, A., *Natural Zeolites in Water Treatment—How Effective Is Their Use*. InTech: Rijeka, Croatia, 2013; p 81-112.
198. Furukawa, H.; Cordova, K. E.; O’Keeffe, M.; Yaghi, O. M., The Chemistry and Applications of Metal-Organic Frameworks. *Science* **2013**, *341* (6149), 1230444.
199. Zhou, H. C.; Long, J. R.; Yaghi, O. M., Introduction to Metal-Organic Frameworks. *Chem. Rev.* **2012**, *112* (2), 673-4.
200. Zhou, H.-C. J.; Kitagawa, S., Metal–Organic Frameworks (Mofs). *Chem. Soc. Rev.* **2014**, *43* (16), 5415-5418.
201. Eddaoudi, M.; Moler, D. B.; Li, H.; Chen, B.; Reineke, T. M.; O’Keeffe, M.; Yaghi, O. M., Modular Chemistry: Secondary Building Units as a Basis for the Design of Highly Porous and Robust Metal–Organic Carboxylate Frameworks. *Acc. Chem. Res.* **2001**, *34* (4), 319-330.
202. Perry Iv, J. J.; Perman, J. A.; Zaworotko, M. J., Design and Synthesis of Metal–Organic Frameworks Using Metal–Organic Polyhedra as Supramolecular Building Blocks. *Chem. Soc. Rev.* **2009**, *38* (5), 1400-1417.
203. Maurin, G.; Serre, C.; Cooper, A.; Férey, G., The New Age of Mofs and of Their Porous-Related Solids. *Chem. Soc. Rev.* **2017**, *46* (11), 3104-3107.
204. Yaghi, O. M.; O’Keeffe, M.; Ockwig, N. W.; Chae, H. K.; Eddaoudi, M.; Kim, J., Reticular Synthesis and the Design of New Materials. *Nature* **2003**, *423* (6941), 705-14.
205. Chen, Z.; Hanna, S. L.; Redfern, L. R.; Alezi, D.; Islamoglu, T.; Farha, O. K., Reticular Chemistry in the Rational Synthesis of Functional Zirconium Cluster-Based Mofs. *Coord. Chem. Rev.* **2019**, *386*, 32-49.
206. Yuan, S.; Qin, J.-S.; Lollar, C. T.; Zhou, H.-C., Stable Metal–Organic Frameworks with Group 4 Metals: Current Status and Trends. *ACS Cent. Sci.* **2018**, *4* (4), 440-450.
207. Burtch, N. C.; Jasuja, H.; Walton, K. S., Water Stability and Adsorption in Metal–Organic Frameworks. *Chem. Rev.* **2014**, *114* (20), 10575-10612.
208. Rieth, A. J.; Wright, A. M.; Dincă, M., Kinetic Stability of Metal–Organic Frameworks for Corrosive and Coordinating Gas Capture. *Nat. Rev. Mater.* **2019**, *4* (11), 708-725.
209. Marshall, R. J.; Forgan, R. S., Postsynthetic Modification of Zirconium Metal-Organic Frameworks. *Eur. J. Inorg. Chem.* **2016**, *2016* (27), 4310-4331.

210. Li, J.; Wang, X.; Zhao, G.; Chen, C.; Chai, Z.; Alsaedi, A.; Hayat, T.; Wang, X., Metal–Organic Framework-Based Materials: Superior Adsorbents for the Capture of Toxic and Radioactive Metal Ions. *Chem. Soc. Rev.* **2018**, *47* (7), 2322-2356.
211. Feng, M.; Zhang, P.; Zhou, H.-C.; Sharma, V. K., Water-Stable Metal-Organic Frameworks for Aqueous Removal of Heavy Metals and Radionuclides: A Review. *Chemosphere* **2018**, *209*, 783-800.
212. Sun, D. T.; Peng, L.; Reeder, W. S.; Moosavi, S. M.; Tiana, D.; Britt, D. K.; Oveisi, E.; Queen, W. L., Rapid, Selective Heavy Metal Removal from Water by a Metal–Organic Framework/Polydopamine Composite. *ACS Cent. Sci.* **2018**, *4* (3), 349-356.
213. Drout, R. J.; Robison, L.; Chen, Z.; Islamoglu, T.; Farha, O. K., Zirconium Metal–Organic Frameworks for Organic Pollutant Adsorption. *Trends Chem.* **2019**, *1* (3), 304-317.
214. Hasan, Z.; Jhung, S. H., Removal of Hazardous Organics from Water Using Metal-Organic Frameworks (Mofs): Plausible Mechanisms for Selective Adsorptions. *J. Hazard. Mater.* **2015**, *283*, 329-339.
215. Dhaka, S.; Kumar, R.; Deep, A.; Kurade, M. B.; Ji, S.-W.; Jeon, B.-H., Metal–Organic Frameworks (Mofs) for the Removal of Emerging Contaminants from Aquatic Environments. *Coord. Chem. Rev.* **2019**, *380*, 330-352.
216. Freire, E.; Mayorga, O. L.; Straume, M., Isothermal Titration Calorimetry. *Anal. Chem.* **1990**, *62* (18), 950A-959A.
217. Freyer, M. W.; Lewis, E. A., Isothermal Titration Calorimetry: Experimental Design, Data Analysis, and Probing Macromolecule/Ligand Binding and Kinetic Interactions. In *Methods in Cell Biology*, Academic Press: 2008; Vol. 84, pp 79-113.
218. Velazquez-Campoy, A.; Freire, E., Isothermal Titration Calorimetry to Determine Association Constants for High-Affinity Ligands. *Nat. Protoc.* **2006**, *1* (1), 186-191.
219. Leavitt, S.; Freire, E., Direct Measurement of Protein Binding Energetics by Isothermal Titration Calorimetry. *Curr. Opin. Struct. Biol.* **2001**, *11* (5), 560-566.
220. Pierce, M. M.; Raman, C.; Nall, B. T., Isothermal Titration Calorimetry of Protein–Protein Interactions. *Methods* **1999**, *19* (2), 213-221.
221. Penn, C. J.; Gonzalez, J. M.; Chagas, I., Investigation of Atrazine Sorption to Biochar with Titration Calorimetry and Flow-through Analysis: Implications for Design of Pollution-Control Structures. *Front. Chem.* **2018**, *6*, 307.
222. Moreno-Pirajan, J. C.; Giraldo, L., Design, Construction, and Calibration of an Isothermal Titration Calorimeter and Its Application in the Study of the Adsorption of Phenolic Compounds. *Rev. Sci. Instrum.* **2012**, *83* (1), 015117.
223. Agostoni, V.; Anand, R.; Monti, S.; Hall, S.; Maurin, G.; Horcajada, P.; Serre, C.; Bouchemal, K.; Gref, R., Impact of Phosphorylation on the Encapsulation of Nucleoside Analogues within Porous Iron(III) Metal-Organic Framework Mil-100(Fe) Nanoparticles. *J. Mater. Chem. B* **2013**, *1* (34), 4231-4242.
224. Aykaç, A. N., M.; Malanga, M.; Agostoni, V.; Casas-Solvas, J. M.; Fenyvesi, É.; Gref, R.; Vargas-Berenguel, A., A Non-Covalent “Click Chemistry” Strategy to Efficiently Coat Highly Porous Mof Nanoparticles with a Stable Polymeric Shell. *Biochim. Biophys. Acta* **2017**, *1861*, 1606-1616.

225. Kato, S.; Drout, R. J.; Farha, O. K., Isothermal Titration Calorimetry to Investigate Uremic Toxins Adsorbing onto Metal–Organic Frameworks. *Cell Rep. Phys. Sci.* **2020**, *1* (1), 100006.
226. Franz, J. E.; Mao, M. K.; Sikorski, J. A., *Glyphosate: A Unique Global Herbicide*. American Chemical Society: 1997.
227. Pankajakshan, A.; Sinha, M.; Ojha, A. A.; Mandal, S., Water-Stable Nanoscale Zirconium-Based Metal–Organic Frameworks for the Effective Removal of Glyphosate from Aqueous Media. *ACS Omega* **2018**, *3* (7), 7832-7839.
228. Yang, J.; Dai, Y.; Zhu, X.; Wang, Z.; Li, Y.; Zhuang, Q.; Shi, J.; Gu, J., Metal–Organic Frameworks with Inherent Recognition Sites for Selective Phosphate Sensing through Their Coordination-Induced Fluorescence Enhancement Effect. *J. Mater. Chem. A* **2015**, *3* (14), 7445-7452.
229. Yang, Q.; Wang, J.; Chen, X.; Yang, W.; Pei, H.; Hu, N.; Li, Z.; Suo, Y.; Li, T.; Wang, J., The Simultaneous Detection and Removal of Organophosphorus Pesticides by a Novel Zr-Mof Based Smart Adsorbent. *J. Mater. Chem. A* **2018**, *6* (5), 2184-2192.
230. Chen, H.; Liao, P.; Mendonca, M. L.; Snurr, R. Q., Insights into Catalytic Hydrolysis of Organophosphate Warfare Agents by Metal–Organic Framework Nu-1000. *J. Phys. Chem. C* **2018**, *122* (23), 12362-12368.
231. Troya, D., Reaction Mechanism of Nerve-Agent Decomposition with Zr-Based Metal Organic Frameworks. *J. Phys. Chem. C* **2016**, *120* (51), 29312-29323.
232. Mondloch, J. E.; Katz, M. J.; Isley Iii, W. C.; Ghosh, P.; Liao, P.; Bury, W.; Wagner, G. W.; Hall, M. G.; DeCoste, J. B.; Peterson, G. W.; Snurr, R. Q.; Cramer, C. J.; Hupp, J. T.; Farha, O. K., Destruction of Chemical Warfare Agents Using Metal–Organic Frameworks. *Nat. Mater.* **2015**, *14* (5), 512-516.
233. Sprankle, P.; Meggitt, W. F.; Penner, D., Adsorption, Mobility, and Microbial Degradation of Glyphosate in the Soil. *Weed Sci.* **1975**, *23* (3), 229-234.
234. Velázquez Campoy, A.; Freire, E., ITC in the Post-Genomic Era...? Priceless. *Biophys. Chem.* **2005**, *115* (2), 115-124.
235. Speight, J. G., Chapter 5 - Sorption, Dilution, and Dissolution. In *Reaction Mechanisms in Environmental Engineering*, Speight, J. G., Ed. Butterworth-Heinemann: 2018; pp 165-201.
236. Peters, A. W.; Otake, K.; Platero-Prats, A. E.; Li, Z.; DeStefano, M. R.; Chapman, K. W.; Farha, O. K.; Hupp, J. T., Site-Directed Synthesis of Cobalt Oxide Clusters in a Metal–Organic Framework. *ACS Appl. Mater. Inter.* **2018**, *10* (17), 15073-15078.
237. Garibay, S. J.; Iordanov, I.; Islamoglu, T.; DeCoste, J. B.; Farha, O. K., Synthesis and Functionalization of Phase-Pure Nu-901 for Enhanced CO<sub>2</sub> Adsorption: The Influence of a Zirconium Salt and Modulator on the Topology and Phase Purity. *CrystEngComm* **2018**, *20* (44), 7066-7070.
238. Liu, T.-F.; Vermeulen, N. A.; Howarth, A. J.; Li, P.; Sarjeant, A. A.; Hupp, J. T.; Farha, O. K., Adding to the Arsenal of Zirconium-Based Metal–Organic Frameworks: The Topology as a Platform for Solvent-Assisted Metal Incorporation. *Eur. J. Inorg. Chem.* **2016**, *2016* (27), 4349-4352.

239. Yu, J.; Park, J.; Van Wyk, A.; Rumbles, G.; Deria, P., Excited-State Electronic Properties in Zr-Based Metal–Organic Frameworks as a Function of a Topological Network. *J. Am. Chem. Soc.* **2018**, *140* (33), 10488-10496.
240. Liu, W.-G.; Truhlar, D. G., Computational Linker Design for Highly Crystalline Metal–Organic Framework Nu-1000. *Chem. Mater.* **2017**, *29* (19), 8073-8081.
241. Bianconi, M. L., Chapter Ten - Avoiding Buffer Interference in Itc Experiments: A Case Study from the Analysis of Entropy-Driven Reactions of Glucose-6-Phosphate Dehydrogenase. In *Methods in Enzymology*, Feig, A. L., Ed. Academic Press: 2016; Vol. 567, pp 237-256.
242. Goswami, S.; Ray, D.; Otake, K.-i.; Kung, C.-W.; Garibay, S. J.; Islamoglu, T.; Atilgan, A.; Cui, Y.; Cramer, C. J.; Farha, O. K.; Hupp, J. T., A Porous, Electrically Conductive Hexa-Zirconium(IV) Metal–Organic Framework. *Chem. Sci.* **2018**, *9* (19), 4477-4482.
243. Wang, X.; Zhang, X.; Li, P.; Otake, K.-i.; Cui, Y.; Lyu, J.; Krzyaniak, M. D.; Zhang, Y.; Li, Z.; Liu, J.; Buru, C. T.; Islamoglu, T.; Wasielewski, M. R.; Li, Z.; Farha, O. K., Vanadium Catalyst on Isostructural Transition Metal, Lanthanide, and Actinide Based Metal–Organic Frameworks for Alcohol Oxidation. *J. Am. Chem. Soc.* **2019**, *141* (20), 8306-8314.
244. Rosen, A. S.; Notestein, J. M.; Snurr, R. Q., Identifying Promising Metal–Organic Frameworks for Heterogeneous Catalysis Via High-Throughput Periodic Density Functional Theory. *J. Comput. Chem.* **2019**, *40* (12), 1305-1318.
245. Kresse, G.; Furthmüller, J., Efficiency of Ab-Initio Total Energy Calculations for Metals and Semiconductors Using a Plane-Wave Basis Set. *Comput. Mater. Sci.* **1996**, *6* (1), 15-50.
246. Kresse, G.; Furthmüller, J., Efficient Iterative Schemes for Ab Initio Total-Energy Calculations Using a Plane-Wave Basis Set. *Phys. Rev. B* **1996**, *54* (16), 11169-11186.
247. Perdew, J. P.; Burke, K.; Ernzerhof, M., Generalized Gradient Approximation Made Simple. *Phys. Rev. Lett.* **1996**, *77* (18), 3865-3868.
248. Grimme, S.; Antony, J.; Ehrlich, S.; Krieg, H., A Consistent and Accurate Ab Initio Parametrization of Density Functional Dispersion Correction (Dft-D) for the 94 Elements H-Pu. *J. Chem. Phys.* **2010**, *132* (15), 154104.
249. Grimme, S.; Ehrlich, S.; Goerigk, L., Effect of the Damping Function in Dispersion Corrected Density Functional Theory. *J. Comput. Chem.* **2011**, *32* (7), 1456-1465.
250. Blöchl, P. E., Projector Augmented-Wave Method. *Phys. Rev. B* **1994**, *50* (24), 17953-17979.
251. Marsh, H.; Reinoso, F. R., *Activated Carbon*. Elsevier: 2006.
252. Hankammer, H. Water Treatment Device. 3747767. July 24th, 1973.
253. Charles Fritter, D. J. Animal Litter Containing Activated Carbon. 20070017453. January 25th, 2007.
254. Sanchez, N.; Fayne, R.; Burroway, B., Charcoal: An Ancient Material with a New Face. *Clin. Dermatol.* **2020**, *38* (2), 262-264.
255. Parlett, C. M.; Wilson, K.; Lee, A. F., Hierarchical Porous Materials: Catalytic Applications. *Chem. Soc. Rev.* **2013**, *42* (9), 3876-3893.

256. Research, G. V. *Catalyst Market Size, Share & Trends Analysis Report by Raw Material (Chemical Compounds, Zeolites, Metals), by Product (Heterogeneous, Homogeneous), by Application, by Region, and Segment Forecasts, 2020 - 2027*; 2020.
257. Baerlocher, C.; McCusker, L. B.; Olson, D. H., *Atlas of Zeolite Framework Types*. Elsevier: 2007.
258. Gottardi, G.; Galli, E., *Natural Zeolites*. Springer Science & Business Media: 2012; Vol. 18.
259. Jacobs, P.; Flanigen, E. M.; Jansen, J.; van Bekkum, H., *Introduction to Zeolite Science and Practice*. Elsevier: 2001.
260. Corma, A., Inorganic Solid Acids and Their Use in Acid-Catalyzed Hydrocarbon Reactions. *Chem. Rev.* **1995**, *95* (3), 559-614.
261. Zhou, H.-C.; Long, J. R.; Yaghi, O. M., Introduction to Metal–Organic Frameworks. *Chem. Rev.* **2012**, *112* (2), 673-674.
262. Furukawa, H.; Cordova, K. E.; O’Keeffe, M.; Yaghi, O. M., The Chemistry and Applications of Metal-Organic Frameworks. *Science* **2013**, *341* (6149).
263. Ding, S.-Y.; Wang, W., Covalent Organic Frameworks (Cofs): From Design to Applications. *Chem. Soc. Rev.* **2013**, *42* (2), 548-568.
264. Islamoglu, T.; Behera, S.; Kahveci, Z.; Tessema, T.-D.; Jena, P.; El-Kaderi, H. M., Enhanced Carbon Dioxide Capture from Landfill Gas Using Bifunctionalized Benzimidazole-Linked Polymers. *ACS Appl. Mater. Inter.* **2016**, *8* (23), 14648-14655.
265. Kaur, P.; Hupp, J. T.; Nguyen, S. T., Porous Organic Polymers in Catalysis: Opportunities and Challenges. *ACS Catal.* **2011**, *1* (7), 819-835.
266. He, Y.; Xiang, S.; Chen, B., A Microporous Hydrogen-Bonded Organic Framework for Highly Selective C<sub>2</sub>H<sub>2</sub>/C<sub>2</sub>H<sub>4</sub> Separation at Ambient Temperature. *J. Am. Chem. Soc.* **2011**, *133* (37), 14570-14573.
267. Hisaki, I.; Xin, C.; Takahashi, K.; Nakamura, T., Designing Hydrogen-Bonded Organic Frameworks (Hofs) with Permanent Porosity. *Angew. Chem.-Int. Edit.* **2019**, *58* (33), 11160-11170.
268. Cui, P.; Svensson Grape, E.; Spackman, P. R.; Wu, Y.; Clowes, R.; Day, G. M.; Inge, A. K.; Little, M. A.; Cooper, A. I., An Expandable Hydrogen-Bonded Organic Framework Characterized by Three-Dimensional Electron Diffraction. *J. Am. Chem. Soc.* **2020**, *142* (29), 12743-12750.
269. Slater, A. G.; Cooper, A. I., Function-Led Design of New Porous Materials. *Science* **2015**, *348* (6238), 8075.
270. Hoshino, M.; Khutia, A.; Xing, H.; Inokuma, Y.; Fujita, M., The Crystalline Sponge Method Updated. *IUCrJ* **2016**, *3* (2), 139-151.
271. Inokuma, Y.; Arai, T.; Fujita, M., Networked Molecular Cages as Crystalline Sponges for Fullerenes and Other Guests. *Nat. Chem.* **2010**, *2* (9), 780-783.
272. Lee, S.; Kapustin, E. A.; Yaghi, O. M., Coordinative Alignment of Molecules in Chiral Metal-Organic Frameworks. *Science* **2016**, *353* (6301), 808-811.
273. Wahiduzzaman, M.; Lenzen, D.; Maurin, G.; Stock, N.; Wharmby, M. T., Rietveld Refinement of Mil-160 and Its Structural Flexibility Upon H<sub>2</sub>O and N<sub>2</sub> Adsorption. *Eur. J. Inorg. Chem.* **2018**, *2018* (32), 3626-3632.

274. Suescun, L.; Wang, J.; Faccio, R.; Peinado, G.; Torres, J.; Kremer, C.; Burrow, R. A., The Structure of Cubic Mof  $[Ca(H_2O)_6]\{Ca_3(O_2CCH_2)_3\}_2 \cdot 4H_2O$ . A Comparison between Structural Models Obtained from Rietveld Refinement of Conventional and Synchrotron X-Ray Powder Diffraction Data and Standard Refinement of Single-Crystal X-Ray Diffraction Data. *Powder Diff.* **2012**, *27* (4), 232.
275. Buru, C. T.; Platero-Prats, A. E.; Chica, D. G.; Kanatzidis, M. G.; Chapman, K. W.; Farha, O. K., Thermally Induced Migration of a Polyoxometalate within a Metal–Organic Framework and Its Catalytic Effects. *J. Mater. Chem. A* **2018**, *6* (17), 7389-7394.
276. Parise, J. B.; Chen, X.; Plonka, A. M.; Woerner, W. R.; Banerjee, D.; Connors, D.; Goroff, N., Xrd-Dsc: A Screening Tool for Identifying Effective Mofs for Selective Gas Sorption from Humid Gas Streams. *Powder Diff.* **2019**, *34* (1), 3-12.
277. Chen, Z.; Wasson, M. C.; Drout, R. J.; Robison, L.; Idrees, K. B.; Knapp, J. G.; Son, F. A.; Zhang, X.; Hierse, W.; Kühn, C., The State of the Field: From Inception to Commercialization of Metal–Organic Frameworks. *Faraday Discuss.* **2021**, *225*, 9-69.
278. James, S. L., Metal-Organic Frameworks. *Chem. Soc. Rev.* **2003**, *32* (5), 276-288.
279. Guillerm, V.; Kim, D.; Eubank, J. F.; Luebke, R.; Liu, X.; Adil, K.; Lah, M. S.; Eddaoudi, M., A Supramolecular Building Approach for the Design and Construction of Metal–Organic Frameworks. *Chem. Soc. Rev.* **2014**, *43* (16), 6141-6172.
280. Tan, J. C.; Cheetham, A. K., Mechanical Properties of Hybrid Inorganic–Organic Framework Materials: Establishing Fundamental Structure–Property Relationships. *Chem. Soc. Rev.* **2011**, *40* (2), 1059-1080.
281. Wilmer, C. E.; Farha, O. K.; Bae, Y.-S.; Hupp, J. T.; Snurr, R. Q., Structure–Property Relationships of Porous Materials for Carbon Dioxide Separation and Capture. *Energy Environ. Sci.* **2012**, *5* (12), 9849-9856.
282. Wu, D.; Yang, Q.; Zhong, C.; Liu, D.; Huang, H.; Zhang, W.; Maurin, G., Revealing the Structure–Property Relationships of Metal–Organic Frameworks for CO<sub>2</sub> Capture from Flue Gas. *Langmuir* **2012**, *28* (33), 12094-12099.
283. Li, H.; Wang, K.; Sun, Y.; Lollar, C. T.; Li, J.; Zhou, H.-C., Recent Advances in Gas Storage and Separation Using Metal–Organic Frameworks. *Mater. Today* **2018**, *21* (2), 108-121.
284. Yang, D.; Gates, B. C., Catalysis by Metal Organic Frameworks: Perspective and Suggestions for Future Research. *ACS Catal.* **2019**, *9* (3), 1779-1798.
285. Chughtai, A. H.; Ahmad, N.; Younus, H. A.; Laypkov, A.; Verpoort, F., Metal–Organic Frameworks: Versatile Heterogeneous Catalysts for Efficient Catalytic Organic Transformations. *Chem. Soc. Rev.* **2015**, *44* (19), 6804-6849.
286. Li, S.; Chen, Y.; Pei, X.; Zhang, S.; Feng, X.; Zhou, J.; Wang, B., Water Purification: Adsorption over Metal-Organic Frameworks. *Chin. J. Chem.* **2016**, *34* (2), 175-185.
287. Boddula, R.; Ahamed, M. I.; Asiri, A. M., *Applications of Metal-Organic Frameworks and Their Derived Materials*. John Wiley & Sons: 2020.
288. Peng, Y.; Huang, H.; Zhang, Y.; Kang, C.; Chen, S.; Song, L.; Liu, D.; Zhong, C., A Versatile Mof-Based Trap for Heavy Metal Ion Capture and Dispersion. *Nat. Commun.* **2018**, *9* (1), 187.
289. Chen, Y.; Zhang, X.; Wang, X.; Drout, R. J.; Mian, M. R.; Cao, R.; Ma, K.; Xia, Q.; Li, Z.; Farha, O. K., Insights into the Structure–Activity Relationship in Aerobic Alcohol

- Oxidation over a Metal–Organic–Framework-Supported Molybdenum(VI) Catalyst. *J. Am. Chem. Soc.* **2021**.
290. Abdel-Mageed, A. M.; Rungtaweeveranit, B.; Parlinska-Wojtan, M.; Pei, X.; Yaghi, O. M.; Behm, R. J. r., Highly Active and Stable Single-Atom Cu Catalysts Supported by a Metal–Organic Framework. *J. Am. Chem. Soc.* **2019**, *141* (13), 5201-5210.
291. He, X.; Looker, B. G.; Dinh, K. T.; Stubbs, A. W.; Chen, T.; Meyer, R. J.; Serna, P.; Roman-Leshkov, Y.; Lancaster, K. M.; Dinca, M., Cerium (IV) Enhances the Catalytic Oxidation Activity of Single-Site Cu Active Sites in Mofs. *ACS Catal.* **2020**, *10* (14), 7820-7825.
292. Thiam, Z.; Abou-Hamad, E.; Dereli, B.; Liu, L.; Emwas, A.-H.; Ahmad, R.; Jiang, H.; Isah, A. A.; Ndiaye, P. B.; Taoufik, M., Extension of Surface Organometallic Chemistry to Metal–Organic Frameworks: Development of a Well-Defined Single Site [(= Zr–O–) W (= O)(CH<sub>2</sub> T Bu) 3] Olefin Metathesis Catalyst. *J. Am. Chem. Soc.* **2020**, *142* (39), 16690-16703.
293. Baek, J.; Rungtaweeveranit, B.; Pei, X.; Park, M.; Fakra, S. C.; Liu, Y.-S.; Matheu, R.; Alshmiri, S. A.; Alshehri, S.; Trickett, C. A., Bioinspired Metal–Organic Framework Catalysts for Selective Methane Oxidation to Methanol. *J. Am. Chem. Soc.* **2018**, *140* (51), 18208-18216.
294. Drout, R. J.; Kato, S.; Chen, H.; Son, F. A.; Otake, K.-i.; Islamoglu, T.; Snurr, R. Q.; Farha, O. K., Isothermal Titration Calorimetry to Explore the Parameter Space of Organophosphorus Agrochemical Adsorption in Mofs. *J. Am. Chem. Soc.* **2020**, *142* (28), 12357-12366.
295. Freire, E.; Mayorga, O. L.; Straume, M., Isothermal Titration Calorimetry. *Anal. Chem.* **1990**, *62* (18), 950-959.
296. Wei, Y.-B.; Wang, M.-J.; Luo, D.; Huang, Y.-L.; Xie, M.; Lu, W.; Shu, X.; Li, D., Ultrasensitive and Highly Selective Detection of Formaldehyde Via an Adenine-Based Biological Metal–Organic Framework. *Mater. Chem. Front.* **2021**, *5* (5), 2416-2424.
297. Angewandte Chemie International Edition Proceedings of the National Academy of Sciences Wang, T. C.; Vermeulen, N. A.; Kim, I. S.; Martinson, A. B. F.; Stoddart, J. F.; Hupp, J. T.; Farha, O. K., Scalable Synthesis and Post-Modification of a Mesoporous Metal–Organic Framework Called Nu-1000. *Nat. Protoc.* **2016**, *11* (1), 149-162.
298. Goldberg, R. N.; Kishore, N.; Lennen, R. M., Thermodynamic Quantities for the Ionization Reactions of Buffers. *J. Phys. Chem. Ref. Data* **2002**, *31* (2), 231-370.
299. Drout, R. J.; Howarth, A. J.; Otake, K.-i.; Islamoglu, T.; Farha, O. K., Efficient Extraction of Inorganic Selenium from Water by a Zr Metal–Organic Framework: Investigation of Volumetric Uptake Capacity and Binding Motifs. *CrystEngComm* **2018**, *20* (40), 6140-6145.
300. Klet, R. C.; Liu, Y.; Wang, T. C.; Hupp, J. T.; Farha, O. K., Evaluation of Brønsted Acidity and Proton Topology in Zr- and Hf-Based Metal–Organic Frameworks Using Potentiometric Acid–Base Titration. *J. Mater. Chem. A* **2016**, *4* (4), 1479-1485.
301. Lin, K.-Y. A.; Chen, S.-Y.; Jochems, A. P., Zirconium-Based Metal Organic Frameworks: Highly Selective Adsorbents for Removal of Phosphate from Water and Urine. *Mater. Chem. Phys.* **2015**, *160*, 168-176.